RHEOLOGY AND FLOW EMPLACEMENT PROCESSES OF THE 1954 LAVAS, MOUNT NGAURUHOE

A thesis

submitted in partial fulfilment

of the requirements for the Degree

of

Masters of Science

in Earth and Ocean Sciences

at

The University of Waikato

By

Fiona Sanders

THE UNIVERSITY OF
WAIKATO
Te Whare Wānanga o Waikato

University of Waikato
2010

"Ka riro au i te tonga! Haria mai he ahi moku!"

("I am borne away in the cold south wind – I perish from the cold! Send fire to warm me!")

According to Maori legend this was the prayer offered up by Ngatoro-i-rangi, a sacred Araki (high priest), after he was caught in a snow storm on the peak of one of the mountains of the central North Island. His sisters in Hawaiki heard his prayer and sent fire demons via White Island, Rotorua and Taupo to the mountain top where he stood. Ngatoro-i-rangi was so grateful for the fire that issued from the mountian top and saved his life that he threw a slave into the fire. The slave's name was Auruhoe and thereafter the mountain was called Ngauruhoe.

Fairy folk Tales of the Maori, James Cowan, Whitcombe and Tombs Ltd, 1925.
Sourced: New Zealand Electronic Text Centre
http://www.nzetc.org/tm/scholarly/tei-CowFair-t1-body-d1-d1.html

Western flanks of Mount Ngauruhoe. 1954 lava flows are the dark flow deposits (Hobden, 1997).

Abstract

The rheology and emplacement dynamics of basaltic and rhyolitic lava flows have been studied extensively, leading to the development of numerous rheological and flow behaviour models; however, the flow dynamics of more intermediate composition lavas, particularly those emplaced on relatively steep slopes, is less well-constrained. The 1954-55 eruption of Mount Ngauruhoe, a young, composite cone of the Tongariro Volcanic Centre, generated at least 11, well-preserved, spatter-fed, basaltic andesite a'a lavas on the steep, north-west flanks of the cone. The rheological properties and flow dynamics of these lavas are quantified by incorporating morphological, petrographic and geochemical data collected from these flow deposits into a range of existing numerical models, and the results compared with documented eye-witness accounts.

The lava flow deposits are typically long, narrow, discrete units characterised by comparable morphological traits on the steep slopes of the cone and varying in dimension, morphology and flow surface features on the shallower slopes. Flow surfaces are typically autobrecciated and display a large-scale, lateral trend in clast size and morphology across flow widths. The 1954 lavas are petrographically and geochemically homogenous with no apparent trends associated with successively emplaced lava flows. The rheological properties of the lavas at the time of initial flow advance are therefore assumed to be comparable for each flow. Lava viscosity was estimated at 10^2 to 10^4 Pa s for the temperature range 1150 to 950°C. Yield strength was difficult to quantify but is assumed in this study to be relatively low (~ 25 Pa). Calculated flow velocity, effusion rate and emplacement duration are not well-constrained against documented eye-witness accounts. Mean flow velocity (0.03 to 0.04 m s^{-1}) was estimated from eye-witness reports, and used to determine flow emplacement durations between ~ 2 to 48 hours, comparable with documented duration times. Effusion rates could not be definitively quantified but flow deposit morphology and documented accounts indicate that intermittent episodes of high effusion rates over a short duration were associated with the emplacement of the 1954 lavas.

Three major controls on the emplacement of the 1954 lava flows have been identified. Effusion rate and duration was the primary control on the development

of single unit lava flows, flow channel drainage on steep slopes and in limiting run-out distances from the vent. Low initial viscosity and yield strength promoted high flow velocities on steep slopes and low surface cooling rates. Relatively short flow emplacement duration times precluded significant downflow viscosity and yield strength increases. Slope gradient and topographic obstacles were major controls on flow emplacement processes. Slope gradient was the dominant control on flow velocity, flow width and depth and surface autobrecciation, while morphology, flow path direction and surface folding were constrained by local slope gradient variations and/or topographic obstacles.

Acknowledgments

This project would not have been possible without the invaluable assistance, support and encouragement I have received from so many people and I am honoured to have the opportunity to acknowledge and thank them in these pages.

I am indebted to my supervisors, Associate Professor Roger Briggs and Dr Adrian Pittari, University of Waikato and Dr Gill Jolly, GNS Science, Wairakei for their guidance, support, endless patience, and importantly the many hours spent editing chapters. I would especially like to thank Gill for suggesting this project and for guidance in choosing appropriate rheology models. Although this research has been challenging at times it has also been a huge and rewarding learning curve.

Also thanks to GNS Science for providing the resources (including a helicopter trip!) for the terrestrial LiDar survey, and in particular the technical wizardry of Neville Palmer, GNS Science, Avalon who performed the TLS survey and developed the DEM model. Thank you also to Geoff Kilgour, GNS Science, Wairakei for assisting with the TLS survey and especially for the much appreciated support and encouragement throughout the duration of this project.

As a fully-fledged numerophobe, choosing a research topic involving numerical modelling was perhaps not the smartest move and I would still be wrestling with rheology equations without the generosity of two researchers whose models have been used in this thesis. Thank you to Hejiu Hui and Aaron Lyman for sending me calculation spreadsheets, explaining the models and answering my questions. Additional thanks must also go to Associate Professor Chris Hendy and Dr Willem de Lange, University of Waikato for geochemical and mathematical assistance.

A very special thank you to all my field assistants, Peach, Alison (& Duck), Bolton, Sarah and Rob, Bram and J9, for the long hours spent in the field with me, carrying rocks, holding measuring staffs, providing a scale in photographs, and generally not looking too bored while I took copious notes and photographs. Thanks for all your hard work and enthusiasm, and especially for writing and performing the best field mascot songs in the world. To our field mascot, Mr Chicken Stick, thanks for being not only a measuring staff, but a walking stick,

guidance system (for lost field assistants), and being the focus of endless hours of entertainment.

Laboratory analysis and field work preparation would not have been possible without the expertise and guidance of the Department of Earth and Ocean Sciences technical staff, Annette Rodgers, Renat Radosinsky, Ganqing Xu, Chris McKinnon and Steve Cook.

My grateful thanks goes to the University of Waikato (Master's Scholarship) and the Broad Memorial Fund for their generous financial support. In addition, I would also like to thank the Department of Conservation for their kind permission to carry out field work and collect rock samples from the National Park, and Linda and Paul at Mangatepopo School Camp for the regular use of the 'flat' at short notice and their welcoming hospitality.

A massive thank you to my fellow EOS colleagues, Renee, Larissa, Ben, Dirk, Andrew, Becky and Bashira, for the overwhelming friendship and support, for keeping the thesis madness at bay, and for keeping me young.

Finally I could not have survived this experience without the love, friendship, patience and understanding of all my friends and family, particularly Sarah, Tracey, Brad, Tehani, Leah, Kim, Marie and Louise. To mum, Bobby and dad, thank you for your constant encouragement, support and unwavering faith in me, and especially to mum for planting the 'volcanology' seed many years ago in Glasgow.

Table of Contents

CHAPTER 3: PETROGRAPHIC, MINERALOGICAL & GEOCHEMICAL CHARACTERSITCS

CHAPTER 4: RHEOLOGICAL PARAMETERS

List of Figures

CHAPTER 1

CHAPTER 2

CHAPTER 3

CHAPTER 4

CHAPTER 5

List of Tables

CHAPTER 1

CHAPTER 2

CHAPTER 3

CHAPTER 4

CHAPTER 1

Introduction

1.1 INTRODUCTION

Lava flows are outpourings of hot, molten rock that emerge from vents or fissures and spread longitudinally across the ground surface. Lava flows rarely pose a direct threat to human life because they advance at relatively slow speeds, enabling people to easily escape harm (Peterson and Tilling, 2000); although 200 hundred lives were lost during two recent (1977, 2002) eruptions at Mount Nyiragongo, Democratic Republic of Congo, as the direct result of the rapid advance of lava down the steep slopes of the volcano (Favalli *et al*., 2009). More commonly, lava flows destroy property, infrastructure, livestock and the productive capability of the land in their flow path, thus indirectly affecting human lives via displacement, famine, disease, disruption to transport, communication and other public services, and economic cost (Peterson and Tilling, 2000). Historic attempts to mitigate the destructive effects of lava flows by slowing flow advance, diverting flow paths or disrupting lava supply at the source, have enjoyed varied success. For example, the combined use of constructed earthen containment barriers and artificial flow channels successfully delayed flow advance and subsequently diverted lava flows during the 1991-92 Mount Etna eruption (Barberi *et al*., 1993). However, an accurate prediction of the intended flow path and emplacement dynamics of the lava flow(s) is necessary to enable comprehensive risk assessment and to determine appropriate mitigation measures.

The ability of a lava flow to propagate away from the source vent or fissure is primarily controlled by the rate and volume of lava effused from the source, the physical properties of the lava, and local environmental conditions (Kilburn, 2000). Although variations in these conditions can produce vastly different lava

flow geometry, morphology and surface features, both between separate lava flow fields and between individual lava flows generated during the same eruption episode, all lava flows display characteristic behavioural trends as a result of their rheological properties (Dragoni, 1993). These rheological properties, viscosity and yield strength, determine the ability of the lava to deform and flow as a fluid body, and are controlled by various physical properties of the lava, including geochemical composition, crystal and volatile content and temperature. Lava flow rheology refers to the study of the deformation and flow behaviour of lava in response to applied stress, and the rheological behaviour of the lava is determined by the relationship between the degree of applied stress and the rate of deformation of the lava (Fig. 1.1). When the deformation rate is equal to the rate of applied stress, the lava behaves as a Newtonian fluid with no viscous strength. The majority of non-Newtonian fluids display pseudoplastic behaviour, where the deformation rate increases with increasing rates of shear stress, thus viscosity reduces as the rate of applied stress increases. Conversely, Bingham fluids possess an internal strength, known as yield strength, which prevents deformation until the applied stress exceeds the yield strength of the fluid; thereafter, the rate of deformation is equal to the applied stress and the substance behaves as a Newtonian fluid (Dragoni, 1993). The viscosity and yield strength of the lava determine its flow behaviour as it moves away from the vent and influences various emplacement processes, for example velocity, lateral spreading and the cooling rate of the lava. Determining the parameters that control lava flow rheology therefore enables a greater understanding of lava flow emplacement processes (Dragoni, 1993).

While numerous models have been developed to determine the rheological behaviour of lava flows most are concerned with basaltic and rhyolitic composition lavas, and less is known about the rheology and emplacement dynamics of intermediate composition lavas, particularly those emplaced on steep slopes. Furthermore, few studies relate to the behaviour and emplacement processes of New Zealand lava flows, although Stevenson (1989) and Stevenson *et al*. (1994a; 1994b) determined the rheology and emplacement processes of two New Zealand rhyolitic lavas, primarily based on the morphological and textural characteristics of these flow deposits. With the development of more recent

rheological and flow behaviour models, for example viscosity models applicable to a wide range of lava compositions and temperatures, and models incorporating the role of surface cooling and crustal growth on flow advance and cessation, the rheological behaviour of intermediate composition lavas can be better constrained. Although the regions surrounding most New Zealand volcanoes are not densely inhabited, and the risk posed by lava flows generated from these vents are relatively low, understanding the factors that affect the flow behaviour of New Zealand lavas remains an important goal, to facilitate hazard assessment and the development of hazard management plans, and to assess the validity of rheological models in predicting flow behaviour. The documented eye-witness accounts and well-preserved flow deposits of the lava flows produced during the 1954-55 Mount Ngauruhoe eruption enable both an estimation of lava flow rheology and flow emplacement dynamics, and a test of rheological model validity against observed behaviour.

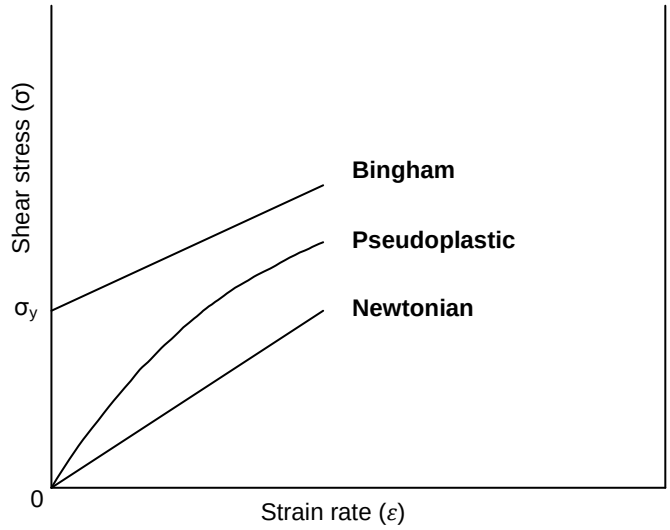

Fig. 1.1 Flow curves for three different types of fluids based on their deformation behaviour (strain rate) in response to applied stress (σ). In Bingham fluids deformation doesn't occur until applied stress exceeds the yield strength (σ_y) of the fluid. Adapted from Dragoni (1993).

1.1.1 Thesis Aims and Objectives

The aim of this thesis research is to determine the rheological behaviour and emplacement processes of the lava flows produced during the 1954-1955 Mount Ngauruhoe eruption. This research has been undertaken in collaboration with

GNS Science, Wairakei and is part of a larger study by GNS Science determining the factors that influence the eruption style variability of this volcano. Collectively this research will enable more accurate monitoring of future volcanic activity, identify appropriate prediction methods to determine the extent of future lava flow hazard, and facilitate development of effective hazard management plans for Tongariro National Park.

The research objectives are:

1. To quantify the parameters that controlled the rheology of the 1954-1955 lavas.
2. To determine the extent to which lava rheology controlled flow emplacement.
3. To gain an understanding of the processes involved during the emplacement of the 1954-55 lava flows.

These objectives are achieved by incorporating morphological, geometric, petrographic and geochemical data collected from identified 1954 lava flow deposits into existing numerical rheological models, and comparing results with eye-witness accounts and lava flow deposit characteristics.

1.2 GEOLOGICAL SETTING

1.2.1 Regional Setting

Mount Ngauruhoe is situated within the Tongariro Volcanic Centre (TgVC), in the southern region of the Taupo Volcanic Zone (TVZ) (Fig. 1.2). The TVZ is a 300 km long, up to 60 km wide, volcano-tectonic complex driven by the oblique westward subduction of the Pacific Plate beneath the Australian Plate off the east coast of the North Island of New Zealand (Houghton *et al*., 1995). It has been the dominant region of volcanic activity in New Zealand since the late Pliocene (Wilson *et al*., 1995) and is characterised by regional crustal extension (Rowland and Sibson, 2001) and anomalously high heat flow (Bibby *et al*., 1995). The continental crust is estimated to be approximately 12-15 km thick within the TVZ region (Price *et al*., 2005). The TVZ has produced over 90% of the known late Pliocene to Quaternary volcanic products in New Zealand (Wilson *et al*., 1995), consisting predominantly of rhyolitic calderas in the central section of the zone,

and andesitic to dacitic composite cones in the northeast and southwest sections (Houghton *et al.*, 1995).

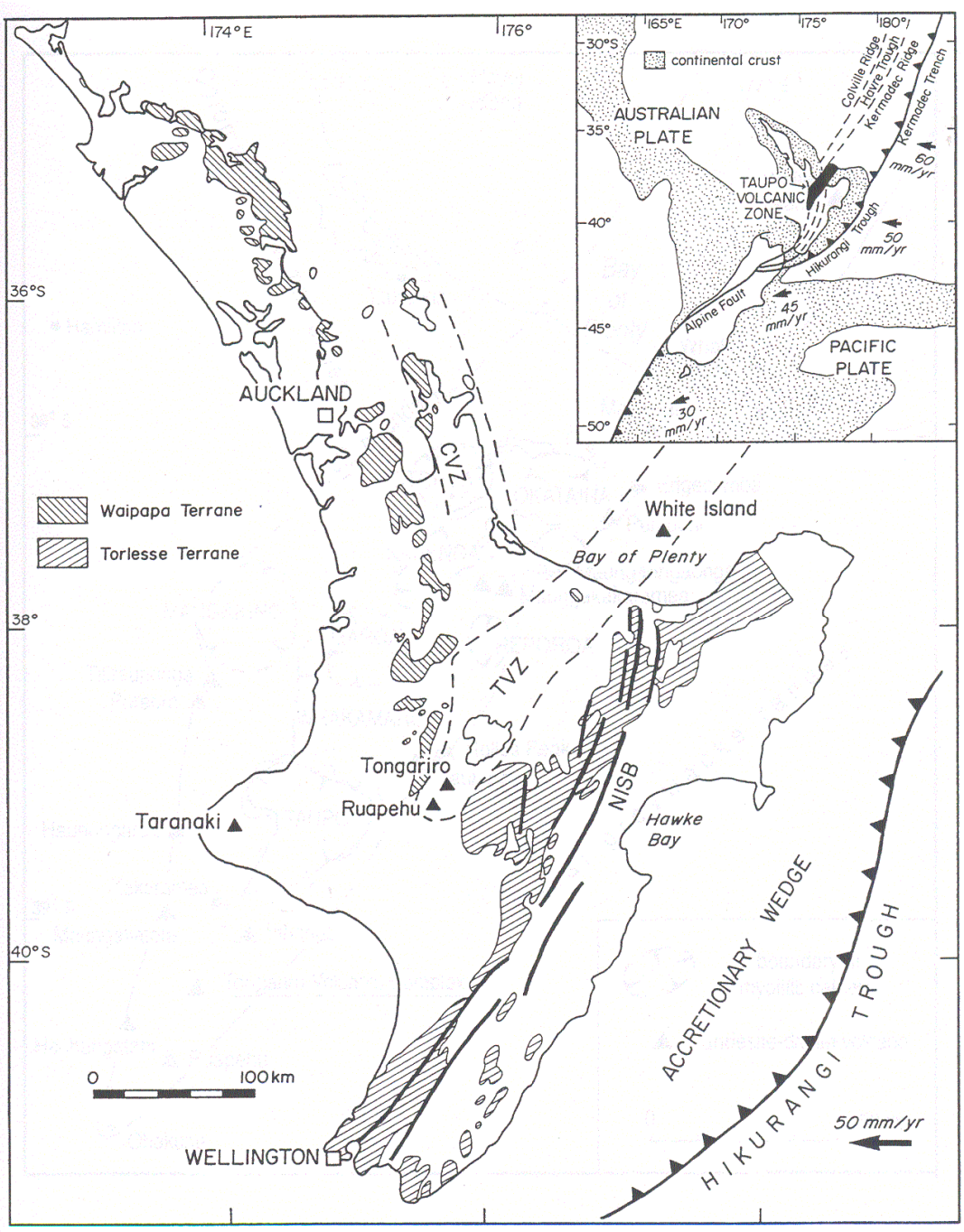

Fig. 1.2 Map of the North Island of New Zealand showing the location of tectonic and geological features and their relation to the Taupo Volcanic Zone (TVZ). CVZ = Coromandel Volcanic Zone. NSIB = North Island Shear Belt. Arrows indicate the direction and rate of subduction of the Pacific Plate beneath the Australian Plate. Inset shows the position of the New Zealand land mass over the plate boundary. After Hobden (1987).

1.2.2 Tongariro Volcanic Centre

The TgVC consists of a cluster of relatively young (c. 275 ka) andesitic composite volcanoes, including the large massifs of Ruapehu, Tongariro, Kakaramea and Pihanga (Cole, 1978), which are underlain by metagreywackes and argillites of Mesozoic age (Torlesse and Waipapa Terranes) and younger Tertiary marine sediments (Gregg, 1960). Tongariro is a frequently active, complex cone comprising a series of discrete and overlapping vents within a 13 km long and 5 km wide vent corridor (Fig. 1.3), representing c. 275 ka of eruptive activity (Hobden *et al*., 1999). Mount Ngauruhoe is the youngest of these vents (c. 2.5 ka) located to the southwest of the main massif and is the principle site of the most recent activity at Tongariro (Hobden *et al*., 2002).

Ngauruhoe is a 2,287 m high, composite, basaltic andesite to andesite cone that has displayed a diverse range of effusive and explosive eruption styles throughout its history (Hobden *et al*., 2002). Frequent eruptive events were witnessed by local Maori prior to European settlement, with written observations recorded following European colonisation of New Zealand in the early 1800s (Gregg, 1960). At least 73 eruptions ejecting volumes of material greater than 10^5 m^3, predominantly ash and some pyroclastic flows, have occurred since 1839 (Bebbington and Lai, 1996), with an average frequency of one eruption every two to three years (Table 1.1) (Hobden *et al*., 2002). Eruption styles at Ngauruhoe vary between

Table 1.1 Dates of Ngauruhoe eruptions producing greater than 10^5 m^3 of ejected material. Columns are grouped into events occuring less than 5 years apart. Adapted from Bebbington and Lai (1996).

1839 to 1845	1855 to 1898	1904 to 1917	1924 to 1940	1948 to 1959	1968 to 1975
1839 - Feb	1855	1904 - Nov	1924 - Jan	1948 - April	1968 - 19 July
1841	1857 - Feb	1906 - March	1925 - Nov	1948 - Sept	1969 - 16 July
1844 - Oct	1859 - Dec	1907 - Feb	1926 - April	1949 - Feb	1972 - 29 April
1845 - Jan	1862 - Jan	1907 - May	1926 - Dec	1950 - 16 June	1973 - 2 Jan
	1863 - Dec	1907 - Nov	1928 - March	1951 - May	1973 - 11 May
	1864 - April	1909 - March	1928 - July	1952 - Nov	1973 - 2 Aug
	1869 - Dec	1909 - July	1931 - Feb	1954 - May	1973 - 15 Dec
	1870 - April	1910 - Jan	1931 - May	1956 - Jan	1974 - 23 Jan
	1875 - 2nd half	1910 - Oct	1934 - June	1958 - Nov	1974 - 28 March
	1878 - 2nd half	1911 - Jan	1934 - Dec	1959 - 1 June	1975 - 19 Feb
	1881 - 6 July	1913 - Jan	1937 - Jan		1975 - 12 May
	1883 - April	1913 - May	1939 - Aug		
	1888 - April	1914 - Sept	1940 - Sept		
	1892 - Feb	1917 - Oct			
	1892 - Nov				
	1897				
	1898 - Jan				

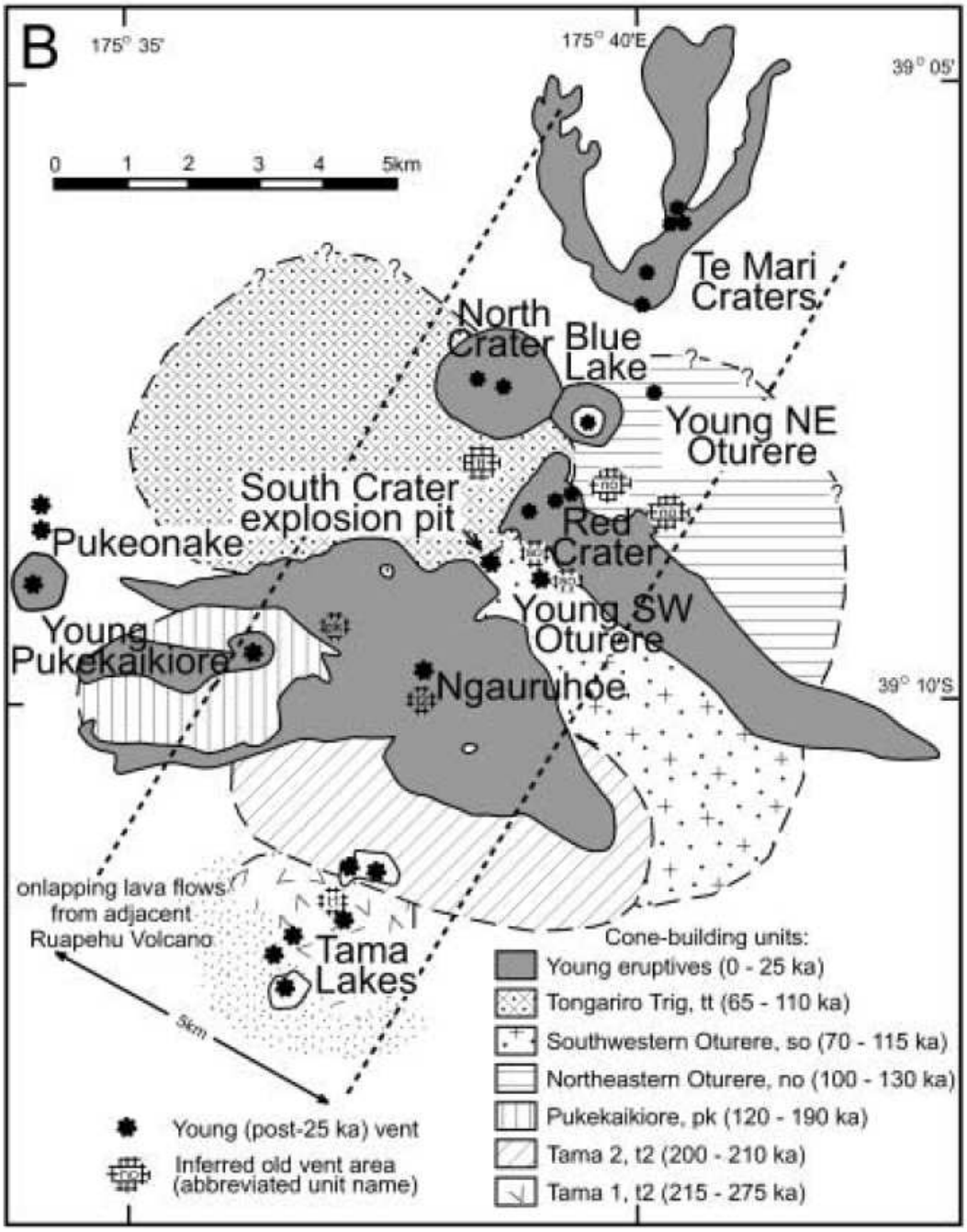

Fig. 1.3 The NE-SW trending vent corridor at Tongariro and the distribution pattern of eruptive products. Note the location of Mount Ngauruhoe to the SW of the main Tongariro vents. After Hobden *et al.* (2002).

effusive, lava flow producing eruptions through to explosive strombolian, vulcanian and sub-plinian eruptions, although frequently more than one of these styles has occurred during any one eruptive event (Hobden *et al.*, 2002). Ngauruhoe eruption products include lava flows, block and ash flows, scoria and ash flows, scoria cones, spatter deposits and ash columns (Hobden, 1997). Of these, lava flow deposits are the most commonly preserved and exposed,

particularly the most recent lava flows produced during the 1954-55 eruption. The last eruption at Mount Ngauruhoe occurred during 1973-75 and was explosive vulcanian to sub-plinian in nature, producing at least five block and ash flows on the north-west flanks of the cone (Hobden *et al*., 2002).

Numerous lava flow deposits are evident on all flanks of the cone, with some extending onto the floor of the Mangatepopo and Waihohonu Valleys (to the NW and SE of the volcano respectively). The majority of these lavas overlie the widespread rhyolitic, 1.85 ka Taupo pyroclastic deposit, although some pre-date this event, and are dominated by a'a to blocky-type deposits with transitional a'a/pahoehoe characteristics evident in some thin basaltic andesite flows near the summit (Hobden *et al*., 2002). Historical effusive eruptions were recorded in 1870 (2 to 3 flows), 1949 (1 flow) (Gregg, 1960) and during the most recent effusive eruption where up to 17 lava flows were produced between June and September 1954 (Gregg, 1956).

1.3 NGAURUHOE CONE EVOLUTION

The distinctive symmetrical Ngauruhoe cone (~ 30-33° slope angles) has evolved due to the pattern of lava emplacement over time, influenced by concurrent changes in crater architecture. Hobden *et al*. (2002) identified five stratigraphically and compositionally distinct groups of lavas and pyroclastic deposits that display a distinct sectorial pattern of distribution over time (Fig. 1.4). The group 1 lavas incorporate nine identifiable flows emplaced on the north-west and eastern flanks of the cone, with one flow, the longest of the Ngauruhoe lavas at 5.2 km long, on the western slopes and extending along the Mangatepopo Valley floor. These are the oldest exposed lavas and underlie the 1.85 ka Taupo pyroclastic deposit. Fourteen flows are included in group 2, some of which pre-date and others overlie the 1.85 ka Taupo deposit. This group was confined to the north-west sector of the cone, with some overlapping the earlier group 1 lavas. Flow emplacement progressed to the south-eastern flanks for the group 3 lavas. Two of the three flows in this group extend approximately 3.4 km onto the Waihohonu Valley floor and all post-date the 1.85 ka Taupo eruption. Most of the

13 group 4 lavas partially overlie group 3 lavas on the southern flanks, with two smaller flows emplaced on the eastern slopes and some emplaced to the south west. These are younger than the group 3 lavas but pre-date the more recent historical lavas of group 5. Twenty historical lavas (between 1870 and 1975) are included in group 5, emplaced predominantly on the north-west slopes, although several smaller flows were also emplaced on the upper eastern slopes of the cone (Hobden *et al*., 2002).

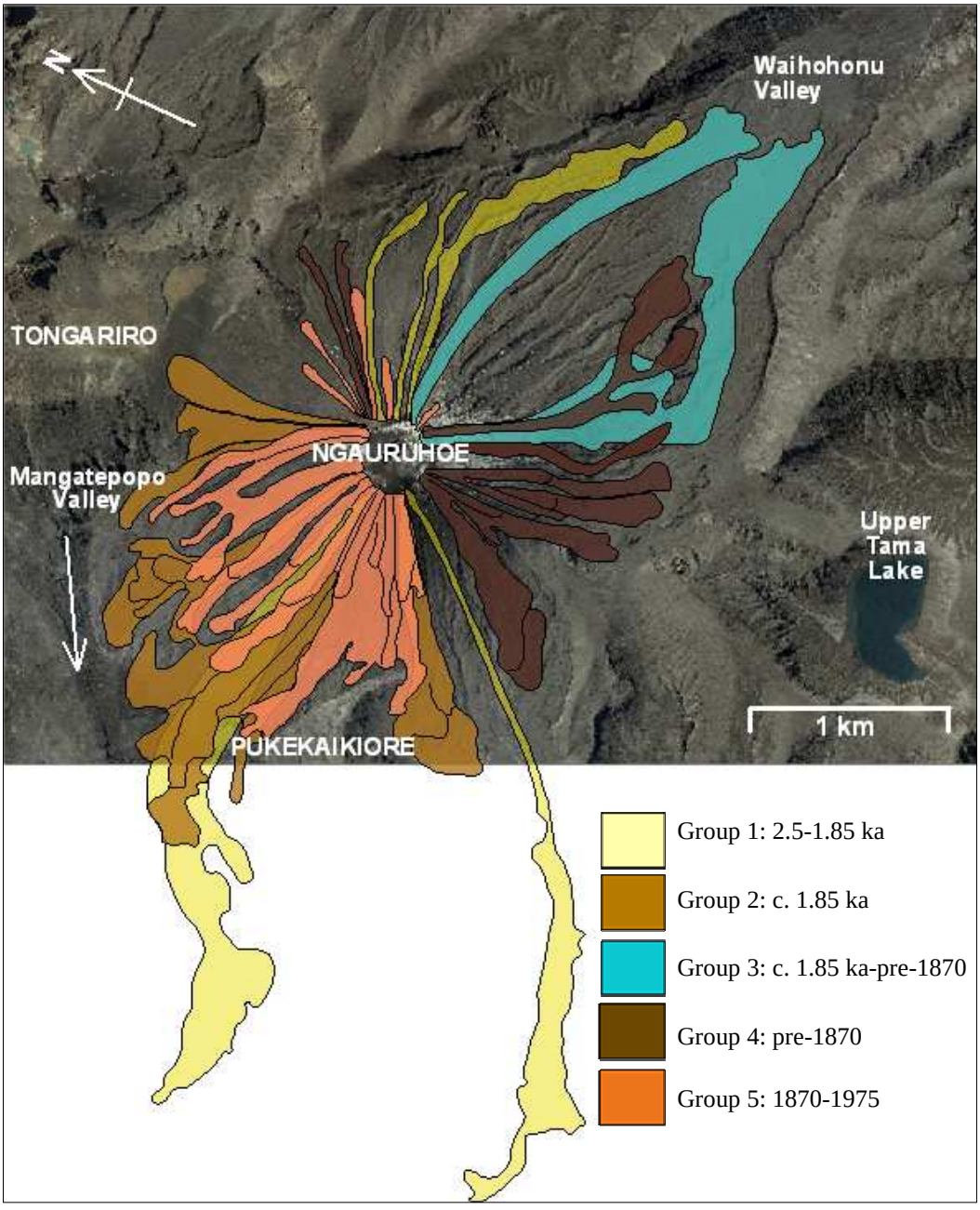

Fig. 1.4 Sectorial Ngauruhoe cone growth showing the chronostratigraphic distribution of groups of lavas. Adapted from Hobden *et al.* (2002).

The sectorial distribution pattern of these lavas is strongly influenced by changes in vent geometry and morphology, modified by the diversity of eruption styles at Ngauruhoe. Chronologically distinct lava groups are generally directed through the lowest points on the crater rim, which alters rapidly over time as demonstrated during the relatively short time period since historical observations began (Fig. 1.5). On some occasions, spatter from fire fountaining episodes may overtop higher parts of the crater rim creating discrete flows isolated from the main chronostratigraphic group, for example the two eastern flows of group 4 (Hobden *et al*., 2002).

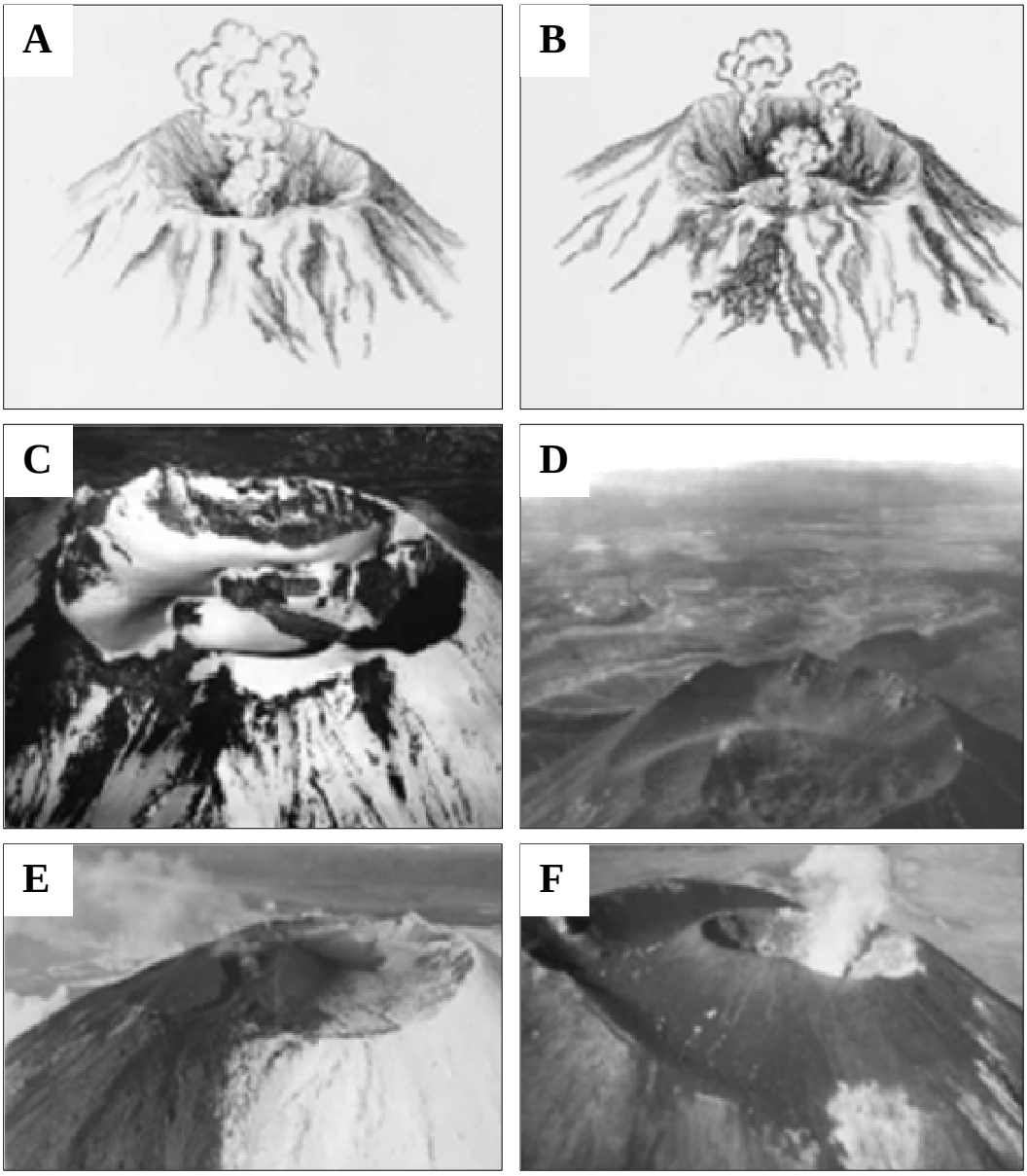

Fig. 1.5 Ngauruhoe summit crater evolution in historical times, A. 1839; B, 1878; C, 1934; D, 1949; E, 1954; F, 1955-present. Adapted from Hobden *et al*. (2002).

1.4 1954-1955 ERUPTION CHRONOLOGY

The 1954-1955 eruption has been well documented by Gregg (1956) and includes a detailed narrative of the lava flow chronology and associated fire fountaining and ash emissions. Gregg's (1956) account is based on many eye-witness observations from scientists and local inhabitants, often based at the Whakapapa Chateau. Much of the eruption occurred during the winter months of 1954 and accurate observation of the eruption was frequently hampered by low cloud cover and poor visibility. The following two subsections summarise Gregg (1956) and provide an overview of the main eruption events and the timing of individual lava flow emplacement. A summarised timeline for these events is shown in Fig. 1.6.

1.4.1 Eruption Overview

Lava was reported in the crater in late December 1953; however, the first sign of explosive activity did not occur until 13th May 1954 with the emission of ash clouds observed above the crater. Lava fountaining was first observed on 2nd June 1954 and the first lava flow was emplaced shortly after this on 4th June, with up to 17 lava flows emplaced, over a maximum duration of one to two days each, in the following four months to the final flow on 26th September 1954. Intermittent ash eruptions and frequent fire fountaining were prominent features of the eruption, with fire fountaining most often associated with lava flow emplacement and the construction of a scoria cone within the original crater. Ash eruptions increased in frequency around the end of September, following emplacement of the final lava flow, with a relatively quiescent period between October and November of 1954. Activity increased again in December 1954 with ash explosions and intermittent fire fountaining which continued until early February 1955. Occasional ash emissions continued until the final explosion, reported on 10th March 1955, although lava was noted within the crater until around June 1955 (Gregg, 1956).

1.4.2 Lava Flow Emplacement Chronology

4th June

Vigorous lava fountaining was observed at 7 am with lava overflowing the crater rim by 8:15 am. Two lava flows were observed on the north-west slopes by

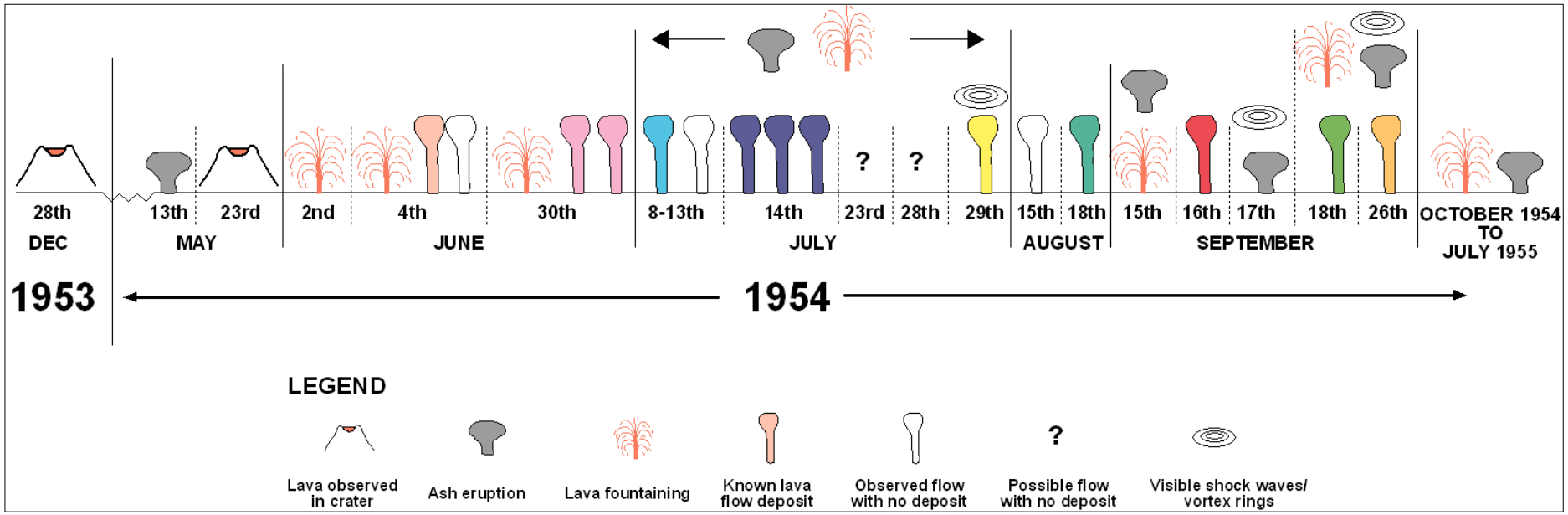

Fig. 1.6 Timeline of successive lava flow emplacement and associated eruption events during the 1954-55 Ngauruhoe eruption.

11 am, one overlying and reaching approximately one third down the length of 1949 flow (Fig. 1.7), and a second flow to the south. Continuous lava fountaining accompanied these flows reaching a height of ~ 300 m above the crater. By the evening of the same day both flows had almost reached their final distance from the vent and had completely stopped flowing by the next day, although loose blocks continued to fall from the front of the northern of the two flows.

30th June

Lava fountaining activity increased vigorously from around 20th June and by the afternoon of 30th June lava just overtopped the western side of the crater rim. The flow had extended to ~ 30 m below the rim by 4 pm and was noted in the evening to be flowing at a rate of approximately 304 m/hr. This flow covered the southern 4th June flow. A second flow was observed just to the south of the first flow at around 8 pm with both flows merging further down slope. Almost continuous lava fountaining occurred until approximately 11 pm that evening, reaching a height of ~ 300 m above the crater, with some fragments reaching ~ 760 m above the crater. The combined flows continued to move slowly the next day, branching into smaller lobes (Fig 1.6), one of which was noted to be moving at a rate of ~ 14 m/hr, with the flow finally coming to a halt on 2nd July.

8-13th July

Four possible flows were observed during this time period although poor weather throughout most of July hampered more detailed observation. At 6:15 pm on 8th July a glowing flow was noted on the western slopes, with a second flow possibly following the path of the earlier flow noted 24 hours later. A third flow was observed advancing over the crater rim on 11th July and on the afternoon of 13th July a flow had reached approximately half way down the western slopes. These latter two flows may possibly be the same flow and only one of the flows from this period has been mapped by Gregg (1956) (Fig. 1.7) as covering part of the upper section of the earlier 30th June northern lobe.

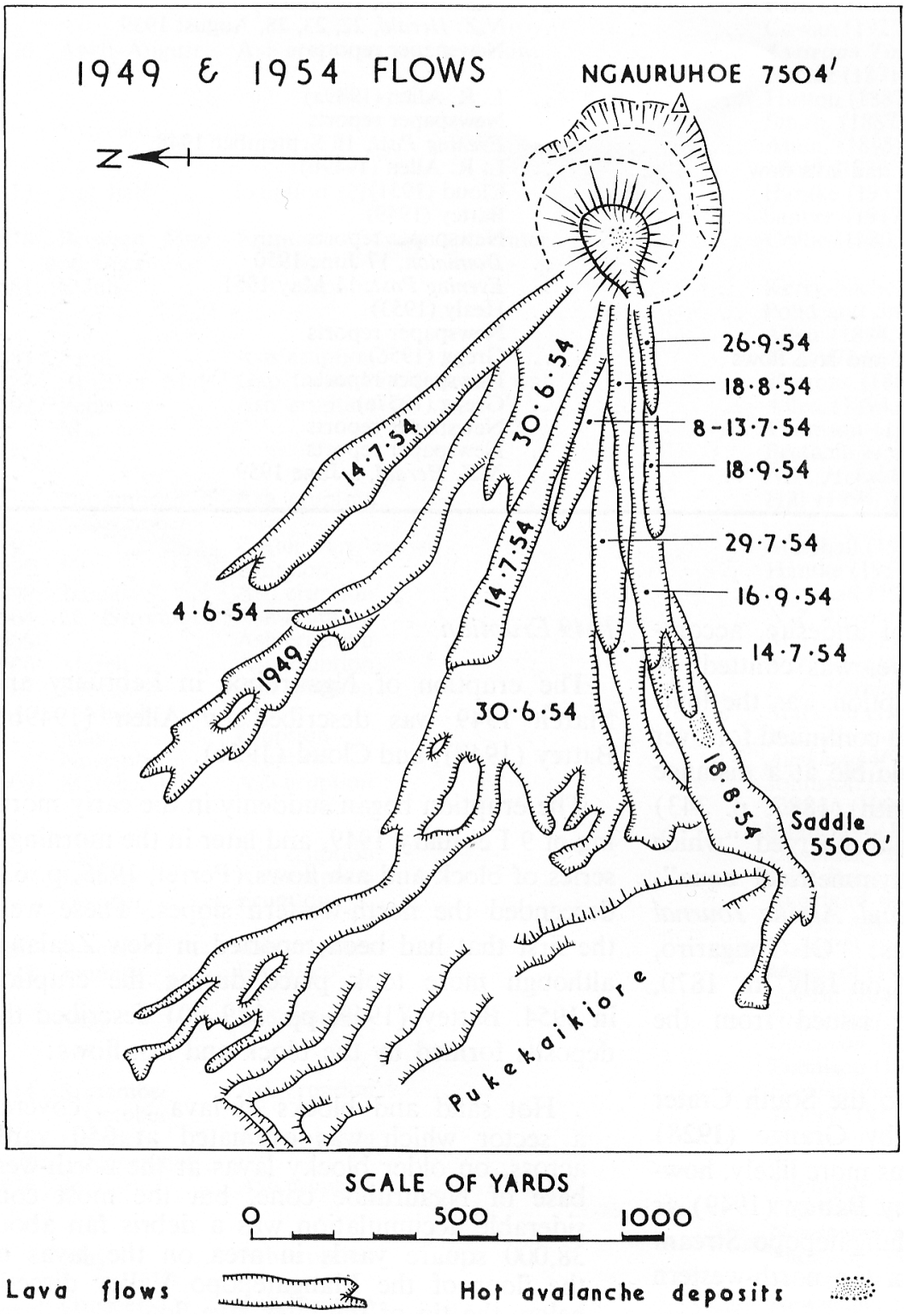

Fig. 1.7 Early map of the 1954 lava flows showing dates of each emplaced flow deposit. After Gregg (1956).

14th July

Three flows were observed to have advanced some distance downslope on the evening of 14th July. The northern-most of these flows was emplaced to the north of the 4th June flow, the southern flow directly to the south of the 30th June flow, and the central flow overlying the upper section of the 30th June flow just to the south of the mapped 8-13th July flow (Fig. 1.7).

23rd & 28th July

Two possible lava flows were reported, one each on 23rd and 28th July respectively, although heavy cloud cover during this time prevented accurate observation and no deposits associated with these flows have been identified or mapped by Gregg (1956).

29th July

During the day a lava flow was observed advancing slowly down the western slopes at the southern margin of the 30th June flow (Fig. 1.7), and had reached approximately 240 m below the crater rim by 10:30 pm. A glowing flow was reported in roughly the same location the next day and may be the same flow. This flow was also accompanied by sharp explosions with visible shock waves and vortex rings moving rapidly away from the crater.

15th August

A small flow was reported to have reached the saddle between Ngauruhoe and Pukekaikiore, although no deposit was identified or mapped by Gregg (1956).

18th August

Lava was observed overtopping the crater rim at 1 am and the flow had reached the saddle between Ngauruhoe and Pukekaikiore by 5 am, probably covering the 15th August flow. At 12:45 pm the flow velocity was estimated at ~ 9 m/hr with a 180 m wide and 15 m high flow front. This advancing flow face had reduced in size by 19th August although the flow continued advancing at the same speed and had reached approximately 300 m around the southern side of Pukekaikiore by 2 pm (Fig 1.6). This flow is reported to have piled up to a thickness of ~ 15m at the saddle and remained warm to the touch up to a year later.

16th September

Continuous lava fountaining was observed on the evening of the 15th September and by the early morning of the 16th September lava was noted flowing over the western crater rim. A hot avalanche of ash and steam was observed rising above the saddle at around 7:30 am. By the afternoon and into the evening two flows (or possibly the same flow split into two lobes) were advancing over the earlier hot ash flow deposits, with associated fire fountaining, and covering the upper section of the northern margin of the 18th August flow (Fig. 1.7).

18th September

A small flow was observed to have advanced ~ 250 m down the western slopes adjacent to the southern margin of the 18th August flow (Fig. 1.7). This flow continued to advance on the following day and was associated with loud explosions.

26th September

On the afternoon of the 26th September a small flow emerged over the crater rim and followed the path of the 18th September flow (Fig. 1.7). This was the shortest of the flows and marked the end of the effusive phase of the 1954-1955 eruption.

1.5 THESIS OUTLINE

The remaining chapters of this thesis are organised by field observations, laboratory analysis, mathematical rheological modelling and flow emplacement dynamics, as follows:

- Chapter 2 describes the morphological, geometric and surface characteristics of the 1954 lava flow deposits as observed in the field and on aerial photograph analysis,
- Chapter 3 details the macroscopic and microscopic petrographic characteristics of the 1954 lavas and presents the results of vesicularity and geochemical analysis,

- Chapter 4 quantifies the rheological properties and eruption conditions of the 1954 lavas using a range of geochemical and physical rheological models,

- Chapter 5 discusses the factors controlling lava flow dynamics and identifies the flow emplacement processes of the 1954 lavas with implications for predicting the behaviour of future lava flows at Mount Ngauruhoe and subsequent hazard management,

- Chapter 6 provides a summary of the research and concluding remarks.

CHAPTER 2

Lava Flow Deposit Geometry and Morphology

2.1 INTRODUCTION

This chapter describes the geometric, morphological and surface feature characteristics of the 1954 lavas and quantifies the dimensions and volume of each identified lava flow. It begins with an overview of previous work undertaken on the 1954 lavas, followed by an account of the field methods employed for this study and an explanation of the enumeration of individual sites visited in the field. A description of the field site and associated eruption deposits is followed by a synopsis of the morphological, geometric and surface feature characteristics of the 1954 lavas. The main part of the chapter focuses on the characteristics of six of the 1954 lava flow deposits, including a comprehensive account of two of these deposits describing their distinctive morphology and surface features.

2.1.1 Previous Work

Gregg (1956) compiled the first map of the 1954 lavas (Fig. 1.7), primarily using sketches of photographs taken during or shortly after the eruption. Of the 17 possible lava flows observed during the 1954-55 eruption, 11 were mapped by Gregg (1956) and this map has been used as the basis of later maps of the 1954 lavas e.g. Hobden and Houghton (2000) (Fig. 2.1) and Hobden *et al*. (2002).

Little work has been published regarding geometric or morphological characteristics specific to the 1954 lavas. Hobden (1997) described the general morphology of all the Ngauruhoe lavas, for example the widened and thickened lobate distal end of some older flows extending to the flat surface of the

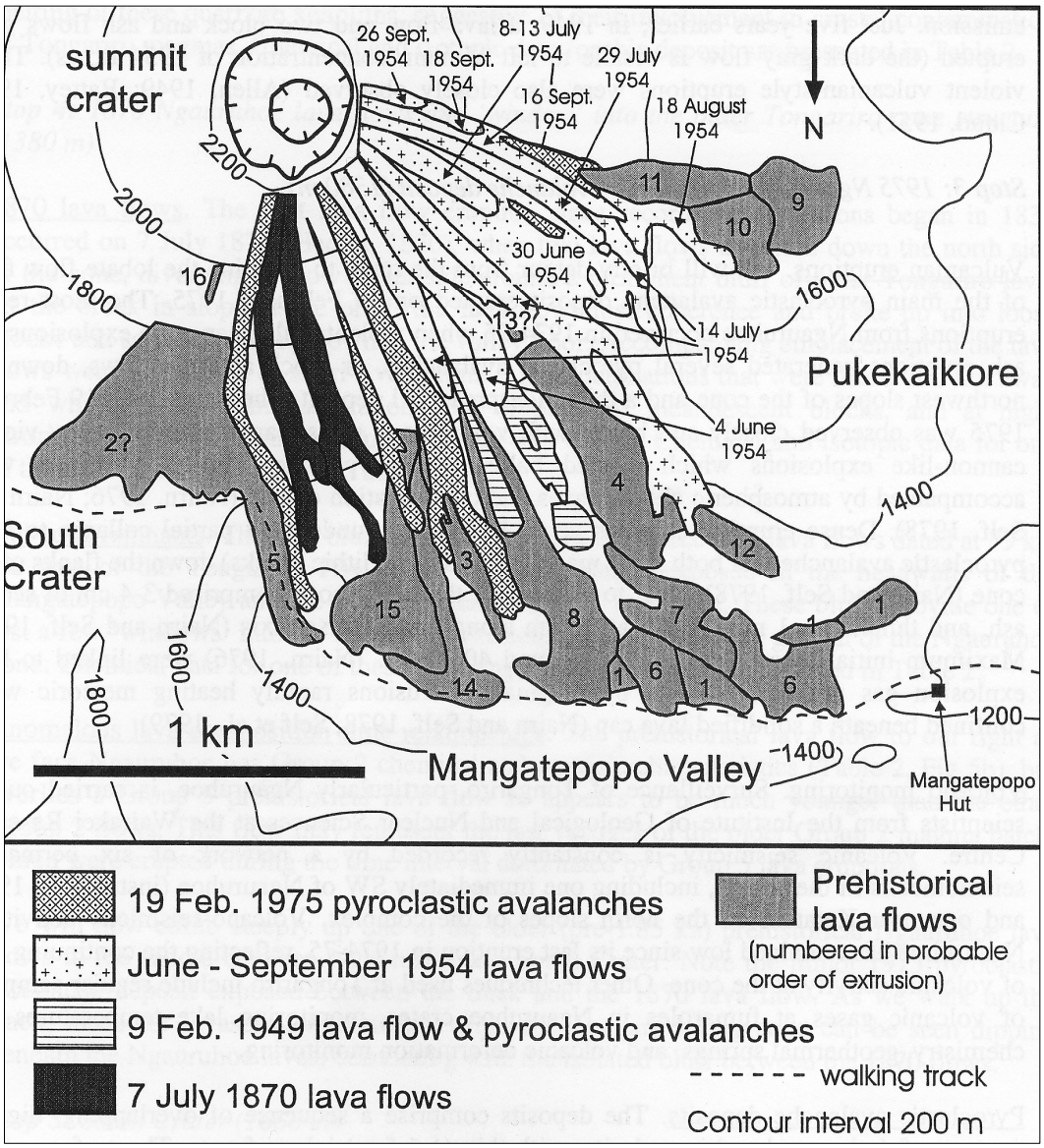

Fig. 2.1 Flow emplacement map of the 1954 Ngauruhoe lavas and other Ngauruhoe eruptive deposits. After Hobden and Houghton (2000).

Mangatepopo Valley floor. Some of these older deposits also display a concave flow surface consisting of a central depression bounded by elevated marginal levees which extend for much of their deposit length. Hobden (1997) suggests that the thick, bulbous frontal zones of these flow deposits were most likely formed as hot lava within the central flow channel drained from the proximal regions of the flow on the steeper slopes into the frontal zone of the flow. Hobden (1997) concludes that the elevated levees of these flow deposits were therefore not constructed above the flow channel surface during flow emplacement but are instead the cooled, lateral margins of the flow which were abandoned by the drainage of the central flow channel.

The single lava flow extruded during the 1949 eruption is described by Allen (1949) and Battey (1949). This flow deposit, overlain by the 4th June 1954 lava, is a discrete, single-lobed unit extending ~ 1.8 km in a relatively straight path from the crater rim on the north-western slopes. The distal margin of the flow bifurcates into two long, thin finger-like lobes ~ 330 m before the terminal end of the deposit (Allen, 1949). The surface of this flow deposit, both during and for a short time after the lava was emplaced, consisted of well-developed, elevated marginal levees bordering two shallow flow channels located either side of a distinctive elevated median ridge along the entire length of the flow (Battey, 1949). Battey (1949) concludes that the crater rim was breached in two adjacent places resulting in a twinned lava flow, with the median ridge marking the cooled, shared boundary between the two flow deposits. Subsequent cooling of the lava resulted in partial collapse of the elevated surface features rendering them barely distinguishable within the following few months (Battey, 1949).

During emplacement of the 1954 lavas Gregg (1956) noted that either flat or convex-shaped flow surface profiles were evident at higher flow velocities, with the formation of marginal levees, and in some instances a central ridge within the flow channel occurring as flow velocity reduced. Gregg (1956) concluded that marginal levee formation resulted from partial collapse of the cooled, slower moving upper surface of the flow as faster moving molten lava continued to flow beneath the cooled surface.

Some 1954 lava flow dimensions and velocities were reported by Gregg (1956), e.g. 30th June and 18th August lavas, estimated during or shortly after their emplacement. Gregg (1956) also estimated the total volume for the 1954 lavas at ~ 3,000,000 to 9,900,000 m^3, based on an average flow thickness of 3 to 9 m. The 30th June lava flow deposit is estimated to account for more than one third of this volume (Gregg, 1956). Hobden *et al*. (2002) calculated a total volume of ~ 6,500,000 m^3 for the combined lavas and scoria cone constructed during the 1954-55 eruption, estimating a volume of 600,000 m^3 for the 30th June lava flow. Based on the total volume of material erupted, Hobden *et al*. (2002) also estimated an overall average discharge rate of ~0.65 $m^3 s^{-1}$ during the 1954-1955 eruption.

2.1.2 Methodology

Prior to undertaking field work individual lava flows from the 1954-1955 eruption were identified by comparing the Gregg (1956), Hobden and Houghton (2000) and Hobden *et al*. (2002) maps with a recent (c. 2001-2004) aerial photograph of the site (Appendix A.1). Of the 11 lava flows mapped by Gregg (1956) six lava flow deposits (4th June; 30th June; southern 14th July; 29th July; 18th August; 16th September) were clearly identifiable on this aerial photograph. Using Macromedia Freehand Version 9.0 software the flow margins from Gregg's (1956) map were superimposed onto the aerial photograph and scaled to match the six identified lava flow deposits in the photograph. This technique enabled a reasonable estimate of the position and dimensions of the remaining five unidentified lava flow deposits (8-13th July; northern and middle 14th July; 18th September and 26th September) and was subsequently used to construct an updated map of the 1954 lava flow deposits (Fig. 2.2).

Lava flow deposits were identified in the field by comparing their relative location and morphological characteristics with the updated flow deposit map. The six lava flow deposits initially identified on the aerial photograph [4th June (A); 30th June (B); southern 14th July (Dc); 29th July (E); 18th August (F); 16th September (G)] were also clearly identifiable in the field and data and samples were collected from these deposits. Two of these flow deposits, 30th June (B) and 18th August (F), were selected for comprehensive data collection. The remaining five lava flow deposits [8-13th July (C); northern and middle 14th July (Da, Db); 18th September (H); 26th September (I)] were not identified in the field, primarily because their margins were obscured either by subsequent 1954 lavas, later pyroclastic deposits or loose scree, and therefore no data or samples were collected from these.

Observations regarding morphological and surface features of the lava flow deposits and their relationship with the underlying topography were recorded in the field. Deposit thickness, levee heights and surface feature dimensions were measured using an aluminium measuring staff and/or measuring tape. A Silva compass was used to determine the slope angle of lava flow margins, levees,

surface features and underlying topography. Where there was no evidence of levee formation flow depth was estimated by measuring the height of the lateral lava flow deposit margins, since flow depth within central flow channels could not be determined where there was no visible contact with the underlying surface.

Lava flow deposit dimensions were calculated using the updated flow deposit map and aerial photograph analysis, a topographic map of the field site (NZMS260-T19) and collected field data. The aerial photograph correlates to known map grid references, thus an accurate scale was formulated and used to calculate flow deposit dimensions. Lava flow deposit margins were superimposed onto a topographic map of the northwestern sector of the cone, and scaled to match the dimensions of the map to enable calculation of underlying slope angle (Appendix A.2). The underlying slope angle (α) at each 100 m change in elevation downslope from the crater rim (2,240 m.a.s.l. contour line) was determined for each of the lava flow deposits using the inverse trigonometric function:

$$\alpha = \sin^{-1}\frac{\Delta E}{D}$$

where ΔE is the change in elevation (m), and D represents the distance between each 100 m elevation change. The length (L) of the lava flow deposit at each 100 m change in elevation was then determined using the trigonometric function:

$$L = \frac{D}{\cos\alpha}$$

and a final flow deposit length calculated as the sum of these measurements.

The narrowest and widest sections of each lava flow deposit were measured using the aerial photograph and an average width determined by ascertaining the most common overall width of each flow. Numerous measurements of lava flow deposit depth were recorded in the field and these data were noted on the aerial photograph at the relevant field locations to determine the variation and average depth for each lava flow deposit The geometric characteristics of the 1954 lavas are summarised in Table 2.1.

Lava flow volume was estimated by calculating the surface area of each flow deposit using a 100 m^2 scale grid superimposed over the updated flow deposit

map (Appendix A.3). A smaller grid composed of 100 squares, each representing 1% surface area, was used to estimate surface area to within a 2% error margin within each 100 m^2 grid square. The combined surface area for each flow deposit was multiplied by its average flow depth to estimate individual flow volume. Average flow depths for the five lava flow deposits not visited in the field [8-13th July (C); northern and middle 14th July (Da, Db); 18th September (H); 26th September (I)] were estimated at 3 m for the three longer flow deposits (C, Da and Db), and 2.5 m for two shortest flow deposits (H and I), based on the relatively similar depths of the other lavas. The estimated error margin for average flow depth was ± 1 m, therefore combined with a 2% error margin in surface area estimation, the error margin ranges between ± 4,000 to 636,000 m^3 for the individual flow deposits with a total of ± 1,110,000 m^3 error for the total volume of the 1954 lavas.

A Terrestrial LiDaR (Light Detection and Ranging) Survey (TLS) was undertaken on the medial zone of the 18th August (F) lava flow deposit, in collaboration with GNS Science, Wairakei and Avalon. The aim of the survey was to obtain high-resolution geometric data for the surface features identified at the medial section of the 18th August lava flow and to test the suitability of the technology for future geomorphological analysis of other lava flow deposits. The technique involved the use of a LiDaR scanner with a GPS unit, GPS aerial and wide-angle lens camera attached (Fig. 2.3A), connected to a laptop computer. Five reflective 'targets' (Fig. 2.3B) were placed in strategic locations within the flow deposit with a clear line of sight to the LiDaR scanner, and a second GPS unit and aerial were placed separately from the scanner, also acting as a reflective 'target'. The two GPS units provided accurate and continuously updated coordinates of the location. A high-resolution overview scan was initially performed to locate and lock in the position of the reflective targets. A second more detailed scan was then performed at the same location and detailed photographs taken using the attached camera. Full LiDaR scans were completed at three different locations on the flow deposit (while the reflective targets remained in the same position) (Fig. 2.4A) and the data from each scan merged using the RiScan software package. GPS data

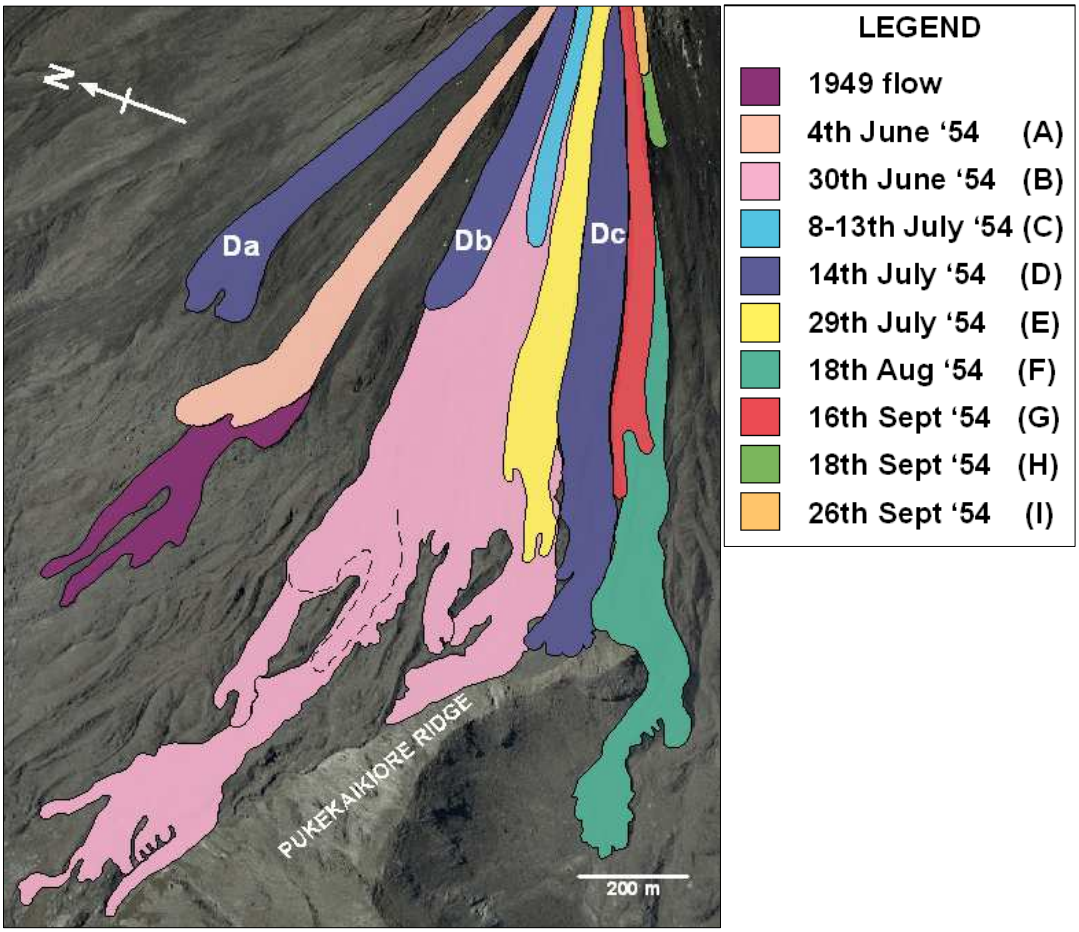

Fig. 2.2 Aerial photograph of the 1954 Ngauruhoe lavas colour coded by date of emplacement. Bracketed letters correspond to field location and rock sample enumeration. The three lava flows emplaced on the 14th July are labelled from north to south, 'Da', 'Db' and 'Dc' respectively. Aerial photograph courtesy of GNS Science, Wairakei.

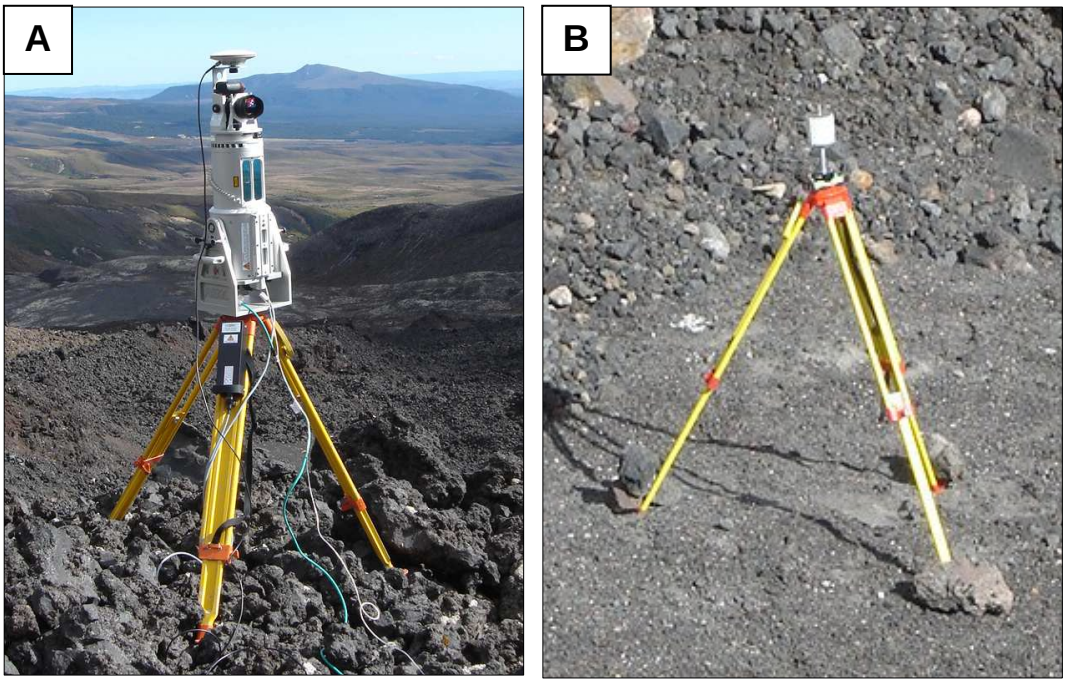

Fig. 2.3 Terrestrial LiDaR equipment used to survey the surface features of the 18th August lava flow deposit. A, Scanner, camera, GPS unit and aerial attached to a tripod; B, reflective target attached to a tripod. Equipment supplied by GNS Science, Avalon and operated by N.Palmer, GNS Science, Avalon.

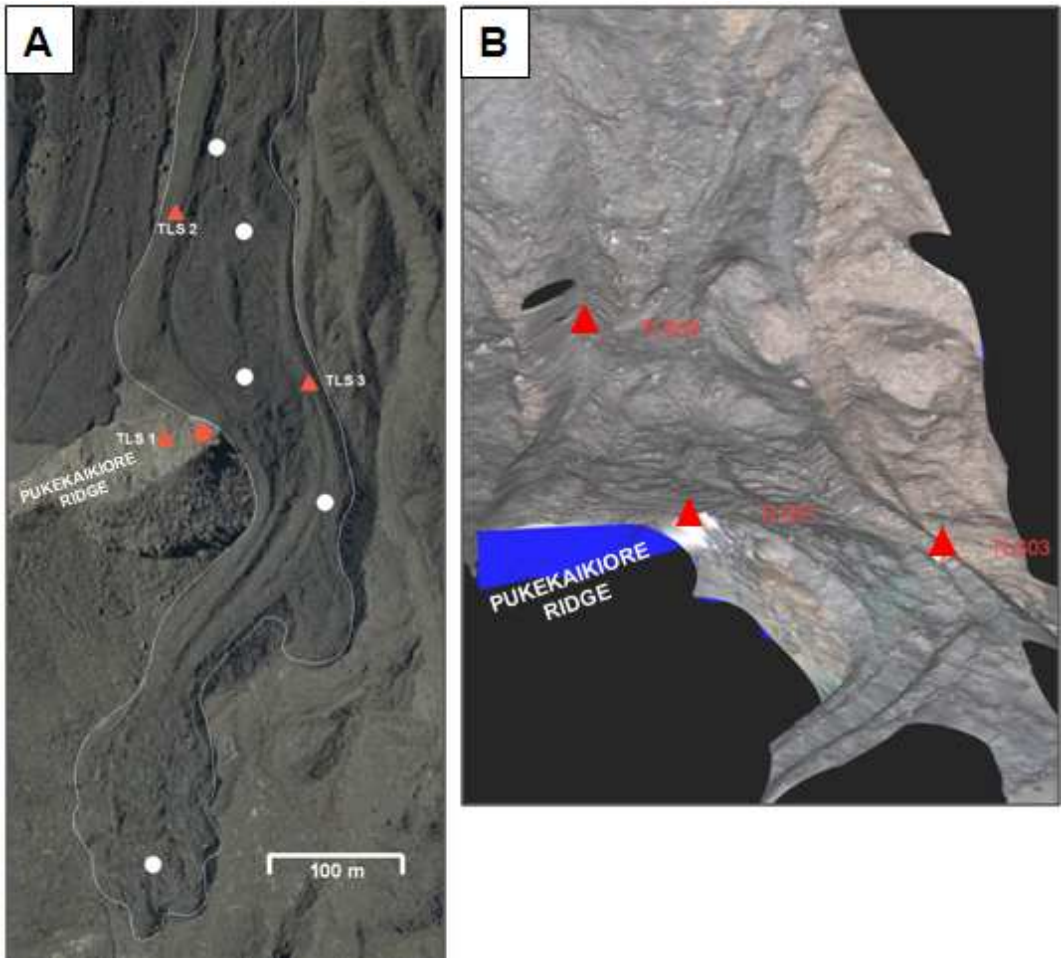

Fig. 2.4 A, aerial photograph of the 18th August lava flow deposit showing the position of the reflective targets (white dots) and the three scanning positions (red triangles) used for the TLS survey. Red dot denotes the position of the second GPS unit and reflective target. B, terrestrial LiDar model of the medial section of the 18th August lava flow. Red triangles correspond to those in A. Model courtesy of N. Palmer, GNS Science, Avalon.

was added to the composite scan to orientate the image, which was then overlain by the photographic images to add colour and perspective to the finished model (Fig. 2.4B). Although this model clearly delineates the margins of the 18th August lava flow deposit, the surface features located within the central flow channel were not clear enough for further geometric analysis.

2.1.3 Field Location Enumeration

Each of the 11 identified 1954 lavas was assigned a letter from 'A' to 'I' relative to its date of emplacement for ease of reference during field site location and sample labelling (Fig. 2.2). The three lava flow deposits emplaced on the 14th July (D) were designated 'Da', 'Db' and 'Dc', referring to the northern, middle and southern lava flow deposits respectively. The multiple lobes of the 30th June (B)

lava flow deposit have been subdivided into the northern lobe group (Bn) and southern lobe group (Bs) for field location and sample numbering, and further sub-divided into individual named lobes within each group (Fig. 2.5) for ease of reference in the text. The distal margin of the longest of these lobes (the lower southern Bn lobe) further sub-divides into separate lobes which have been labelled distal lobes 1 to 6 (Fig. 2.5-inset). The 18th August (F) lava flow deposit has been sub-divided into four separate flow zones, the proximal, medial, distal and frontal zones (Fig. 2.5).

The locations visited at each lava flow deposit and samples collected from these locations have been labelled by the designated letter for that flow followed by a number specific to each location, corresponding to the number of locations visited at that flow (e.g. location F21 represents the 21st location visited at the 18th August (F) lava flow deposit). Flow locations (underlined) referred to in this chapter are shown in Fig. 2.5 with a list of field descriptions and relevant GPS references given in Appendix A.4. A complete map and list of all the field locations visited is given in Appendix D.1.

2.1.4 Field Site Description

The 1954 lavas are situated within an approximately 2 km^2 area extending from the northwestern region of the crater rim (2240 m elevation a.s.l.) down the northwestern and western flanks of the cone to ~ 1330 m elevation, the lowest point of the flow deposits. The field area is partially bounded to the west by the eastern flanks of the main Pukekaikiore massif, and a steep-sided ridge, approximately 100 m high and 70 m wide, extending southwards from the eastern flanks of Pukekaikiore (Figs. 2.2 and 2.5) and forming the saddle between Pukekaikiore and Ngauruhoe. The slope angle of Ngauruhoe cone ranges from ~ 50° at the top ~ 300 m of the cone height to ~ 16° from the base of the cone to 1600 m elevation a.s.l., with an overall average slope angle of 33°.

There are no established fluvial drainage systems on the north-western sector of the cone, although some upper slope erosion, possibly due to surface water drainage from precipitation and snow melt, is evident. The geomorphic landscape

of the cone is dominated by numerous ridges and gullies of varying dimensions and displaying variable degrees of weathering and vegetation cover. These clearly represent the flow deposits and levee and channel formations of earlier lavas. These remnant flow features are more pronounced on the south-eastern flanks of the cone, where they have not yet been covered by recent lavas. The north-western flanks would likely have been of similar appearance but the lavas in this sector are older (Fig. 1.4), and therefore more subdued by weathering, than those to the south-east and have also since been modified by the more recent eruptive products from historic Ngauruhoe eruptions.

2.1.5 Pyroclastic Deposits

A variety of pyroclastic material associated with both the 1954-55 and 1973-75 Ngauruhoe eruptions is evident in the field area, both overlying and emplaced between the 1954 lava flow deposits.

Ballistic Bombs

Numerous large (up to ~ 6 m diameter), round boulders are scattered throughout the field area, lying on top of and in the spaces between the 1954 lava flow deposits. They are predominantly distributed in a scattered line that generally follows a similar elevation (~ 1600 to 1640 m a.s.l.) from north to south on the slopes of the cone (Fig. 2.6A). These boulders are characterised by the dense interiors, radial joint patterns and large impact fractures typically associated with ballistic ejecta (Figs. 2.6B and 2.6C). Their position on the flow surfaces of the 1954 lavas suggests they were ejected either towards the final phases of the 1954-1955 eruption or during the later 1973-75 eruption. One distinctive boulder (Fig. 2.6D), emplaced on the southern margin of the southern 14th July (Dc) flow deposit, can be positively identified as a 1954-55 ballistic bomb as it features in film footage of the 1954-1955 eruption (*Ngauruhoe Erupts*, 2003).

Block and Ash Flows

Several ‘hot avalanches’ were documented during the 1954-55 eruption, some associated with lava flow extrusion (Gregg, 1956). Hobden *et al*. (2002) described these as block and ash flows that were probably triggered by the sudden collapse

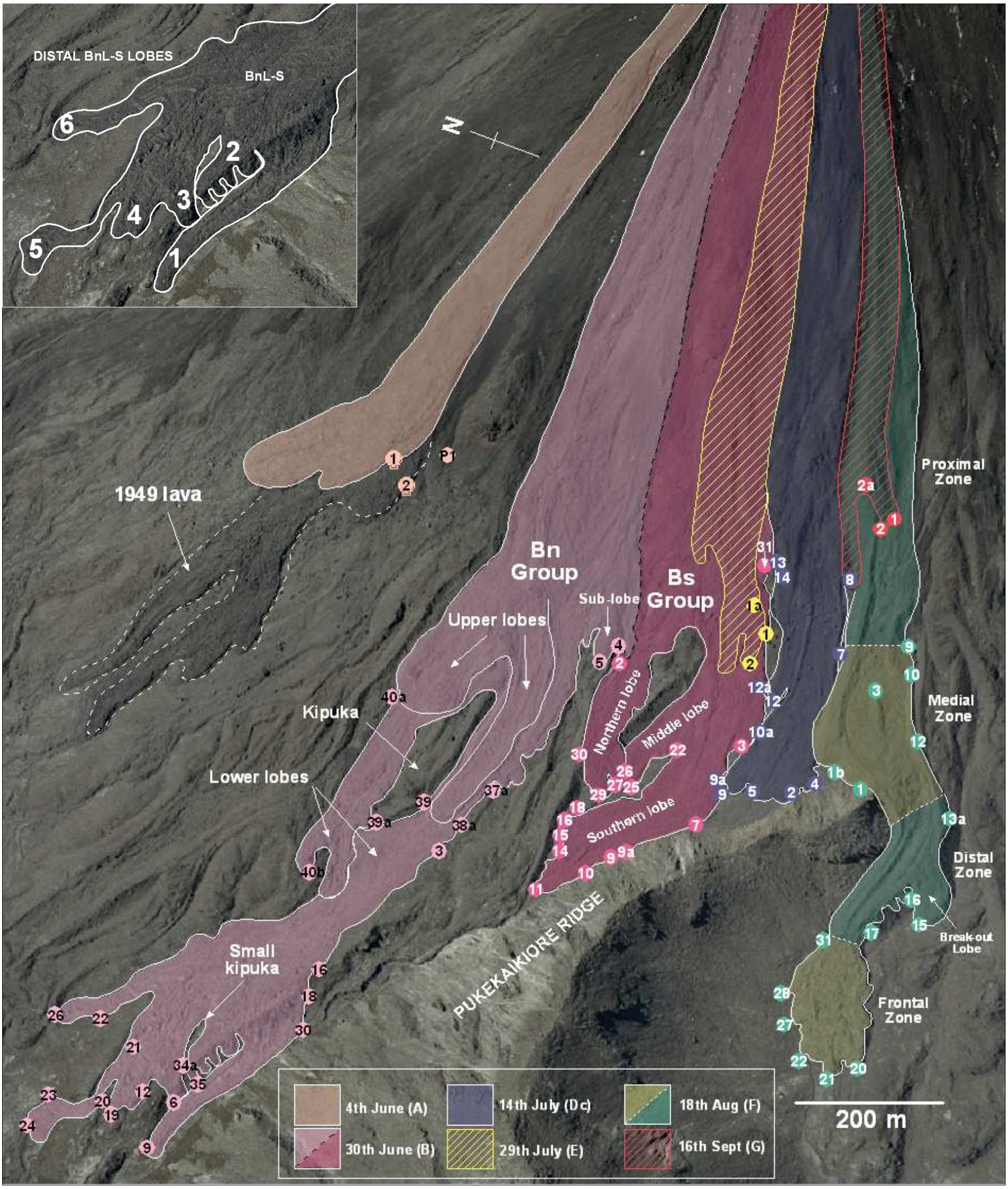

Fig. 2.5 Aerial photograph showing the six lava flow deposits visited in the field and the relative position of field locations referred to in Chapter 2. Field locations are marked with coloured dots corresponding to the relevant colours for each of the lava flow deposits. The 30th June lava flow deposit is shaded in two tones of pink to represent the two lobe groups (Bn and Bs). Dashed black line denotes inferred margin between these two lobe groups. Individual lobes within these groups are labelled. The 18th August lava flow deposit is shaded in two tones of green to represent the sub-division of the separate zones of the deposit. Dashed white line marks the inferred boundary between the zones. Inset: Enumeration of the distal lobes (1-6) of the lower southern Bn lobe (BnL-S), 30th June (B) lava flow deposit.

of unstable lava flow fronts or over-spilled, ponded lava from the crater rim. A hot avalanche' was observed descending the cone slopes on the 4th June 1954; its deposit subsequently covered in part by the southern-most of the two 4th June lava flows, while two others were observed on the 28th June, possibly emplaced to the north of the later 30th June lava flow deposit (Gregg, 1956).

During field work for this study, a block and ash flow deposit was noted lying immediately adjacent to the southern margin of the exposed, northern-most 4th June (A) lava flow deposit. It appears as a thin (< 0.5 m thick), heterogeneous mix of angular, relatively dense blocks (~ 40 to 50 cm diameter), numerous rounded, hydrothermally altered clasts (~ 10 to 20 cm diameter) and coarse ash particles (Fig. 2.7). This may be the deposit of one of the three 'hot avalanches' reported by Gregg (1956) to have occurred during the month of June 1954.

Scoria and Ash Flows

Another 'hot avalanche' was recorded by Gregg (1956) occurring on the western slopes of the cone on the morning of the 16th September and emplaced over the top of the earlier 18th August (F) lava flow deposit. This hot avalanche deposit was described as consisting of up to 3 m-sized "angular to rounded blocks of lava embedded in and coated with light-grey ash" (Gregg, 1956, p. 686). However, several block and ash flows, resulting from the collapse of eruption columns during the 1973-1975 Ngauruhoe eruption, were also recorded; one of these mapped by Hobden and Houghton (2000) overlies the 18th August (F) lava flow deposit (Fig. 2.1).

At the field site, a pyroclastic deposit was observed lying immediately adjacent to the southern margin of the 18th August (F) lava flow deposit on the upper slopes of the cone. Approximately 1 km down slope from the crater rim the pyroclastic deposit curves northwards to overlie the southern margin of the 18th August (F) lava flow deposit, subsequently breaching the southern margin and terminating on the lava flow surface (Fig. 2.8). The pyroclastic deposit consists primarily of a thin (0.1 to 0.5 m) heterogeneous layer of sub-rounded, vesicular, light grey and hydrothermally altered clasts and coarse ash that appears typical of a scoria and

ash rather than a block and ash flow deposit. The nature and location of this pyroclastic deposit matches the description of the hot avalanche reported by Gregg (1956) on 16th September 1954, with no evidence of the dense, angular material that would be consistent with the reported later 1973-75 block and ash flow (Hobden and Houghton, 2000).

A narrow (~ 10 m) scoria and ash flow deposit, consisting of similar material to the deposit adjacent to the 18th August (F) lava flow deposit, also overlies the southern section of the 29th July (E) lava flow deposit (Fig. 2.9). This scoria and ash flow deposit curves southward and is emplaced down the southern margin of the 29th July (E) lava flow deposit, terminating between the southern margin of the 30th June (B) and the northern margin of the 14th July (Dc) lava flow deposits. No hot avalanche deposits were reported or mapped in this location by Gregg (1956), although the extrusion of the 29th July (E) lava flow was accompanied by sharp explosions and visible shock waves which may have triggered such an event. Hobden and Houghton (2000) mapped a small pyroclastic deposit overlying the 30th June (B) lava flow deposit, adjacent to the northern margin of the 29th July (E) lava flow but not overlying it. Therefore the emplacement date of this scoria and ash flow deposit is not known.

2.2 LAVA FLOW DEPOSIT CHARACTERISTICS

Field observations and aerial photograph analysis of the 1954 lava flow deposits show similar geomorphological trends between the deposits, with only one or two exceptions. This section provides a synopsis of the overall deposit characteristics of the 11 lava flows identified by Gregg (1956). The characteristics of the five flows not visited in the field are inferred using Gregg's (1956) map (Fig. 1.7) and the updated flow deposit map (Fig. 2.2).

2.2.1 Morphology

With the exception of the northern 14th July (Da) lava flow, which was emplaced to the north of the 4th June (A) lava flow deposit, the 1954 lavas were generally emplaced in chronological succession from the north-western to the western slopes. The 1954 lavas generally display similar planimetric forms in that they are

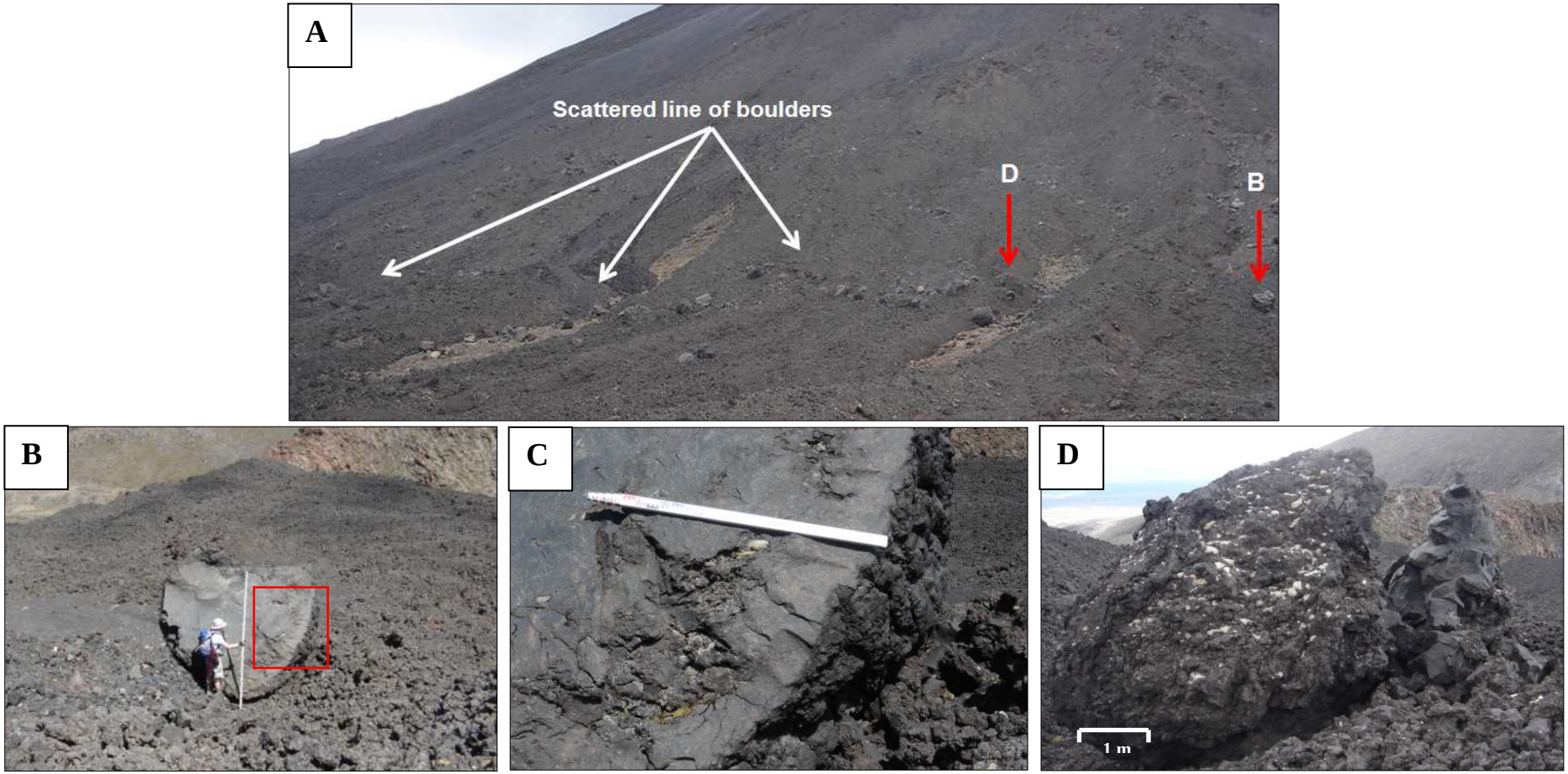

Figure 2.6 Scattered ballistic boulders emplaced over the 1954 lavas (dark deposits). A, north-south trending linear distribution of ballistics on the north-western flanks of Ngauruhoe. Red arrows show location of boulders B (in photographs B & C) and D (photograph D); B, ballistic boulder on the surface of the 18th August lava flow deposit. Red square denotes area of close-up view in photograph C. Measuring staff is 3 m height; C, radial jointing pattern on the outer rim of boulder B. Measuring staff is 1 m length; D, fractured ballistic bomb on the southern margin of the 14th July (Dc) lava flow deposit known to have been ejected during the 1954-1955 eruption.

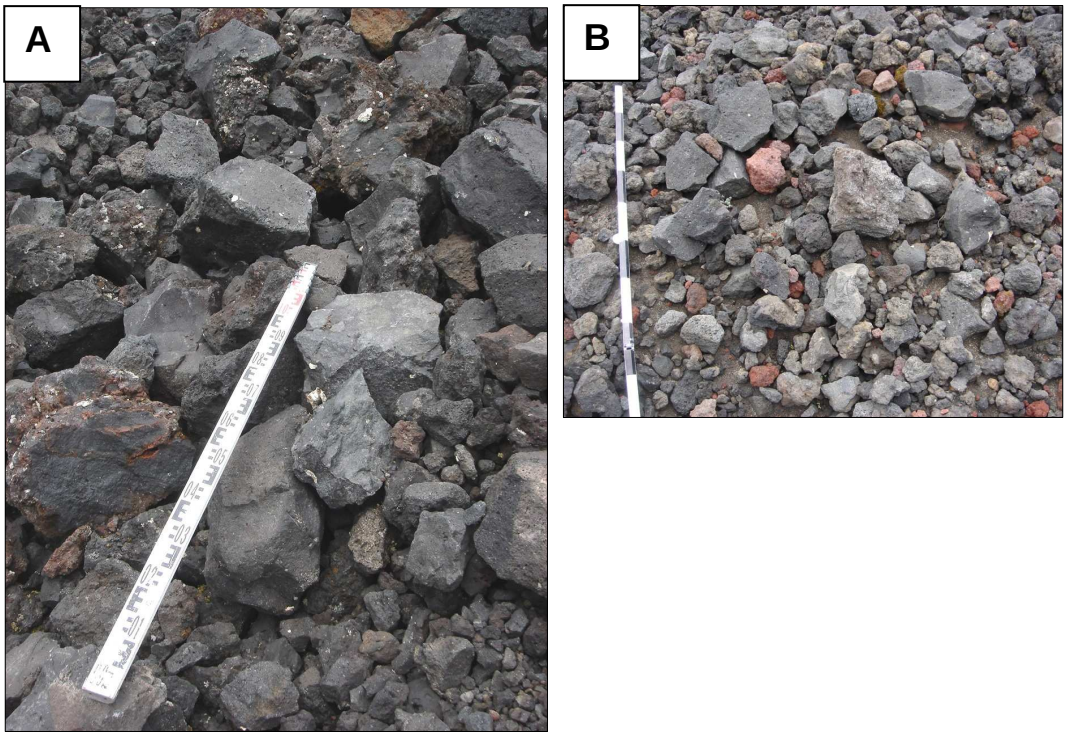

Fig. 2.7 Block and ash flow deposit emplaced adjacent to the 4th June lava flow deposit. A, dense, angular blocks within the block and ash flow deposit. Measuring staff is 1 m length. B, heterogeneous mix of angular blocks, rounded and hydrothermally altered clasts and coarse ash. Ruler is shaded in 10 cm sections.

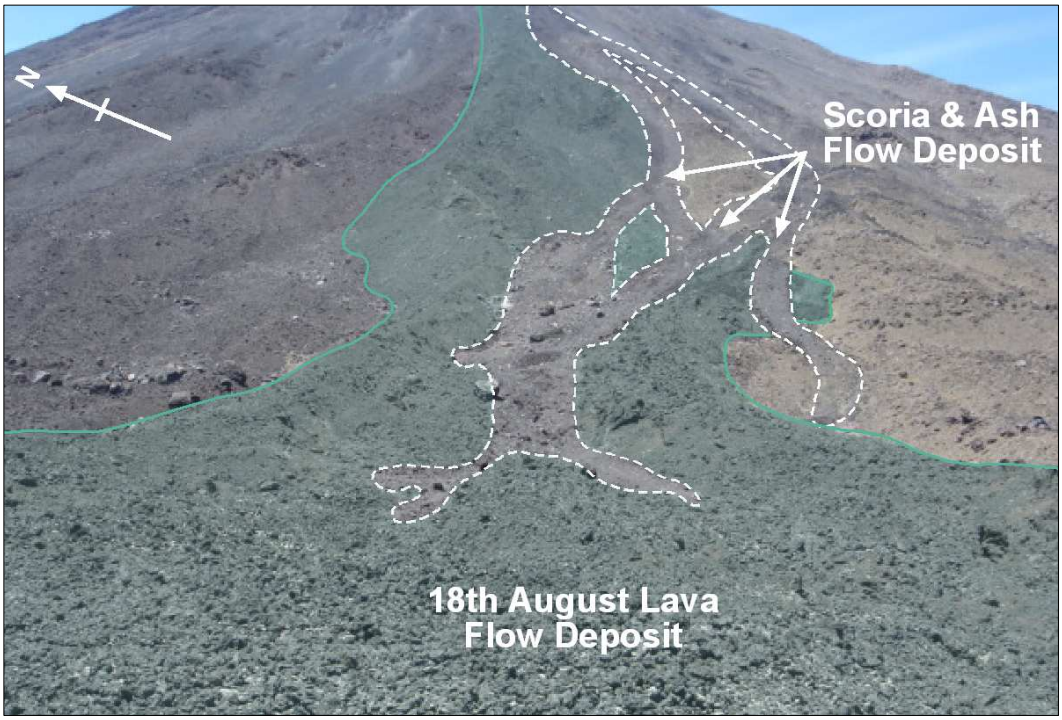

Fig. 2.8 Upflow view of the 18th August lava flow deposit (shaded green) showing the emplacement of the scoria and ash flow deposit (dashed white line) adjacent to and breaching the southern margin of the lava flow deposit.

relatively narrow, single-lobed, discrete units, terminating at rounded, steep-angled flow fronts (Fig. 2.2). Flow fronts are commonly subdivided into multiple, rounded, or in the case of 4th June (A) and 29th July (E) lava flows, sub-angular flow toes. The exception is the 30th June (B) lava flow which divided into multiple lobes, with some elongated finger-like lobes at the distal end of the deposit (Fig. 2.5-inset). All the lavas, except the 18th August (F) lava flow, were emplaced in a relatively straight path from the crater rim for most of their deposit lengths, with the flow direction changing towards the distal end of several flows. The 18th August (F) flow initially followed a straight path from the crater rim but displays a distinct s-shaped curve approximately two-thirds downflow (Fig. 2.5).

2.2.2 Geometry

The 1954 lavas exhibit similar flow deposit widths and depths, with greater variability between individual flow lengths (Table 2.1). The second of the 1954 lavas to be emplaced [30th June (B)] is the longest of the flow deposits (2.3 km), while the two shortest lavas (0.4 and 0.2 m) where the last of the 1954 lavas to be emplaced [18th (H) and 26th (I) September]. Lava flow deposit widths range from ~ 20 m to 230 m, although this is more difficult to quantify as the deposit margins proximal to the crater rim are not clearly defined. However, based on contemporary photographs of the 1954-55 eruption (Gregg, 1956), the lava flow deposits are assumed to maintain relatively constant widths from the crater rim throughout most of their deposit lengths. Average flow deposit widths therefore range between 40 to 150 m for all the lavas except the two shortest flows [18th (H) and 26th September (I)] which have an average width of 20 m. Lava flow depth averages 2 to 3 m for each of the flow deposits visited, but is extremely variable within individual flow deposits, varying by several meters (e.g. 0.3 to 6 m) at different locations of the flow. The exception is the two upper lobes (BnU-N and BnU-S) of 30th June northern lobe group (Bn), averaging ~ 9 m thick each.

The estimated volume of material emplaced with each lava flow unit ranges between 6,500 ± 3,600 m^3 [26th September (I) flow] and 2,289,600 ± 636,000 m^3 [30th June (B) flow]. The total volume of lava has been estimated at 3,802,000 ± 1,060,000 m^3, consistent with Gregg's (1956) estimate of between 3,000,000 and

Table 2.1 Summary of 1954 lava flow deposit geometry and volumes. Length and width are given to the nearest 50 m and 10 m respectively. Volume (x10^3 m^3) is shown with an error margin assuming 2% error in surface area estimation and a 1 m error in average flow depth. Volumes are given separately for the two main lobe groups (Bn and Bs) of the 30th June lava flow deposit, assuming the flow width of each lobe group on the upper slopes equals half of the width of the main 30th June deposit.

FLOW DEPOSIT	LENGTH (m)	WIDTH (m)		DEPTH (m)			UNDERLYING SLOPE ANGLE (°)		FLOW MARGIN SLOPE ANGLE (°)			VOLUME (x 10^3 m^3)	
		Range	Ave	Range	Ave	Flow Front	Range	Ave	Range	Ave	Flow Front	Volume	Error Margin
4th June (A)	1400	60 to 110	80	2.5 to 3.5	3	3.5	27 to 56	42	/	31	/	183	72
30th June (Bn)	2350	50 to 210	100	0.3 to 9	3	3.2 to 4	14 to 57	37	5 to 55	40	42 to 44	1748	437
30th June (Bs)	1750	50 to 230	150	0.7 to 4.6	3	2.7 to 5	13 to 56	35	18 to 44	40	36 to 42	542	199
Total 30th June Volume												**(2290)**	**(636)**
8/13th July (C)[1]	650	N/A	42	/	3	/	42 to 53	46	/		/	53	22
14th July (Da)[1]	1200	50 to 150	60	/	3	/	35 to 53	42	/		/	154	60
14th July (Db)[1]	850	N/A	70	/	3	/	26 to 56	42	/		/	110	44
14th July (Dc)	1550	50 to 140	90	1 to 6	3	5 to 6	14 to 60	39	32 to 44	40	40 to 44	264	103
29th July (E)	1350	50 to 90	60	3 to 4	3.5	4.8	19 to 49	37	38 to 40	40	45	210	73
18th Aug (F)	1900	50 to 160	100	6 to 12[2] 2.8 to 7.5[2]	10 (N)[2] 6 (S)[2]	4.5	9 to 53	28	30 to 47	38	38	425	/
16th Sept (G)	1200	40 to 70	50	2 to 3	2.5	3	34 to 51	39	31 to 32	32	40	91	42
18th Sept (H)[1]	400	20 to 30	20	/	2.5	/	33 to 49	41	/		/	15	8
26th Sept (I)[1]	200	N/A	20	/	2.5	/	N/A	36	/		/	7	4
											TOTAL	**3802**	**1060**

[1] Values derived from aerial photograph analysis.
[2] Values refer to marginal levees. N = northern levee; S = southern levee
/ Data not obtained
N/A Not applicable - flow width is relatively constant throughout flow deposit length

9,000,000 m^3, and just over half of the value estimated by Hobden *et al*. (2002) for the combined 1954 lavas and scoria cone. The 30th June (B) lava flow accounts for almost two thirds of the total volume of the 1954 lavas, greater than the one third percentage suggested by Gregg (1956).

2.2.3 Surface Features

Most of the 1954 lavas exhibit relatively flat, uniform flow surfaces with no clear evidence of a central flow channel or elevated marginal levees. The exception is the 18th August (F) lava flow deposit which displays a distinctive central flow channel bound by elevated marginal levees. The extent of lava deposition within this central flow channel is variable throughout the length of the flow deposit. The distal regions of some of the 1954 lava flow deposits display low-relief surface features and a slight increase in flow depth.

2.3 LAVA FLOW DEPOSIT DESCRIPTIONS

This section presents a detailed description of the geometric, morphological and surface feature characteristics of each of the six 1954 lavas visited in the field [4th June (A); 30th June (B); southern 14th July (Dc); 29th July (E); 18th August (F); 16th September (G)]. Comprehensive data were collected from the 30th June (B) and 18th August (F) lava flow deposits and the sections describing these deposits are sub-divided into lobe groups and individual lobes (30th June), and separate flow zones (18th August).

2.3.1 4th June (A) Lava Flow Deposit

The 4th June lava flow deposit was the first of the 1954 lavas to be emplaced and is a single-lobed, discrete unit overlying the earlier 1949 lava flow deposit (Fig. 2.5). It lies in a straight path from the crater rim for most of its length but curves northwards for the last ~ 200 m. The flow front is divided into two asymmetrical, angular toes, the northern toe slightly longer and wider than the southern toe. The base of the southern margin (A1) of the 4th June lava deposit is obscured by its emplacement over the earlier 1949 flow deposit (A2), and the presence of the block and ash flow deposit (P1) immediately adjacent to the southern margin

(Fig. 2.10). The average slope angle underlying the 4th June lava flow deposit is 42°, although the distal margin rests on a gentler slope angle (~ 30°).

The flow surface of the 4th June lava flow deposit is relatively flat with no apparent central flow channel or identifiable marginal levees, compatible with the homogenous flow surface evident on aerial photographs.

2.3.2 30th June (B) Lava Flow Deposit

This deposit is the second and the longest of the 1954 lavas to be emplaced. Gregg's (1956) account records two initially separate lava flows that merged part way down the flanks of the cone then divided into several separate lobes further down the slope. The proximal section of these flows have subsequently been overlain by some of the July 1954 lavas [8-13th (C), 14th (Db); 29th July (E)] and pyroclastic products from the 1954-55 and 1973-75 Ngauruhoe eruptions, thus any evidence of separate lava flow margins higher up the slope have been obscured. The currently exposed 30th June (B) lava flow deposit initially appears as a single, relatively wide (~ 250 m) flow unit for the proximal half of its length, although the lateral margins are not well-defined. The deposit divides into two distinct 'groups' of lobes (Bn and Bs) ~ 940 m from the crater rim at ~ 1,620 m elevation, with a short minor lobe (Bm) emplaced between the two lobe groups (Fig 2.5). The proximal section of the 30th June lava flow deposit rests on an underlying slope angle of ~ 40°. Downflow the slope angle gradually decreases to ~ 16° at the distal margin, although localised slope angles are more variable, particularly underlying each of the Bn group distal lobes.

The descriptions in this section have been sub-divided into the northern (Bn) and southern (Bs) lobe groups, with further sub-headings referring to the individual lobes within each group.

Northern Lobe Group (Bn)

This group consists of two 'lower' lobes (BnL) that bifurcate approximately 75 m downflow from the division between this lobe group and the southern group of lobes (Bb). Overlying these two BnL lobes are two shorter length, but markedly

thicker, 'upper' lobes (BnU) that bifurcate at the same position as the underlying lobes. Both sets of lobes are separated by a ~ 260 m long, lens-shaped paleo-topographical high point (kipuka), approximately 10 to 15 m higher than the surrounding slopes (Fig. 2.5).

Lower Bn Group Lobes (BnL)

The shorter of the two lower lobes is a narrow (~ 61 m wide), single lobe that extends 1.8 km from the crater rim and lies in a relatively straight path around the northern side of the kipuka (BnL-N). This lobe divides into two short, narrow toes (Bn40b) approximately 80 m before its distal end; the northern-most of these terminating at a narrow, rounded flow front. The southern toe curves southward and overlaps the northern margin and flow surface of the lower southern Bn lobe (BnL-S) (Bn39a) (Fig. 2.11), tapering into several thin fingers as it overlaps the lower southern lobe flow surface. The lower northern lobe averages ~ 2.8 m depth, increasing to ~ 3m at the flow front of the northern toe.

The southern-most of the two lower Bn lobes (BnL-S) is the longest section of the 30th June flow and extends initially as a narrow (~ 45 to 50 m width), single lobe for approx 480 m following the point of bifurcation of the northern lobes, curving to the south around the kipuka. The lobe then widens to ~ 90 m (Bn16) before dividing into several smaller lobes (BnL-S1 to BnL-S6) that mark the distal end of the lower southern Bn lobe (Fig. 2.5-inset).

BnL-S-1:

The southern-most of the distal BnL-S lobes was emplaced down the slopes of a steep (~ 30 to 35°), high-elevation, south-west facing, pre-existing ridge (Bn18) and diverted westward (Bn30) into a small stream valley that lies between the ridge and the northern slopes of Pukekaikiore (Fig. 2.12A). The lobe deposit partially infills the stream valley, extending as a narrow, elongated finger-like deposit ~ 270 m along the gently sloping (~ 15°) valley floor. The width of the lobe deposit is approximately ~ 110 m from the top to the base of the underlying ridge, narrowing to ~ 20 to 25 m width as it is confined along the valley floor. Lobe depth varies between ~ 0.2 to 4 m, and terminates at a rounded, ~ 3 m deep flow front (Bn9)

BnL-S-2:

The main section of the BnL-S lobe was emplaced along the top of the high-elevation, pre-existing ridge, bifurcating around a low-elevation kipuka on the upper surface of the ridge (Bn34a) (Fig. 2.5). The flow deposit to the southern side of the kipuka develops into a series of small lobes (grouped as distal lobe 2) that were emplaced down the south-western ridge slope in several places along its length (Fig. 2.12B). These 'overspill' lobes are generally < 0.5 m deep with each of the small lobes terminating at the northern margin of the distal lobe 1 deposit. Contact between the distal margins of these overspill lobes and the northern margin of distal lobe 1 (BnL-S-1) is minimal, with patches of the underlying surface visible in places and no thickening of the deposit noted at the distal margins of the BnL-S-2 lobes (Bn35).

BnL-S-3:

To the north of the kipuka (Bn34a) flow emplacement continued in a relatively straight path along the top of the high-elevation ridge dividing into a further three distal lobes (BnL-S-3,4 and 5) (Fig. 2.5). BnL-S-3 curves to the south and forms the final lobe to be emplaced down the south-west slope of the pre-existing ridge, terminating at the northern margin of BnL-S-1 adjacent to BnL-S-2 (Bn6) (Fig. 2.12B). As with the other overspill lobes (BnL-S-2), there is minimal contact between the front of this lobe and the northern margin of BnL-S-1, with no evidence of overlapping of the two lobes. The lobe is ~ 3 m deep at the top of the ridge, thinning to ~ 0.5 to 1 m on the ridge slope to the base of the lobe.

BnL-S-4:

This distal lobe continues along the main flow path on top of the high-elevation pre-existing ridge, extending a further 80 m beyond the division from BnL-S-3 (Fig. 2.5). It is a ~ 30 m wide deposit averaging ~ 5 m depth and terminating at a steep (~ 42°), rounded flow front ~ 5.5 m deep (Bn19) that rests on the gently downward-sloping (~ 4 to 6°) surface of the underlying ridge (Bn12).

BnL-S-5:

This lobe marks the longest section of the 30th June flow deposit, extending ~ 2.2 km from the crater rim (Table 2.1). It separates from the northern margin of BnL-S-4 approximately 45 m before the front of lobe 4, with a low-elevation

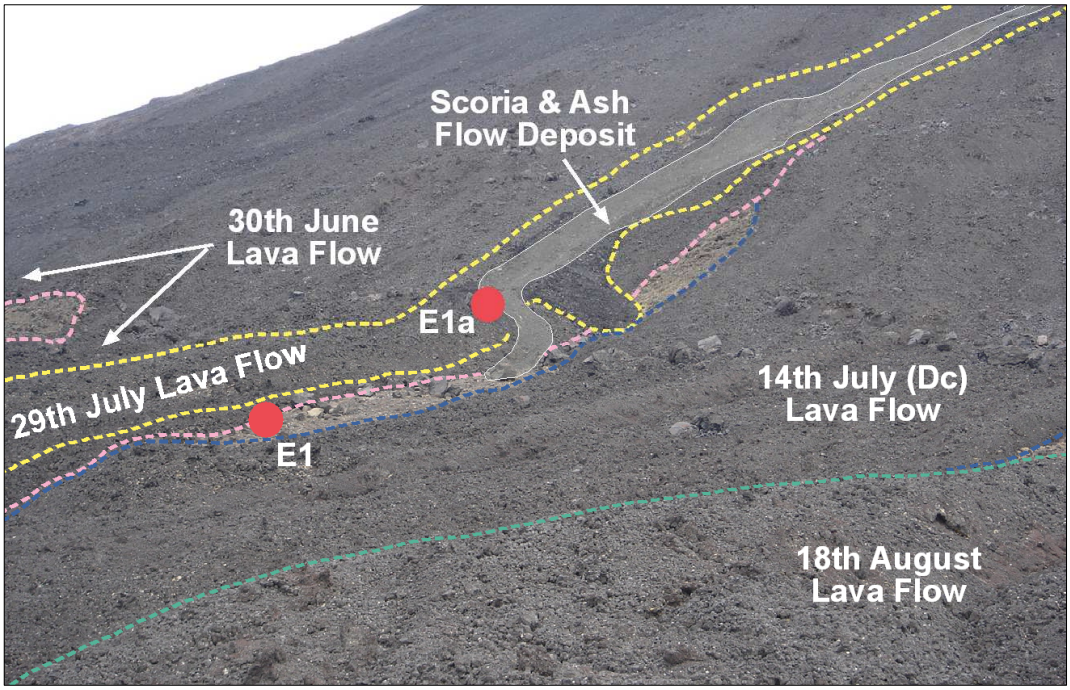

Fig. 2.9 View of the scoria and ash flow deposit (shaded grey) overlying the flow surface of the 29th July (E) lava flow deposit (dashed yellow line). The margins of the 30th June (B) (dashed pink line), 14th July (Dc) (dashed blue line) and 18th August (F) (dashed green line) lava flow deposits are shown. Red dots denote field locations.

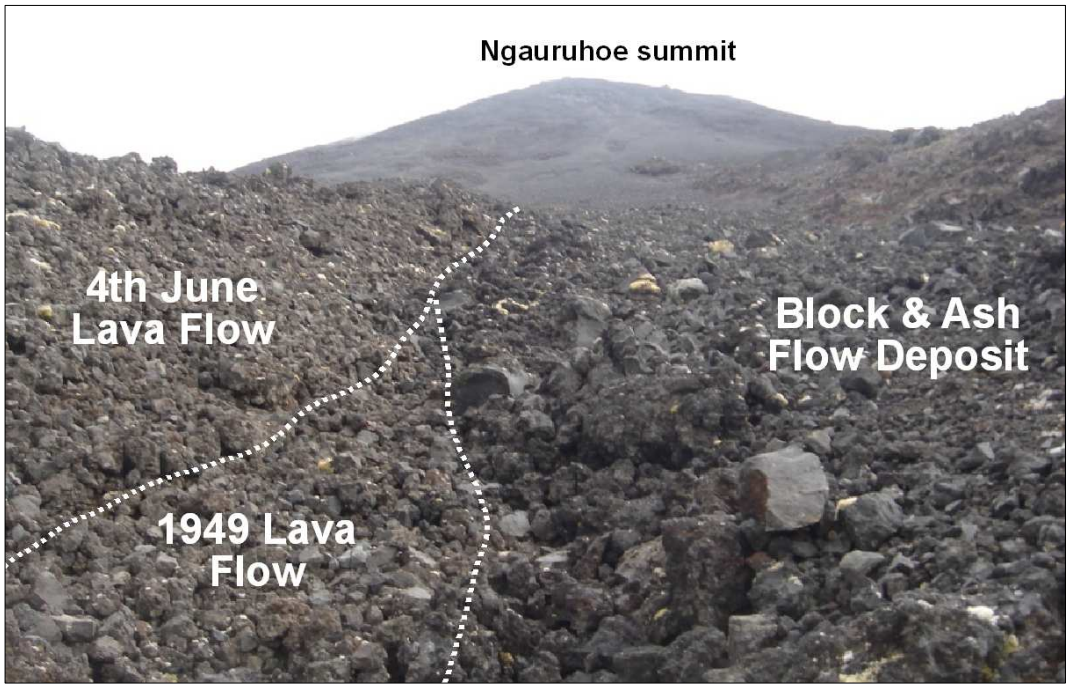

Fig. 2.10 Upflow view of the southern margin of the 4th June (A) lava flow deposit and the underlying 1949 lava flow deposit from location A1. Note the darker colour and blockier texture of the adjacent block and ash flow deposit.

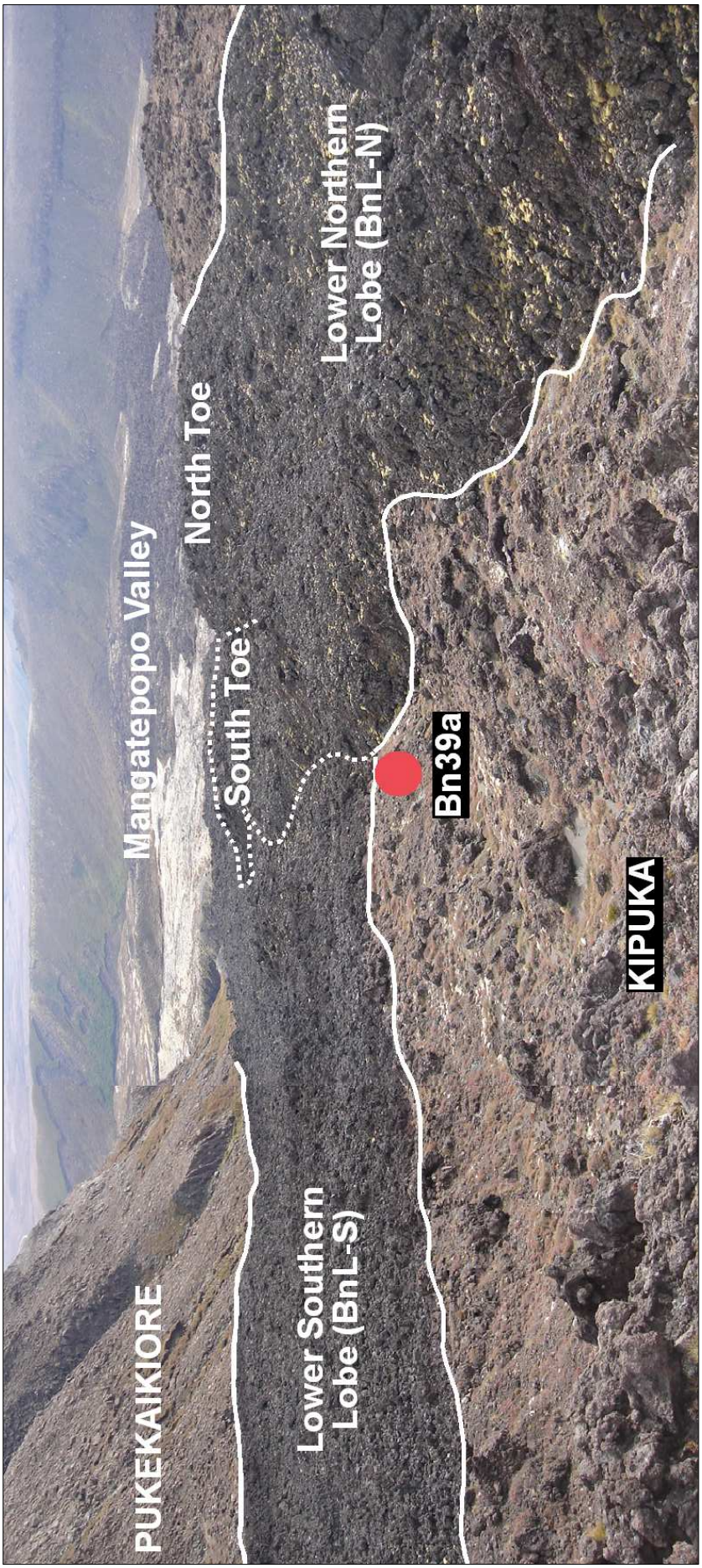

Fig. 2.11 Downflow view of the two lower (BnL) lobes, 30th June lava flow, showing the overlap of the northern toe of the lower northern Bn lobe (BnL-N) onto the northern margin and flow surface of the lower southern Bn lobe (BnL-S). Red dot denotes field location.

(~ 3 to 4 m) pre-existing ridge separating the two (Bn20) and confining the northern margin of lobe 5 (Fig. 2.13-inset). The ~ 15 m wide deposit was emplaced down the steep (~ 36°) northern slope of the high-elevation, pre-existing ridge (Bn23) (Fig. 2.13), extending as an elongated finger-like deposit ~ 140 m beyond its division from BnL-S-4. At the base of the underlying ridge the lobe finger broadens to a width of ~ 40 m, extending a further ~70 m beyond the ridge base on a gently westward sloping (~ 6 to 7°) underlying surface. Lobe depth ranges between 2 to 3 m, increasing to ~ 3.5 m at the front of the lobe (Bn24).

BnL-S-6:

This is the northern-most distal lobe of the 30th June lava flow deposit, dividing from the northern margin of BnL-S-5 approximately 190 m from the point where the lower southern Bn lobe (BnL-S) widens (at the northern flow margin opposite location Bn16). This lobe deposit was emplaced in a north-westerly direction down the steep (~ 32°), north-facing slope of the high-elevation, pre-existing ridge (Bn22), extending ~ 135 m into an elongated finger-like deposit after separating from the rest of the flow. At the top of the ridge the deposit is ~ 150 m wide, narrowing to ~ 25 m width on the ridge slope where the northern margin is confined by a low-elevation ridge (Fig. 2.14). The deposit terminates at a rounded, 3 m deep flow front that is confined by, and partially fills, a shallow hollow between two low-elevation ridges.

Upper Bn Group Lobes (BnU)

Two distinctive 'upper' lobes were emplaced over the proximal section of the longer lower northern (BnL-N) and southern (BnL-S) Bn lobes, bifurcating around the lens-shaped kipuka (Fig. 2.5) at the same location as the lower lobes. Both upper lobes are ~ 9 m deep compared to the ~ 2.5 to 3 m average depth of the lower lobes. The upper northern lobe (BnU-N) extends 1.5 km from the crater rim terminating in a steep (44°), broadly rounded flow front approximately 90 m wide (Bn40a). The upper southern lobe (BnU-S) is a ~ 9 m deep, narrow (~ 45 m) flow deposit extending ~ 1.6 km from the crater rim and terminating with a steep (44°), narrow, rounded flow front (Bn38a) (Fig. 2.15).

Most of the flow surface of both the upper and lower Bn group lobes is relatively uniform with no evidence of a central flow channel or elevated marginal levees. However, an approximately 120 m long, low-elevation levee occurs along part of the southern margin of the lower southern Bn lobe (BnL-S), between locations Bn37a and Bn3, adjacent to the southern margin of the overlying upper southern Bn lobe (BnU-S). The south-facing outer wall of this levee is ~ 3 m high (Fig. 2.15), and the north-facing inner wall ~ 8 m high. A similar feature, with broadly comparable inner and outer wall dimensions, is also evident on the northern margin of this lobe, directly adjacent to the south-facing slope of the kipuka around which the lobes of the Bn group bifurcate. The flow surface between these levee structures lies approximately 8 to 10 m lower than the surface of the underlying topography adjacent to the outer walls of each levee, suggesting that this part of the flow was partially confined between the south-facing slopes of the kipuka at the northern margin and an underlying ridge at the southern margin, with the southern flow deposit margin overtopping this ridge and forming a small levee at the ridge top.

For the remainder of the lobe length the levees of the lower southern Bn lobe (BnL) merge into flow margins that are at a similar level to the flow surface, with no apparent evidence of a deep-seated flow channel. The flow surface of the distal end of this lobe is characterised by complex surface features dominated by numerous, low-elevation ridges and shallow depressions on the flow surface (Fig. 2.16). Most of these are orientated in the general direction of the flow and may represent shallow flow channels towards the terminal ends of the distal lobes, e.g. the flow surface of distal lobe 6 (BnL-S-6) (Fig. 2.14).

Minor Lobe (Bm)

This small lobe (Bn5) marks the point of separation between the Bn and Bs lobe groups (Fig. 2.5). It is a ~ 45 m long, ~ 30 m wide lobe deposit, approximately 1 to 2 m deep, that was emplaced over the top of, and at the western end of, a pre-existing ridge; an extension of which also confines the northern margin of the northern Bs lobe (Fig. 2.17). This lobe appears to have separated from the southern margin of the lower southern Bn lobe (BnL-S) (thus field locations are

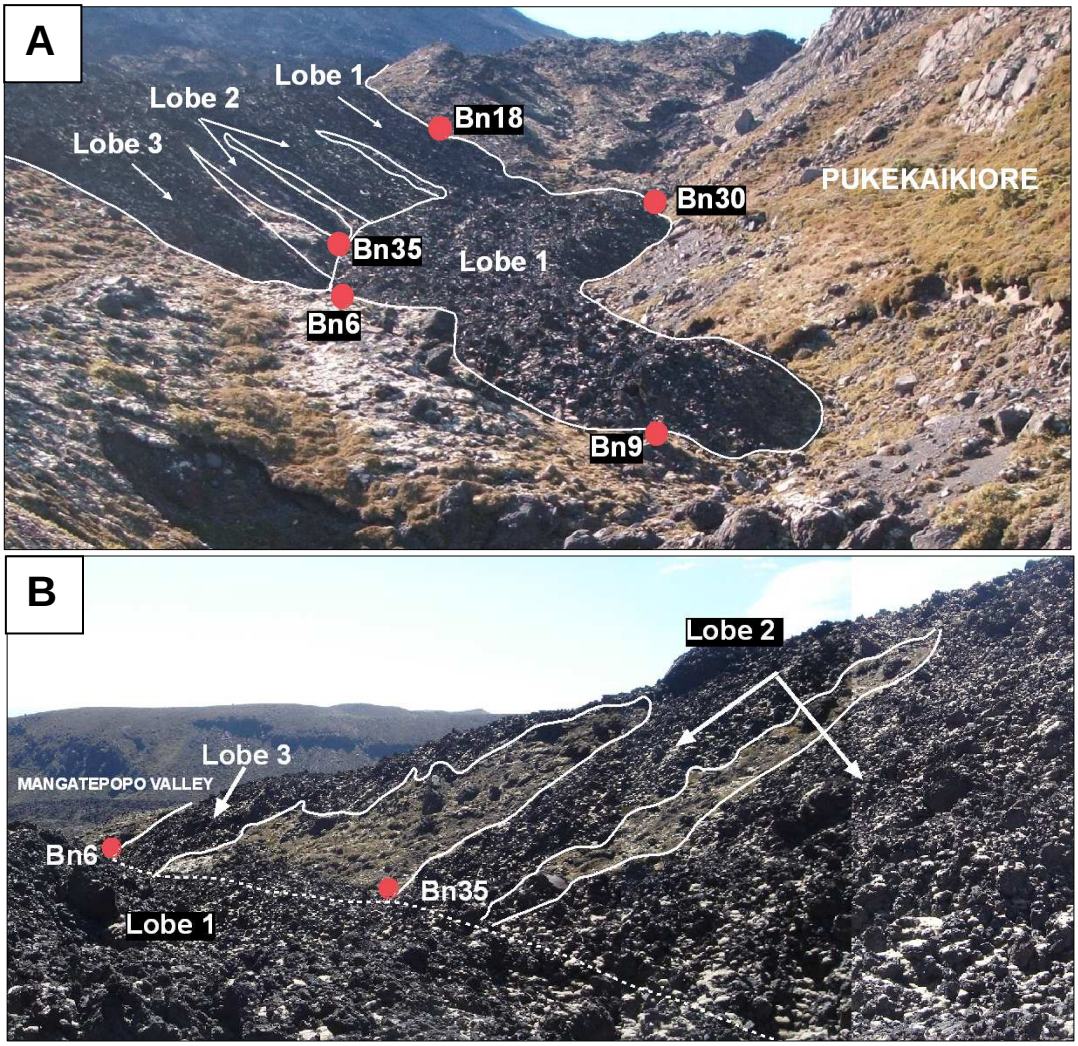

Fig. 2.12 Distal lobes 1,2 and 3 located at the distal end of the lower southern (BnL-S) lobe, 30th June lava flow. Red dots denote field locations. A, upflow view of distal lobes 1,2 and 3 emplaced down the south-west facing slope of a pre-existing ridge. Lobe 1 extends as an elongated lobe deposit infilling the stream valley. B, downflow view of lobes 2 and 3 emplaced down the south-facing slope of the pre-existing ridge and coming into contact with the northern margin (dashed white line) of distal lobe 1.

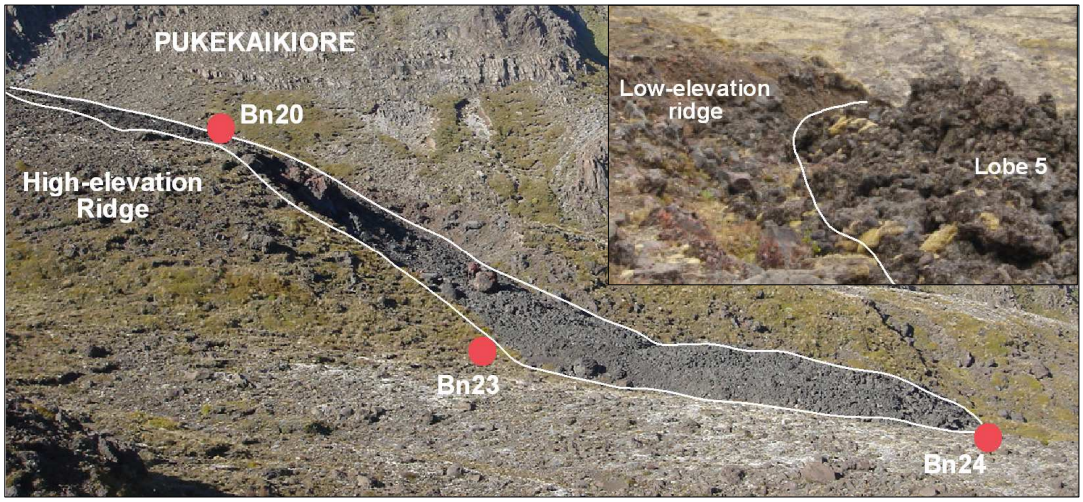

Fig. 2.13 View of the northern margin of distal lobe 5, lower southern (BnL-S) lobe, 30th June lava flow. Lobe 5 is emplaced down the north-west facing slope of the pre-existing, high-elevation ridge. Inset: downflow view of the southern margin (white line) of lobe 5 confined by the north-facing slope of a pre-existing, low-elevation ridge from location Bn20.

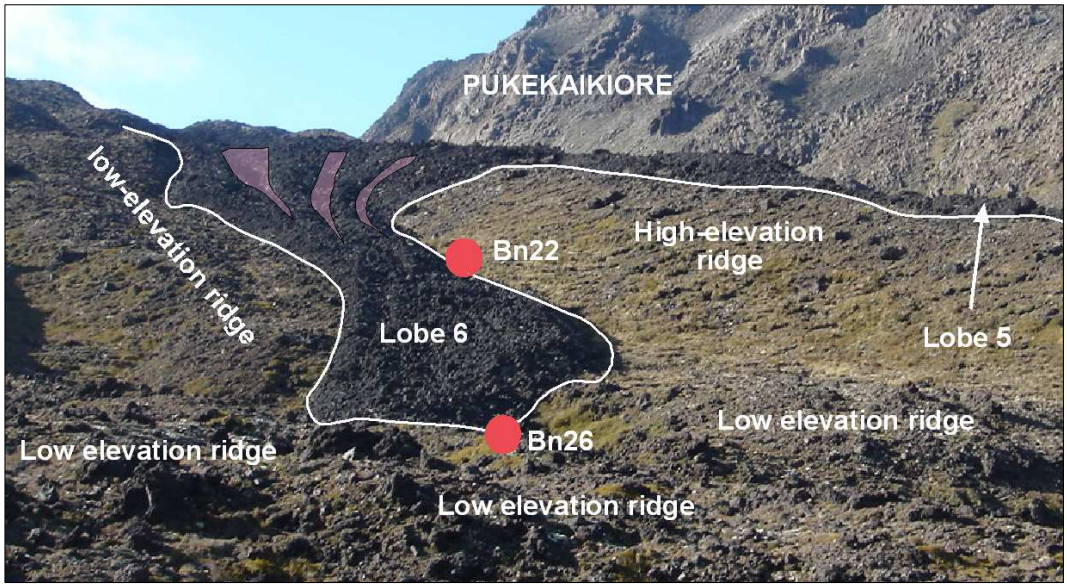

Fig. 2.14 Upflow view of distal lobe 6, lower southern (BnL-S) lobe, 30th June lava flow. Deposit width decreases downflow as the northern margin is confined by the south-west facing slope of a low-elevation ridge. Low-elevation ridges also confine the distal end of the lobe deposit. Pink shaded areas denote shallow depressions on the flow surface, orientated in the same direction as the flow. Red dots denote field locations.

labelled 'Bn'). A smaller ~ 10 to 15 m wide, 3.5 m deep lobe appears to have separated from the southern margin of the Bm lobe (Bn4), extending ~ 45 m over the flow surface of the northern Bs lobe (Fig. 2.17).

Southern Lobe Group (Bs)

The southern lobe group (Bs) consists of three discrete lobes, labelled northern Bs lobe, middle Bs lobe and southern Bs lobe, emplaced to the south of the northern (Bn) group (Fig. 2.5).

Northern Bs Lobe:

This lobe extends ~ 1.5 km from the crater rim, dividing from the southern Bs lobe approximately 1.2 km downflow (at ~ 1620 m elevation). It is an approximately 53 m wide flow unit that curves initially to the northwest relative to the southern Bs lobe, then curves southward as the distal end is emplaced down the ~ 15 m high, south-west facing, 32° slope of a pre-existing ridge. It terminates at an approximately 4 m deep, double-toed flow front (Bs27, Bs29), with the south-eastern toe overlapping the flow front of the middle Bs lobe (Bs26) (Fig. 2.18). A low-elevation (1-2 m) ridge, extending from the western end of the ridge

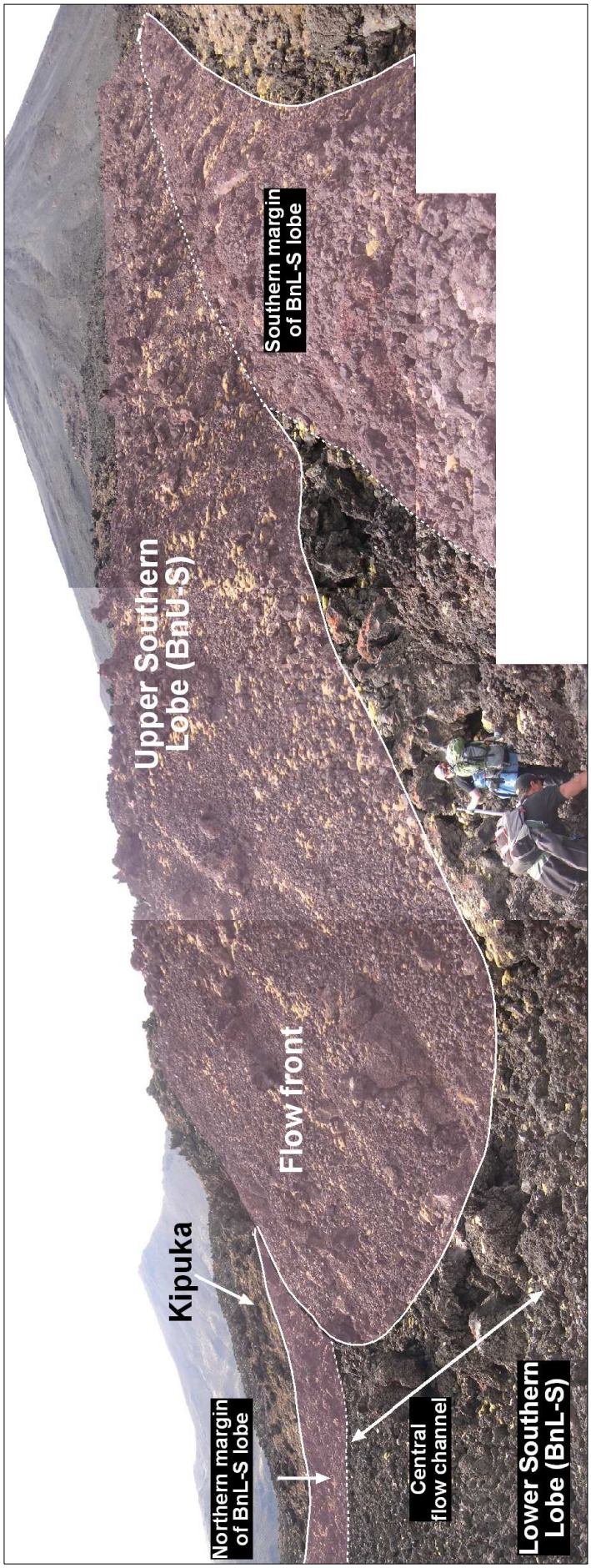

Fig. 2.15 Flow front of the upper southern (BnU-S) lobe, 30th June lava flow, from location Bn38a. The upper southern lobe (BnU-S) and margins of the lower southern lobe (BnL-S) are shaded pink. The extent of the central flow channel on the lower southern (BnL-S) lobe surface is shown with a white double-headed arrow. Note the difference in height between the north-facing, inner wall and south-facing, outer wall of the southern margin of the lower southern (BnL-S) lobe. Measuring staff held by person wearing green back pack is at 1 m height.

Fig. 2.16 Aerial photograph of the distal flow end of the lower southern (BnL-S) lobe, 30th June lava flow (white outline). Pink dashed lines denote shallow depressions on the flow deposit surface.

underlying the minor (Bm) lobe (Bn5) appears to confine the northern margin of the northern Bs lobe, between locations Bs2 and Bs30 (Figs. 2.5 and 2.17)

Middle Bs Lobe:

This is the shortest of the three Bs group lobes, extending ~ 1.3 km from the crater rim. It divides from the northern margin of the southern Bs lobe approximately 60 m downflow from the division of the southern and northern Bs lobes, and was emplaced at an approximate 45° angle from the northern margin of the southern Bs lobe on the north-west facing slope of an underlying ridge (Bs22) (Fig. 2.18). The northern margin of this middle Bs lobe is confined by the base of the south-west facing ridge that underlies the distal margin of the northern Bs lobe (Fig. 2.18). Flow deposit depth averages ~ 3.5 m and appears to terminate in a single, rounded flow front (Bs25), although the northern section of the flow front is obscured by the overlying south-eastern toe of the northern Bs lobe.

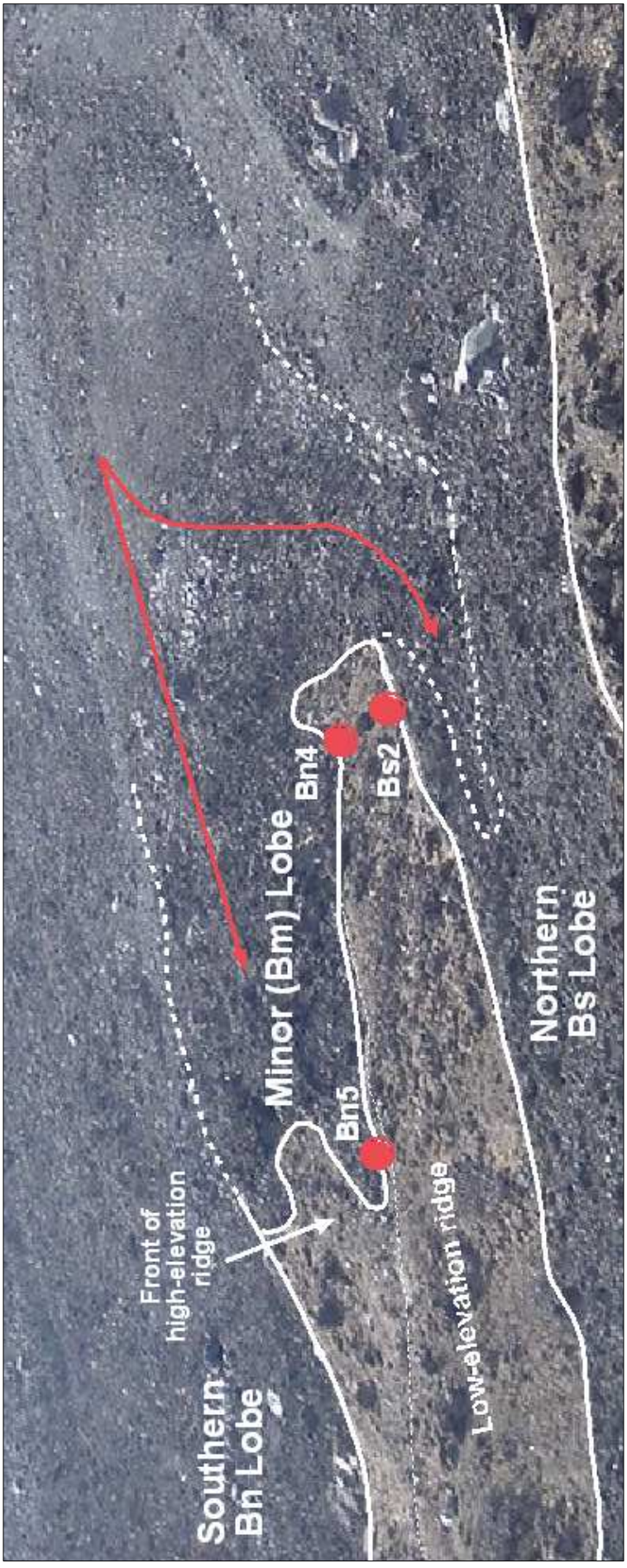

Fig. 2.17 View of the minor (Bm) lobe located between the Bn and Bs lobe groups, 30th June lava flow. The Bm lobe has been emplaced over a high-elevation, pre-existing ridge. Note the location of a low-elevation ridge between the southern margin of the Bm lobe and the northern margin of the northern Bs group lobe. Dashed white line denotes the inferred margin of the Bm lobe. Red arrows denote inferred flow direction. Red dots denote field locations.

Fig. 2.18 Across-flow view of the northern and middle Bs lobes, 30th June lava flow deposit. The distal end of the northern Bs lobe is emplaced down the south-west facing slope of a pre-existing ridge and divides into two toes at the lobe front. The south-eastern toe is emplaced over the flow surface and flow front of the middle Bs lobe. Dashed line denotes contact between the lower surface of the northern Bs lobe and the upper surface of the middle Bs lobe. The middle Bs lobe separates from the northern margin of the southern Bs lobe at the top of a pre-existing ridge and is emplaced down its north-west facing slope. Red dots denote field locations.

Southern Bs Lobe:

This is the longest of the three Bs group lobes with a total length of ~ 1.7 km from the crater rim and terminating with a broad (~ 100 m) flow front comprised of a series of several small, rounded toes (Bs 11, Bs14, Bs15, Bs16, Bs18) (Fig. 2.5). It is a single, ~ 80 m wide unit emplaced in a straight path from the crater rim for approximately 1.4 km of its total length, curving to the north-west along the base of the north-facing flanks of Pukekaikiore for the remaining ~ 300 m (Fig. 2.19). A small sub-lobe (Bs3) extends ~ 170 m along the southern margin of this lobe, terminating approximately 100 m before the southern Bs lobe is diverted northwards. Lobe deposit depth ranges between 0.5 to 3.6 m, with an average of ~ 3 m, increasing to 3.5 to 4 m depth at the flow front.

The southern, northern and north-eastern flow margins of the southern Bs lobe are unconfined by underlying topographical features and appear to be emplaced on a relatively flat, featureless paleo-surface, whereas the south-western margin is bounded by the base of the north-facing Pukekaikiore slopes (Fig. 2.19). However, although the flow direction changed significantly as the deposit reached the base of the ridge, some sections of the south-western flow margin, e.g. location Bs7, barely come into contact with the base of the ridge (Fig. 2.20A), whereas other sections, e.g. location Bs10, fully abut against the base of the ridge, obscuring the outer wall of the flow margin (Fig. 2.20B). A pre-existing, 10 to 15 m high, south-facing ridge is located directly adjacent and parallel to the multi-toed flow front of the southern Bs lobe. However, with the exception of the western-most and eastern-most toes, the remainder of the flow front toes do not come into contact with the base of the ridge, terminating 0.5 to 20 m before the ridge base (Fig. 2.21).

The proximal section of the southern Bs lobe deposit, from the point where the southern margin of the lobe becomes clearly separated from the northern margin of the 14th July (Dc) flow deposit (Bs31) to the front of the sub-lobe on the southern margin of the southern Bs lobe (Bs3), rests on a relatively gentle underlying slope angle of ~ 15°. This slope angle decreases to 8 to 10° at the distal section of the southern Bs lobe, once the flow direction changes towards the north-west (Bs7 to Bs11).

The flow surfaces of the southern Bs lobe group display a similar pattern of low-elevation ridges and shallow depressions to those noted at the distal margin of the lower southern Bn lobe, although some of these appear to be more randomly orientated in places along the flow surface (Fig. 2.22). A distinctive ridge crest is evident near the centre of the flow surface of the southern Bs lobe. The northern margin of the southern Bs lobe is emplaced down the north-facing slope of this ridge and it appears that it is this ridge slope that the middle Bs lobe was also emplaced down (Fig. 2.18). The crest of the ridge appears to follow the curve of the southern Bs lobe as its flow direction changes northward alongside the base of the Pukekaikiore ridge.

2.3.3 14th July Lava Flow Deposit – Southern (Dc) Flow

The southern-most of the three 14th July lavas is a single-lobed, discrete unit emplaced immediately adjacent to, and intermittently in contact with, the southern margin of the southern Bb lobe of the 30th June (B) lava flow deposit (Fig. 2.5). Part of the southern margin and flow surface of the 14th July (Dc) lava flow deposit is completely overlain by the northern margin of the later 18th August (F) lava flow deposit. Contact with the 30th June (B) lava flow deposit occurs in three locations along the northern margin of the 14th July (Dc) lava flow deposit (Dc9a, Dc10a and Dc12a), with no evidence of the 14th July (Dc) lava flow overlapping the flow surface of the earlier 30th June (B) lava flow. The points of contact between these two lava flow deposits involve only the basal sections of each flow margin (Fig. 2.23), with the underlying surface intermittently visible between the two flow margins. Although it has been mapped by Gregg (1956) as a separate flow, the proximal margins of the 14th July (Dc) lava flow deposit are not clearly defined and the flow appears to have separated from the southern margin of the southern Bs lobe of the 30th June lava flow ~ 1.2 km from the crater rim (Dc13) (Fig. 2.24). The flow width of the 14th July (Dc) deposit averages ~ 90 m for most of the flow length, broadening towards the flow front to a maximum of ~ 140 m just behind the flow front.

The flow deposit terminates with the formation of four rounded toes (Dc2, Dc4, Dc5, and Dc9) (Fig. 2.25) and a smaller sub-lobe is evident on the northern flow

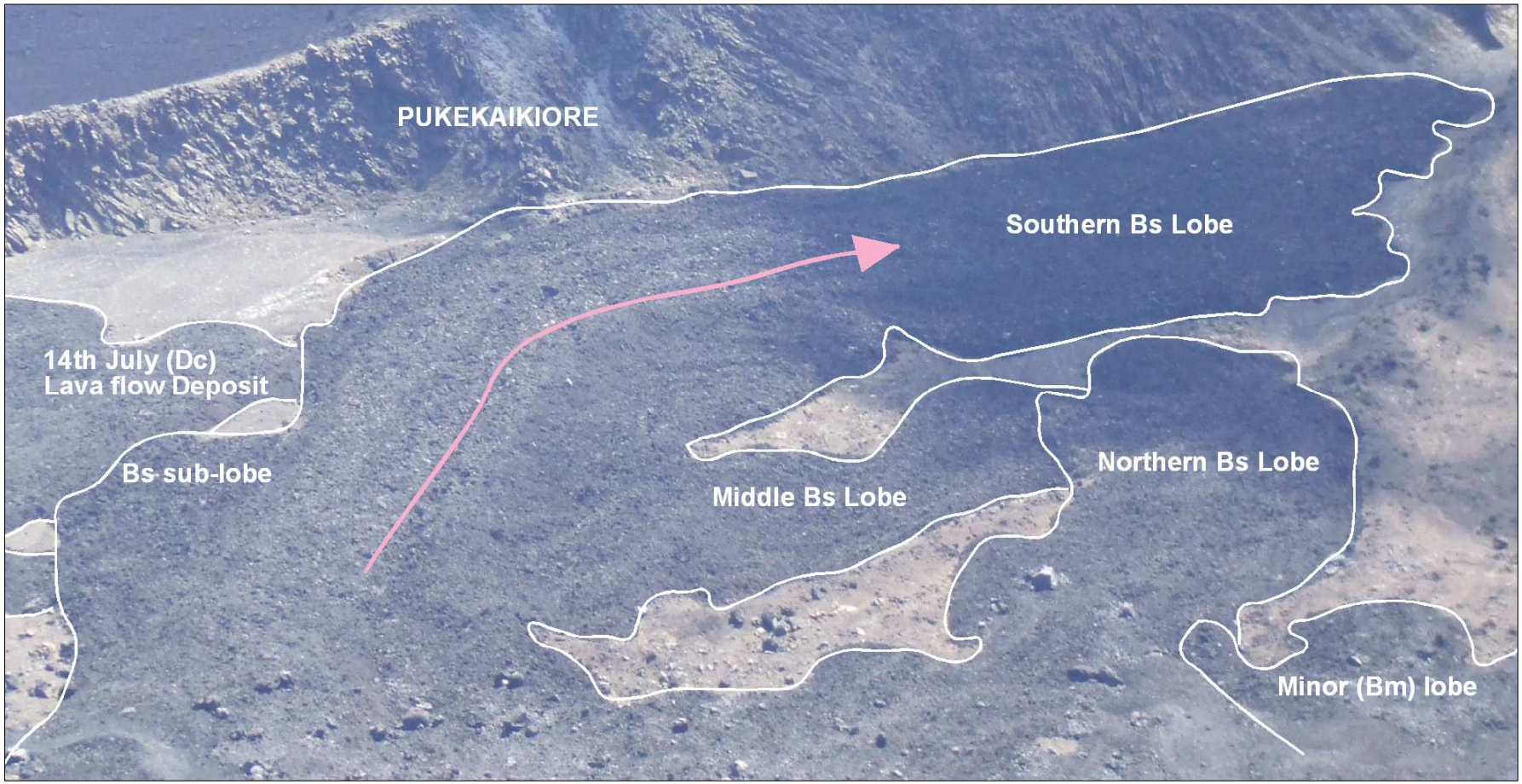

Fig. 2.19 Downflow view of the Bs lobe group, 30th June lava flow. The flow direction of the southern Bs lobe is diverted westward (pink arrow) along the base of the north-facing Pukekaikiore ridge and terminates at a broad, multi-toed flow front. Photograph taken from Ngauruhoe summit courtesy of J. Krippner.

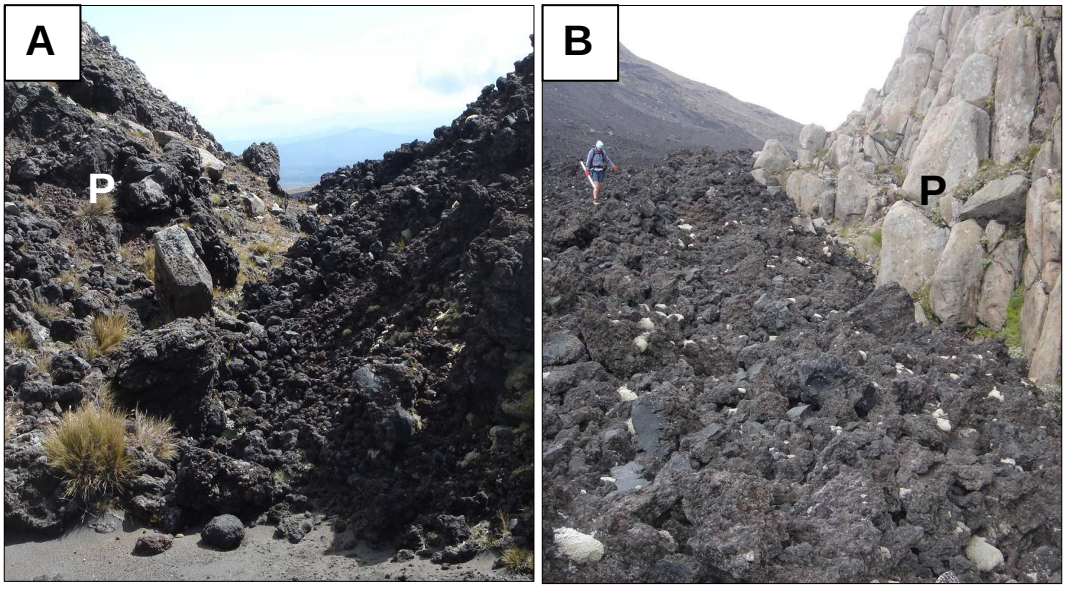

Fig. 2.20 Relationship between the base of Pukekaikiore ridge and the south-western margin of the southern Bs lobe, 30th June lava flow. P = Pukekaikiore ridge. A, minimal contact between the base of south-western flow margin and the base of Pukekaikiore ridge at location Bs7. B, south-western flow margin abuts against the base of Pukekaikiore ridge at location Bs10.

margin, the front of which lies approximately 130 m behind the front of toe 4 (Dc12). This sub-lobe is separated from the northern margin of the main flow deposit by a narrow ridge of lava, similar in appearance to a levee structure, and it is this section of the flow which appears to be a continuation of the 30th June (B) flow. A small lobe extending ~ 1.2 km from the crater rim (Dc14) overlies the flow surface of the northern sector of the 14th July (Dc) flow deposit, terminating ~ 50 m downflow from the point where the underlying flow deposit appears to separate from the 30th June (B) flow (Fig. 2.24).

The underlying slope angle for most of the flow length is approximately 39°, decreasing considerably to ~ 9° for the last ~ 280 m of the flow. The flow deposit appears to be unconfined by pre-existing topographical features, with the exception of the distal flow margin. Here the southern segment of toe 3 (Dc2) abuts the basal section of the Pukekaikiore ridge, obscuring the outer margin of the flow front (Fig. 2.26A), although there is no evidence of thickening of the flow deposit at the point of contact. However the flow front of toe 2 (Dc4) and the northern segment of toe 3 (Dc9) have not been confined by the Pukekaikiore ridge, with toe 2 terminating approximately 0.5 m before the ridge base (Fig. 2.26B), while toe 4 terminates ~ 30 m before the base of the ridge (Fig. 2.5).

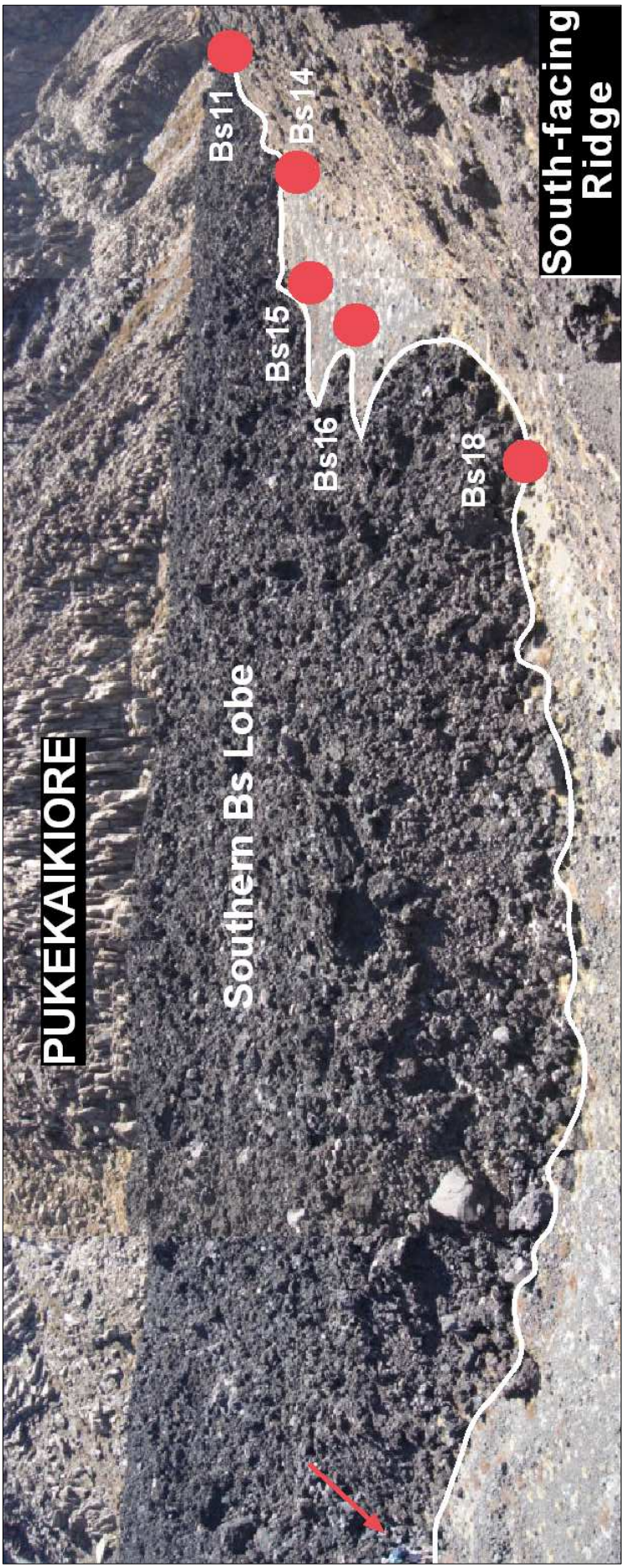

Fig. 2.21 Across-flow view of the multi-toed flow front of the southern Bs lobe, 30th June lava flow deposit. Red arrow to the left of the photograph marks a person wearing a light blue jacket for scale. Red dots denote field locations.

Fig. 2.22 Aerial photograph of the Bs lobe group (white outline), 30th June lava flow. Dashed pink line denotes shallow depressions on the flow surface. Solid pink line denotes location of a known, high-elevation ridge crest underlying the flow surface.

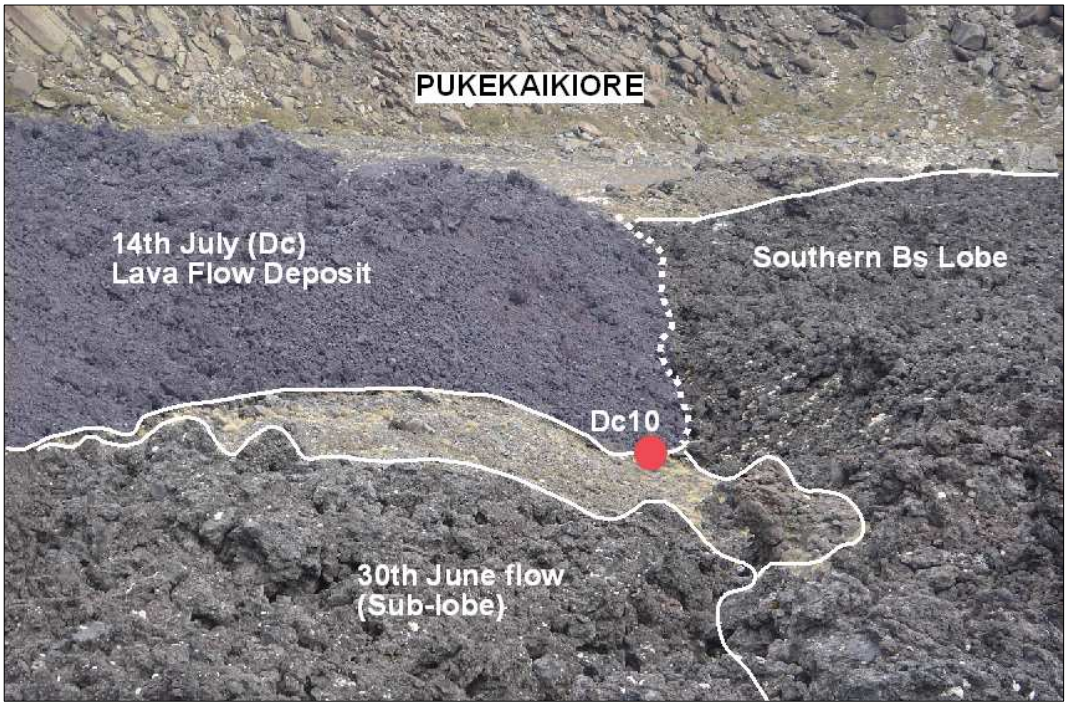

Fig. 2.23 Downflow view of one of the points of contact (Dc10) between the northern margin of the southern 14th July (Dc) lava flow deposit (shaded blue) and the southern margin of the southern Bs lobe, 30th June lava flow. Dashed white line denotes approximate position of contact between the two lava flow deposits. Red dot denotes field location.

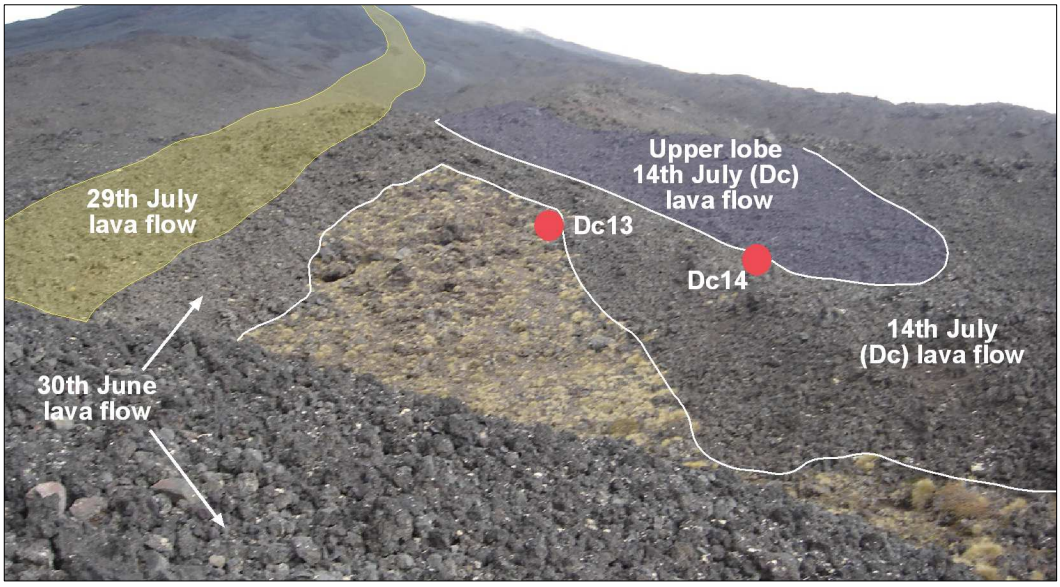

Fig. 2.24 Upflow view of the northern margin of the southern 14th July (Dc) lava flow deposit and the southern margin of the southern Bs lobe, 30th June lava flow deposit. The two flows appear to diverge upflow from location Dc13 with no obvious margin between them. A small upper lobe (shaded blue) (Dc14) overlies the 14th July (Dc) lava flow deposit.

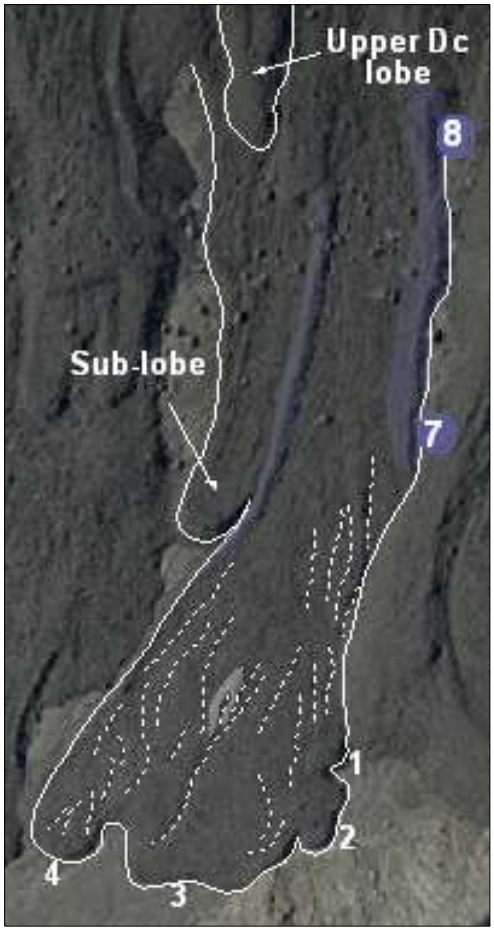

Fig. 2.25 Aerial photograph of the 14th July (Dc) lava flow deposit (white outline). Numbers 1-4 (white) denote multiple toes at the distal end of the flow deposit. The position of the marginal levees (shaded blue) are shown and the pattern of shallow depressions (white dashed lines) on the flow surface. Note the v-shaped ridge (shaded grey) located behind the flow front. Blue dots denote field locations.

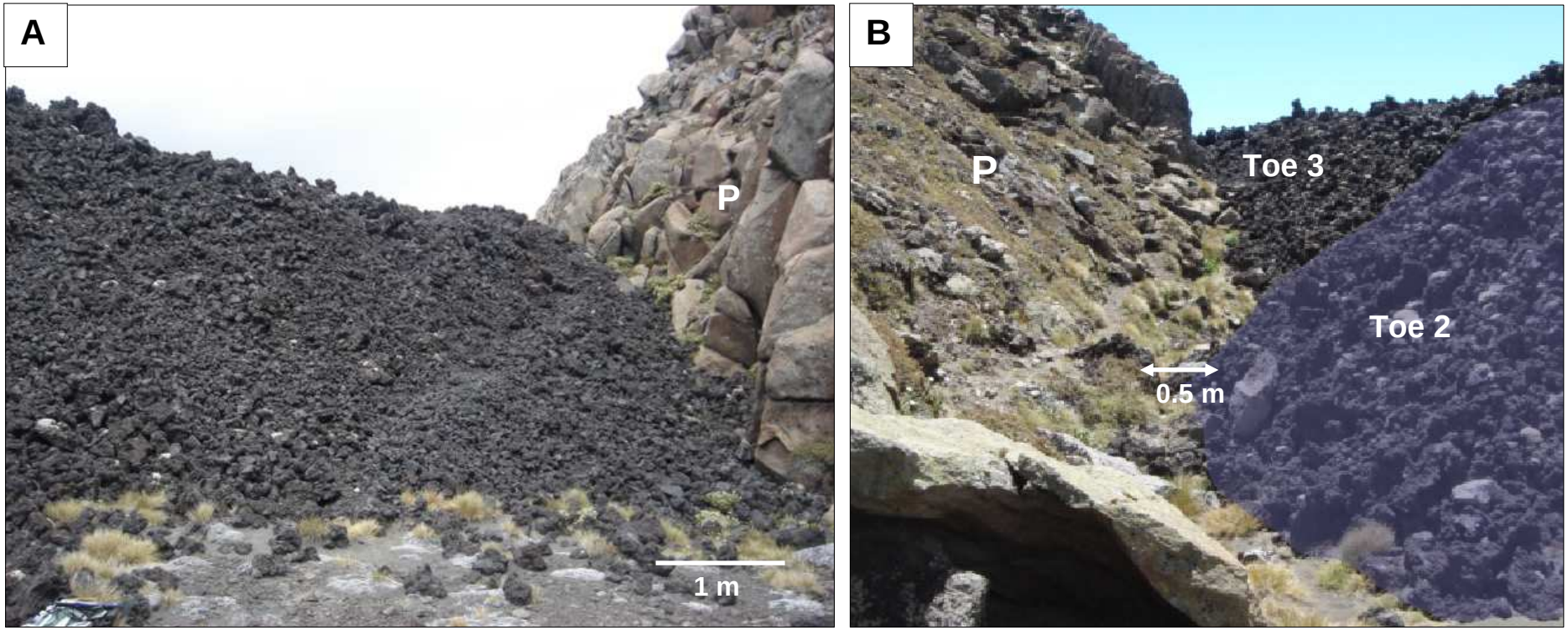

Fig. 2.26 View of two of the toes at the distal margin of the 14th July (Dc) lava flow deposit. A, southern section of toe 3 abutting the base of the Pukekaikiore ridge (P). B, southern margin of toes 2 and 3 showing the distance between the front of toe 2 (double-headed arrow) and the base of Pukekaikiore ridge (P).

There is no distinctive flow channel within the 14th July (Dc) flow deposit, although low elevation levees are apparent on sections of both flow margins (Fig. 2.25). The southern margin levee occurs between the point where the southern flow margin first becomes clearly distinguished from the northern margin of the 18th August (F) flow (Dc8) and the point where the southern margin becomes overlain by the northern margin of the 18th August (F) flow (Dc7). The south-facing, outer wall of this levee is ~ 3.7 m high, with a slope angle of 32°. The top surface of the levee is relatively broad (~ 4.5 m), and the 2 m high, north-facing, inner levee wall slopes at a gentle ~ 15° angle. The levee structure on the northern flow margin is located between the main flow deposit and the sub-lobe on the northern margin, extending ~ 22 m beyond the front of this sub-lobe but tapering out before the front of the main flow deposit. Flow deposit depth ranges from 1 to 6 m, average 3 m, increasing to 5 to 6 m depth at the flow front.

The flow surface of the broad, multi-toed flow front is composed of a series of shallow depressions, predominantly orientated in the same direction as the flow, separated by variable height, low-elevation ridges (Fig. 2.25). A small, inverse v-shaped ridge, orientated in the direction of the flow and surrounding a deep, narrow depression, is evident at the approximate centre of the broad lobe front, the flow deposit appearing to have been emplaced around either side of this high point.

2.3.4 29th July Lava Flow Deposit (E)

The fifth of the 1954 lavas to be emplaced, this flow deposit is a single-lobed, discrete unit, extending in a straight path from the crater rim and overlying the southern margin of the southern Bb lobe of the 30th June flow (Fig. 2.5). The deposit divides into two angular flow toes (E2) approximately 50 m from the distal flow front. The contact between the base of the 29th July (E) flow and the upper flow surface of the underlying 30th June (B) deposit is not well defined along most of the southern margin (E1), the outer margins of the two flow deposits appearing as one deep deposit (Fig. 2.27A). The contact between the two margins becomes more apparent approximately 45 m before the front of the southern toe, as the southern margin curves slightly to the north-west and the

underlying 30th June (B) lava flow deposit continues in a straight path (Fig. 2.27B).

The slope angle of the southern margin is between 38 to 40°, increasing to a 45° angle at the front of the southern toe. The angle of the underlying slope averages 37° for most of the flow deposit length, decreasing to ~ 19° for the last approximately 100 m. The flow surface of this deposit appears relatively uniform with no evidence of a central flow channel or marginal levees noted in the field or on aerial photograph analysis.

2.3.5 18th August Lava Flow Deposit (F)

This is the second longest of the 1954 lavas, extending ~ 1.8 km from the crater rim (Table 2.1). It is a narrow, single-lobed, discrete unit (Fig. 2.5) that displays a range of well-defined morphological and surface features not evident at the other 1954 lavas. These features vary along the length of the flow, enabling the flow deposit to be divided into four distinct zones characterised by their different features.

Proximal Zone

This section of the flow extends in a relatively straight line for the first ~ 1.3 km of the flow length, from the crater rim to ~ 1620 m elevation, ending approximately 70 m upflow from the point where the flow deposit broadens (Fig. 2.5). A scoria and ash flow deposit lies adjacent to the southern margin of the proximal zone, breaching the southern levee approximately 1 km downflow from the crater rim, and overlying the flow surface of the 18th August lava. The later 16th September (G) flow deposit is emplaced over the upper part of the northern levee of the 18th August flow deposit, its flow front extending down and terminating at the base of the south-facing, inner wall of the northern levee (G1) (Figs. 2.5 and 2.28).

The proximal zone of the 18th August flow deposit rests on an average underlying slope angle of 40° and is characterised by a central flow channel bounded by

Fig. 2.27 View of 29th July (E) lava flow deposit overlying the 30th June (Bs) lava flow deposit. A, the southern margin of 29th July (E) lava flow deposit and the underlying 30th June (Bs) lava flow deposit appear as one margin, with no clear contact evident between the two (E1). Measuring staff is at 5 m height. B, upflow view of the southern margin and the front of the southern flow toe of the 29th July (E) lava flow deposit (shaded yellow) where the distal flow margin of the 29th July flow curves to the north-west. Red dots denote field location numbers. Measuring staff to left of photograph at 5 m height.

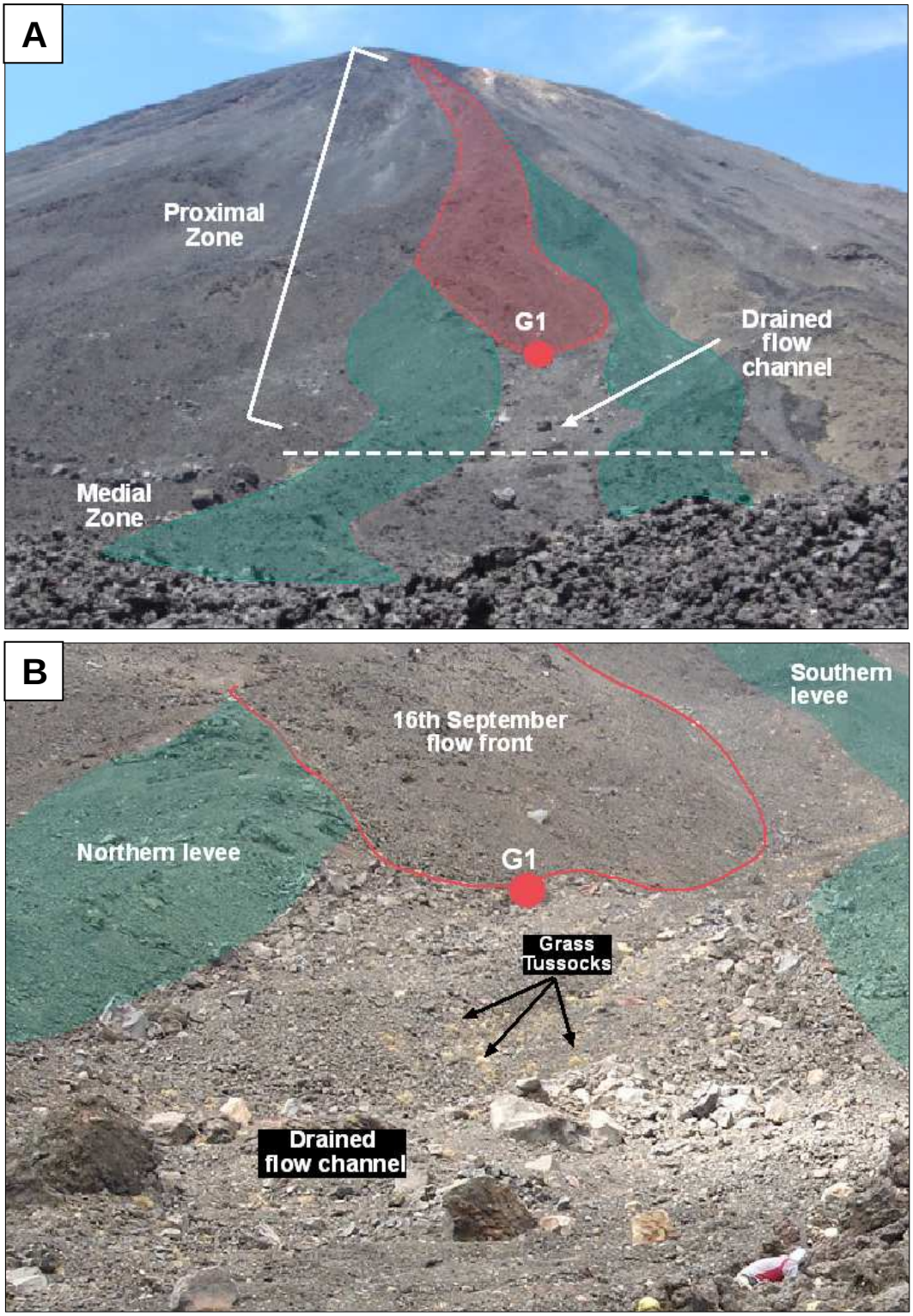

Fig. 2.28 Upflow view of the proximal zone of the 18th August (F) lava flow deposit. Red dot denotes field location. A, extent of the proximal zone showing marginal levees (shaded green) and drained flow channel. Red shaded area denotes location of the 16th September (G) lava flow deposit. White dashed line denotes the line of division between the proximal and medial sections. B, drained central flow channel surface of the proximal zone overlain by heterogeneous scoria and ash flow deposit. Marginal levees shaded green. 16th September (G) flow front outlined with solid red line. Note person (bending forward) at the bottom right of the photograph for scale.

distinctive marginal levees (Fig. 2.28A). Levee height ranges from 2 to 12 m with the northern margin levee significantly higher than the southern margin levee. The 16th September (G) flow deposit fills the central flow channel of the 18th August deposit on the upper slopes of the proximal zone, with no evidence of 1954 lava deposition within the central flow channel between the distal margin of the 16th September (G) flow and the distal end of the proximal zone. Instead the underlying paleo-slope surface of the cone is visible as small grassy tussocks and old, weathered boulders, overlain with a relatively thin layer of heterogeneous scoria and ash flow clasts (Fig. 2.28B).

Medial Zone

The medial zone of the 18th August flow deposit extends downflow for approximately 200 m from 1620 m elevation a.s.l. (the base of the proximal zone) and is characterised by a distinctive s-shaped curve (~ 1.3 km downflow from the crater rim) towards the south around the southern end of the Pukekaikiore ridge (F1) (Fig. 2.5). This zone ends at the centre of the final curve in the deposit at the southern end of the Pukekaikiore ridge at 1580 m elevation a.s.l. The curve of the deposit is more pronounced on the northern margin where the flow width broadens to ~ 130 m, overlying the southern margin and part of the flow surface of the 14th July (Dc) flow deposit. At the central portion of the curve, the northern margin (F1) and northern section of the flow surface are situated at a relatively higher elevation (~ 15 to 20 m) than the southern margin, with a distinct 23 to 24° dip of the flow surface towards the southern margin (Fig. 2.29A) suggesting that the flow was emplaced both around and over the top of the southern end of the Pukekaikiore ridge. At the base of the medial zone flow width narrows to ~ 80 m as it overtops and curves around the southern end of the Pukekaikiore ridge.

The medial zone of this flow deposit is also characterised by a marked reduction in underlying slope angle to 9° at the east-facing base of the distal end of Pukekaikiore ridge. The flow deposit in this zone remains bounded by levees on both margins, ranging in height between 2 to 12 m, with the northern margin levee again significantly higher than the southern levee. The medial zone is also characterised by the deposition of a'a lava, exhibiting distinctive surface features,

within the central flow channel. A ~ 4 m high, lens-shaped crest is located in the centre of the flow channel (F3), approximately 53 m long, 20 m wide and orientated in a downflow direction (Fig. 29B). A series of regularly spaced, low-elevation ridges, separated by shallow troughs, are distributed roughly perpendicular to the flow direction on either side of this crest (Fig. 2.29A). These ridges extend at varying lengths (Table 2.2) from the base of the central crest to the base of the inner levee walls, curving slightly downflow towards the levee walls. The top of these ridges are generally of a similar height but there is a noticeable difference in the depths of the interspaced troughs, ranging in depth from 0.5 to 3.7 m (Table 2.2). The ridge slope angles are generally gentler on the stoss (upflow facing) slopes, and steeper on the lee (downflow facing) slopes. The ridges on the south side of the central crest terminate just beyond the western end of the central crest, while the ridges on the northern side continue beyond the western crest-end to the point where the flow overtops the southern end of the Pukekaikiore ridge.

With the exception of the southern end of the Pukekaikiore ridge, there is no evidence that the northern margin of the medial zone was confined by the underlying topography. However, the southern margin appears to have been partially confined by a low-elevation (2 to 3 m), pre-existing ridge before the flow reached the southern end of the Pukekaikiore ridge (F9 to F12) (Fig. 2.30).

Distal Zone

This zone extends ~ 220 m from the base of the medial zone to the narrowest point of the flow deposit (at 1520 m elevation a.s.l.), with an underlying slope angle of ~ 16°. The deposit narrows to around 46 m width as it extends beyond the southern end of Pukekaikiore ridge and is characterised by a markedly narrow (8 m) flow channel bounded by two levees at either margin (Fig. 2.31). A shallow (~ 0.5 m) depression separates the inner and outer levee at each flow margin.

The southern margin of this zone appears to overtop an underlying, high-elevation (~ 10 m) ridge approximately 80 m downflow from the western end of the low-elevation ridge noted upflow at the southern margin of the medial zone (between

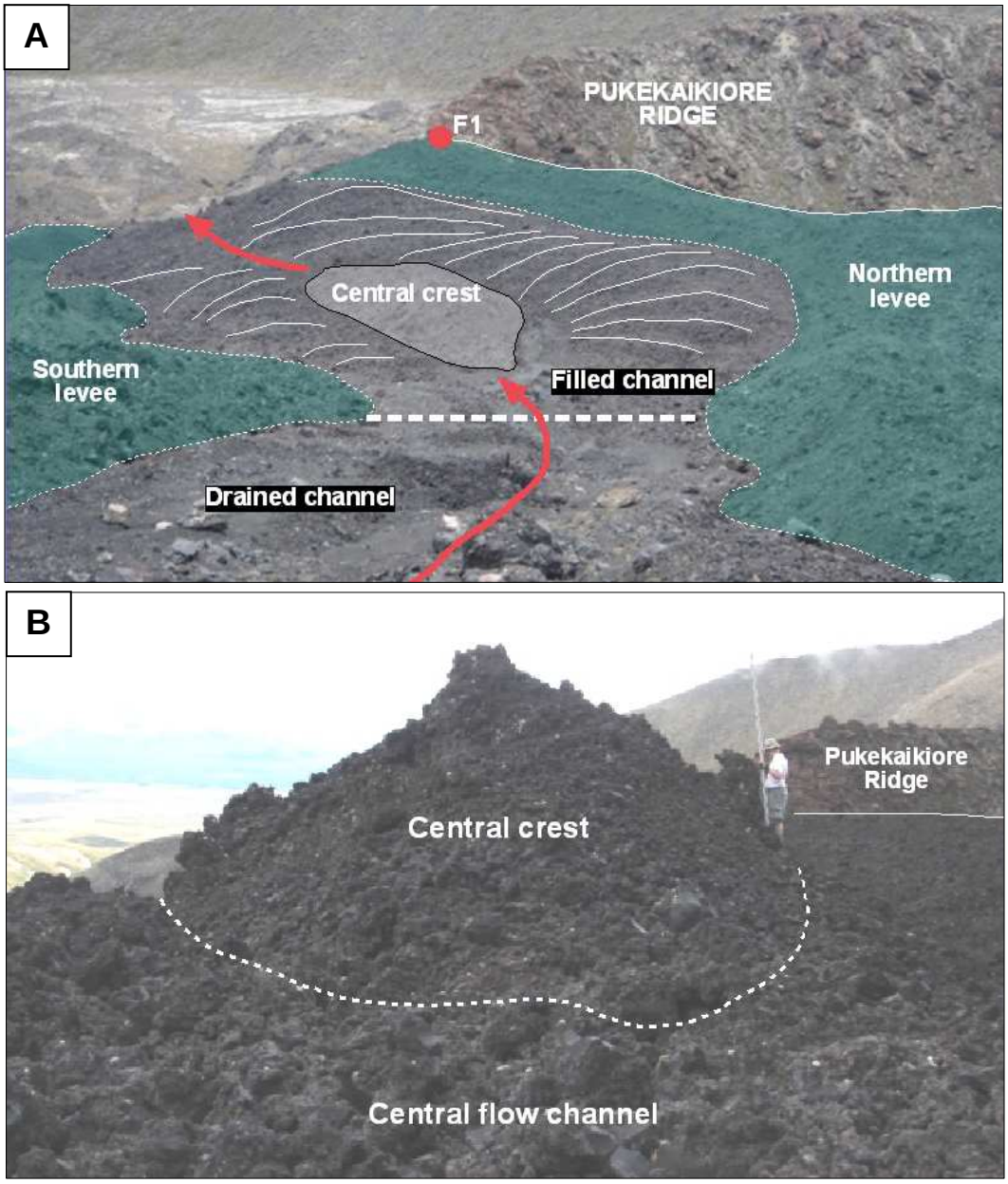

Fig. 2.29 Medial zone surface features of the 18th August (F) lava flow deposit. A, downflow view of the medial zone. Flow surface features include a central crest (shaded white), perpendicular ridges (ridge tops marked with solid white line) and marginal levees (shaded green). Base of levees denoted by fine dashed white line. Note higher elevation of the northern margin (F1) compared to the southern margin and the south-ward orientated camber of the flow surface as it overlaps the southern end of Pukekaikiore ridge. Flow direction indicated by red arrows. Thick, dashed white line denotes margin between the proximal and medial zones. Red dot denotes field location. B, view of the eastern end of the central crest at location F3. Measuring staff is at 4 m height.

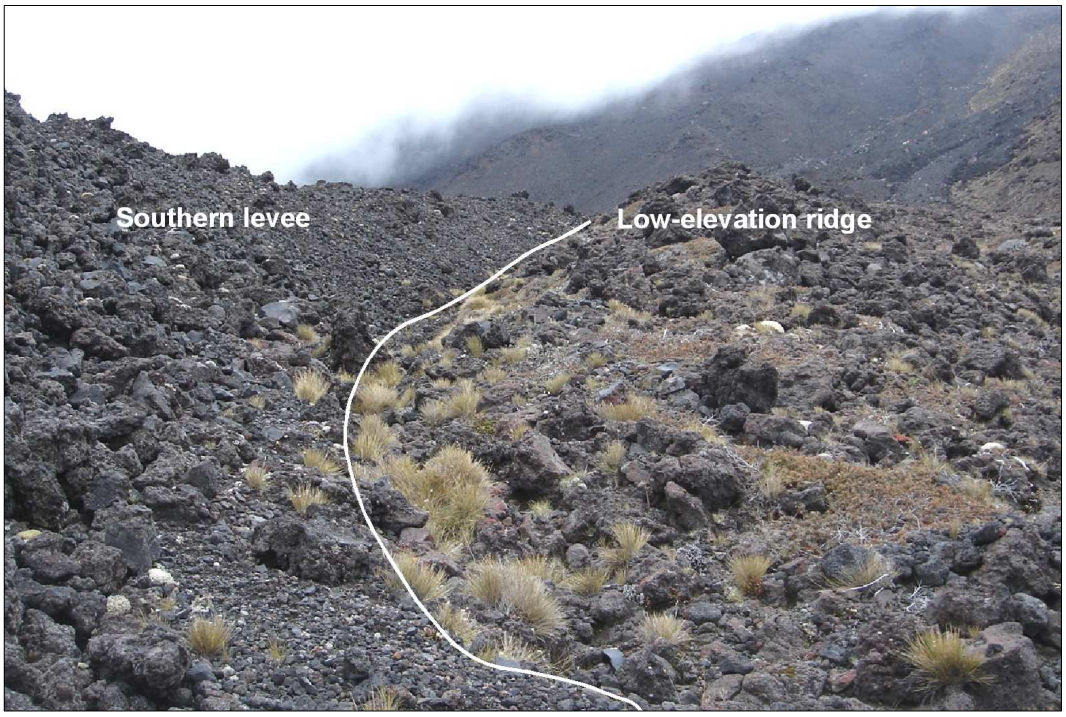

Fig. 2.30 Upflow view of the southern levee of the 18th August (F) lava flow deposit confined by a low-elevation, pre-existing ridge at location F12.

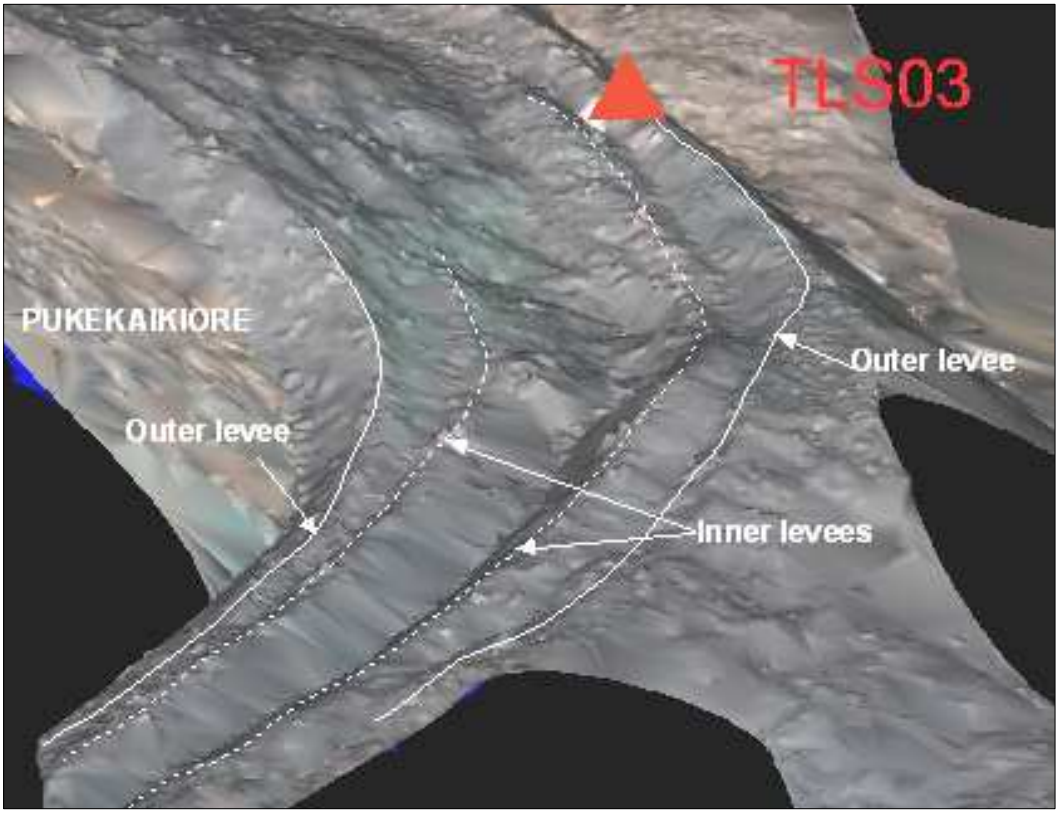

Fig. 2.31 TLS model of the distal zone of the 18th August (F) lava flow deposit showing the location of double levees on both flow margins. Solid white line denotes the crest of the outer levee, dashed white line denotes the crest of the inner levee. Red triangle denotes the location of the third TLS survey position (TLS03) (see Fig. 2.4).

Table 2.2 Dimensions and slope angles of the flow surface ridges located on the northern and southern sides of the lens-shaped crest in the centre of the medial zone flow channel, 18th August (F) lava flow deposit. Ridge height measured from the ridge crest to the base of adjacent troughs on either side of the ridge (stoss and lee slopes), reflecting both the ridge height and the depth of each trough. Distance between ridges measured from the centre of each ridge crest to the next ridge.

Northern Ridges

Ridge No.	Stoss side height (m)	Lee side height (m)	Stoss slope angle (°)	Lee slope angle (°)	Ridge Length (m)	Distance to next ridge crest (m)
NR1	1.45	1.8	32	37	20	9.7
NR2	1	1.25	16	26	20.7	8.3
NR3	0.9	1	12	18	25.5	14
NR4	1.05	1.32	16	28	23	10
NR5	1.32	1	14	36	20	7
NR6	0.91	0.81	18	24	14	8.5
NR7	1.35	0.84	16	7	18.5	21
NR8	1.25	2.15	10	36	29	20.5
NR9	1.82	1.7	28	32	21	9.6
NR10	1.8	1.45	20	32	22.1	9.7
NR11	2.5	3.7	36	40	16.1	N/A

Southern Ridges

Ridge No.	Stoss side height (m)	Lee side height (m)	Stoss slope angle (°)	Lee slope angle (°)	Ridge Length (m)	Distance to next ridge crest (m)
SR1	0.5	1.7	26	32	14.1	9.6
SR2	0.7	1.8	22	30	14.2	13.3
SR3	1.4	0.9	24	30	8.6	5
SR4	0.7	2.3	20	38	18.5	13
SR5	1.3	1.7	24	38	12.7	6.2
SR6	0.8	2.1	26	38	17.7	10.4
SR7	1.6	1.6	24	36	18.1	8.3
SR8	1.2	1.35	28	28	10.9	10.5
SR9	1.2	1.55	28	30	16	N/A

locations F9 and F12). A thin (< 0.5 m) deposit of lava initially overspills the south-facing slopes of this ridge (F13a) (Fig. 2.32A), completely covering the ridge slope ~ 20 m downflow from this point (Fig. 2.32B). Approximately 30 m further downflow a small, rounded, 35m wide 'break-out' lobe (F15) is evident (Figs. 2.4, 2.5), overtopping the pre-existing ridge and extending ~ 50 m beyond the base of the ridge. On the western margin of the break-out lobe the southern margin of the flow deposit can be clearly seen emplaced on top of the underlying ridge, with a thin (< 0.5 m) veneer of lava partially emplaced on the south-facing slope of the ridge (F16, F17). The western end of this pre-existing ridge marks the narrowest part of the flow and base of the distal zone. Although there is no evidence of an underlying ridge at the northern margin, both the northern and southern flow margins reduce significantly in height at this point, from ~7 to 3 to 4 m (Fig. 2.33), at a 28 to 30° slope angle (F31).

Frontal Zone

Approximately 190 m before the distal flow front the deposit broadens into a ~ 65 m wide, fan-shaped lobe (Fig. 2.5) resting on a relatively flat (~ 9°) underlying surface, and forming multiple rounded toes at the flow front (F20, F21, F22, F27, F28) (Figs. 2.5 and 2.34). There is no distinct central flow channel within this zone of the deposit and the margins of the deposit are generally the same depth as the surface of the flow. Deposit depth is variable in this zone, ranging from 2.2 to 7 m.

The flow surface of the frontal zone is similar to that seen on the surface of the 30th June and 14th July (Dc) deposits, characterised by complex ridges and depressions orientated in the general direction of the flow (Fig. 2.34). Some of these appear to be associated with the margin between the flow front toes.

2.3.6 16th September Lava Flow Deposit (G)

Two flows were reportedly observed on this date, although only one flow with a double-lobed flow front was mapped by Gregg (1956); the southern lobe the longer of the two. Later maps, e.g. Hobden and Houghton (2000), exhibit a single

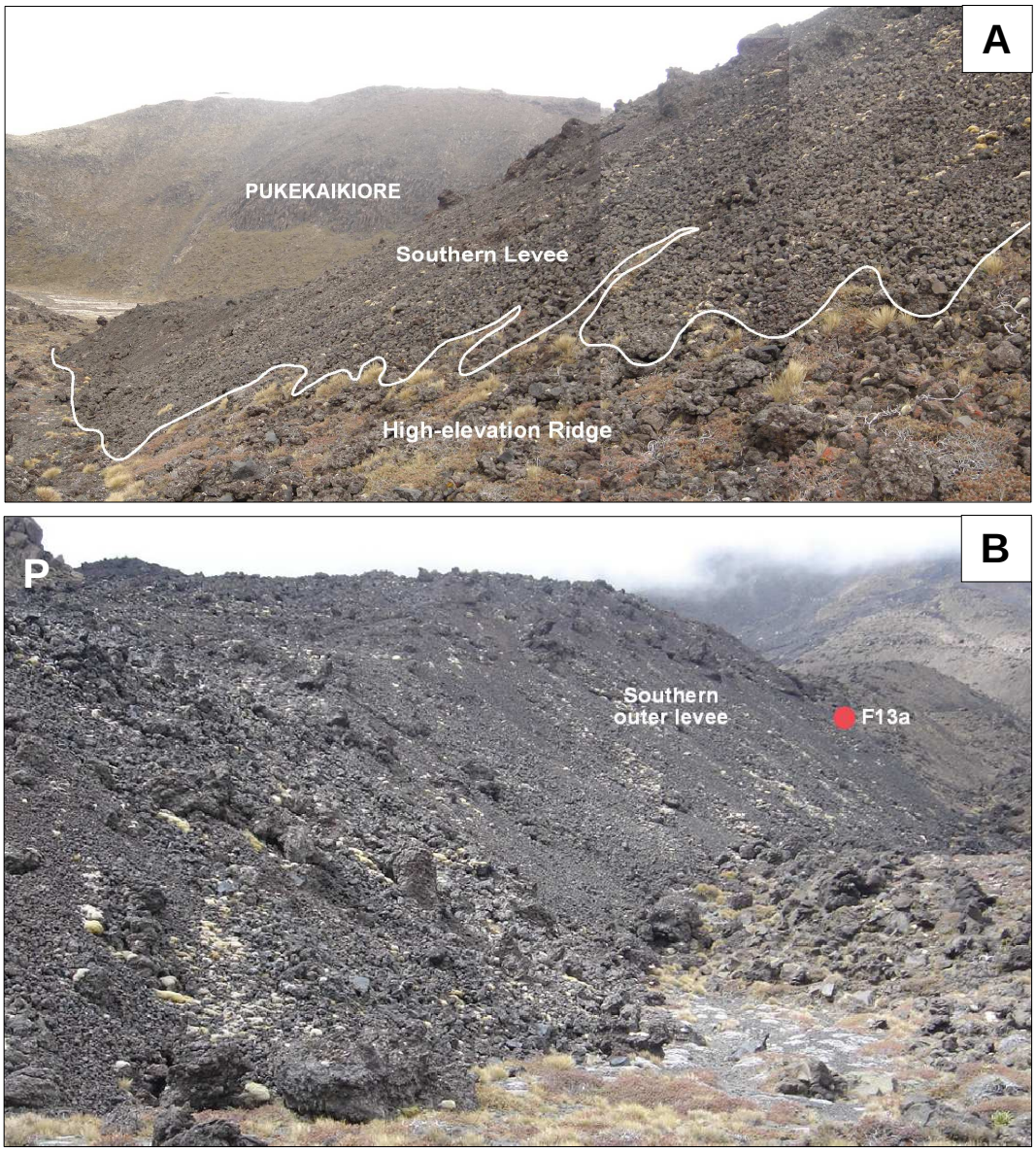

Fig. 2.32 Southern levee of the 18th August (F) lava flow deposit at the distal zone. A, downflow view of the southern levee emplaced down the south-facing slope of a high-elevation, pre-existing ridge at location F13a. B, upflow view of the southern levee showing the emplacement of lava covering the south-facing slope of the high-elevation ridge. Red dot denotes field location.

flow unit with a single-lobed flow front. This is inconsistent with the deposit observed in the field, which initially appears as a discrete ~ 1 km long, ~ 38 m wide, single-lobed unit, emplaced in a relatively straight path from the crater rim along the northern levee of the proximal zone of the 18th August (F) flow deposit (Fig. 2.5). However, a small discrete lobe was observed between the northern margin of the 18th August (F) flow deposit and the southern margin of the 14th July (Dc) flow deposit (Dc8), at the point where the two margins become clearly identifiable (Fig. 2.35). This lobe extends ~ 1.2 km (Table 2.1) from the crater rim

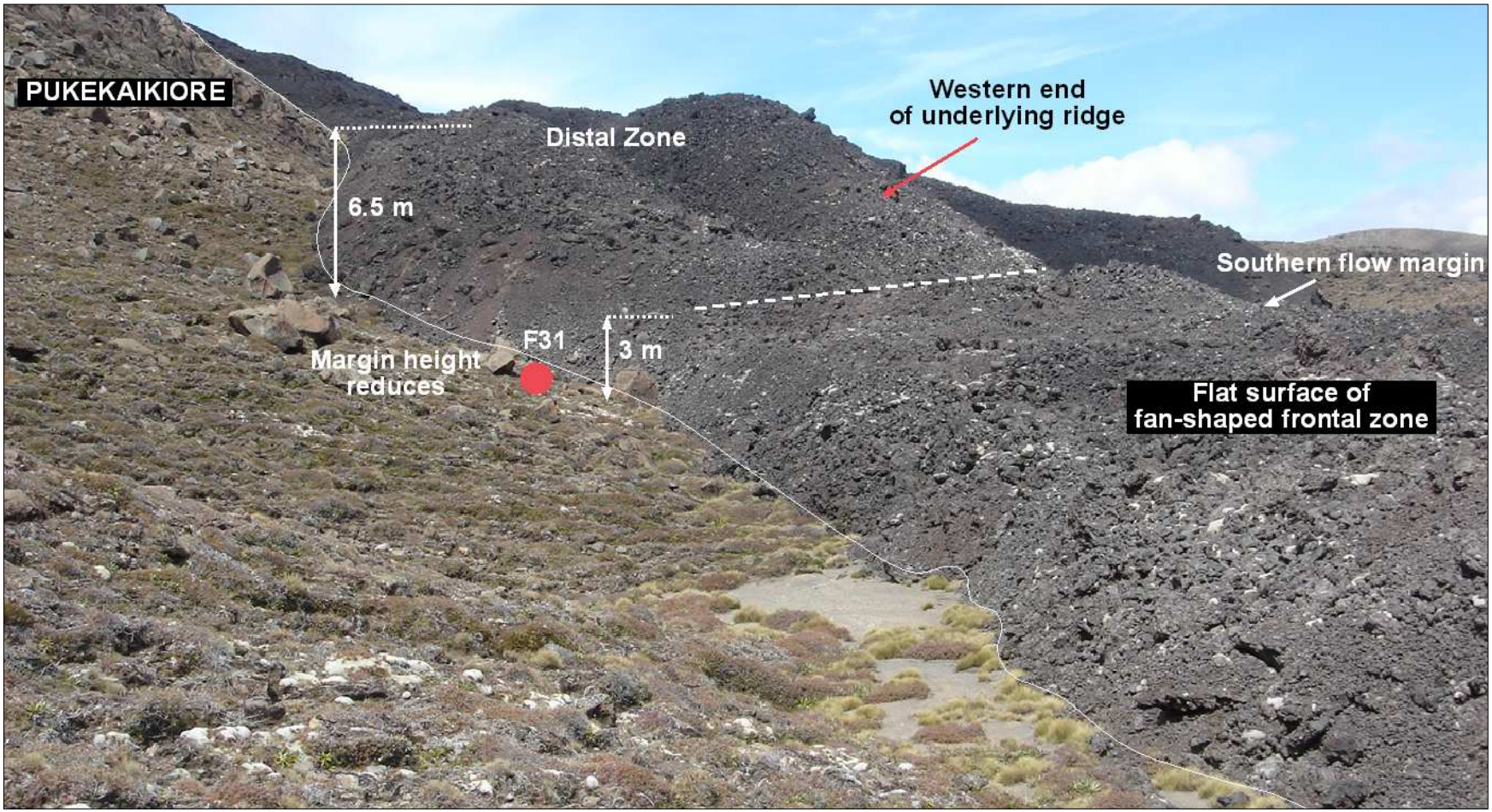

Fig. 2.33 Upflow view of the northern margin of the distal zone of the 18th August (F) lava flow deposit. Note the significant decrease in deposit height at the western end of the underlying ridge prior to the spreading out of the fan-shaped lobate frontal zone. Thick dashed line denotes boundary between distal and frontal zones. Red dot denotes field location.

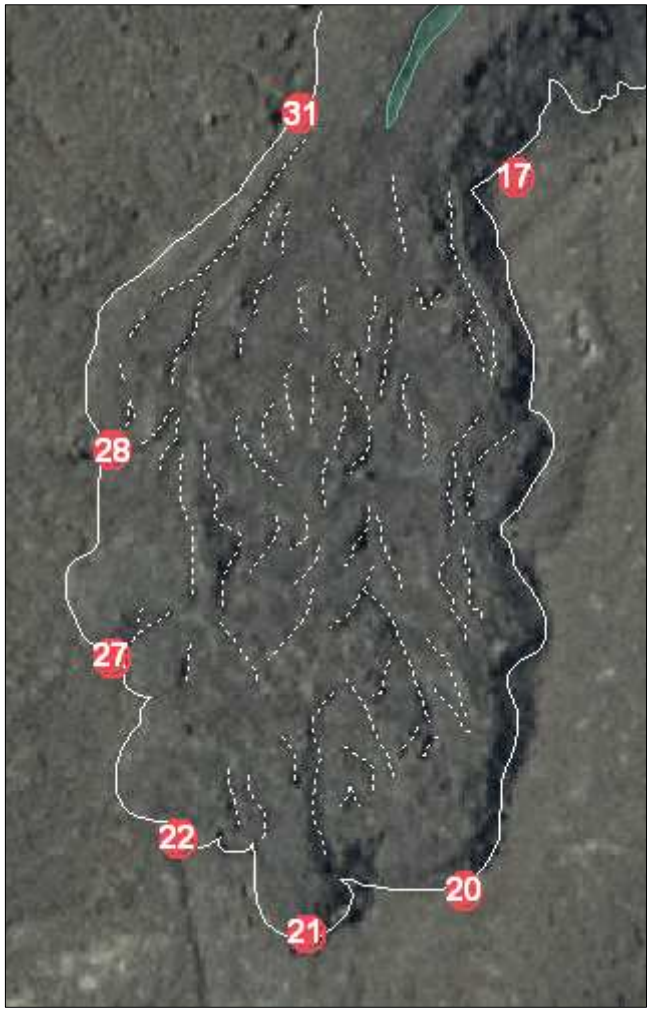

Fig. 2.34 Aerial photograph of the frontal zone of the 18th August lava flow deposit (white outline). Location of depressions in the flow surface marked by dashed white lines. Central flow channel of the distal zone behind the frontal zone is shaded green. Red dots denote field locations.

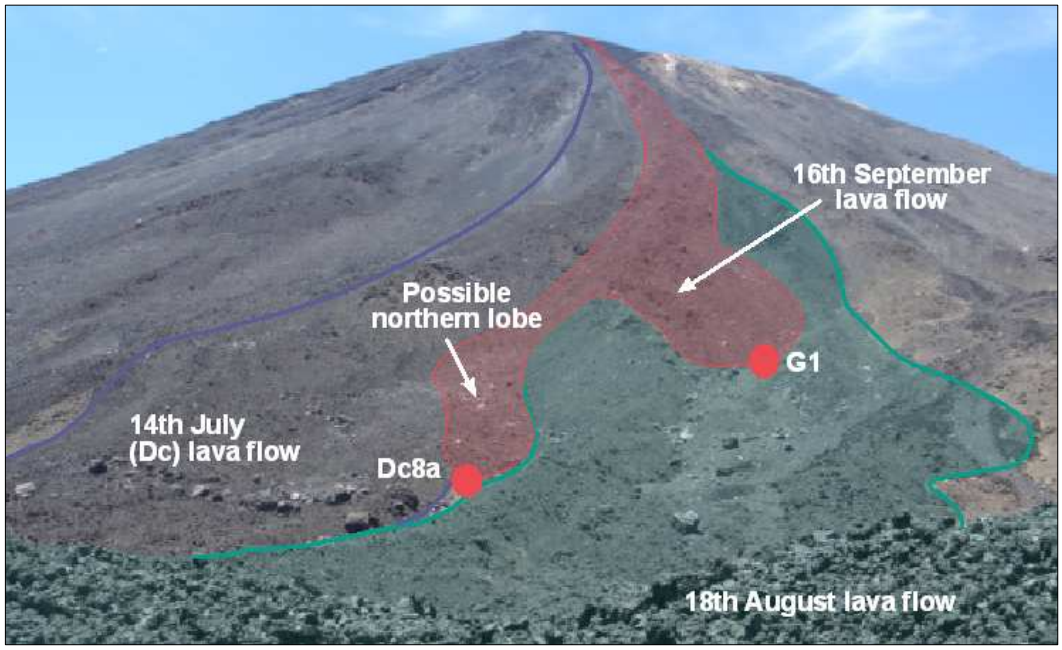

Fig. 2.35 Upflow view of the 16th September lava flow deposit (shaded red) showing the possible emplacement of a northern lobe of the 16th September lava flow (Dc8a) between the northern margin of the 18th August lava flow deposit (shaded green) and the southern margin of the 14th July (Dc) lava flow deposit (blue outline). Red dots denote field locations.

and appears to be emplaced adjacent to the northern margin of the 16th September flow deposit. It has therefore been mapped as part of the 16th September flow for this study, and may either be the second 16th September flow of Gregg's (1956) account or the northern lobe of the 16th September flow mapped by Gregg (1956).

The main flow unit, from the crater rim to the flow front emplaced over the northern levee of the 18th August (F) flow (G1), lies in a straight path from the crater rim over an average underlying slope angle of 39°. The distal end curves slightly to the south and was emplaced down the south-facing, inner, northern levee wall of the 18th August (F) flow deposit (Fig. 2.35). The deposit terminates at a well-rounded flow front that partially encroaches over the central flow channel of the 18th August deposit (Figs. 2.28 and 2.35). Flow depth appears to be approximately 2 to 3 m, although this was difficult to determine as the contact between the base of the 16th September deposit and the top of the northern levee of the 18th August deposit is unclear. There did not appear to be any thickening at the flow front although again this was difficult to quantify due to the manner of emplacement of the flow down the south-facing, inner slope of the 18th August levee. The distal margin of the 16th September deposit rests on the ~ 26° slope angle of the south-facing, inner levee wall, with the flow front resting on the localised 28° slope angle of the underlying 18th August central flow channel.

The flow surface immediately before the deposit was emplaced down the inner levee wall of the 18th August flow (G2a) appears relatively flat and featureless. The remainder of the surface was not observed in the field, and there is no evidence of channel and levee structures or other distinctive surface features on aerial photograph analysis.

CHAPTER 3

Petrographic, Mineralogical & Geochemical Characteristics

3.1 INTRODUCTION

This chapter details the results of laboratory analyses carried out on a number of individual samples collected from each of the six 1954 lava flow deposits visited in the field, with the aim of quantifying the petrographic and geochemical parameters of the 1954 lavas. Whole rock morphology, texture and the size distribution of clasts within lava flow deposits are described. Thin section analysis is used to describe the micro-textures and crystal content of the lavas, with emphasis on phenocryst, vesicle and groundmass ratios, individual mineral modal abundances and descriptions of mineral species observed in thin section. Vesicularity is described in hand specimen and thin section analysis, and quantified by gas pycnometry and statistical analysis of field data. Geochemical analysis was undertaken to determine the geochemical signature of the 1954 lavas and to ascertain any significant trends or differences in chronologically successive lavas from the 1954 eruption. Several lava flow deposit features in the field could not be assigned to specific flows with certainty, and therefore an attempt has been made to use the geochemical characteristics of the known lavas to correlate them.

3.2 METHODOLOGY

3.2.1 Sample Enumeration

Rock samples were labelled according to the field location numbers where they were collected, and the number of samples obtained from each location. Therefore, where only one rock sample was obtained from a field location the designated sample number is the same as the field location number (e.g. one rock

sample from location F21 was given the sample number 'F21'). Where more than one rock sample was collected from the same location an individual sample number follows the field location number (e.g. the two samples from location F15 were enumerated F15-1 and F15-2). Thin sections, pycnometer, and XRF samples were labelled in the same manner.

Where selected whole rock samples displayed differential vesicle zonation between the inner and outer segment of the clast, two thin sections were prepared to enable comparison of the vesicularity between the different vesicle zones. These samples were labelled with either an 'X' or a 'Z' in front of the sample number, representing the outer and inner zones of the whole rock sample respectively (e.g. thin sections prepared from the outer and inner zone of whole rock sample Bs8-2 were labelled XBs8-2 and ZBs8-2 respectively). Each side of these thin sections was also labelled to orientate the thin section slide as to the direction of the outer and inner zones (X and Z) relative to the whole rock sample. A list of the selected whole rock samples and analyses undertaken is presented in Appendix B.1. Field locations (underlined) referred to in this chapter and/or those corresponding to sample numbers referred to in this chapter, are shown either in Fig. 2.5, or in Appendix D.1.

As discussed in Chapter 2, some localised lava deposits (e.g. the lobe overlying the 14th July (Dc) flow deposit at location Dc14) were associated with known lava flows but could not be confidently correlated to specific lava flow deposits of known emplacement dates. Samples from these deposits are distinguished from those of 'known' lava flows as 'unknown' samples.

3.2.2 Whole Rock Sample Descriptions

Numerous whole rock samples from six 1954 lava flow deposits [4th June (A), 30th June (B), 14th July (Dc), 29th July (E), 18th August (F), 16th September (G)] were collected to represent the variation in morphology, texture and vesicularity of individual clasts. These were described and photographed in the laboratory prior to preparation for analysis. In the field, the size and distribution of lava clasts at various locations on each of the flow deposits was recorded.

3.2.3 Thin Section Petrography

Covered thin sections were made using standard petrographic techniques for selected samples representing 'known' and 'unknown' flow deposits. Two thin sections corresponding to the outer scoriaceous and less vesicular inner zones of individual clasts were prepared for those whole rock samples displaying distinctly different degrees of vesicularity between the two zones. Six polished thin sections were prepared to identify opaque minerals. Modal abundance data were obtained using a standard point count technique with 400 counts per thin section. Detailed petrographic descriptions of mineral, vesicle and groundmass textures and componentry were carried out on 29 known 1954 samples, and modal abundance analyses on 36 known and unknown 1954 samples.

3.2.4 Vesicularity

Vesicle abundance, morphology, size range and distribution patterns were determined by modal point count and visual examination of thin sections and vesicularity quantified by gas pycnometer analysis and statistical analysis of bulk flow deposit vesicularity using the methods described in this section.

Gas Pycnometry

Eight whole rock samples, representing the range of inner zone vesicle abundance and size observed in the 1954 flow deposits, were selected for pycnometer analysis. The pycnometer sample cells into which prepared whole rock samples were placed for analysis are cylindrical, and ideally prepared rock samples should also be cylindrical and closely match sample cell dimensions to maximise analytical accuracy. However, the necessary resources required to cut cylindrical samples from whole rock clasts at diameters matching pycnometer sample cell sizes are not currently available at the University of Waikato. Pycnometer samples were therefore prepared by cutting sample blocks from whole rock samples to a specific size to (a) maximise the volume of the cylindrical pycnometer sample cell filled by the lava block sample and thus reduce analytical error, and (b) enable comparison of results between sample blocks of the same size. Greater analytical accuracy is obtained with large sample block sizes (e.g. 75 x 32 x 32 mm);

however, the inner zones of the whole rock samples were generally not large enough to prepare large-size sample blocks for analysis, therefore medium-sized sample blocks (36 x 28 x 28 mm) were prepared. The outer, scoriaceous zone of these samples was generally ~ 2 cm thick and therefore medium-size sample blocks could not be prepared from this zone. Instead, small-sized sample blocks (21 x 17 x 17 mm) were prepared from both the outer zone and inner zone of five of the whole rock samples to enable comparison. Thus, a total of 13 small-sized sample blocks and eight medium-sized sample blocks were analysed. The sample blocks were dried overnight at 110°C, and block dimensions measured using digital callipers. Four length measurements and two each of the width and depth of each sample block were recorded to obtain an average length, width, and depth to the nearest 0.01 mm, and sample block volume calculated from these. Each sample block was weighed to the nearest 0.01 g to enable calculation of bulk density (bulk density$_T$) of the whole sample block.

Pycnometer density (bulk density$_{pyc}$), i.e. the bulk density$_T$ excluding exposed vesicles, and solid density (dense rock equivalent-DRE density) was determined using an Ultrapycnometer 1000 gas pycnometry analyser based at the University of Waikato. The pycnometer was calibrated according to manufacturer's instructions, an error margin set at 0.005% and the weight of each sample block entered into the pycnometer prior to analysis. The pycnometer ran multiple analyses on each sample block to determine the volume of gas displaced by the sample block, until three consecutive analyses were within 0.005% error, or until eight runs were completed. The pycnometer calculated the average volume from either the three consecutive analyses, or the final three analyses results from eight completed runs. Bulk density$_{pyc}$ for each sample block was then determined by the pycnometer using the average volume and weight of the sample block.

Following analysis, the sample blocks were crushed to powder, weighed and reanalysed in the same manner to calculate the average solid density value (DRE density) for each sample block. Total vesicularity (V_T) (%) was calculated using the equation:

$$V_T = 100\left(\frac{\text{DRE density} - \text{bulk density}_T}{\text{DRE density}}\right)$$

Isolated vesicle abundance (V_I) (%) was calculated by:

$$V_I = \frac{100\left(\text{DRE density} - \text{bulk density}_{pyc}\right)}{\text{DRE density}}$$

Connected vesicle abundance (V_c) (%) is then calculated by:

$$V_c = V_T - V_I$$

Pycnometer results and vesicularity calculations are presented in Appendix B.2.

Quantitative Bulk Lava Flow Deposit Vesicularity Analysis

Bulk lava flow deposit vesicularity was determined by estimating bulk vesicle abundance at two locations on the southern margin of the 18th August (F) lava flow, to assess potential changes in vesicularity along the long axis of the flow. The proximal flow zone site (F38) was selected as the furthest upflow position at which the southern margin levee was easily distinguishable from other flow deposits. The frontal flow zone site (F39) was located 30 m behind the front of the southern-most flow-front toe formation, immediately behind the point where the frontal zone of the flow deposit divides into individual flow toes. A 1 x 1 m square grid divided into 20 cm squares (Fig. 3.1-inset) was used to randomly select 100 lava clasts at each site. The grid was placed on the south-facing outer levee in four adjacent places in a square formation (i.e. two upper positions and two positions immediately below these) (Fig. 3.1) at each site. The clast closest to the centre of each 20 cm square within the grid was selected, the maximum diameter of the clast and mean maximum diameter of exposed vesicles measured, and a percentage of vesicle abundance estimated visually using a comparator. Vesicle abundance was noted separately for inner and outer zones of the clasts where differential vesicle zonation was apparent. Clasts larger than 20 cm diameter (and therefore extending into adjacent squares) were allocated to the square in which the clast was dominant. Once data were recorded for this clast, it was removed and the underlying clast at the centre of the other affected squares was selected for data collection.

Statistical analysis was carried out using Microsoft Excel software. Mean and standard deviation values were obtained for the total data at each site and for each grid. A two-tailed student's t-test, assuming equal variances between the sample populations, was used to determine any significant difference in the mean values of each site and to ascertain if significant variation occurs between the two upper and two lower grid positions (i.e. the upper and lower sections of the levee) at each site.

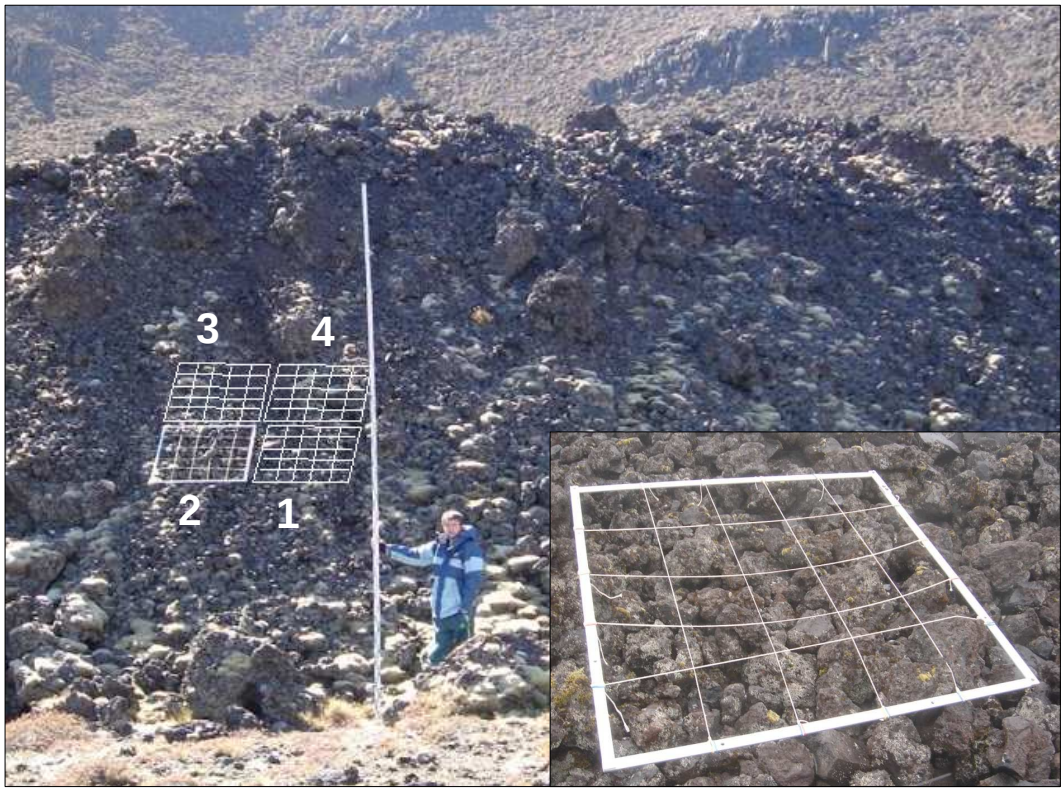

Fig. 3.1 Method used to randomly select lava blocks for quantitative field vesicularity analysis along the longitudinal axis of the 18th August lava flow deposit. Positioning of the square grid on the outer margin of the southern levee at location F39 in numbered order is shown. Measuring staff is at 5 m height. Inset: Square grid positioned at location F38. Frame is 1 x 1 m size, with divisions in 20 cm squares.

3.2.5 X-Ray Fluorescence Analysis

Eighteen representative samples (including known and unknown 1954 samples and one known 1949 sample) were selected for whole rock major and trace element analysis using a Spectro X-Lab 2000 fully automated X-Ray fluorescence (XRF) spectrometer at the University of Waikato. Ten major elements (SiO_2, TiO_2, Al_2O_3, Fe_2O_3*, MnO, MgO, CaO, Na_2O, K_2O, P_2O_5) and 21 trace elements

(S, Cl, V, Cr, Co, Ni, Cu, Zn, Ga, As, Rb, Sr, Y, Zr, Nb, Ba, La, Ce, Pb, Th, U) were measured.

Small sections were cut from whole rock samples and dried overnight at 80°C. Once cooled the samples were broken into small fragments with a heavy hammer, using heavy paper beneath and on top of the sample to prevent contamination from previous samples. Rock fragments from individual whole rock samples were ground to fine powder in a tungsten carbide ring mill, which was thoroughly cleaned and dried between each sample to prevent cross-contamination of samples. Powdered samples were stored in glass jars, re-dried overnight at 80°C and cooled prior to further preparation.

Major Elements

Fused glass discs were produced by mixing 0.35g of the powdered whole rock sample with 2.5-2.55g of 35% Li-tetraborate/65% Li-metaborate flux in a platinum crucible. The samples were then step-heated over a period of 30 minutes to 1040°C in a Broadway Fusion Furnace and the resultant molten sample poured onto a heated graphite disc and pressed to produce glass discs. The glass discs were cooled slowly, trimmed and labelled. Standard techniques were used to prevent cross-contamination between samples during sample preparation.

Trace Elements

Pressed powder pellets were prepared for trace element XRF analysis by mixing 5g of the powdered whole rock sample with ~ 15 drops of liquid PVA binder. The powder/PVA mix was pressed into an aluminium cup using a hydraulic press, labelled and dried in an oven at 70°C overnight to evaporate the PVA binder.

Loss on Ignition

Volatile content was determined by heating 2g of the powdered whole rock sample in a silica crucible at 1000°C for one hour. The samples were then cooled and weighed to ascertain the weight loss of the sample as a crude estimate of the volatile content lost on heating. Most of the samples analysed returned a negative

weight loss value indicating oxidation of the sample, therefore volatile content could not be ascertained.

3.3 WHOLE-SCALE AUTOBRECCIA CHARACTERISTICS

The 1954 lava flow deposits are typically comprised of rubbly, vesicular a'a displaying marked autobrecciation throughout the flow deposits. No apparent large-scale differences in clast size, morphology or texture were observed between the different 1954 lava flow deposits. However, clast size, morphology and texture are notably variable between individual autoclasts within each of the flow deposits, as described in the following sub-sections.

3.3.1 Autoclast Size and Distribution

Individual autoclasts within each of the lava flow deposits typically range from 5 to 50 cm diameter, although larger blocks of 1 to 2 m diameter are common. Autoclast sizes at lateral flow deposit margins tend to be relatively uniform, with a narrower average size range of 5 to 20 cm noted at most lateral flow margins (Figs. 3.2A, B). Larger average autoclast sizes, ~ 30 cm diameter, generally dominate at locations where the overall lava flow deposit thickness is less than 2 m, for example towards the distal margin of the 30th June BnL-S-1 lobe at location Bn27 (Fig. 3.2C). A wider range of autoclast sizes (~5 to 40 cm) is also typical at these locations. Wide clast size ranges, with numerous autoclasts ~ 1 to 2 m diameter, are commonly distributed on flow channel surfaces, the tops of levees, and at the frontal margin of flow deposits (Fig 3.3).

A number of accretionary lava balls, typically 5 to 6 m diameter, were emplaced on flow deposit surfaces at various distances from the vent; some resting on the steep sloping surface of flow deposits emplaced on underlying ridge slopes e.g. location Bn18 (Figs. 3.4A, B). These accretionary lava balls differ in appearance to the ballistic bombs scattered within the lava flow field (Fig. 2.6) in that they display massive, highly dense interiors encased within a 50 to 60 cm thick, scoriaceous carapace (Fig. 3.4C). This carapace is typically comprised of several well-defined, ~ 10 to 20 cm thick layers of highly vesicular, scoriaceous material, each containing a thin (~ 5 to 10 cm), dense inner core (Fig. 3.4D).

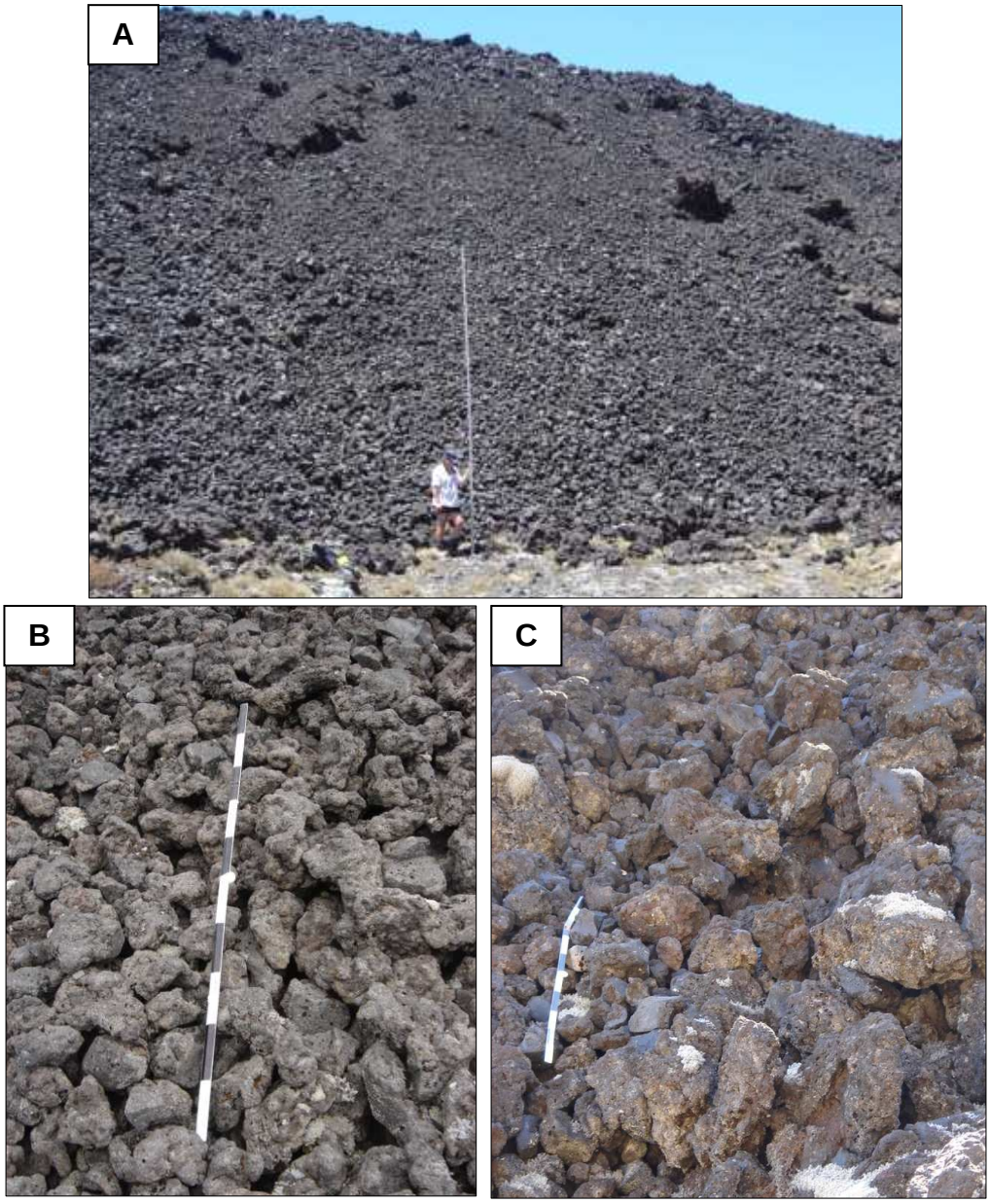

Fig. 3.2 Range of autoclast sizes at lateral flow deposit margins. A, relatively uniform autoclast sizes at the northern levee of the 18th August lava flow deposit (F1b). Measuring staff is at 5 m height. B, close up view of uniform autoclast sizes (G1). C, larger average autoclast sizes noted at flow margins where the overall deposit thickness is < 2 m (Bn27). Ruler in B & C is shaded in 10 cm sections.

3.3.2 Autoclast Morphology

Individual autoclasts within the 1954 lava flow deposits are predominantly autobrecciated, and commonly display a combination of relatively coarse, scoriaceous, rounded to sub-rounded, 'outer' surfaces (Fig. 3.5A), and smooth, angular, brecciated surfaces on which the clast interior is visible (Fig. 3.5B). Large-scale morphological zonation of autoclasts is evident at some flow deposits,

with whole or minimally autobrecciated, rounded to sub-rounded clasts more common at outward-facing lateral flow margins, and markedly autobrecciated clasts predominantly distributed on flow channel surfaces and at flow front margins. This trend coincides with the trend in clast size distribution, in that the smaller clast sizes that are dominant at lateral flow margins are commonly whole or minimally autobrecciated (Figs. 3.2A, B), while the larger clast sizes present at flow channel surfaces and at frontal flow margins display varying degrees of autobrecciation (Fig. 3.3). Other, less common autoclast morphologies include completely angular blocks with no scoriaceous outer zone (Fig. 3.5C), partially autobrecciated, irregular-shaped clasts (Fig. 3.5D), cauliflower-shaped clasts

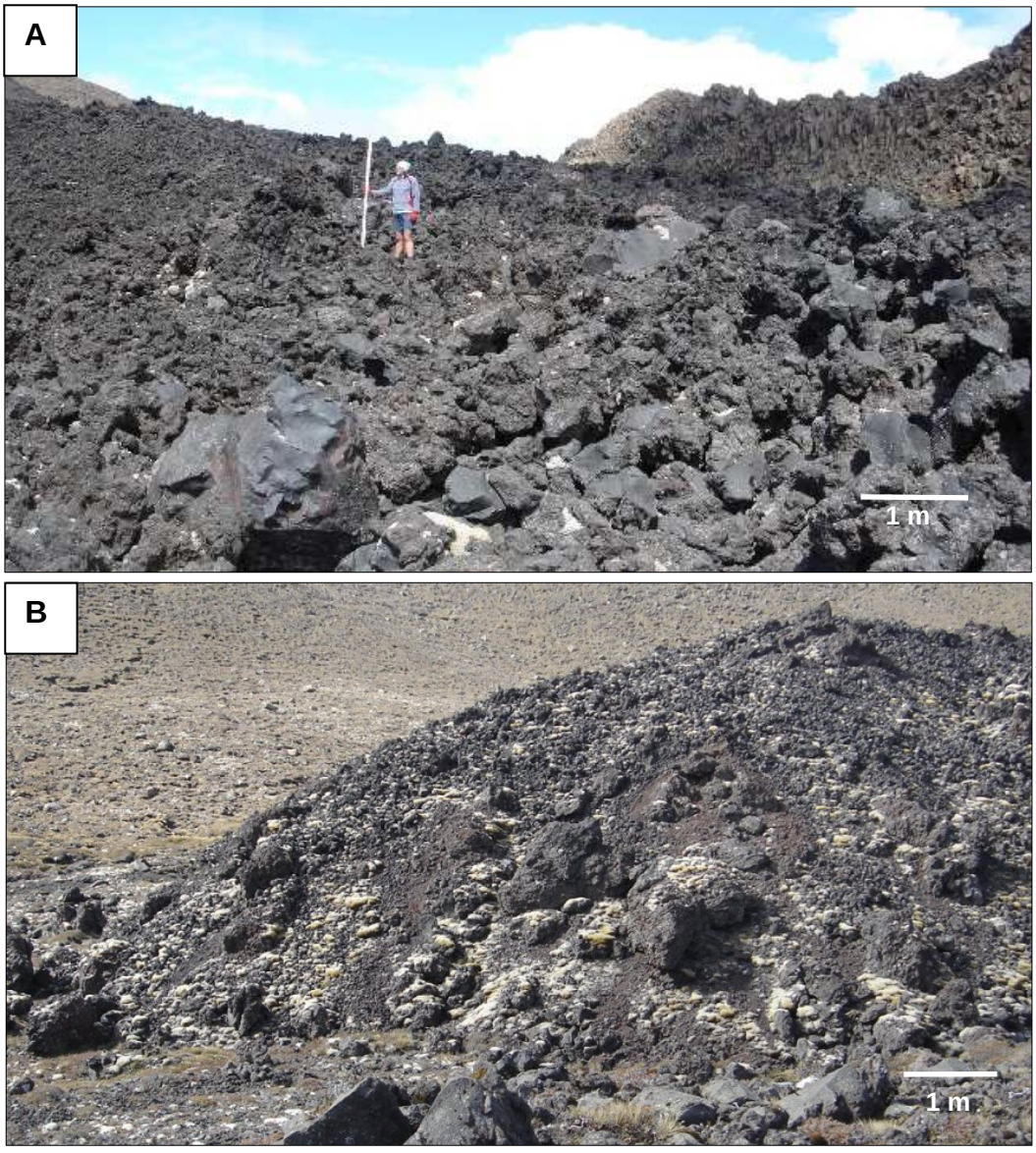

Fig. 3.3 Distribution of large autoclasts on A, the flow surface of the 30th June flow deposit, southern Bs lobe, location Bs8 (measuring staff is at 2 m height); and B, the flow front of the 18th August flow deposit, location F20.

comprising a sub-rounded, dense inner core encased within a relatively thick, bulbous, scoriaceous outer rim (Fig. 3.5E), and curved, fluidal morphologies (Fig. 3.5F). Large autoclasts rarely occur as vertical, spinose-like protrusions on some flow surfaces, both within the central flow channel (Fig. 3.6A), and at the frontal margin of the flow deposits (Fig. 3.6B).

Fig 3.4 Accretionary lava ball resting on the steep sloping flow surface of the 30th June BnL-S-1 lobe, location Bn18. A, position of accretionary lava ball (red circle) on sloping flow surface, B, long axis dimension (6 m), C, short axis dimension (5.5 m) and view of the massive interior with part of the outer carapace missing; D, dense, massive interior (bottom left) and layered scoriaceous carapace. Measuring staff in B and C is at 5 m length; ruler in D is shaded in 10 cm sections.

3.4 AUTOCLAST TEXTURE AND COMPONENTRY

3.4.1 Macroscopic Characteristics

The 1954 lavas are typically dark grey, although some discolouration due to hydrothermal alteration is evident in places, and porphyritic in texture. Visible phenocrysts, predominantly plagioclase with rare olivine, range between 0.5 to ~ 2 mm size. Large (up to ~ 5 cm), white, sugary quartzite xenoliths are

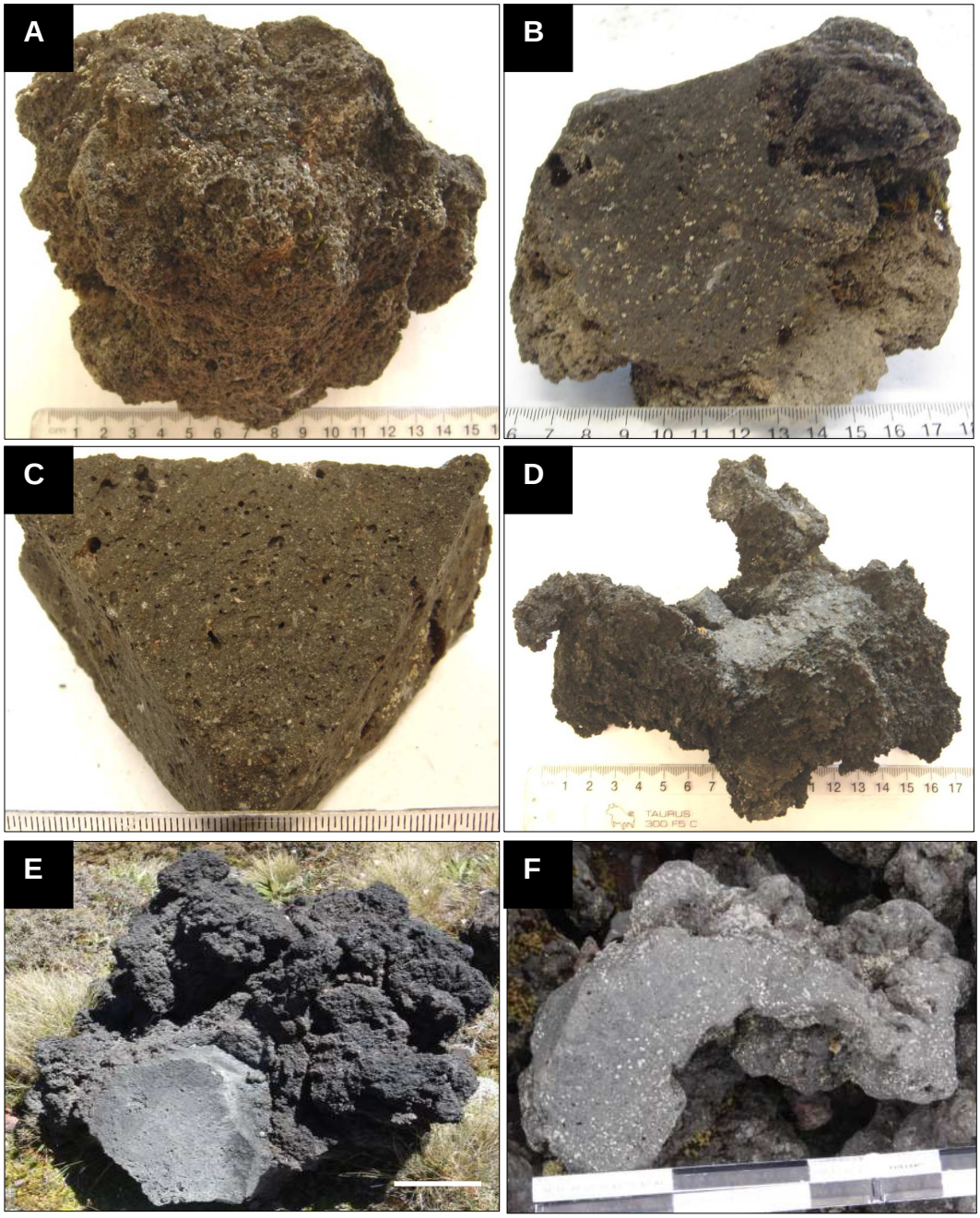

Fig. 3.5 Individual autoclast morphologies of the 1954 lavas. A coarse, scoriaceous, rounded to sub-rounded outer surface, combined with B, smooth, angular inner surface of the same clast (Bn25); C, angular block with no scoriaceous outer surface (Dc14); D, irregular-shaped, partially autobrecciated clast (Bn17-1); E, cauliflower-shaped clast (Location Bn15); F, curved, fluidal-shape (Location F3). Scale in A, B, D in 1 cm increments, and in C, 1 mm increments. Ruler in F shaded in 10 cm sections.

commonly seen within individual autoclasts (Fig. 3.7A) on all the flow deposits, with occasional larger xenoliths (~ 6 to 10 cm) forming completely separate clasts. Numerous smaller-sized (5 to 20 mm) white quartzite, and light-grey coloured metagreywacke and feldspathic xenoliths are also visible (Fig. 3.7B). Groundmass texture in hand specimen is microcrystalline to slightly glassy.

Individual autoclasts are generally characterised by two distinct zones of differing vesicle abundance (Fig. 3.8A). The outer zone is a scoriaceous carapace, consisting of abundant (30 to 40%) tiny vesicles (Fig. 3.8B, C). The thickness of this outer zone varies but is generally around 5 to 10 mm. The inner zone is generally less vesicular, varying in abundance between individual clasts from zero to approximately 40%. Vesicle abundance is often patchy over exposed inner zone clast faces. The majority of vesicles display spherical to slightly ellipsoidal morphologies with no apparent alignment of vesicles within clasts.

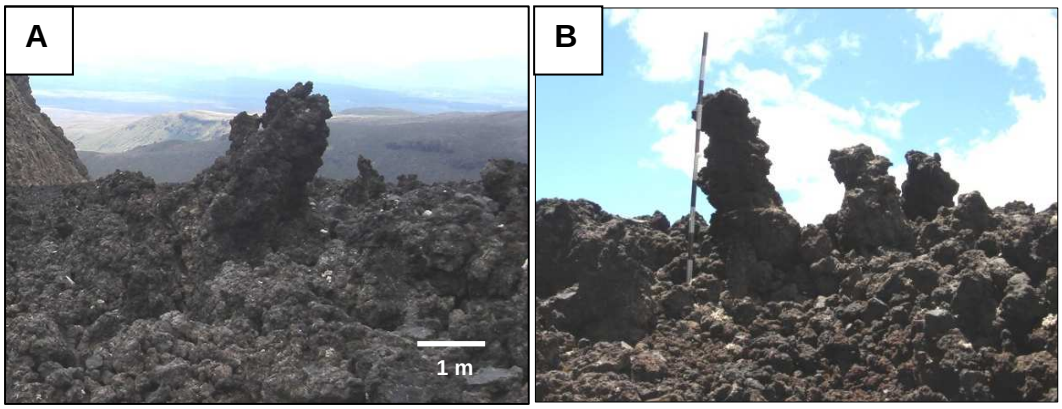

Fig. 3.6 Spinose lava structures protruding from flow deposit surfaces. A, flow surface of central flow channel, southern Bs group lobe, 30th June flow (location Bs3a); B, frontal flow margin of 14th July (Dc) flow (location Dc2). Ruler in B is shaded in 10 cm sections.

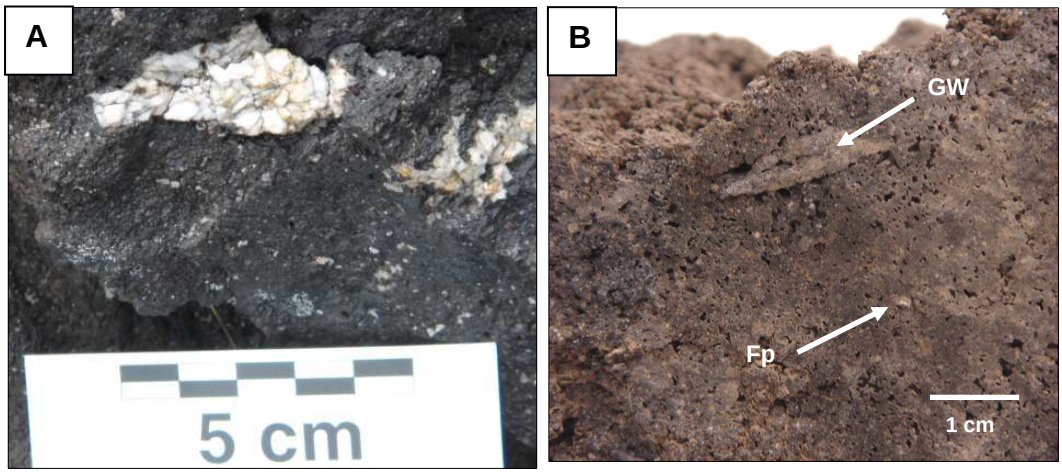

Fig. 3.7 Visible xenoliths within individual 1954 lava clasts. A, Quartzite xenolith (location Dc6; B, Metagreywacke (GW) and cognate feldspathic (Fp) xenolith in sample Dc1-2.

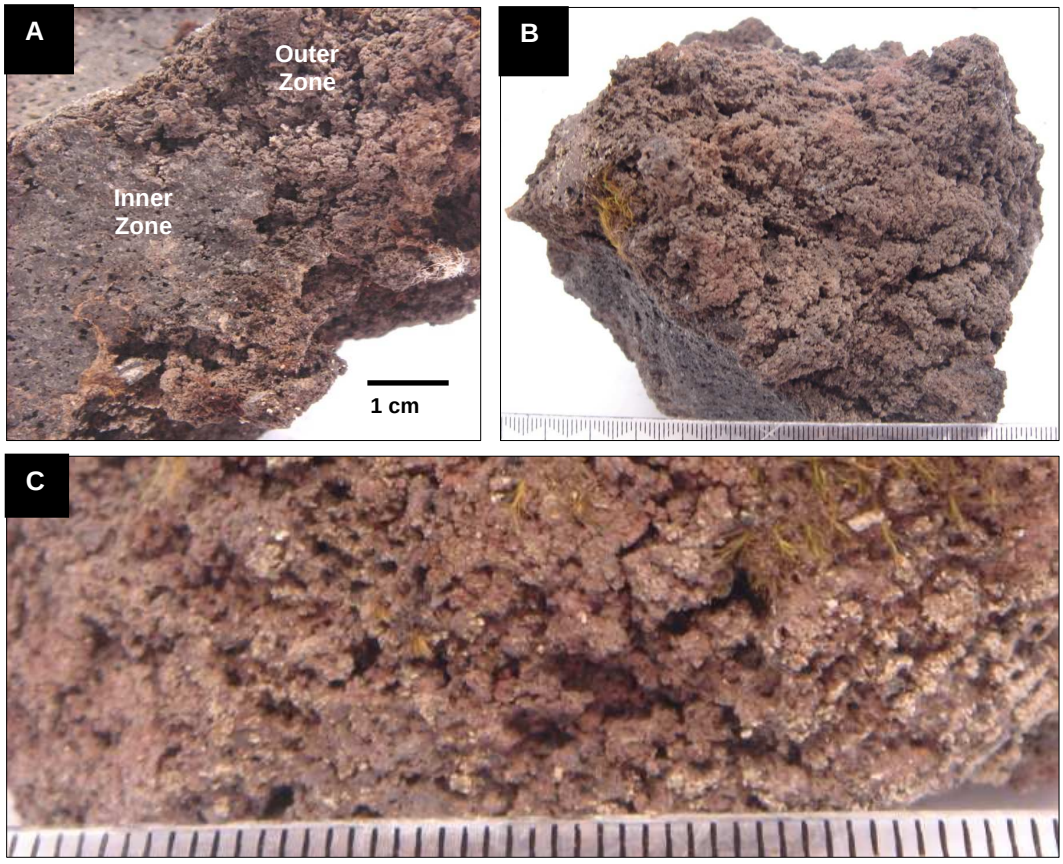

Fig. 3.8 Distinctive vesicle zonation between inner and outer sections of individual 1954 lava clasts. A, difference in texture and vesicularity between outer and inner sections of clast (Bs8-1); B, highly vesicular, scoriaceous outer zone (Dc11-1); C, close-up view of scoriaceous outer zone (Bn21-1a). Scale in B is in 1 cm increments, scale in C is in 1 mm increments.

3.4.2. Modal Abundance of Autoclast Components

Phenocryst, groundmass and vesicle modal abundance is given in Table 3.1 and vesicle modal abundance is discussed in Section 3.5.1. Phenocryst abundance ranges between 18 to 36%, with an average of ~ 27%. Plagioclase is the dominant phenocryst, accounting for ~ 66% of the total phenocryst population, with much lower abundances of orthopyroxene (opx) and clinopyroxene (cpx, augite) and traces of olivine and opaque Fe-Ti oxide minerals present. Groundmass typically accounts for approximately 50% of the total thin section, although groundmass abundance ranges from ~ 33 to 61%. However, only two samples contain groundmass abundance < 40%, whereas the groundmass abundance of approximately half of the samples is 40 to 50%. Phenocryst and vesicle abundance is generally more variable between each sample. There is no apparent phenocryst-vesicle-groundmass ratio trend with successive lava flows (Fig. 3.9A)

and mineral abundance is variable across the chronological flow succession (Fig. 3.9B).

Table 3.1 Modal abundance (%) of selected 1954 lavas. Plag = Plagioclase; Opx = Orthopyroxene; Cpx = Augite; Ol = Olivine; Opq = opaques; GW = metagreywacke xenolith; Qtz = quartzite xenolith; p/cryst = phenocryst; GM = groundmass. The final three columns represent p/cryst:GM:vesicle ratios. Average values given for inner zone samples only, outer zone samples only and total average for all samples.

Sample No.	Plag.	Opx.	Cpx.	Ol.	Opq.	GW	Qtz.	Other x/lith	Total x/lith	Total p/cryst	GM	Vesicle
A1	22	6	3							31	52	17
Bn26	13	6	3				1		1	23	40	37
Bn38	20	11	1							32	54	14
ZBs3-1	17	3	2		1		8		8	31	61	8
Bs3-2	17	4	4							25	42	33
ZBs8-2	19	4	2				1		1	26	59	15
ZBs11-1	19	5	2					1	1	27	59	14
ZBs11-2	14	2	2							18	43	39
Z1-Bs31	17	3	2							22	54	24
Z2-Bs31	19	6	3	2						30	53	17
ZBs32	21	4	3							28	47	25
Dc6	21	6	3	2						32	54	14
Dc8-3	17	6	1	1						25	54	21
Dc13	17	6	3							26	61	13
Dc14	15	7	2	1		2			2	27	53	20
E1-1	22	5	4	0.5			0.5		0.5	32	45	23
E2	16	7	2					1	1	26	56	18
ZF10	21	5	2			8			8	36	49	15
ZF13	25	4	2	1						32	50	18
ZF15-1	19	2	2			4	3		7	30	45	25
ZF15-2	15	2	5				1		1	23	43	34
ZF20	17	3	2							22	43	35
F21	13	3	3		1					20	45	35
G1	17	2	2	1		11			11	33	55	12
G2	13	9	2			2	1		2	26	46	28
Average[1]	**17.8**	**4.8**	**2.5**	**0.3**	**0.1**	**1.1**	**0.6**	**0.1**	**1.7**	**27.3**	**50.5**	**22.2**
XBs3-1	18	11	3							32	56	12
XBs8-2	21	4	3							28	50	22
XBs11-1	21	8	4			1		1	1	34	57	9
XBs31	16	2	2					1	1	21	33	46
XBs32	15	3	0							18	47	35
XF10	18	6	4							28	58	14
XF15-1	18	3	5	1			4		4	31	43	26
XF15-2	18	6	2							26	40	34
XF20	11	3	4			6			6	24	38	38
Average[2]	**17.3**	**5.1**	**3.0**	**0.1**	**0.0**	**0.8**	**0.4**	**0.2**	**1.3**	**26.9**	**46.9**	**26.2**
Total Average[3]	**17.7**	**4.9**	**2.6**	**0.3**	**0.1**	**1.0**	**0.6**	**0.1**	**1.6**	**27.2**	**49.6**	**23.2**

[1] Mean % for inner zone samples
[2] Mean % for outer zone samples
[3] Mean % for all samples

3.4.3. Phenocryst Mineralogy and Abundance

Plagioclase

Plagioclase phenocrysts are relatively abundant in all 1954 lava samples, with a modal abundance range of 11 to 25%, average ~ 18%, accounting for ~ 65% of the total phenocryst population. Phenocrysts are generally euhedral to subhedral and range in size from ~ 0.1 to 0.9 mm, average ~ 0.25 to 0.5 mm. Plagioclase also occurs as large (~ 1 to 5.5 mm), subhedral to anhedral 'megacrysts' in all but two of the thin sections examined, accounting for an average ~ 10% of the total plagioclase population (commonly ~ 4 to 5 megacrysts in each thin section). Pristine phenocrysts are rare (~ 4% of the total plagioclase population), with the majority of plagioclase phenocrysts and megacrysts displaying a range of resorption textures, including various disequilibrium sieve texture patterns, and embayed and/or frayed rims (Fig. 3.10). These textures typically represent magma mixing or decompression resorption within the magma reservoir (Hobden, 1997). Complex oscillatory zoning, possibly due to convection processes within the magma reservoir (Hobden, 1997) and/or polysynthetic twinning occurs in most phenocrysts and megacrysts. Plagioclase phenocrysts generally display rectangular lath to sub-angular morphologies, whereas megacrysts are commonly sub-rounded or display irregular, angular morphologies. Glass inclusions within sieved phenocrysts and megacrysts are common, with pyroxene and rare Fe-Ti oxide inclusions observed in larger megacrysts. Epidote is present within the central sieved core of some larger megacrysts, giving evidence of hydrothermal alteration of these crystals. Plagioclase phenocrysts and/or megacrysts commonly occur as plagioclase-only glomerocrysts, and as either the dominant member or minor component of plagioclase, orthopyroxene, and clinopyroxene glomerocryst assemblages.

Plagioclase also occasionally presents as a rim of small laths enclosing tightly-packed clusters of Fe-Ti oxide grains (Fig. 3.11) and these are included in the 'other xenolith' group for modal abundance (i.e. < 0.1% modal abundance). Small pyroxene inclusions and/or phenocrysts are rarely present as members of the plagioclase rims. The plagioclase/Fe-Ti oxide clusters range in size from ~ 0.45 to 1.6 mm. The central Fe-Ti oxide core is generally rounded to sub-rounded, with

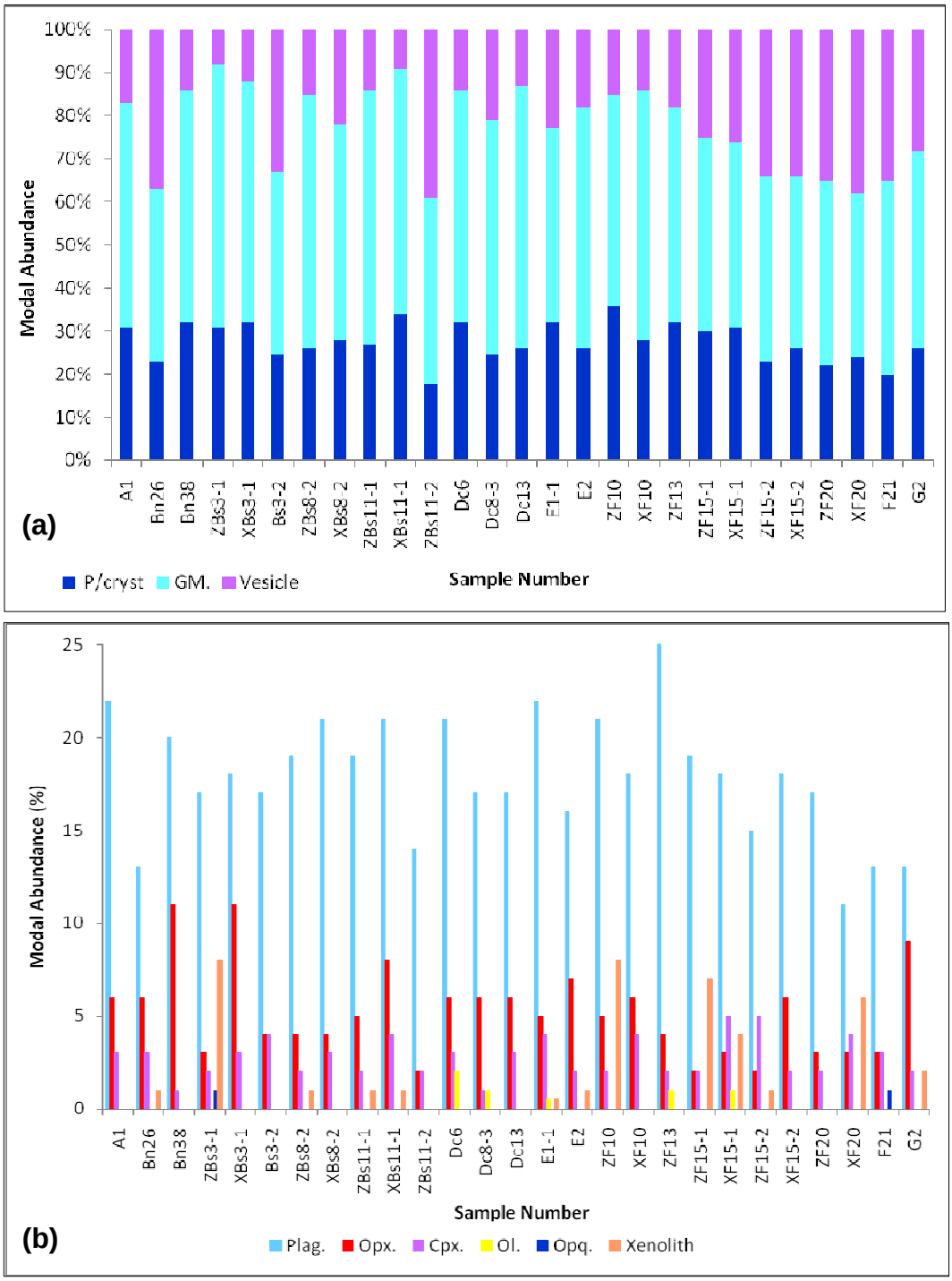

Fig. 3.9 Plots of modal abundance versus successive 1954 lava flow deposits [4th June (A), 30th June (B), 14th July (Dc), 29th July (E), 18th August (F), and 16th September (G)] using known samples. (a) comparison of modal phenocryst, vesicle and groundmass abundance; (b) modal abundance of phenocryst components in successive 1954 lavas. Plag. = plagioclase; Opx = Orthopyroxene; Cpx = Clinopyroxene (Augite); Ol. = olivine; Opq. = opaque minerals; Xenolith = total xenolith population.

the overall 'cluster' displaying a sub-rounded to sub-angular morphology. Plagioclase/Fe-Ti oxide clusters were present in 10 of the thin sections examined, with no more than one or two clusters present in each.

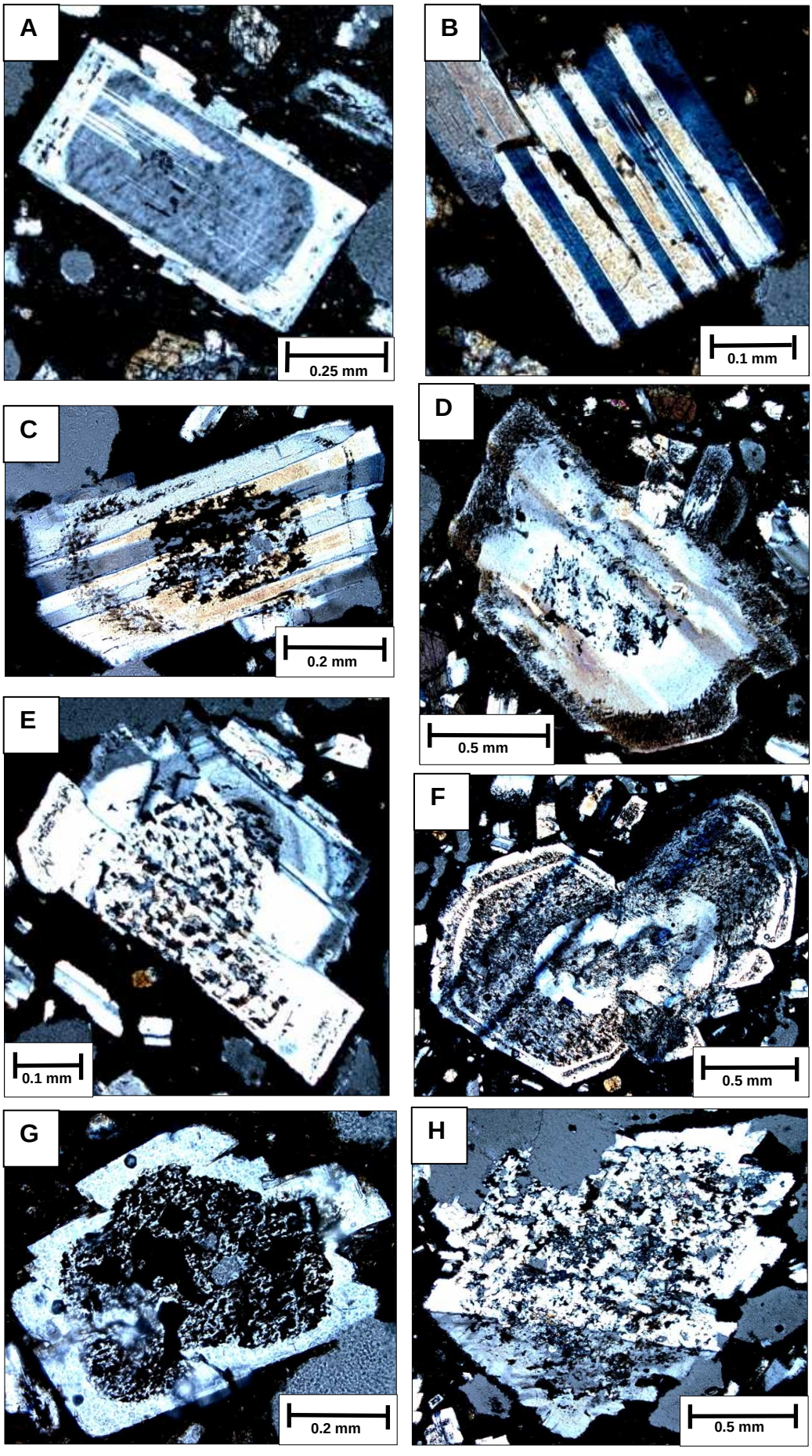
A
0.25 mm
B
0.1 mm
C
0.2 mm
D
0.5 mm
E
0.1 mm
F
0.5 mm
G
0.2 mm
H
0.5 mm

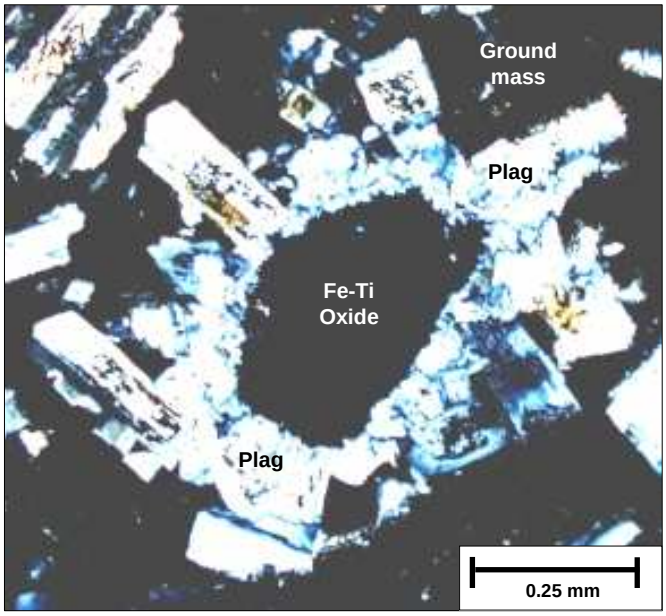

Fig. 3.11 Plagioclase laths encasing a cluster of Fe-Ti oxide grains in thin section (sample Z1-Bs31). Photograph taken under crossed polarised light.

Plagioclase/Fe-Ti oxide clusters may represent remnants of totally resorbed amphibole, which has altered in reaction to magma decompression (Stewart *et al*., 1996). Stewart *et al*. (1996) described similar clusters of clinopyroxene, plagioclase and Fe-Ti oxides in Mount Taranaki basaltic andesite lavas, also noting a decrease in modal amphibole abundance in flow deposits at increasing distance from the vent, suggesting continued amphibole alteration and resorption during lava flow emplacement. Furthermore, Hobden (1997) reports the presence of amphibole in older Tongariro andesite lavas, although none were observed in the younger Ngauruhoe lavas examined in either that or this study.

Plagioclase megacrysts are clearly 'foreign' to the host magma in terms of their size, however their origin is unclear. They may represent cognate xenocrysts that originated as magma chamber cumulates from previous lavas and have been entrained by the ascending 1954 magma batch. Conversely, they may not be

Fig. 3.10 (previous page) Range of plagioclase textures and morphologies in thin section. Sample numbers given in parentheses. A, pristine lath with slight polysynthetic twinning (A1); B, marked polysynthetic twinning (G2); C, heavily sieved centre, lightly sieved outer rim and frayed edges (E2); D, light central sieving with heavily sieved outer rim and irregular boundary (A1); E, intergrown laths with oscillatory zoning and central sieving (Bn26); F anhedral shape, with heavily sieved rim (Dc6); G, subhedral, heavily sieved with intact rim and small Fe-Ti oxide inclusions (F21); H, partially resorbed crystal, heavily sieved with embayments, pyroxene and glass inclusions (Bn26). All photographs taken under crossed polarised light.

foreign to the 1954 magma, simply representing plagioclase phenocrysts that have continued to grow while being transported around a convecting magma reservoir, and subjected to partial resorption due to magma mixing or decompression resorption towards the top of the reservoir.

Orthopyroxene

Orthopyroxene is the dominant of the two pyroxenes present in the 1954 lavas, with a modal abundance range of ~ 2 to 11% and an average of ~ 5%, accounting for ~ 19% of the total phenocryst population. It generally occurs as discrete, euhedral to subhedral prisms, ranging in size from ~ 0.1 to 0.9 mm, average size ~ 0.3 mm. Orthopyroxene megacrysts are also present as discrete prismatic or sub-rounded crystals in around two thirds of the thin sections examined, ranging in size from 1.2 to 2.5 mm, average 1.75 mm. Megacrysts account for ~ 14 to 47% of orthopyroxene crystals where present in thin section, with ~ one to three megacrysts in each of these thin sections. Typically orthopyroxene phenocrysts and megacrysts are fractured (Fig. 3.12A) and frequently only partial crystal fragments are present. Many phenocrysts and most megacrysts display coarse sieve textures within the central portion of the crystal, generally infilled with glass (Figs. 3.12B, C, D). Orthopyroxene also commonly occurs either next to (Fig. 3.12D), or intergrown with clinopyroxene crystals, as the dominant members of pyroxene/plagioclase glomerocrysts (Fig. 3.12E), as the dominant member of the mixed pyroxene rims observed around most olivine phenocrysts, and as inclusions within larger plagioclase phenocrysts and megacrysts. Orthopyroxene is rarely observed with either a clinopyroxene rim (Fig, 3.12D), or as the rim around a clinopyroxene phenocryst (Figs. 3.12F). As with plagioclase, the coarse sieve textures observed indicate resorption processes and are suggestive of magma mixing, recharge or transport processes within the magma reservoir or conduit (Hobden, 1997).

Clinopyroxene

Clinopyroxene phenocrysts average ~ 2.5% abundance (range 0 to 5%), and accounts for ~ 10% of the total phenocryst population. Phenocrysts are generally subhedral to anhedral, ranging in size from 0.1 to 0.6 mm, average size

~ 0.25 mm. Clinopyroxene commonly occurs as discrete, rounded to sub-rounded or sub-prismatic megacrysts ranging in size from 1 to 3.5 mm, average size 1.75 mm. These megacrysts are present in all but three of the thin sections examined, accounting for ~ 7 to 64% of the total clinopyroxene population (modal abundance > 30% in 75% of thin sections). Clinopyroxene phenocrysts and megacrysts are generally fractured to varying degrees and frequently fragmented, particularly where they are located at vesicle boundaries (Fig. 3.12G). Polysynthetic twinning is evident with some phenocrysts (Fig. 3.12H). Phenocrysts and megacrysts commonly occur as clinopyroxene-only glomerocrysts (Fig. 3.12G) consisting of two or more megacrysts and/or smaller phenocrysts, and frequently occur adjacent to orthopyroxene crystals and as reaction rims around orthopyroxene (Fig. 3.12D) and olivine crystals. Rarely clinopyroxene is bounded by an orthopyroxene reaction rim (Fig. 3.12F), or is present as small inclusions within larger plagioclase megacrysts.

Olivine

Olivine is present as a minor phenocryst component in most of the 1954 lavas with a modal abundance average of 0.9%. Although in modal analysis it appears in only eight of the 36 thin sections analysed, olivine phenocrysts were present in all but five (Bn26, Bn38, ZBs8-2, ZBs11-1, XF10) of the thin sections described. In the remaining thin sections, one to eight olivine phenocrysts were present, with an average of four crystals in each. Olivine crystals are generally sub-rounded and range in size from 0.125 to 2 mm. Almost all olivine phenocrysts were bounded by a mixed orthopyroxene and clinopyroxene reaction rim, averaging ~ 0.7 mm thick (Figs. 3.13A, B). Reaction rims usually comprised small granular crystals but were frequently made up of discrete, easily identifiable pyroxene phenocrysts. Rarely, olivine occurred either as a discrete phenocryst with no reaction rim, a discrete phenocryst bounded by an iddingsite reaction rim, or within a pyroxene/plagioclase glomerocryst (Fig. 3.13C).

Fe-Ti Oxides

Fe-Ti oxides are moderately to highly abundant as tiny scattered granules in the groundmass of most of the 1954 lavas, with only five samples (ZF20, F21, G2,

Z1-Bs31, Dc8-1) containing either very rare, or no separate Fe-Ti oxide grains within the groundmass; although Fe-Ti oxides were present as inclusions in these thin sections. Rarely Fe-Ti oxides occur as small (0.02 to 0.175 mm), discrete phenocrysts but were more commonly present as either inclusions within large plagioclase phenocrysts, as members of mixed plagioclase and pyroxene glomerocrysts, or within quartzite, metagreywacke and feldspathic xenoliths. Occasionally multiple Fe-Ti oxide grains occur as tightly-packed groups enclosed within a rim of small plagioclase laths (Fig. 3.11). Titanomagnetite is the most common of the Fe-Ti oxide minerals present, both as discrete euhedral to subhedral phenocrysts, and as small rounded grains within the groundmass. Rare pyrite, sphalerite, chalcopyrite, ilmenite and pyrrhotite grains were also observed, with pyrite grains typically including sphalerite or chalcopyrite as either a rim or veins within the crystal.

Glomerocrysts

Glomerocrysts are distinguished from feldspathic xenoliths in this study primarily because their constituent phenocrysts generally appear relatively pristine in comparison to those included in xenoliths, for example there is less evidence of resorption textures and clear, relatively intact crystal boundaries. Glomerocrysts comprising assemblages of single-mineral compositions (e.g. plagioclase-only, clinopyroxene-only) and multiple-mineral compositions are approximately equally common. Multiple-mineral glomerocryst assemblages include, plagioclase + orthopyroxene + clinopyroxene ± olivine ± Fe-Ti oxide (where either plagioclase or orthopyroxene is the dominant member) (Fig. 3.12E) and orthopyroxene + clinopyroxene ± plagioclase ± olivine ± Fe-Ti oxide (where orthopyroxene is usually the dominant member). Glomerocryst modal abundance was not specifically determined for the 1954 lavas, given the diverse nature of assemblages, although individual phenocryst members were included in relevant point counts where appropriate.

Fig. 3.12 (next page) Orthopyroxene and clinopyroxene textures in thin section. Sample numbers given in parentheses. A, fractured and sieved orthopyroxene (E2); B, embayed orthopyroxene (G2); C, sieved orthopyroxene rim (G2); D, orthopyroxene with clinopyroxene rim (Dc6); E, orthopyroxene-dominant glomerocryst with plagioclase and clinopyroxene members (E2); F, clinopyroxene with orthopyroxene rim (Dc6); G, large, intergrowing clinopyroxene crystals with one shattered by a vesicle (A1); H, polysynthetic twinning on clinopyroxene (Dc6). All photographs taken under crossed polarised light.

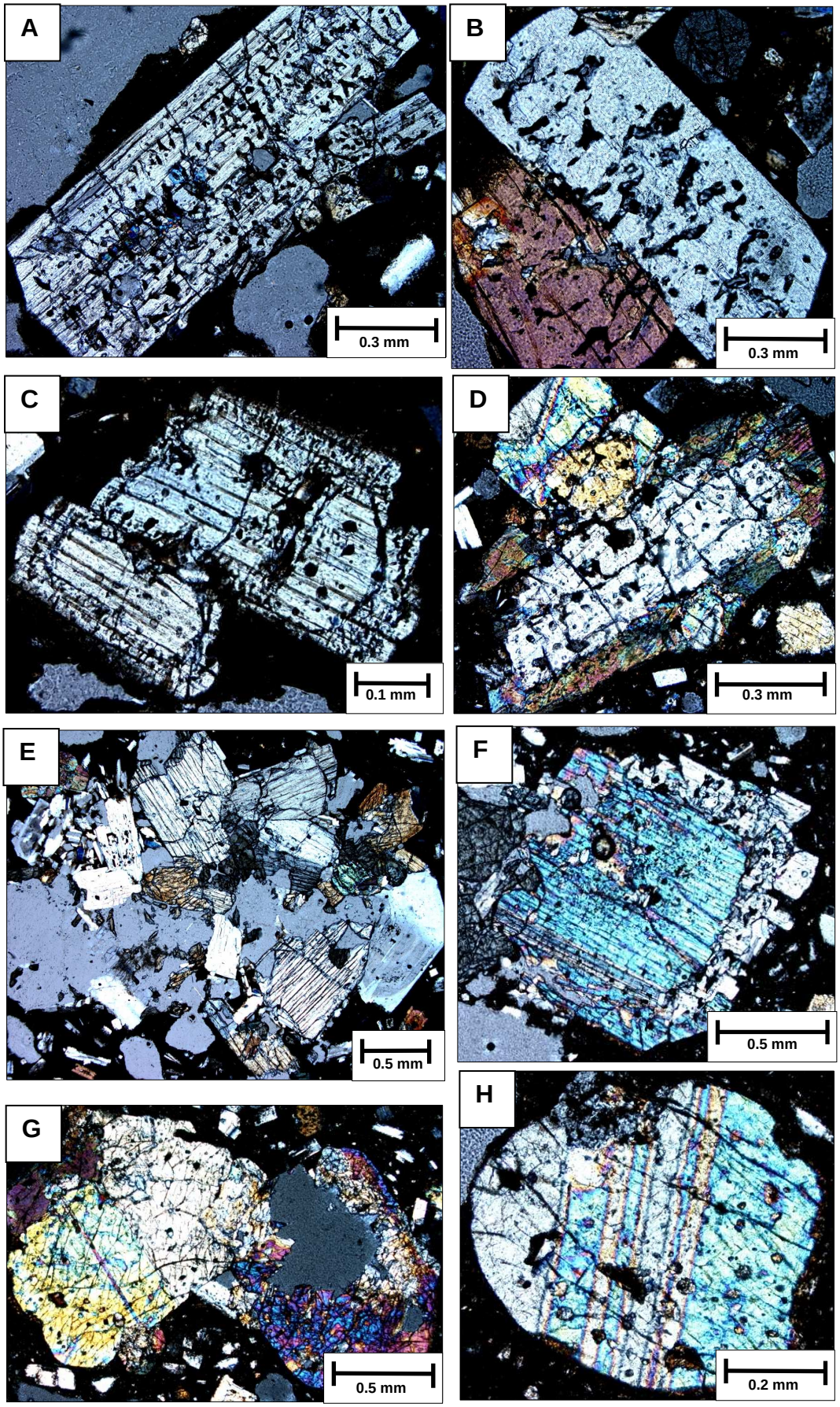
A
0.3 mm
B
0.3 mm
C
0.1 mm
D
0.3 mm
E
0.5 mm
F
0.5 mm
G
0.5 mm
H
0.2 mm

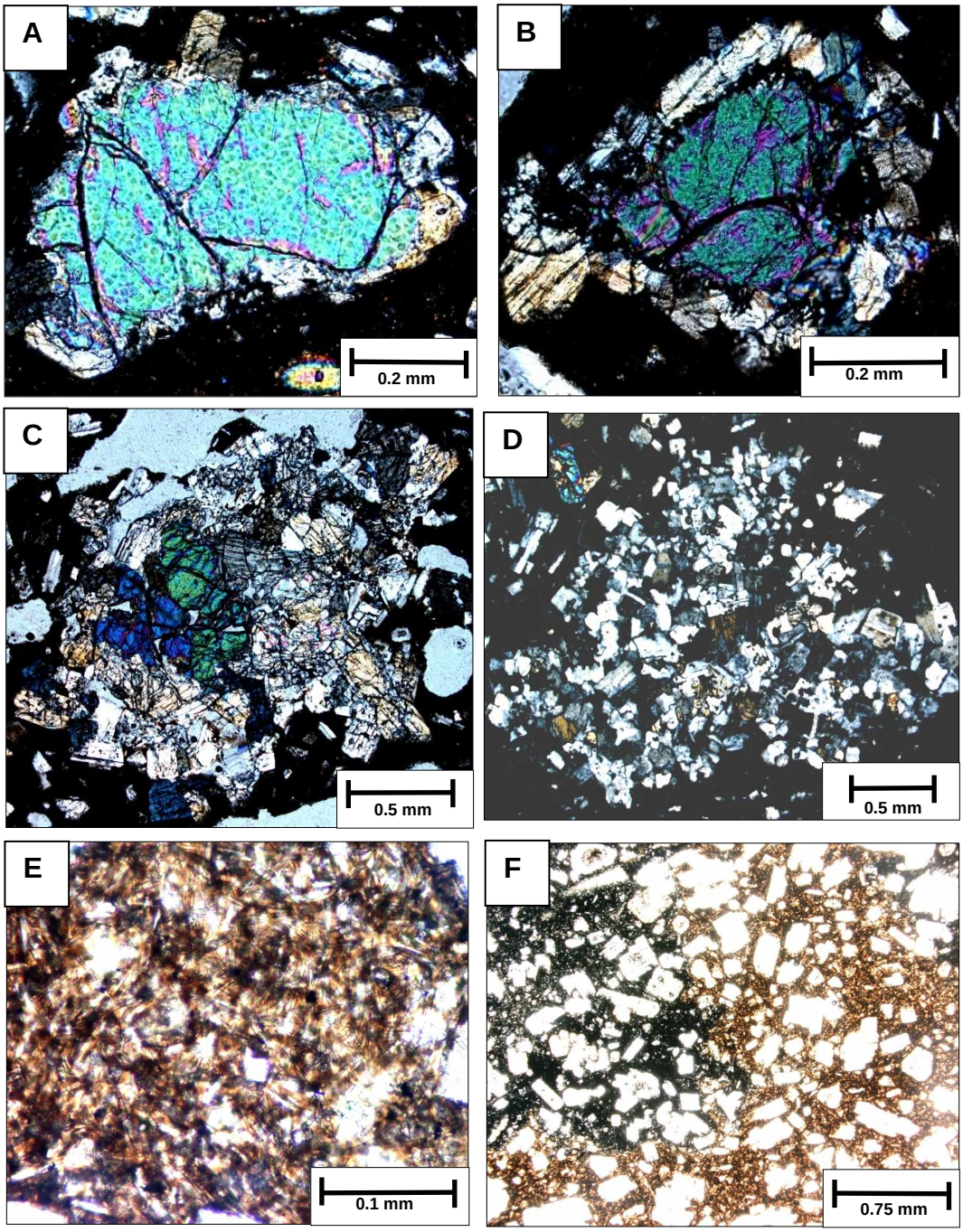

Fig.3.13 Olivine, Fe-Ti oxide, and groundmass textures in thin section. Sample numbers given in parentheses. A, fractured olivine with thin pyroxene rim (Dc6); B, olivine with rim of pyroxene crystals (E2); C, small olivine within mixed pyroxene and plagioclase glomerocryst (E2); D, feldspathic xenolith with pyroxene and Fe-Ti oxide inclusions (A1); E, microlites within dark brown glass (Z1-Bs31); F, dark brown and black patchy groundmass (A1). Photographs A-D taken under crossed polarised light, E and F under plane polarised light.

3.4.4 Xenoliths

Xenoliths are relatively abundant components of the 1954 lavas, with an overall abundance range of zero to 11% (average ~ 2%). Xenolith types are sub-divided into accidental xenoliths (quartzite and metagreywacke) bearing no direct

relationship to the host magma, and cognate (feldspathic) xenoliths that are genetically related to the host magma (Hobden, 1997).

Accidental Xenoliths

Quartzite

Accidental quartzite xenoliths are relatively common in the 1954 lavas, with average modal abundance ~ 0.6% (modal range 0 to 4%). However, although quartzite xenoliths were only counted in a small number of thin sections (8 of 36) during modal analysis, it was visibly present in all but four (Z1-Bs31, ZBs32, Dc8-3, G1) of the thin sections described, with between one to five xenoliths (average one to two) present in each thin section. Quartzite xenoliths are typically sub-angular to sub-rounded and range in size from ~ 0.4 to 11.5 mm, average size ~ 2 mm. Some quartzite xenoliths (e.g. XBs3-1, Dc14) appear relatively pristine, comprising ~ 90 to 100% equigranular quartz grains with a mosaic texture, clear crystal boundaries and sharp contact with the surrounding lava. However, most xenoliths are associated with varying abundances of plagioclase ± pyroxene ± Fe-Ti oxide inclusions, and many xenolith boundaries are either fully or partially surrounded by small plagioclase ± pyroxene phenocrysts. Glass inclusions and/or glass-filled embayments are also relatively common.

Metagreywacke

Metagreywacke appears more abundant than quartzite on modal analysis (average 1%), although it appears in less of the thin sections described than quartzite. It is present in all but seven (XBs3-1, Bs3-2, ZBs11-2, Dc8-1, Dc8-3, Dc13, ZF10) of the thin sections described, with one to five xenoliths (average one to two) present in each thin section. Metagreywacke is typically sub-angular to sub-rounded and ranges in size from 0.38 to 8 mm. 'Pristine' metagreywacke is absent, with all xenoliths displaying some degree of partial melting e.g. 'frayed' boundaries and unclear contact with the surrounding magma. Occasionally xenoliths display mild foliation textures. Most metagreywacke xenoliths are associated with a moderate to large abundance of Fe-Ti oxide inclusions, predominantly occurring as tiny grains although often larger Fe-Ti oxide grains are present. Many xenoliths also contain small plagioclase ± pyroxene ± glass inclusions, with clusters of small

plagioclase ± pyroxene phenocrysts gathered around part, or all, of the xenolith boundary.

Cognate Feldspathic Xenoliths

Feldspathic xenoliths are particularly common in the 1954 lavas, and are present in all but one (ZF10) of the thin sections described. In modal analysis, it is included in the 'other xenolith' group (along with plagioclase/Fe-Ti oxide clusters), giving < 0.1% average modal abundance. However, one to six feldspathic xenoliths were observed in each thin section, with commonly three to four present in most thin sections. The xenoliths are typically angular to sub-rounded, ranging in size from ~ 0.5 to 6.75 mm, average size ~ 1 mm, commonly with poorly defined xenolith/host magma boundaries. Feldspathic xenoliths are typically composed of varying abundances of plagioclase, pyroxene and Fe-Ti oxides.

Varying abundances of Fe-Ti oxides and glass occur both as inclusions within the individual crystal components of these xenoliths and in the interstitial spaces within the xenolith. The majority of crystals within these xenoliths typically display marked sieve textures, fractures, and poorly defined crystal boundaries. Xenoliths are often partially surrounded by a plagioclase rim, distinguished by less marked resorption textures. Cognate feldspathic xenoliths appear to represent coarse-grained, crystalline, genetically-related equivalents of the host magma groundmass, which crystallised out of the melt, relatively slowly, at the slightly cooler margins of narrow, hypabyssal magma conduits (Hobden, 1997).

3.4.5 Groundmass Mineralogy and Texture

The groundmass of the 1954 lavas has a hyalopilitic texture in thin section, dominated by abundant microlitic plagioclase laths and some pyroxenes. Microlites are generally < 0.025 to ~ 0.375 mm size with minimal interstices between them, and no apparent preferential orientation or alignment (Fig. 3.13E). Tiny Fe-Ti oxide grains are also abundant throughout the groundmass of most samples examined. Glass is generally medium to dark brown with scattered dark-brown to black patches in some samples (Fig.3.13F). Commonly the darker glass

patches coincide with patches of high abundance of Fe-Ti oxide grains, although dark brown glass occasionally occurs in the absence of abundant oxides (e.g. sample F21).

3.5 VESICLE ABUNDANCE, TEXTURE AND DISTRIBUTION

3.5.1 Petrographic Observations

Vesicle modal abundance varies from 8 to 46% between the known 1954 samples (Table 3.1). A small modal difference in vesicularity is evident between thin sections prepared separately from the outer and inner zones of whole rock samples (average ~ 22% and 26% respectively), although the range of vesicle abundances between the two groups is similar (8 to 39% in the inner zone group, and 9 to 46% in the outer zone group). On visual inspection, most thin sections (e.g. Dc13) showed no difference in vesicle abundance between the outer and inner zones (Fig. 3.14A). Vesicle sizes range from < 0.02 to 9.5 mm diameter, most commonly ≤ 2 mm. Within individual thin sections average vesicle sizes are frequently bi-modal, with smaller average sizes (~ 0.08 to 0.5 mm) generally more common towards the inner (Z) zone sector of the thin section, and larger average sizes (0.75 to 1 mm) generally more common towards the outer (X) zone sector (Fig. 3.14B). In some samples (e.g. ZF15-2) this trend is reversed, with larger average vesicle sizes concentrated towards the inner (Z) zone sector of the thin section, and smaller average vesicle sizes concentrated towards the outer (X) zone (Figs. 3.14C, D). Small- to medium-sized vesicles are generally spherical to ellipsoidal and appear isolated (Figs. 3.14B, D). Medium- to large-sized vesicles range from ellipsoidal to irregular morphologies (Figs. 3.14D to G) with the irregular morphologies representing either connected or partially collapsed vesicles. There is no apparent alignment of vesicles in terms of shape or direction in most thin sections, although samples ZF15-2, XBs-32 and ZF20 display some degree of alignment of the relatively elongated vesicles towards the outer (X) zone of each sample (Figs. 3.14D, F, G). Vesicle alignment in these samples may be the result of outer zone compaction prior to solidification rather than representing shearing forces within the lavas.

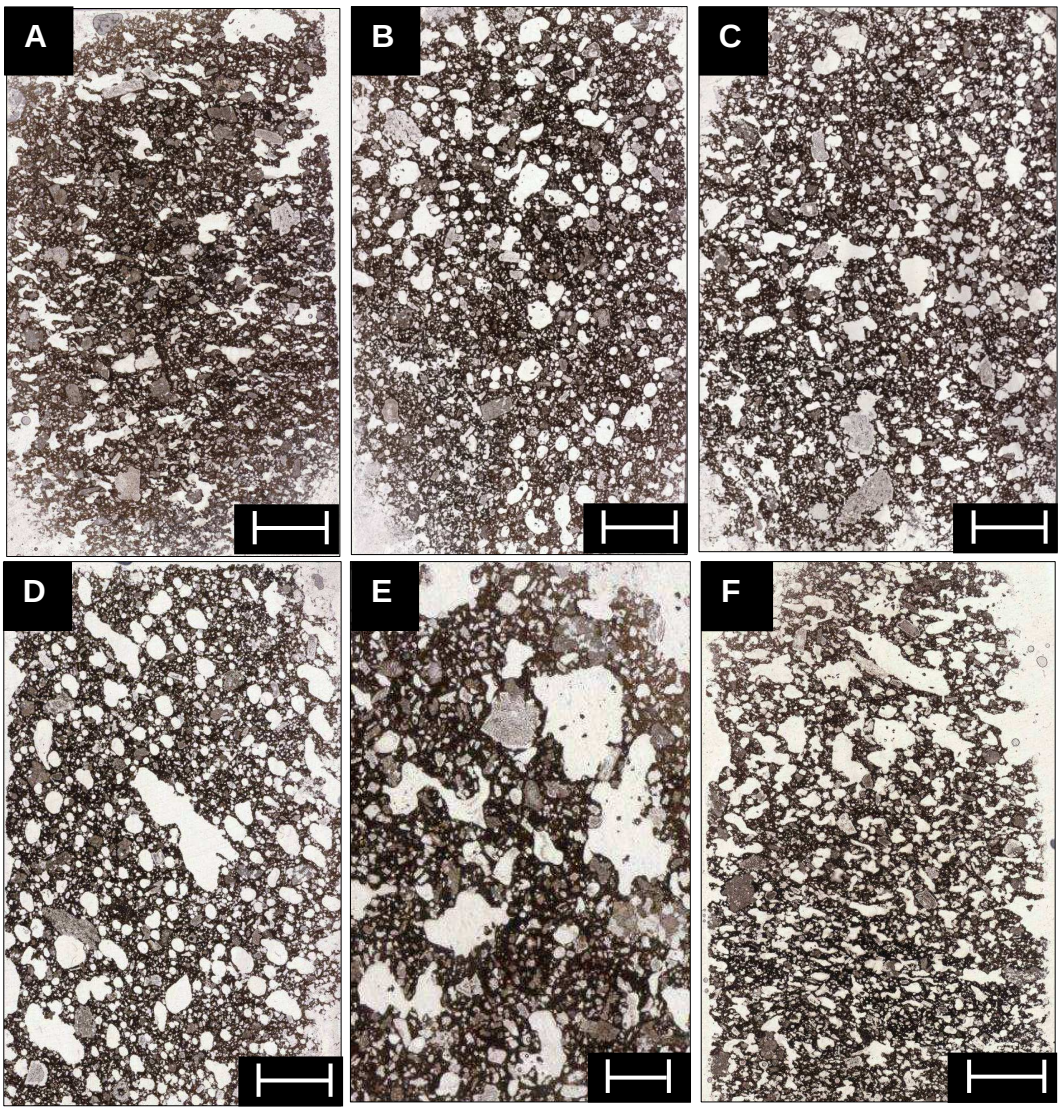

Fig. 3.14 Vesicle abundance and morphologies within individual clasts of the 1954 lavas, from thin section scans. Unless otherwise stated the outer (X) zone is orientated towards the top, and the inner (Z) zone towards the base of each figure. Sample numbers are given in parentheses. Scale bars are 5 mm length in all figures except E, 2mm length. A, similar vesicle abundance in both the outer and inner zones (Dc13); B, larger vesicle sizes towards the outer zone and smaller vesicle sizes towards the inner zone, note spherical to slightly ellipsoidal morphology of smaller vesicles (Dc8-3); C, smaller vesicle sizes in the outer zone (XF15-2) compared to D, larger vesicle sizes in the inner zone (ZF15-2) of the same whole rock sample (F15-2), note spherical to ellipsoidal morphology of small to medium-sized vesicles, and some alignment of larger vesicles towards the outer zone (X is orientated to the right in figure C); E, irregular-shaped morphologies of larger vesicles representing partially collapsed or connected vesicles (Z2-Bs31); F, alignment of elongated vesicles close to the outer rim of the outer (X) zone (XBs-32); G, relative alignment of larger, irregular-shaped vesicles of the inner zone but orientated towards the outer zone of the sample (ZF20).

3.5.2. Gas Pycnometry Analysis

Total vesicularity (%), and isolated and connected vesicle abundance (%) derived from gas pycnometer analysis is given in Table 3.2. The total vesicularity of the outer zone sample blocks ranges from 14 to 31%, with an average of 23%, lower than the visually estimated ~ 30 to 40% vesicularity of this zone for the majority of the 1954 autoclasts. Three of the five outer zone sample blocks analysed (Bn6-4, Bs27 and Dc2-1) show less total vesicularity than the inner zone block samples from corresponding whole rock samples, which was not apparent on visual estimation.

Total inner zone vesicularity ranged from 17 to 49% over the two sample block sizes (S and M), averaging 29% and 27% respectively. Most of the corresponding small- and medium-sized sample blocks of each whole rock sample recorded similar total vesicularity values, with a difference of ~ 1 to 2% between the calculated values of each sample block size; although the small inner (S) sample blocks of two samples (Bn20-2 and Dc3-1) showed 6 and 8% greater vesicularity respectively than the medium sample block sizes. Five whole rock samples have greater calculated total inner vesicularity values than visually estimated values, with samples Bn40, F2 and Dc3-1 displaying similar visual and calculated values.

Connected vesicle abundance ranges from ~ 11 to 44%, equating to 84 to 96% of the total vesicle population. Average connected vesicle abundance between the two inner sample block sizes is similar at 25 to 26% (91 to 93% of total vesicles), with slightly less abundance (~ 21%; ~ 87% of total vesicles) of connected vesicles recorded in the outer sample blocks. Of the five outer sample blocks analysed, two (Bn19 and Bn40) show a higher proportion of connected vesicles than their corresponding inner block samples.

Isolated vesicle abundance ranges from ~ 2 to 6%, with minimal difference in the abundance of isolated vesicles between the outer and inner sample blocks (average 3 and 2% respectively). The range of isolated vesicles abundances is 1 to 3% in the majority of sample blocks, with one outer sample block (Bn19), and one

Table 3.2 Total, isolated and connected vesicularity of selected 1954 lava samples using gas pycnometry analysis. Inner zone vesicularity and vesicle size range estimated visually prior to analysing samples. Inner (S) refers to small-sized sample blocks, and inner (M) refers to medium-sized sample blocks.

Sample no.	Estimated inner zone vesicularity (%)	Vesicle size range (mm)	Total vesicularity (%)			Isolated vesicles (%)			Connected vesicles (%)		
			Outer	Inner (S)	Inner (M)	Outer	Inner (S)	Inner (M)	Outer	Inner (S)	Inner (M)
Bn6-4	7-10	0.1-0.2	13.9	19.4	18.3	3.1	3.0	1.7	10.8	16.4	16.6
Bn19	1-2	0.1-0.5	31.4	23.1	22.7	5.0	2.9	2.3	26.3	20.3	20.4
Bn20-2	10-15	1-10	N/A	49.3	43.4	N/A	5.7	1.9	N/A	43.7	41.5
Bn40	10-15	0.2-8	22.0	17.0	18.6	1.8	2.3	1.6	20.2	14.6	17.0
Bs27	5-10	0.2-2	21.4	25.4	26.0	1.6	1.5	2.2	19.8	24.0	23.8
Dc2-1	10-15	0.2-5	27.4	31.8	30.6	1.7	2.2	1.8	25.7	29.6	28.8
F2	20-30	0.1-20	N/A	22.9	24.5	N/A	1.4	1.8	N/A	21.5	22.7
Dc3-1	25-30	0.2-5	N/A	43.5	35.9	N/A	1.6	1.7	N/A	42.0	34.2
Average			**23.2**	**29.1**	**27.5**	**2.6**	**2.6**	**1.9**	**20.6**	**26.5**	**25.6**

small inner sample block (Bn20-2) displaying 5 to 6% isolated vesicle abundance respectively. Small-sized sample blocks show slightly higher isolated vesicle abundance (0.4 to 3.8% greater abundance) in five of the eight whole rock samples compared to their corresponding medium-sized sample blocks, with average isolated abundances of 2.6 and 1.9% respectively.

Minor differences in vesicle abundance between sample blocks from the same whole rock sample are most likely the result of natural variability within individual whole rock clasts. However, this does not explain the relatively high ratio (approximately 9:1) of connected to isolated vesicles, which is not consistent with the dominance of small- to medium-sized isolated vesicles visually observed in thin section. The disparity between measured and estimated isolated vesicle abundance may reflect unreliable pycnometer data due to (a) the use of block-shaped samples instead of cylindrical samples, which reduced the total filled volume of the pycnometer sample cells, and (b) the use of small- and medium-sized sample blocks instead of the more analytically reliable large-sized sample blocks. Both of these points are particularly important if the method by which the pycnometer measures volume and density of the rock samples within the sample cell is considered. The pycnometer calculates bulk density$_{pyc}$ by measuring the volume of introduced gas displaced by the sample block. The displaced volume is reduced if the rock sample does not take up the entire volume of the pycnometer sample cell, affecting the analytical accuracy of the results. Introduced gas permeates all vesicles connected to the surface of the sample block and this pore volume is thus also excluded from the measurement. The volume of displaced gas is therefore related to the volume of solid rock and any interior isolated vesicles. This has important implications in terms of sample block (or cylinder) size because vesicles that would otherwise be completely isolated within the interior of large-sized samples are increasingly likely to become either exposed at, or connected to, exterior sample surfaces with decreasing sample size. This is shown in five of the eight whole rock samples analysed, where isolated vesicle abundance is marginally higher in the small-sized sample blocks compared to the corresponding medium-sized sample blocks, and an overall difference of 0.7% between the average abundances of the two groups.

Conversely, the visual estimation of isolated vesicle abundance on thin section analysis is limited by the two-dimensional plane of the thin section. Small-sized, spherical vesicles which appear isolated in thin section may actually represent the cross-section of a connected vesicle or the narrow end of a larger, irregular-shaped vesicle in three-dimensional space. However, small to medium-sized, spherical to ellipsoidal vesicles were significantly more abundant than the large, irregular-shaped vesicles on thin section analysis, therefore it is unlikely that a large proportion of these apparently isolated vesicles represent cross-sectional portions of larger, connected vesicles.

Given the potential analytical error in the pycnometer results associated with the size of sample blocks used, and allowing for the considerably lower number of samples analysed by gas pycnometry compared to the number of thin sections examined, vesicle modal abundance data is used as the primary vesicularity parameter in rheology calculations (Chapter 4).

3.5.3 Quantitative Bulk Lava Flow Deposit Vesicularity Analysis

Measured autoclast size, mean vesicle sizes (maximum diameter), and visually estimated outer and inner zone vesicle abundance (%) data for each of the four grid positions at the proximal and frontal flow zone sample sites respectively on the 18th August (F) lava flow deposit are presented in Appendix B.3. The results of statistical analysis of this data are presented in Table 3.3. Autoclast sizes range from 3.5 to 60 cm maximum diameter, with an average of 13.7 cm and 8.7 cm at the proximal and frontal flow zone sites respectively. Clast sizes were measured primarily to provide a more complete data set and this marked difference between the average clast sizes at the two sample sites was not expected. However, the calculated t-test value shows that the difference in average clast size is highly significant ($P = 0.24^{-9}$). The difference in average clast sizes between the two upper grid positions and the two lower grid positions at the frontal flow zone site is also reasonably significant as $P = 0.01$, and suggests that larger clast sizes tend towards the lower sections of the outer flow margins. This is not shown, however at the proximal flow zone site, although the levee height is considerably lower at

Table 3.3 Vesicularity statistics for the two samples sites on the southern margin of the 18th August lava flow deposit. Prox. = Proximal flow zone site (F38); Front. = Frontal flow zone site (F39). Ave. = average; σ = standard deviation. Values are given for each grid sampled, the total for each site and the combined upper and lower grids at each site. P value results of two-tailed t-test analyses, assuming equal variance, are presented in bold type.

	Grid	Clast Size (cm)			Inner Ves. (%)			Outer Ves. (%)			Ves. Size (mm)		
	No.	Ave.	σ	2σ	Ave.	σ	2σ	Ave.	σ	2σ	Ave.	σ	2σ
Prox.	1	15.0	6.2	12.4	11.2	6.2	12.3	36.9	4.1	8.2	2.5	2.2	4.4
	2	14.5	10.6	21.1	10.0	5.3	10.6	36.4	3.7	7.4	2.4	2.5	5.0
	3	10.7	2.9	5.8	10.4	7.6	15.2	37.0	3.9	7.9	3.1	5.3	10.5
	4	14.4	5.8	11.6	9.3	6.8	13.5	36.0	4.4	8.8	2.4	2.8	5.6
Front.	1	9.2	1.9	3.8	15.2	4.2	8.4	37.6	3.6	7.1	2.9	3.3	6.6
	2	9.4	2.0	4.0	14.5	5.0	10.0	36.5	3.8	7.5	3.1	2.6	5.2
	3	8.7	3.0	6.0	11.5	5.0	10.0	36.0	3.2	6.5	3.0	2.4	4.9
	4	7.6	2.1	4.1	13.1	6.8	13.5	36.6	3.5	6.9	2.1	2.6	5.2
Prox.	Total	13.7	7.0	14.1	10.2	6.2	12.5	36.5	3.8	7.6	2.6	3.4	6.8
Front.	Total	8.7	2.3	4.7	13.6	5.4	10.9	36.7	3.5	7.0	2.8	2.7	5.5
T-Test[1]		**0.24^{-9}**			**0.39^{-4}**			**0.68**			**0.65**		
Prox.	3 & 4	12.6	4.9	9.8	9.8	7.1	14.3	36.5	4.2	8.4	3.1	4.2	8.4
	1 & 2	14.8	8.6	17.2	10.6	5.7	11.4	36.6	3.9	7.7	2.4	2.3	4.7
T-Test[2]		**0.12**			**0.47**			**0.63**			**0.61**		
Front.	3 & 4	8.2	2.6	5.2	12.3	5.9	11.9	36.3	3.3	6.6	2.6	2.5	5.0
	1 & 2	9.3	1.9	3.8	14.9	4.6	9.2	37.0	3.7	7.3	3.0	3.0	5.9
T-Test[3]		**0.01**			**0.02**			**0.29**			**0.44**		

[1] Comparison of the mean total vesicularity between the two sample sites;
[2] Comparison of the mean vesicularity of the combined upper (3 & 4) & combined lower (1 & 2) grids at the Proximal flow zone site;
[3] Comparison of the mean vesicularity of the combined upper (3 & 4) & combined lower (1 & 2) grids at the Frontal flow zone site.

this site (~ 3.6 m) compared to the frontal flow zone site (~ 5.5 m).

Inner zone vesicularity of individual autoclasts ranged from 0.5 to 25% throughout the two sample sites. The overall average inner zone vesicularity increases from ~ 10% at the proximal flow zone site to ~ 14% at the frontal flow zone sample site. Although this is a relatively small increase, a P value of 0.39^{-4} indicates that the difference in inner zone vesicularity between the two sample sites is highly significant. There is also a reasonably significant difference (P = 0.02) between the upper and lower grid positions at the frontal zone site, with increased average vesicularity at the lower section of the levee, although this was again not evident at the proximal flow zone site. Outer zone vesicularity is much less variable, ranging from 25 to 40%, with an average vesicularity of 36% and 37% at the proximal and frontal flow zone sites respectively, and a P value of 0.68, showing no significant difference between the two sites.

Maximum vesicle diameters ranged from 0.5 to 25 mm, although diameters greater than 5 mm were relatively rare. Average maximum vesicle diameters at the proximal and frontal flow zone sample sites were 2.6 and 2.8 mm respectively, with a P value of 0.65, showing no significant difference between the two sites. There may be some correlation between vesicle diameter and inner zone vesicle abundance at both sample sites, with a slightly stronger correlation occurring at the proximal flow zone site (Fig. 3.15). While this may hold some significance in terms of vesicle growth and degassing processes, it is also possible that visual estimation of vesicle abundance was heavily influenced by vesicle size.

The high degree of significance in the difference between average inner zone vesicularity at the two sample sites may provide evidence of downflow spatial variations in vesicle abundance related to degassing processes during flow emplacement. However, as the two sample sites were located on outward-facing lateral flow margin levees, the results are not necessarily representative of vesiculation and degassing processes within the moving flow channel; instead they are more likely to represent the effect of cooling lava at the flow margin on vesiculation processes. Analysis of bulk flow vesicularity across multiple transects of the flow deposit at increasing distances from the vent would provide a

more accurate assessment of lateral and downflow spatial variations in vesiculation and degassing processes during lava flow emplacement.

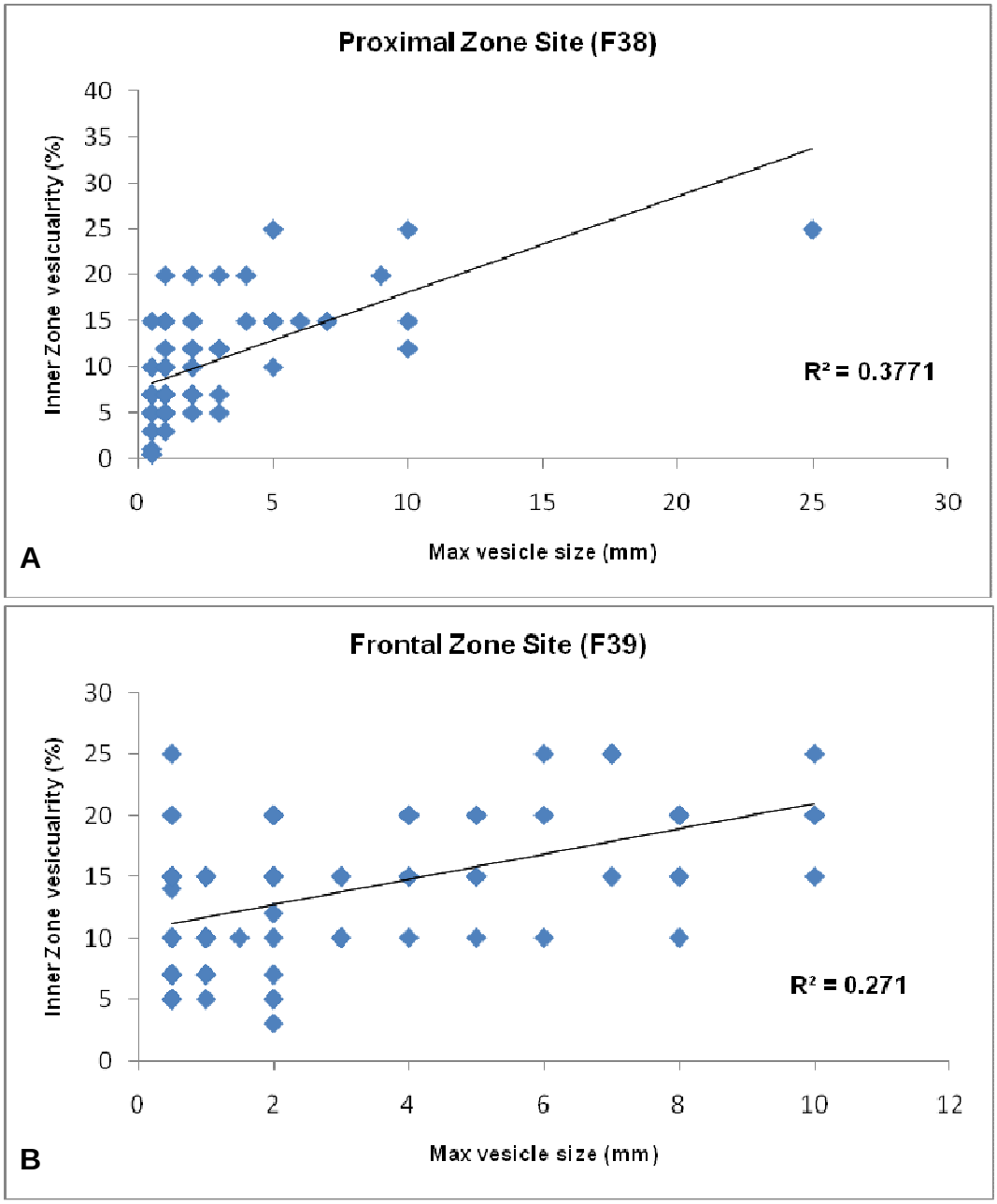

Fig. 3.15 Scatter plot of maximum vesicle diameter (mm) versus inner zone vesicle abundance (%) at A, proximal flow zone sample site, and B, frontal flow zone sample site. Trend line in black with R^2 value shown.

3.6 MAJOR AND MINOR ELEMENT ANALYSIS

3.6.1 Whole Rock Classification

In a plot of K_2O versus SiO_2 (wt. %) (Fig. 3.16), the 1954 lavas are closely grouped within the medium-K range of the calc-alkaline series, after the classification scheme of Rollinson (1993), and are of basaltic andesite composition. This is consistent with the findings of Patterson and Graham (1988), Graham *et al*. (1995), Hobden (1997), and others for TgVC and other TVZ basaltic andesites. The earlier 1949 lava also falls within the basaltic andesite composition range (56.49 wt. % SiO_2) although it lies closer to the basaltic andesite/andesite boundary.

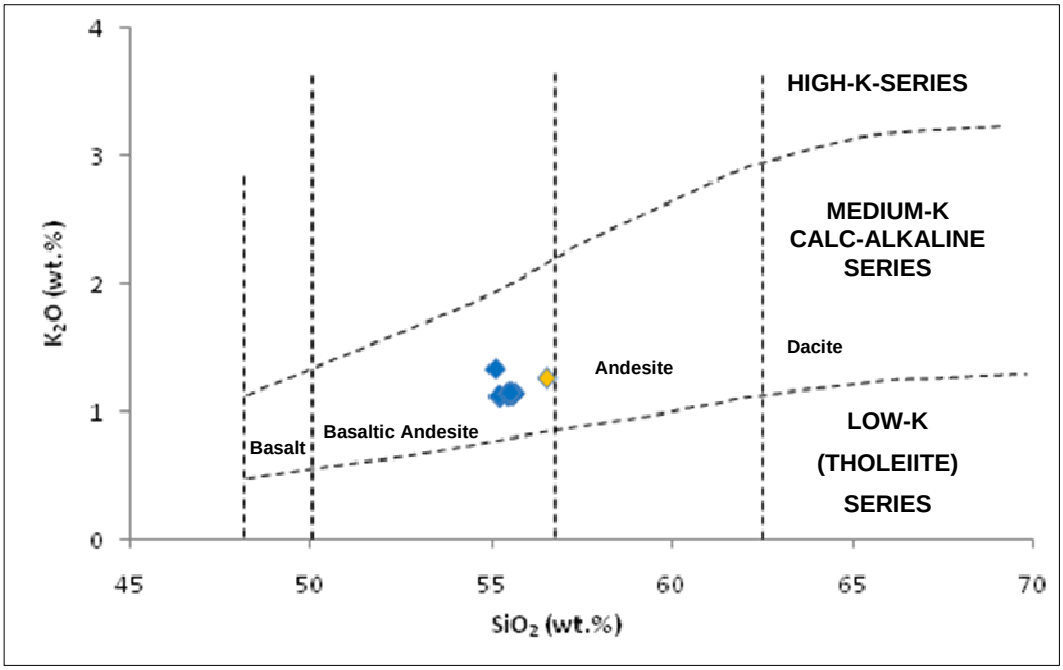

Fig. 3.16 Whole rock classification diagram of SiO_2 vs K_2O (wt. %) showing composition of the 1954 Ngauruhoe lavas (blue symbols) and the 1949 lava (orange symbol). Total alkali versus silica composition boundaries (vertical lines) after Rollinson (1993).

3.6.2 Major Element Composition

Whole rock major element data for selected 1954 Ngauruhoe lavas are presented in Table 3.4, assuming a ± 1% analytical error margin, and are normalised to 100% excluding H_2O content due to the negative volatile content results obtained following oxidation of the samples. Major element composition is consistent with

Table 3.4 Major and trace element data for selected 1954 Ngauruhoe lavas and one known 1949 lava sample (Z1), determined by XRF analysis. Major elements are normalised without H_2O and presented in wt. %, trace elements values are in ppm.

	A1	A2	Bn26	Bn38	Bs3-2	Bs11-1	Bs31	Bs32	Dc6	Dc8-1	Dc8-2	Dc14	E2	F15-1	F21	G1	G2	Z1
SiO_2	55.60	56.66	55.61	55.25	55.50	55.48	55.15	55.64	55.51	55.68	55.28	55.50	55.24	55.54	55.56	55.46	55.54	56.52
TiO_2	0.76	0.77	0.75	0.76	0.75	0.75	0.71	0.76	0.77	0.76	0.76	0.76	0.77	0.75	0.76	0.77	0.76	0.77
Al_2O_3	17.10	17.13	17.19	16.98	16.77	16.92	16.93	16.95	16.84	17.00	17.13	16.86	17.02	16.95	16.85	16.79	16.70	16.97
Fe_2O_3	8.47	8.21	8.46	8.66	8.41	8.50	8.51	8.43	8.48	8.42	8.59	8.67	8.76	8.49	8.55	8.68	8.56	8.35
MnO	0.14	0.14	0.14	0.15	0.14	0.15	0.16	0.14	0.14	0.14	0.15	0.15	0.15	0.14	0.14	0.15	0.15	0.14
MgO	5.18	4.72	5.25	5.51	5.43	5.36	5.45	5.35	5.39	5.33	5.21	5.39	5.38	5.32	5.32	5.32	5.45	4.73
CaO	8.33	7.80	8.33	8.42	8.34	8.46	8.55	8.35	8.44	8.31	8.54	8.39	8.40	8.33	8.35	8.41	8.35	7.77
Na_2O	3.13	3.13	2.99	3.04	3.06	3.11	3.08	3.10	3.15	3.06	3.10	2.98	3.02	3.16	3.17	3.14	3.16	3.12
K_2O	1.12	1.27	1.13	1.11	1.13	1.12	1.34	1.14	1.14	1.15	1.12	1.13	1.13	1.15	1.16	1.15	1.15	1.26
P_2O_5	0.14	0.18	0.14	0.14	0.47	0.15	0.13	0.14	0.15	0.15	0.13	0.19	0.13	0.16	0.13	0.13	0.17	0.37
TOTAL	100.00	100.00	100.00	100.00	100.00	100.00	100.00	100.00	100.00	100.00	100.00	100.00	100.00	100.00	100.00	100.00	100.00	100.00
H_2O	-0.02	0.02	-0.01	-0.03	0.00	-0.02	-0.05	-0.02	-0.05	-0.03	-0.04	-0.05	-0.01	-0.01	0.05	-0.01	-0.03	0.08
S	37	91	47	58	54	42	24	31	57	45	25	43	101	42	56	41	73	237
Cl	375	307	427	353	389	332	362	327	386	366	358	401	407	386	378	327	335	365
V	242	241	238	241	235	238	237	244	236	236	231	245	245	239	245	241	254	234
Cr	91	71	96	105	101	98	99	97	98	100	95	106	102	97	98	103	105	73
Co	69	49	42	41	44	44	41	41	41	49	42	34	57	45	50	47	30	54
Ni	34	23	32	33	33	31	31	29	32	31	28	29	32	28	31	27	32	23
Cu	34	40	42	42	40	38	44	41	41	42	38	39	39	40	40	33	41	38
Zn	87	86	86	88	85	88	87	85	85	88	86	88	88	87	88	86	85	89
Ga	19	17.4	17.5	17.6	18.7	17.8	18.5	19.4	17.8	18.4	18.2	18	17	17.9	18.2	18.4	16.6	18
As	1.4	0.9	1.4	0.6	0.7	0.6	0.4	0.4	0.6	1	0.8	< 0.5	0.5	1.1	0.7	1.3	< 0.5	1.3
Rb	35	42	37	36	36	35	36	38	37	37	36	36	36	37	38	37	37	42
Sr	237	229	238	238	235	235	236	237	237	235	241	239	237	237	234	233	229	228
Y	21	22	21	21	21	20	21	27	21	21	22	22	21	22	21	21	21	22
Zr	94	104	96	96	97	94	97	102	97	99	98	96	96	98	96	97	98	105
Nb	4.4	5	4.9	4.7	5	4.5	4.9	7.1	4.8	5.1	4.7	4.7	4.7	5.1	4.9	5.2	4.8	5.6
Ba	208	243	216	215	218	220.7	221	218	223	222	215	213	210	218	219	222	216.5	253.8
La	9	6.8	8	9.6	8	8.6	10.7	8.1	9.4	9.5	5.5	8.5	9.3	5.3	7.5	8.6	6.3	12.5
Ce	20.8	23	19.8	19.2	21.2	23.6	22.9	19.3	21.1	22.1	20	18.4	22.5	19.8	20.6	24.2	21.4	22.5
Pb	8.7	8.5	7.3	7.6	7.9	6.7	7.9	8.4	7.9	8.1	7.9	6.9	8.1	9.2	8.1	7.6	7.2	9.7
Th	4	3.7	3.9	5.1	4.2	3.6	4.3	14.2	3.5	4.6	5	2.8	3.9	3.9	3	6	4.4	5.9
U	1.2	1.2	2.2	2.4	1.9	1.3	2.5	15.6	2.3	2.7	2.2	2.6	2	2.8	1.8	3.7	1.5	2.8

previous TgVC studies (e.g. Graham *et al*., 1995; Hobden *et al*., 1999; Hobden *et al*., 2002; Krippner, 2009), although generally displays a narrower composition range than those reported for other TgVC lavas. For example, in this study, SiO_2 content of the 1954 lavas (with the exception of one sample) lies within the range 55.15 to 55.64 wt. %, compared to the reported SiO_2 ranges of 52.7 to 66.3 wt. % for TgVC eruptives (Graham *et al*., 1995); 54.2 to 58.6 wt. % for all Ngauruhoe eruptive products (Hobden *et al*., 2002); and 54.88 to 57.37 wt. % for identified 1954-5 Ngauruhoe eruptives deposited in the inner crater (Krippner, 2009). However, Hobden *et al*. (1999) reports SiO_2 contents of 55.59 to 55.94 wt. % for three 1954 lava flows, consistent with and comparable to the narrow range observed in this study. Other major elements also display a consistently narrow range of between 0.01 to 0.5 wt. % difference between minimum and maximum values; however, due to the narrow SiO_2 wt. % range, the trends of decreasing Mg, Fe or Ca with increasing SiO_2 wt. % in TgVC magmas reported by Graham *et al*. (1995) and Hobden (1997) cannot be determined in these lavas (Fig. 3.17). MgO composition range of the 1954 lavas is consistent with the trend reported by Hobden (1997), where olivine-bearing Ngauruhoe lavas are associated with high MgO (> 4 wt. %), and lavas with < 4 wt. % MgO contained little or no olivine crystals.

One 1954 sample (A2) lies outside the narrow major element composition range, displaying higher SiO_2 (56.66 wt. %) and K_2O and lower MgO and CaO wt. % contents, although with the exception of SiO_2, these values remain within the analytical error margin for the 1954 lavas. Sample A2 was collected at the base of the southern margin of the 4th June lava flow deposit and it was unclear whether this part of the flow deposit correlated to the earlier 1949 lava flow or the overlying 4th June 1954 lava flow. However, comparison with the major element composition of the 1949 (Z1) sample analysed in this study (Fig. 3.17) indicates that the A2 sample is more closely geochemically related to the earlier 1949 (Z1) flow than to the 1954 lavas, thus enabling a clear delineation between the flow boundaries of these two flow deposits.

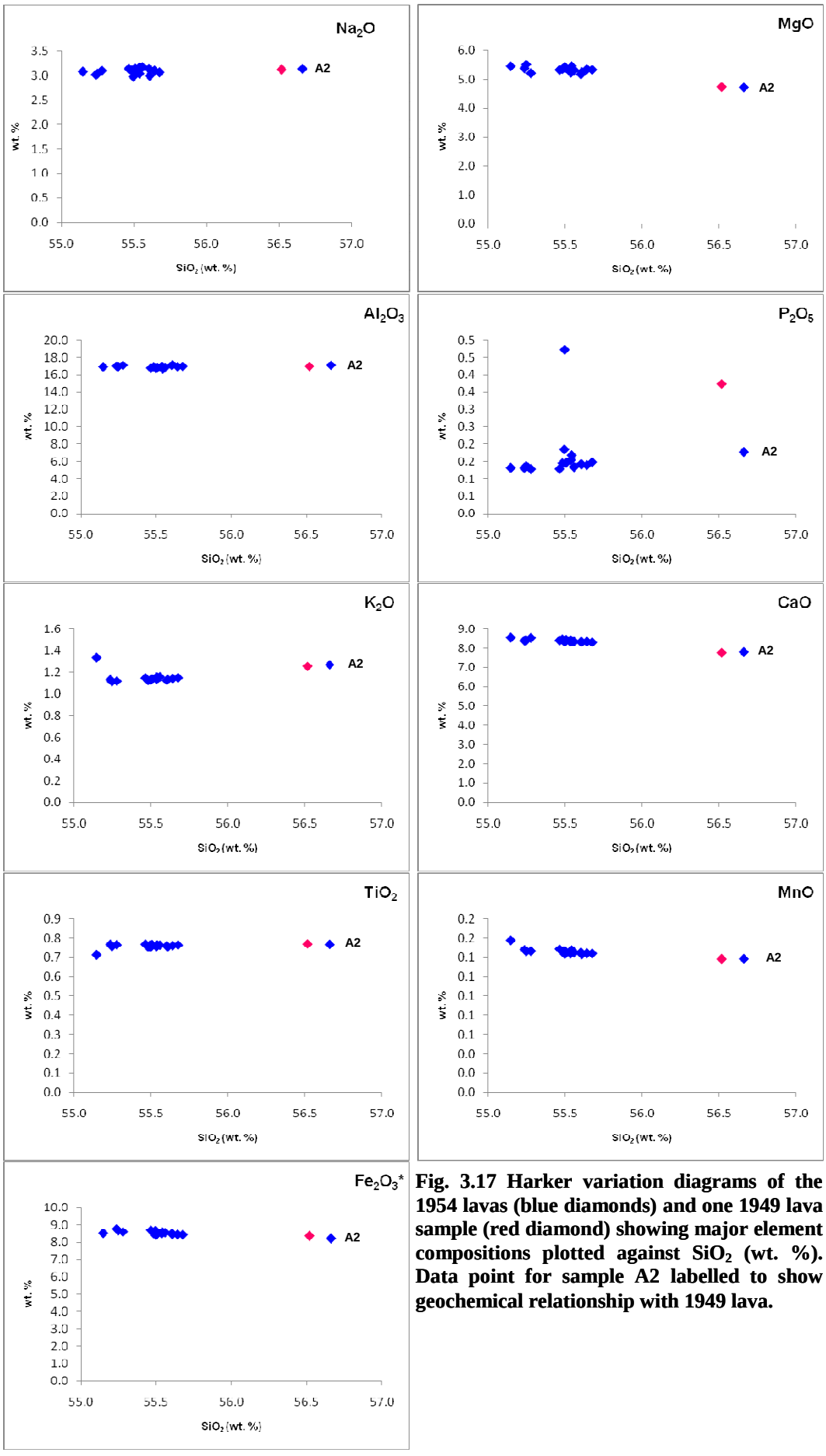

Fig. 3.17 Harker variation diagrams of the 1954 lavas (blue diamonds) and one 1949 lava sample (red diamond) showing major element compositions plotted against SiO_2 (wt. %). Data point for sample A2 labelled to show geochemical relationship with 1949 lava.

3.6.3 Trace Element Composition

Trace element compositions of the known 1954 samples are plotted on a multi-element diagram, normalised against primordial mantle (Fig. 3.18). The 1954 lavas display a trend comparable with subduction zone arc magmas, for example enriched large ion lithophile elements (LILE), particularly Rb, Ba and K, slightly enriched rare earth elements (REE), for example La and Ce, and depleted high field strength elements (HFSE) with a pronounced Nb trough. This trend, including elevated Pb concentrations, is consistent with reported studies on other Tongariro and Ruapehu eruptives (e.g. Patterson and Graham, 1988; Hobden, 1997; Price *et al*., 2005). The peak in U concentration appears relatively more pronounced than the general trend for Tongariro eruptives, although it is consistent with the trend reported by Hobden (1997) for the younger Ngauruhoe eruptives.

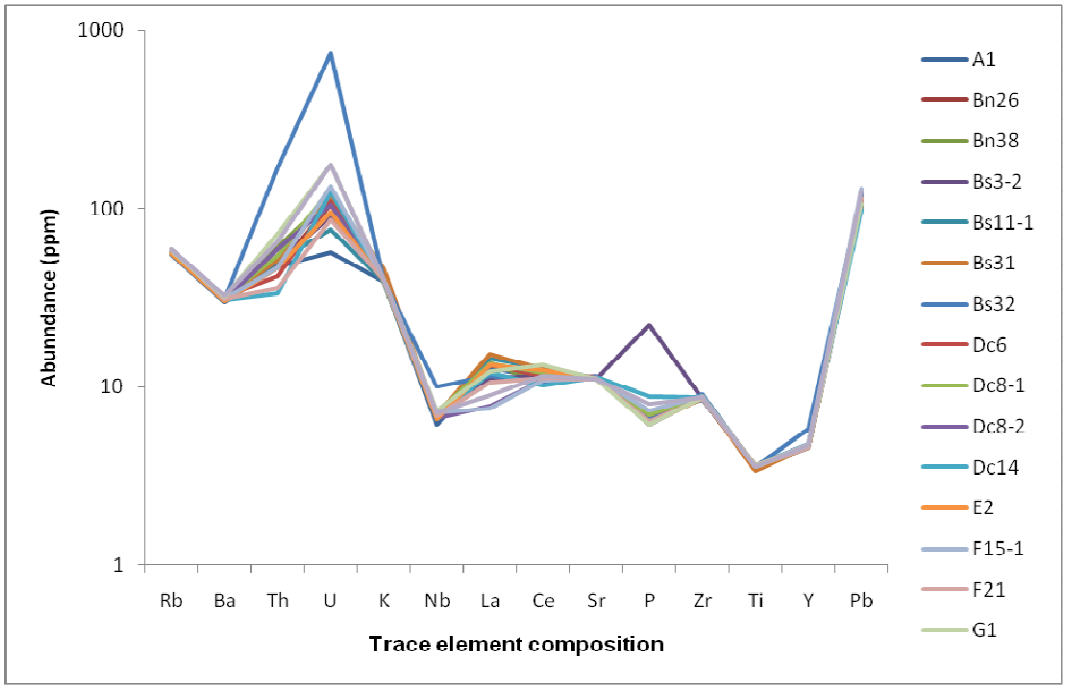

Fig. 3.18 Multi-element diagram for the 1954 Ngauruhoe lavas. Trace elements normalised against the primordial mantle values of McDonough *et al*. (1992).

Harker variation diagrams, plotting SiO_2 (wt. %) against selected trace elements (Ba, Zr, Rb, Ni, Sr, La, Y, V, Cr, and Th), for known 1954 samples are presented in Fig. 3.19. As with major element composition, the range of SiO_2 wt. % compositions is too narrow to detect the general trends reported for TgVC

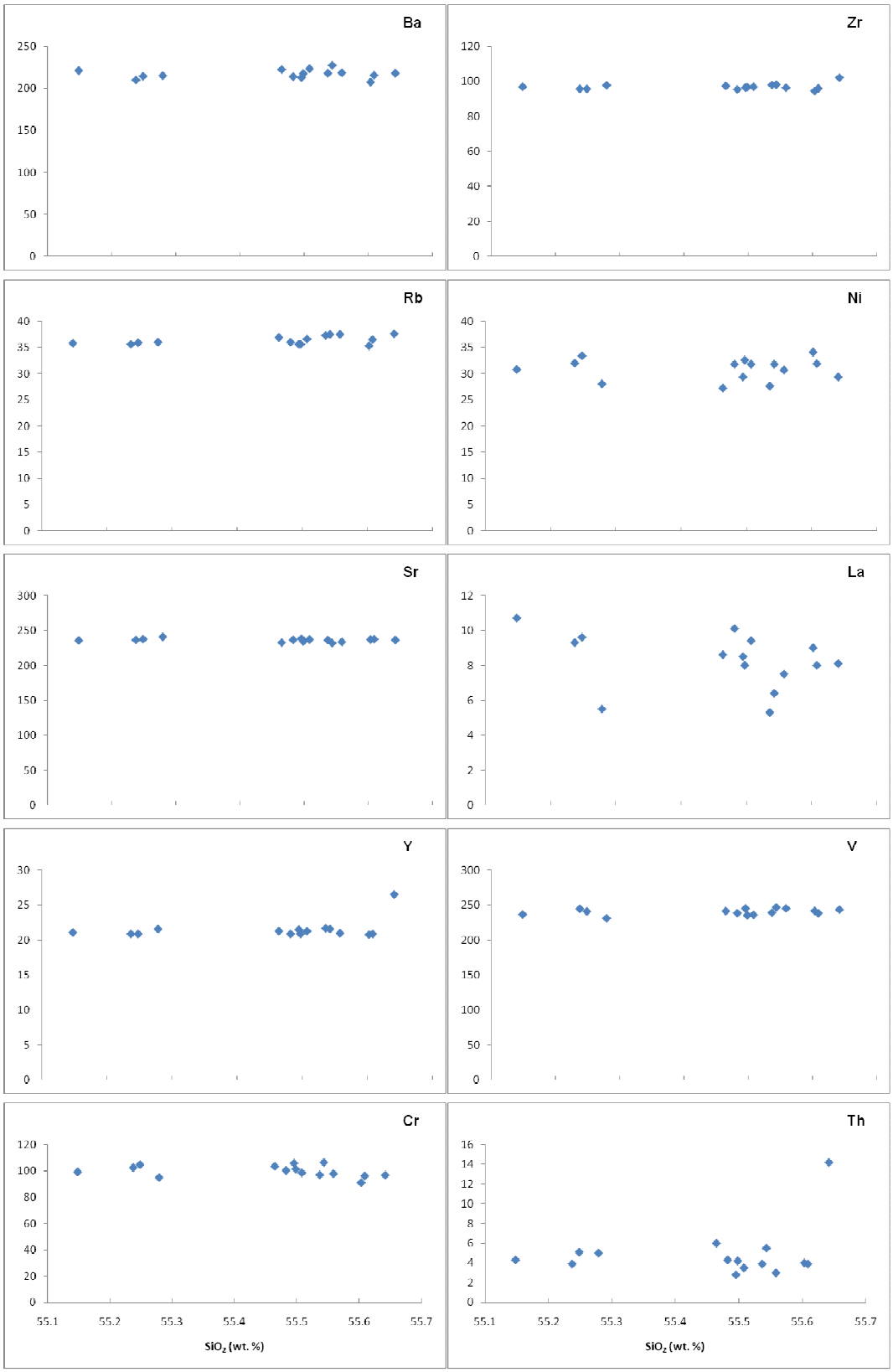

Fig. 3.19 Harker variation diagrams for selected trace element composition (ppm) of the 1954 lavas plotted against SiO_2 wt. % composition.

magmas by Graham *et al*. (1995) and Hobden (1997). Within the narrow SiO_2 wt. % composition range, trace element composition of the 1954 lavas predominantly remains consistent with increasing SiO_2, although some minor variability is evident with Ni and La. A marked increase in Th associated with the highest SiO_2 value is evident (sample Bs32), however this does not correlate to any other significant variation in major or trace element composition for this sample and is therefore assumed to be the result of natural variability of the porphyritic lavas. As with the major elements, there is no trend in trace element composition over the chronological succession of lavas and, with the exception of sample A2 which shows close correlation to the trace element composition of the 1949 lava sample (Z1), none of the known 1954 lavas have a distinguished geochemical signature to enable confident identification of the unknown samples.

There is no apparent chronological trend in either the major or trace element composition of successive lavas and minor differences in composition are considered to be a function of analytical error and the natural variability typical of porphyritic lavas. The 1954 lavas are therefore essentially homogenous and it is not possible to infer distinctly separate geochemical signatures to individual lava flows of the 1954 eruption. Therefore, with the exception of sample A2 as described above, unknown samples cannot be geochemically correlated to known flow deposits.

CHAPTER 4

Rheological Parameters

4.1 INTRODUCTION

Lava flow rheology is primarily controlled by the chemical composition, volatile content, temperature, crystallinity, vesicularity and yield strength of the lava. The aim of this chapter is to quantify the rheological properties of the 1954 lava flows using the morphological, petrographic and geochemical lava flow deposit data collected for this study. Viscosity and yield strength have been calculated using geochemical and petrographic data; velocity, effusion rate, flow emplacement duration and Grätz numbers calculated using geometric and morphological data; and the role of surface crust strength has been determined using a combination of these. This chapter is subdivided into sections relating to each of these rheological properties. Each section contains a description of the models, parameters and assumptions used, and the results of the calculations which are used to quantify the relevant rheological property of the 1954 lavas.

There was no significant difference noted between the petrographic or geochemical signatures of the individual lava flow deposits, therefore the 1954 lavas are treated as a single homogenous lava batch in all rheological calculations. Rheology models involving flow deposit geometry parameters are calculated for six individual lava flow deposits [4th June (A), 30th June (BnL), 14th July (Dc), 29th July (E), 18th August (F), and 16th September (G)] based on the measured and estimated flow deposit dimensions of these lavas given in Table 2.1. For the purposes of these calculations, it is assumed that width and depth remain relatively constant throughout the length of each lava flow deposit, therefore mean width and depth values are used. The relevant equations used to calculate each rheological property are referenced within the chapter by author, year, equation number (where applicable) and page number for the publication in which they

were sourced, and are reproduced with a list of relevant symbols and their descriptions in Appendix C.1.

4.2 LAVA VISCOSITY

4.2.1 Temperature and Major Element Composition

Models and Assumptions

Temperature is a major control on magma viscosity (η), which can change by a factor of 10^{13} as it cools through a temperature interval of 200°C (Pinkerton and Stevenson, 1992). It is also well known that there is a significant difference between the viscosities of geochemically diverse magmas, due in part to the difference in the degree of polymerisation of melts, with different geochemical compositions (Pinkerton and Stevenson, 1992). Three 'geochemical' viscosity models were used to calculate 1954 lava viscosity based on major element composition and temperature. The results of each of these models are compared to determine the most appropriate viscosity value for the 1954 lavas.

The Shaw (1972, equation 3, p.873) viscosity model uses the Arrhenian principle that there is a simple linear relationship between temperature and viscosity, based on the assumption that temperature is the only major control on magma viscosity. However, it is widely accepted that although magma behaves as a Newtonian fluid at superliquidus temperatures, and can therefore be described by the Arrhenius equation (Hui and Zhang, 2007), more recent research has shown that over a wide temperature range silicate melts generally exhibit non-Arrhenian behaviour (e.g. Hess and Dingwell, 1996; Whittington *et al*., 2000; Giordano and Dingwell, 2003).

The Hui and Zhang (2007, equation 11, p.412) viscosity model is intended to represent a wide temperature range (~ 300 to 1700°C), that can be applied as accurately as possible to natural, multicomponent, anhydrous and hydrous silicate melts. This model reproduces the entire viscosity database for a greater range of melt compositions and temperatures, and to a greater accuracy than earlier models, with a 2σ error margin of 0.61 log viscosity; although other, melt-specific

models have reported lower 2σ error margins, for example, the Zhang *et al*. (2003) anhydrous and hydrous rhyolitic melt model has a 2σ uncertainty of 0.36 log viscosity.

Giordano *et al*. (2008, equation 1, p.125) developed a multicomponent viscosity model that is applicable across the entire magmatic composition and temperature spectrum of the known viscosity database, accommodating both Arrhenian and non-Arrhenian temperature dependence behaviour. This model particularly utilises the effects of dissolved volatiles (H_2O and F) on magma viscosity and uses a lower number of model parameters (18) than earlier models. The Giordano *et al*. (2008) viscosity model appears to accommodate both Arrhenian and non-Arrhenian temperature dependent melts equally well, with a 2σ error margin of 0.40 log viscosity. Furthermore, the authors report that their model can be extrapolated for melt compositions and temperatures beyond their calibration database.

Due to the high microlite abundance within the groundmass it was not possible to isolate the glass component of the 1954 lavas for melt-specific major element composition analysis. Therefore whole rock major element compositions from quenched lava samples have been used to calculate viscosity, and these values assumed to be 'melt' viscosity (η_l) values in subsequent viscosity calculations including crystal and bubble content (sections 4.2.2 and 4.2.3). Of the major elements, SiO_2 has the greatest effect on viscosity, therefore the minimum and maximum wt. % SiO_2 values of all the 1954 samples analysed were determined from non-normalised XRF major element data, the individual samples containing these SiO_2 values identified (Table 4.1), and minimum and maximum viscosity values for the 1954 lavas calculated using the major element composition of these specific samples. Non-normalised major element data was used because major element values are normalised as part of the calculation process for each of the geochemical viscosity models.

Volatile content could not be measured for the 1954 lava samples due to oxidisation of the samples during loss on ignition analysis, therefore the

minimum, maximum and average wt. % H_2O values obtained from stratigraphic units B to D of the 1954-55 inner crater eruptive deposits (Krippner, 2009) are assumed to represent the volatile content of the 1954 lavas (Table 4.1). Volatile content for units A (the lower-most 1954-55 deposit) and E (the upper-most 1954-55 deposit) have not been included. The volatile content of unit A is significantly higher (2.56 to 4.75 wt. %) than the other 1954-55 stratigraphic units due to hydrothermal alteration, while unit E was deposited as a result of Vulcanian activity towards the end of the 1954-55 eruptive episode (Krippner, 2009), and therefore not related to the Strombolian activity and lava flow emplacement that occurred during the earlier phase of the eruption. The low volatile content values obtained by Krippner (2009) are consistent with the anhydrous mineral assemblages observed in thin section, particularly the relatively high abundance of plagioclase (~ 65% of the total phenocryst population), which implies an H_2O content < 2 to 5% (Gill, 1981).

The eruption temperature of the 1954 lavas could not be determined with the available data. Hobden (1997) used the two-pyroxene geothermometer method to calculate an eruption temperature range of 1000 to 1100 ± 50°C for each of the

Table 4.1 Whole rock major element composition, volatile content and phenocryst and vesicle abundance values used to determine the viscosity of the 1954 lavas.

	Minimum (%)	Maximum (%)	Average (%)
Phenocryst[1]	11.6	40.5	27.1
Vesicles[1]	0.7	46.0	22.9
H_2O[2]	0.02	0.95	0.40
Major Elements (wt. %)[3]			
SiO_2	54.77	56.51	/
TiO_2	0.76	0.76	/
Al_2O_3	16.97	17.47	/
Fe_2O_3	8.51	8.60	/
FeO	0.00	0.00	/
MnO	0.14	0.15	/
MgO	5.17	5.33	/
CaO	8.46	8.46	/
Na_2O	3.07	3.04	/
K_2O	1.11	1.15	/
P_2O_5	0.13	0.14	/
Sum	99.08	101.62	/

[1] Minimum, maximum and average phenocryst and vesicle abundance values derived from modal abundance data for all 1954 samples (Table 3.1).
[2] H_2O values obtained from 1954-55 Ngauruhoe inner crater deposits (Krippner, 2009).
[3] Major element compositions are not normalised and are based on the 1954 samples containing minimum and maximum wt. % SiO_2 (Dc8-2 and Bn26 respectively).

five identified Ngauruhoe lava groups, therefore 1954 lava viscosity was calculated for eruption temperatures ranging from 950 to 1150°C.

Melt Viscosity

Fig. 4.1 illustrates the effect of temperature, major element composition and water content variation on the calculated melt viscosity (η_l) of the 1954 lavas. As expected, viscosity values markedly increase (by one to three orders of magnitude) with decreasing temperature at all the major element and water compositions calculated, and with each of the three geochemical viscosity models used. There is little difference in viscosity between minimum and maximum wt. % SiO_2 composition (Figs. 4.1a, b, c), with the greatest difference occurring at the lowest temperature (950°C), and smallest difference occurring at 1150°C in each of the models. For example, the Shaw (1972) model calculates ~ 750 Pa s difference between viscosity at minimum and maximum wt. % SiO_2 composition at 950°C, reducing to ~ 30 Pa s difference at 1150°C (Fig. 4.1a). The viscosity values obtained using the Hui and Zhang (2007) model (Fig. 4.1b) show a greater difference (~ 14,900 Pa s) between viscosity at minimum and maximum wt. % SiO_2 compositions at 950°C, decreasing to ~ 130 Pa s difference at 1150°C. The Giordano *et al*. (2008) model produces the least difference between viscosity values of minimum and maximum wt. % SiO_2 composition (Fig. 4.1c), with a difference of ~ 100 Pa s at 950°C, reducing to ~ 1 Pa s at 1150°C. The generally small difference in calculated viscosity values between minimum and maximum wt. % SiO_2 composition is most likely a consequence of the relatively homogenous geochemical composition of the 1954 lavas, in particular, the narrow range of SiO_2 compositions obtained on XRF analysis (i.e. 1.74 wt. % difference between minimum and maximum non-normalised values).

Conversely, small changes in volatile content (i.e. 0.02 to 0.95 wt. % H_2O) appear to have a more significant effect on the calculated viscosity values for the 1954 lavas (Figs. 4.1d, e, f). The Hui and Zhang (2007) (Fig. 4.1e) and Giordano *et al*. (2008) (Fig. 4.1f) models produced a much greater difference in viscosity between minimum and maximum wt. % H_2O at 950°C (~ 1,300,000 Pa s and ~ 15,500 Pa s difference respectively) than the Shaw (1972) model (5,500 Pa s difference)

(Fig. 4.1d). As with major element composition, the difference in viscosity values over the range of H_2O compositions reduces significantly once the temperature increases to ~ 1000 to 1050°C, with minimal difference noted at 1150°C. With both the major element and H_2O composition viscosity values, the greatest decrease in viscosity occurs between 950 and 1000°C, the next largest

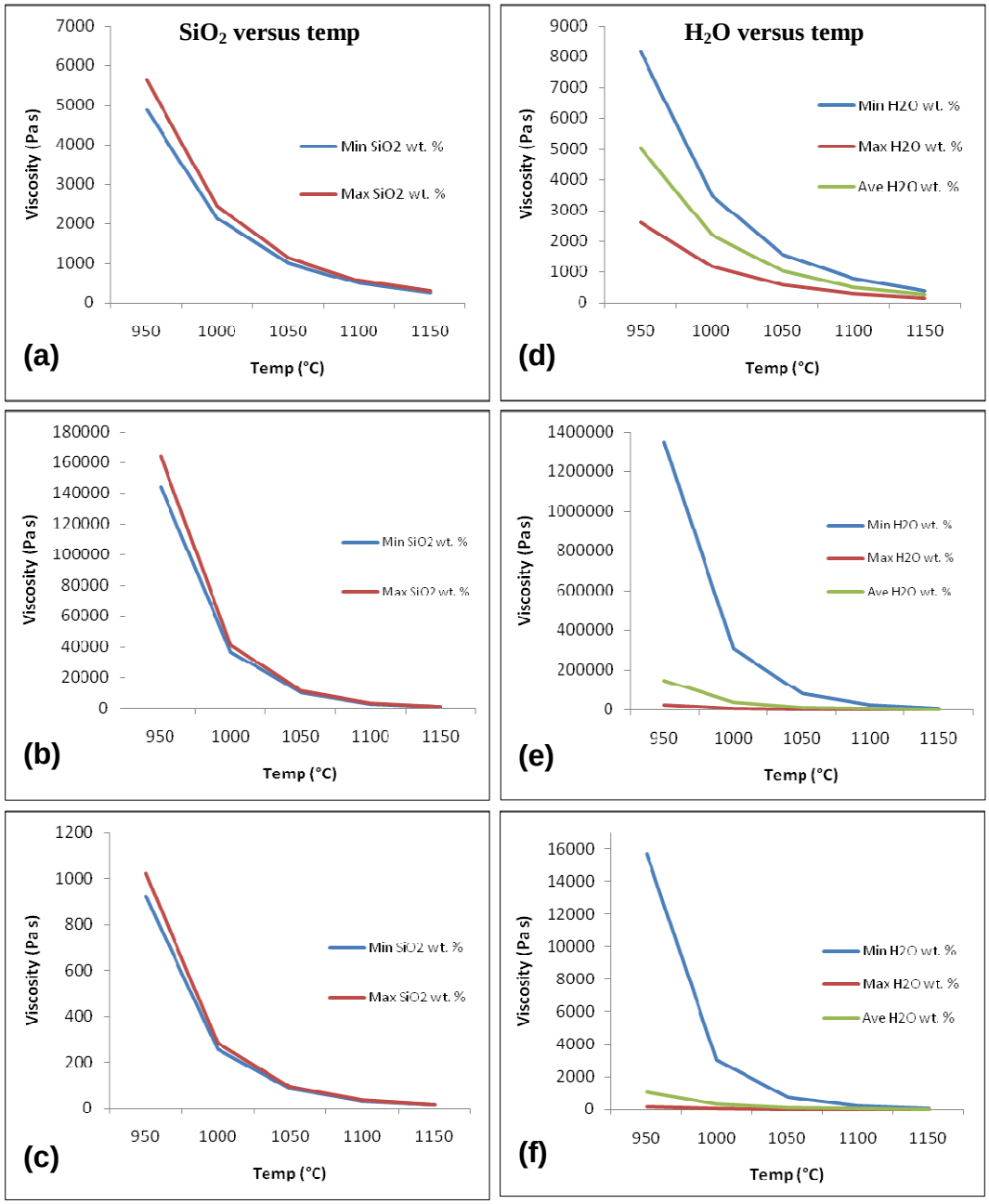

Fig. 4.1 The effect of major oxide composition (a), (b), and (c) and H_2O content (d), (e), and (f) versus temperature on 1954 lava viscosity (Pa s) using three calculation models. (a), (b), and (c) calculated viscosity values for major oxide composition (wt. %) of samples with minimum and maximum SiO_2 (wt. %) content and average H_2O content (0.40%); (d), (e), and (f) calculated viscosity values for minimum, maximum and average H_2O (wt. %) content with maximum SiO_2 composition (wt. %). (a) and (d) calculated using Shaw (1972); (b) and (e), Hui and Zhang (2007); and (c) and (f), Giordano *et al.* (2008).

decrease occurs between 1000 and 1050°C, and minimal reduction in viscosity occurs between 1050 and 1150°C, which may reflect the liquidus-solidus boundary of these lavas.

Table 4.2 compares the viscosity values obtained using the three geochemical viscosity models for minimum and maximum wt. % SiO_2 composition of the 1954 lavas, assuming an average H_2O content (0.40 wt. %), over the temperature range 950 to 1150ºC. There is a marked difference between the viscosity values obtained from each of these models over the temperature range calculated. Viscosity values obtained using the Hui and Zhang (2007) model are considerably greater (by one to three orders of magnitude) than those calculated using the Shaw (1972) and Giordano *et al*. (2008) models, whereas the viscosity values obtained using the Giordano *et al*. (2008) model are lower than those of the Shaw (1972) model by about 1 order of magnitude. The Shaw (1972) model assumes Newtonian behaviour at all temperatures, although it primarily focuses on the viscosity of magma at temperatures of ~ 1200 to 1700°C; however, as previously discussed, lavas are known to display non-Newtonian behaviour at temperatures below their liquidus. The viscosity values derived from the Shaw (1972) model, particularly over the lower temperature range i.e. < 1050°C, are therefore less likely to be representative of the viscosity of non-Newtonian lava.

Conversely, the Giordano *et al*. (2008) model assumes non-Newtonian behaviour at lower temperatures and was therefore expected to give higher viscosity values than those of the Shaw (1972) model; although the viscosity value calculated for maximum wt. % SiO_2 composition at 950°C using the Giordano *et al*. (2008) model (~ 1,000 Pa s) is within the same order of magnitude as reported basalt and basaltic andesite viscosities (e.g. Walker, 1973). The Giordano *et al*. (2008) model takes into account the effect of fluorine (F) on lava viscosity, although the authors note that the model works equally well without including this parameter in their calculations. Fluorine was not included in the calculations for this study because, if it is present, it is present at concentrations below the level of detectability of the XRF spectrometer. The omission of F in the 1954 viscosity calculations does not, however, explain the lower than expected viscosity values obtained using this

Table 4.2 Comparison of viscosity values (Pa s) calculated for the 1954 lavas over a temperature range of 950 to 1150°C using 8 different models. Values are calculated for the major oxide composition of samples with minimum (Min.) and maximum (Max.) wt. % SiO_2 composition and assumes average H_2O content (0.40 wt. %). Melt viscosity (η_l) values are presented in the first six columns, calculated using three geochemical viscosity models (Sh, HZ and Gio). The two 'PS' columns give calculated suspension viscosity (η_s) values for minimum (11%) and average (27%) crystal abundance and are based on the Gio melt viscosity (η_l) values. Columns G-17 and G-19 give calculated differential viscosities for maximum crystal abundance (41%) at low (η_o) and high (η_{inf}) strain rates respectively. The final three 'LM' columns give bubble-suspension viscosity (η_v) values for the melt including crystal and bubble content at average crystal (27%) and vesicle (23%) abundance. Columns LM-7 and LM-9 represent the minimum and maximum possible bubble-suspension viscosity (η_v) values respectively, at average SiO_2 (wt. %), and the final LM column gives an overall average total viscosity value (η_T) for the 1954 lavas.

	Sh		HZ		Gio		PS (11%)		PS (27%)		G-17 (41%)		G-19 (41%)		LM-7	LM-9	LM
	η_l		η_l		η_l		η_s		η_s		η_o		η_{inf}		η_v	η_v	η_T
Temp (°C)	**Min.**	**Max.**	**Min.**	**Max.**	**Min.**	**Max.**	**Min.**	**Max.**	**Min.**	**Max.**	**Min.**	**Max.**	**Min.**	**Max.**	**Min.**	**Max.**	**Ave.**
950	4899	5645	144045	163947	921	1020	1530	1694	4123	4566	2909	3221	16660	18447	6119	15684	10902
1000	2142	2452	36605	41490	258	283	428	470	1153	1267	814	894	4659	5120	1704	4369	3037
1050	997	1134	10361	11702	86	94	143	156	384	419	271	296	1552	1694	566	1450	1008
1100	491	555	3224	3630	33	36	55	59	147	160	104	113	595	646	216	555	385
1150	254	285	1091	1225	14	15	24	25	63	69	45	48	256	277	93	238	166

Sh = Shaw (1972, Equation 3, p. 873)
HZ = Hui and Zhang (2007, Equation 11, p. 412)
Gio = Giordano *et al.* (2008), Equation 1, p. 125)
PS = Pinkerton and Stevenson (1992, Equation 1, p. 49)
G-17 = Gay *et al*. (1969, Equation 17, p.817)
G-19 = Gay *et al*. (1969, Equation 19, p.817)
LM-7 = Llewellin and Manga (2005, Equation 7, p.210)
LM-9 = Llewellin and Manga (2005, Equation 9, p. 210)

model because fluorine is known to increase water solubility and melt diffusivity and to decrease density, thereby reducing lava viscosity (Giordano *et al*., 2004). Furthermore, following the work of Giordano *et al*. (2004), the effect of fluorine is known to be greatly reduced in non-hydrous melts. Therefore, assuming that the F content of the 1954 lavas is considerably less than H_2O content, the omission of F in the viscosity calculations should have no significant affect on the results.

The Hui and Zhang (2007) model (also assuming non-Newtonian behaviour at lower temperatures) produced relatively high viscosity values, particularly at 1150°C (~ 10 to 12 x 10^3 Pa s), given that a viscosity of ~ 1 to 10 Pa s is expected for basaltic lavas at 1150°C (Sparks, 1992). Hui and Zhang (2007) note that due to the large number of parameters involved in their model calculations (Table C.2, Appendix C.1), the fitting parameters themselves are not well constrained for extrapolation beyond the model limitations i.e. binary silicate systems, viscosities above 10^{15} Pa s, temperatures < 573K (~ 300°C), H_2O content > 5 wt.% for melts other than rhyolite, and pressure conditions > 5 kbar. However, the composition of 1954 lavas falls within the constraints of this model, therefore the accuracy of these viscosity calculations should not be affected. The Hui and Zhang (2007) model has a greater 2σ error margin than the Giordano *et al*. (2008) model (0.61 log η compared to 0.41 log η, equivalent to ~ 4 Pa s and 2.6 Pa s respectively), therefore, although the Giordano *et al*. (2008) model produced lower viscosity values than expected, these values have been used in subsequent rheology calculations as the most likely 'melt' viscosity (η_l) values for the 1954 lavas.

4.2.2 Crystal Content

Models and Assumptions

Although the aforementioned geochemistry-based models include the major element composition of whole rock samples, and therefore include the geochemical composition of crystals, they do not take into account the physical effect of crystals as solid particles suspended within the melt on magma viscosity. The importance of particle concentration and the viscosity of the host liquid in controlling the overall viscosity of dilute suspensions is well documented (e.g. Shaw *et al*., 1968; Gay *et al*., 1969; Marsh, 1981; Ryerson *et al*., 1988; Pinkerton

and Stevenson, 1992). This can be described by the Einstein-Roscoe equation (Pinkerton and Stevenson, 1992), which takes into account the relationship between the viscosity of the liquid phase of the melt (η_l), the concentration of crystals (by volume) within the melt (ø) and the maximum concentration that can be attained by the crystals ($ø_{max}$) and still enable the lava to flow. Pinkerton and Stevenson (1992) note that melts with relatively low crystal concentrations (i.e. < 30%) tend to behave as Newtonian fluids because there is minimal contact, and therefore minimal friction, between individual crystals. They conclude that the Einstein-Roscoe equation is currently the most appropriate method for estimating the effect of crystal content on the viscosity of relatively dilute melts (< 30% concentration) where particle shapes are relatively uniform and spheroid. However there is some disagreement regarding the most appropriate maximum crystal concentration ($ø_{max}$) value for this model. Some researchers suggest a $ø_{max}$ value of 0.74 (e.g. Shaw *et al*., 1968), corresponding to 74% crystal concentration, while others suggest a value of 0.6 (60% crystal concentration) as a more appropriate value for magmas (Marsh, 1981; Pinkerton and Stevenson, 1992). The latter value appears to give a closer approximation of viscosity at low crystal concentrations, although it is accepted that a better estimation of the maximum crystal concentration at which lava can flow is needed to improve the method (Pinkerton and Stevenson, 1992).

Several authors (e.g. Gay *et al*., 1969) have shown that suspensions with a high particle concentration develop substantially different viscosities over low and high strain rates. In an analysis of the Gay *et al*. (1969) calculation methods, Pinkerton and Stevenson (1992) conclude that this is a valid method for determining differential viscosity at crystal concentrations between 30 to 50%. Furthermore, when incorporated with the Gay *et al*. (1969) models determining yield strength (section 4.2.4), these models are equally valid for medium to high concentration suspensions containing a range of particle shapes and sizes (Pinkerton and Stevenson, 1992).

The 'melt' viscosity (η_l) values used in these calculations were derived from the Giordano *et al*. (2008) 'geochemical' viscosity model (Table 4.2). Suspension viscosity (η_s) was calculated using the Einstein-Roscoe equation (Pinkerton and

Stevenson, 1992, equation 1, p. 49) for minimum and average phenocryst abundance of the 1954 lavas, derived from modal abundance analysis (Tables 3.1 and 4.1), and assuming a maximum crystal concentration ($ø_{max}$) value of 0.6. Differential viscosity at low (η_o) and high (η_{inf}) strain rates was calculated using the models of Gay *et al*. (1969, equations 17 and 19, p. 817) for the 1954 lavas at maximum crystal abundance (41%). Phenocryst abundance data are based on modal abundance analysis of quenched, whole rock samples; although in these calculations they are assumed to represent crystal abundance at the time of eruption.

Suspension Viscosity

Calculated suspension (η_s) and differential (η_o and η_{inf}) viscosity values for the 1954 lavas at minimum and maximum wt. % SiO_2 composition are presented in Table 4.2. Comparison with the Giordano *et al*. (2008) melt viscosity (η_l) values shows a relatively small increase in viscosity at low crystal abundance (11%) at both minimum and maximum wt. % SiO_2 compositions, although η_s values remain within the same order of magnitude as η_l values. Average crystal abundance (27%) increases viscosity by one order of magnitude at 1100°C to 1000°C, although at 950°C η_s values at minimum and maximum wt. % SiO_2 composition are within the same order of magnitude as η_l at maximum wt. % SiO_2 (~ 10^3 Pa s). Viscosity values at maximum crystal abundance (41%) and high strain rates (η_{inf}) show the greatest difference with melt viscosity (η_l), with values of one order of magnitude higher at 1150°C and 2 orders of magnitude greater at 1050°C, although the difference decreases to one order of magnitude at 950°C. Crystal abundance has a minimal effect on viscosity values at higher temperatures, with η_s remaining < 100 Pa s at 1150°C for both minimum (11%) and average (27%) crystal abundances, increasing by one order of magnitude to 10^2 Pa s at maximum crystal abundance and high strain rates (η_{inf}). At all crystal abundances viscosity values increase by two orders of magnitude between 1150 and 950°C.

Interestingly, viscosity values calculated at maximum crystal abundance (41%) and low strain rates (η_o) are of the same order of magnitude as those of minimum (11%) and average (27%) crystal abundance at each of the temperatures

calculated, except at 1000°C, where viscosity at maximum crystal abundance and low strain rate is one order of magnitude lower than viscosity at average crystal abundance. However, using the Einstein-Roscoe equation to calculate lava viscosity at maximum crystal abundance gives viscosity values in the range of 254 to 18,274 Pa s over minimum and maximum wt %. SiO_2 composition, comparable to those calculated for maximum crystal abundance at high strain rates (η_{inf}). It appears, therefore, that the difference in viscosity at maximum crystal abundance between low and high strain rates is related to the relationship between viscosity and the yield strength of the lava. Blakeney (1966, cited in Pinkerton & Stevenson, 1992) showed that interparticle contact can occur under shear stress conditions in suspensions containing relatively low concentrations (~ 5%) of rod-shaped particles, and that at higher crystal concentrations (e.g. ~ 20%) increased particle contact will require significantly greater stresses to overcome the friction between connecting particles and thus initiate movement. Therefore, at low sheer stress-strain rates deformation of the lava is not sufficient for particles at moderate to high concentrations to come into contact with each other, thus viscosity and yield strength are relatively low compared to conditions where sheer stress-strain rates are greater.

4.2.3 Vesicle Content

Models and Assumptions

Although models incorporating crystal content provide greater constraints on the viscosity of crystalline lavas, they do not take into account the effect of vesicles on lava viscosity. It is well-accepted that the exsolution of volatiles from the melt increases melt viscosity (Manga & Loewenburg, 2001), however the physical effect of bubbles within the melt is not so well understood (Pinkerton and Norton, 1995). Several recent studies (e.g. Bagdassarov and Dingwell, 1992; Stein and Spera, 1992; Pal, 2003) have shown that the physical presence of bubbles has the effect of either increasing or decreasing the viscosity of the suspension. Manga *et al*. (1998) explain this contrasting behaviour by showing that deformed bubbles provide less resistance to the flowing melt than spheroid bubbles, thus total shear viscosity is reduced in melts where deformed bubbles dominate. Llewellin and Manga (2005) developed a method for including bubble-suspension rheology in

magma conduit flow models, which recognises the difference in the viscosity behaviour of melts containing either spheroid or deformed bubbles. Two dynamic viscosity regimes are described in the conduit flow model, which are controlled by the capillary number (C*a*): a dimensionless number which describes the degree of viscous stress (i.e. the stress applied to the external bubble surface by the surrounding magma) relative to the degree of internal stress within the bubble, which enables it to retain or to restore sphericity. In regime 1, C*a* $\ll 1$ represents conditions where internal bubble stresses are greater than external viscous stresses, bubbles remain spherical, and shear viscosity increases with increasing gas volume-fraction; whereas C*a* $\gg 1$ (regime 2) occurs during conditions of high viscous stress relative to internal bubble stress, bubbles deform and become elongate, and shear viscosity decreases with increasing gas volume-fraction (Llewellin and Manga, 2005).

This model is intended to represent magma viscosity and flow processes within a closed conduit system, in which the shear strain-rate of the flowing magma increases along the radial axis from the centre of the conduit to the conduit walls. However, it has been applied to the unconfined 1954 lava flows because, (a) variations in shear strain-rate along the cross-sectional profile of the magma conduit are comparable to vertical and lateral variations in shear strain-rate between the base of a flowing lava and the central core, the central core and the cooling surface of the lava, and the central channel and the cooling lateral margins of the flow (e.g. Dragoni *et al*., 1986), and (b) unlike other models, the Llewellin and Manga (2005) model parameters do not include conduit dimensions, and therefore no relationship is assumed between conduit dimensions (or flow volume) and bubble viscosity, thus the model is more easily adapted to unconfined lava flows.

A capillary number for the 1954 lavas could not be quantified with the available data; however, the majority of vesicles observed on thin section analysis displayed spheroid to ellipsoid morphologies, while elongated, stretched vesicles were rarely observed. Thus the conditions described by the Llewellin and Manga (2005) regime 1 model, i.e. C*a* $\ll 1$, are assumed for bubble viscosity calculations in this study. Calculations for bubble-suspension viscosity (η_v) assume average

vesicle abundance (23%), derived from modal abundance data (Tables 3.1 and 4.1), and the suspension viscosity (η_s) values obtained for average crystal abundance (27%) derived from the Pinkerton and Stevenson (1992) model (Table 4.2). Vesicle modal abundance was derived from quenched lava samples and therefore represents bubble content during the final stages of flow emplacement; however, for this study vesicle abundance is assumed to represent the bubble content of the newly erupted melt.

Llewellin and Manga (2005) present two equations in the regime 1 model that give the likely range of bubble-suspension viscosity (η_v) for any specific vesicle content value. The equations are used to calculate the minimum (equation 7, p.210) and maximum (equation 9, p.210) possible bubble-suspension viscosity (η_v) of the 1954 lava with an average vesicle abundance. Minimum and maximum η_v was therefore calculated at both minimum and maximum wt. % SiO_2 compositions, as with previous viscosity calculations. An average value for minimum η_v was then derived by averaging the η_v values obtained using equation 7 for minimum and maximum wt. % SiO_2 composition at each temperature calculated. The same technique was also used to obtain an average value for maximum η_v (derived from equation 9) between the two wt. % SiO_2 compositions at each temperature calculated. Finally, for the purposes of subsequent rheology calculations, the average of these two end-member bubble-suspension viscosity (η_v) values has been calculated and used as the total viscosity (η_T) of the 1954 lavas at each of the temperatures in the calculated range.

Bubble Viscosity and Total 1954 Lava Viscosity

Average minimum and maximum bubble-suspension viscosity (η_v) values and the total viscosity (η_T) values of the 1954 lavas over the temperature range 950 to 1150°C are presented in Table 4.2. Incorporating the effects of bubble content on lava viscosity results in a further increase in viscosity from suspension viscosity (η_s) values when average crystal abundance (23%) is assumed, although the lowest possible η_v values (column LM-7) remain within the same order of magnitude as η_s values at average crystal abundance and at each temperature calculated. Maximum possible η_v values (column LM-9) are generally ~ half to

one order of magnitude higher than η_s values at average crystal abundance for each temperature. Total viscosity (η_T) values (column LM) for the 1954 lavas fall within the range of 1.66 x 10^2 to 1.09 x 10^4 Pa s over the temperature range 950 to 1150°C. These values assume average wt. % SiO_2 and H_2O composition, average crystal and vesicle abundance, and denote the average value over the range of possible bubble viscosities (η_v). Total viscosity (η_T) values are assumed to represent overall 1954 lava viscosity at the range of temperatures calculated and are used in subsequent rheology calculations.

4.3 YIELD STRENGTH

Models and Assumptions

It is generally accepted that melts composed of crystal concentrations > 30% develop yield strength and thus behave in a non-Newtonian manner (e.g. Shaw, 1969; Krieger, 1972; Chan and Powell, 1984; Marsh, 1987; Reyerson *et al*., 1988). Yield strength develops where a touching framework of crystals exists throughout the suspension as a result of interparticle contact (Kerr and Lister, 1991). It is therefore possible for suspensions of non-spherical particles to develop yield strength at particle concentrations < 30%. Blakeney (1966, cited in Pinkerton and Stevenson, 1992) showed that rod-shaped particles with axial ratios of 10:1 (comparable with slender plagioclase laths) can develop a bridging framework at concentrations as low as 20%, requiring significant stress to initiate flow and thus causing the development of yield strength within the lava. Pinkerton and Stevenson (1992) argue that any method employed to determine the yield strength of lava must therefore incorporate crystal shape and size distribution data. By modifying the models of Gay *et al*. (1969), Pinkerton and Stevenson (1992) developed a method to calculate yield strength for suspensions that include particles with a diverse range of size and shape distributions, over the particle concentration range $0.52<(ø/ø_{max})<0.82$ (i.e. 30 to 50% crystal concentration).

The onset of yield strength at moderate crystal concentrations is strongly supported by field and laboratory yield strength measurements of natural basalts

(e.g. Pinkerton and Norton, 1995; Cashman *et al*., 1999; Hoover *et al*., 2001). Zhou *et al*. (1995) suggest that there is a minimum particle concentration ($ø_c$) at which yield strength develops, which is controlled by the size, shape and orientation distribution of the particles. Based on the models of Zhou *et al*. (1995), Hoover *et al*. (2001) used experimental data to calculate $ø_c$ values of 0.09 to 0.3 (9 to 30% particle concentration) where particle axis ratios are between 1:1 to 10:1, confirming the influence of crystal shape on yield strength. In comparing their results with other research (e.g. Pinkerton and Norton, 1995; Cashman *et al*., 1999; Saar *et al*., 2001), Hoover *et al*. (2001) conclude that a finite yield strength may develop in basaltic lavas with crystal concentrations of ~ 15 to 40%.

Many researchers have used the dimensions, morphology, and in some cases the slope angle of the underlying topography of lava flow deposits to infer rheological properties, including yield strength, of lava. A model developed by Johnson (1970) to determine the flow behaviour of Bingham fluid within a semi-circular channel was modified by Hulme (1974) to apply to flowing lavas. Hulme (1974) attributes the formation of lateral levees and central flow channels to the internal yield strength of the lava by theorising that yield strength controls the extent of lateral spread and thinning of the flow, and therefore the depth of the flow margin is determined by the minimum depth permitted by the yield strength of the lava. The yield strength of the flow can thus be determined as a function of mean flow deposit depth and underlying slope angle. Orowan (1949, cited in Moore *et al*., 1992) devised a similar model based on mean flow width and depth that does not include the gradient of the underlying slope, which has been used extensively in situations where slope angle is unknown, for example extra-terrestrial lavas. Comparisons of yield strength values derived using the Hulme (1974) and Orowan (1949) models (e.g. Moore *et al*., 1992: Stevenson *et al*., 1994a) show that the two models produce reasonably similar values.

The yield strength (τ_y) of the 1954 lavas was calculated using three models: the petrography-based Pinkerton and Stevenson (1992, equation 3, p.53) model incorporating crystal abundance, size and habit, and the two morphology-based models (Hulme, 1974 and Orowan, 1949, cited in Moore *et al*., 1992, equation 1,

p.13,488) based on the dimensions of the lava flow deposits. The Pinkerton and Stevenson (1992) model calculates yield strength as a function of crystal abundance, size and habit, the bulk density of the lava, and gravitational acceleration. Although this model is intended for lavas with crystal abundance > 30%, yield strength has been calculated for minimum, average and maximum crystal abundance values of the 1954 lavas, following the conclusions of Hoover *et al*. (2001). The minimum, average and maximum bulk density (ρ) values used in these calculations are derived from the bulk density of powdered whole rock samples (dense rock equivalent), quantified during gas pycnometry analyses of the 1954 lavas (Appendix B.2), and therefore assumes a bubble-free melt. Mean particle diameter (D_p) was determined using the long axis dimensions of 300 randomly selected crystals in thin section. The thin section containing the greatest crystal abundance was selected for each of the six lava flows sampled and fifty intact (or mostly intact) tabular plagioclase and prismatic orthopyroxene crystals were measured along cross-sectional transects of each thin section. Rounded, fragmented, very large (> 1 mm) and very small (< 0.1 mm) crystals were not measured. The shape factor (ξ) is defined as the "ratio of the surface area of a sphere of equivalent volume to the surface area of the particle" (Pinkerton and Stevenson, 1992, p.53). Particle surface area was calculated using the long- and short-axis dimensions of the same crystals used to measure mean particle diameter. Volume was calculated by assuming prismatic crystal habit and therefore that the short axis (width) measurement is equivalent to depth. The geometric standard (σ_{sd}) was derived from a plot of particle diameter versus cumulative proportion (p) of particles where σ_{sd} equals p<50% size/p<15.87% size. Values for each of these parameters are given in Table 4.3 and raw data for the calculation of these values in Appendix C.2.

The morphology-based models determine yield strength as a function of average bulk density (ρ), gravitational acceleration (g), mean flow deposit depth and either (a) underlying slope angle (Hulme, 1974), or (b) mean flow deposit width (Orowan, 1949). Yield strength was calculated for mean flow depths of 2.5, 3 and 3.5 m, and a range of average underlying slope angles and mean flow widths common to the 1954 lava flow deposits (Table 2.1). As previously stated, the use

of mean flow dimension values in these calculations is based on the assumption that flow deposit width and depth remain constant throughout the length of the flow.

Table 4.3 Parameter values used to calculate yield strength using the Pinkerton and Stevenson (1992) models.

Symbol	Definition		Value(s)
R	Inverse of maximum solid concentration		1.67
$ø_{max}$	Maximum concentration that can be attained by crystals in the melt (volume-fraction)		0.6
ø	Crystal abundance (volume-fraction)[1]	Min	0.11
		Ave	0.27
		Max	0.41
ρ	Bulk lava density (DRE) (g cm^{-3})[2]	Min	2.85
		Ave	2.88
		Max	2.91
g	Gravitational acceleration (m s^{-2})		9.80
D_p	Mean particle diameter (μm)[3]	Min	125
		Ave	359
		Max	1000
ξ	Shape factor[4]	Min	0.64
		Ave	0.75
		Max	0.80
$σ_{sd}$	Geometric standard deviation[5]		3.04

[1] Minimum, average and maximum crystal abundance derived from modal analysis (Table 3.1 and 4.1).
[2] Bulk density is derived from pycnometer analysis of powered whole rock samples and therefore assumes a bubble-free melt (Appendix B.2).
[3] Mean particle diameter (D_p) is derived from long axis measurements of 300 crystals in thin section (Appendix C.2).
[4] Crystal habit is quantified by the shape factor (ξ), the ratio of the surface area of an equivalent volume sphere to the surface area of the crystal, derived from dimension of 300 crystals in thin section (Appendix C.2).
[5] Geometric standard is derived from a plot of particle diameter versus cumulative proportion (p) of particles calculated by p<50% size/p<15.87% size (Appendix C.2).

Yield Strength

Yield strength values for the 1954 lavas calculated using the petrography-based Pinkerton and Stevenson (1992) model are presented in Table 4.4. Yield strength ranges between ~3 to 72 Pa over the range of crystal abundance, bulk density, mean particle diameter and shape factor values calculated. As expected, maximum crystal abundance gives the highest yield strength values over each of the parameters calculated. The difference between minimum and maximum bulk density values of the 1954 lavas is minimal (0.06 g cm^{-3}), therefore no significant difference (~ 0.1 to 1.5 Pa difference) was apparent in the calculated yield strength values over the range of bulk densities. Mean particle diameter has the greatest effect on yield strength values, with ~ 65% difference between yield strength values at minimum and average, and average and maximum D_p. Yield

strength is ~ one order of magnitude greater at maximum D_p than at minimum D_p, at each crystal abundance value calculated, and at average D_p with minimum crystal abundance. Crystal habit also has a reasonably significant effect on yield strength, with a 28% reduction in yield strength between minimum and maximum ξ values.

Table 4.4 Yield strength (τ_y) (Pa) of the 1954 lavas as a function of crystal abundance, size (D_p) and habit (ξ) using the models of Pinkerton and Stevenson (1992).

Crystal Abundance	Bulk Density	Min D_p[1] τ_y (Pa)	Ave D_p[1] τ_y (Pa)	Max D_p[1] τ_y (Pa)	Min ξ[2] τ_y (Pa)	Max ξ[2] τ_y (Pa)
11%	Min	3.40	9.79	27.24	12.29	8.80
	Ave	3.43	9.87	27.46	12.40	8.87
	Max	3.47	9.98	27.78	12.54	8.97
27%	Min	5.06	14.53	40.44	18.26	13.06
	Ave	5.10	14.65	40.78	18.41	13.17
	Max	5.16	14.82	41.26	18.62	13.32
41%	Min	8.78	25.24	70.25	31.71	22.69
	Ave	8.85	25.45	70.82	31.97	22.87
	Max	8.96	25.75	71.65	32.34	23.14

[1] Yield strength at minimum, average and maximum D_p calculated at average ξ.
[2] Yield strength at minimum and maximum ξ, calculated at average D_p.

Although the Pinkerton and Stevenson (1992) model is intended for crystal abundances > 30% and Hoover *et al*. (2001) showed that yield strength develops at crystal concentrations ~ 15%, a crystal abundance of 11% in this study does display a small degree of yield strength (~ 10 Pa) at average mean diameter (D_p) and shape factor (ξ) values. This may be due to the relatively large average mean particle diameter size (359 µm) measured for the 1954 lavas, compared to those used by Pinkerton and Stevenson (1992) for Mount St Helens dacite (e.g. 50 and 183 µm). For example, calculating yield strength at minimum crystal abundance (11%) and a mean particle diameter size of 183 µm reduces the yield strength to ~ 5 Pa, and at a mean particle diameter of 50 µm, to ~ 1.4 Pa. Although the mean particle diameter size used in the 1954 calculations (359 µm) is based on the measured dimensions of only 300 crystals, it is consistent with the size range observed on thin section analysis of all the 1954 samples for plagioclase and

orthopyroxene phenocrysts (100 to 900 µm, and 100 to 600 µm respectively). Furthermore, mean particle diameter may have been underestimated because the relatively abundant larger megacrysts and xenoliths observed in thin section were not included in the measurements.

The yield strength values calculated using the petrography-based Pinkerton and Stevenson (1992) model are ~ 10^4 to 10^2 times lower than those calculated using the morphology-based models (Table 4.5), which generate yield strength values in the range of ~ 1,700 to 66,000 Pa. The Hulme (1974) model, incorporating underlying slope angle, generally gives a range of yield strength values ~ one order of magnitude higher than the Orowan (1949) model incorporating mean flow widths, with the exception of the lowest mean flow deposit width (20 m) which has calculated yield strength values of the same order of magnitude as the Hulme (1974) model values at the two greater mean flow depths (3 and 3.5 m). This is inconsistent with the findings of Moore *et al*. (1992) and Stevenson *et al*. (1994a), who found that both models gave yield strength values within the same order of magnitude.

Table 4.5 Yield strength (τ_y) values (Pa) calculated for the 1954 lavas based on a range of flow deposit dimensions and underlying slope angles using two morphology-based models.

	Underlying slope angle (°)[2]					Mean flow deposit width (m)[3]				
	9	19	28	37	42	20	40	60	80	100
H (m)[1]	τ_y (Pa)	τ_y (Pa)	τ_y (Pa)	τ_y (Pa)	τ_y (Pa)	τ_y (Pa)	τ_y (Pa)	τ_y (Pa)	τ_y (Pa)	τ_y (Pa)
2.5	11,034	22,964	33,114	42,449	47,197	8,817	4,408	2,939	2,204	1,763
3	13,241	27,556	39,737	50,938	56,636	12,696	6,348	4,232	3,174	2,539
3.5	15,448	32,149	46,359	59,428	66,075	17,281	8,640	5,760	4,320	3,456

[1] Mean flow deposit depth.
[2] Yield strength calculated as a function of density, gravitational acceleration, mean flow depth and underlying slope angle using the Hulme (1974) model.
[3] Yield strength calculated as a function of density, gravitational acceleration, mean flow depth and mean flow width using the Orowan (1949, cited in Moore *et al*., 1992) model.

Differences in underlying slope angle and mean flow depth have a marked affect on calculated yield strength using the Hulme (1974) model, although they remain within the same order of magnitude. For example, yield strength increases by 52% between 9 and 19° slope angles, and by 22% between 28 and 37° slope angles, with an overall increase of 77% between 9° and 42°. At each slope angle calculated, yield strength increases by 17% between 2.5 to 3 m mean flow depth,

and 14% between 3 and 3.5 m mean flow depth. Yield strength values calculated as a function of mean flow width and depth based on the Orowan (1949) model also vary, with yield strength values decreasing with increasing mean flow width. The greatest decrease in yield strength (50%) occurs between 20 and 40 m mean flow width, with a 20% reduction in yield strength between 80 and 100 m. A difference of 0.5 m mean flow depth has a greater effect on yield strength calculated using this model than that using the Hulme (1974) model, with a 31% increase in yield strength between 2.5 and 3 m flow depth, and a 27% increase in yield strength between 3 and 3.5 m mean flow depth.

Given the range of results derived using the petrography- and morphology-based calculation methods it is difficult to quantify the yield strength of the 1954 lavas. The yield strength values obtained using the petrography-based method (Pinkerton and Stevenson, 1992) are comparable to those obtained by Pinkerton and Stevenson (1992) for a Mt St Helen's dacite with similar crystal characteristics and abundance to the 1954 lavas. Similarly, Pinkerton and Norton (1995) measured yield strength values ranging between 0 to 78 Pa for a 1983 Mt Etna lava, using a rotating viscometer at a temperature range of 1090 to 1125°C. Pinkerton and Sparks (1978), however, measured *in situ* yield strengths in the range of 400 to 6,000 Pa for 1975 Mt Etna basalts. Stevenson *et al*. (1994a) calculated yield strength values in the range of ~ 160,000 to 300,000 Pa for two Okataina Volcanic Centre rhyolite lava flows, based on the Hulme (1974) and Orowan (1949) morphology-based models, while Moore *et al*. (1992) used the same models to calculate yield strength values of ~ 280,000 to 330,000 Pa for two unspecified rhyolite lava flows. These results are comparable to the estimated internal yield strengths (~ 30,000 to 500,000 Pa) derived by Fink and Griffiths (1998) for several identified rhyolite lava domes based on their morphological characteristics.

Based on these reported values, it is reasonable to suggest that a yield strength of ~ 10^4 to 10^5 Pa is representative of rhyolitic lavas, and consequently a yield strength ~ one to two orders of magnitude lower (i.e. ~ 10^2 to 10^3 Pa) can be inferred for basaltic andesite lavas. Thus, the high yield strength values (~ 1.1 to 6.6 x 10^4 Pa) derived using the Hulme (1974) model appear to be inconsistent with

the implied yield strength of basaltic andesite lavas. In a comparison with laboratory-measured yield strengths, Sparks *et al*. (1975) found that the Hulme (1974) method significantly overestimated yield strength, particularly in cases where flow width and depth vary over the length of the flow deposit due to changes in underlying slope and topography. It can therefore also be argued that downflow variations in flow deposit dimensions may have a similar effect on the accuracy of the Orowan (1949) model. Given that mean flow deposit dimensions were used in these calculations, thereby assuming constant width and depth throughout the length of the flow deposit, it appears that these morphology-based models may not be a reliable method for determining the yield strength of the 1954 lavas.

The low yield strength values obtained for the 1954 lavas using the Pinkerton and Stevenson (1992) model appear to be closer to the expected range of yield strengths for basaltic andesite lavas. Subsequent rheology calculations therefore assume the maximum yield strength (~ 25 Pa) calculated for the 1954 lavas based on maximum crystal abundance, and average mean particle diameter (D_p) and shape factor (ξ) values, although comparisons are made with yield strengths of one and two orders of magnitude greater where appropriate to ascertain the effect of greater yield strength on the results of these models.

4.4 FLOW VELOCITY, EFFUSION RATE AND DURATION

4.4.1 Lava Flow Velocity

Models and Assumptions

As with yield strength estimates, lava flow deposit dimensions have been used extensively to estimate conditions of flow emplacement, including flow velocity, effusion rate and flow emplacement duration. The Jeffreys equation (Jeffreys, 1925, cited in Kilburn and Lopes, 1991) is commonly used to determine mean lava flow velocity (e.g. Booth and Self, 1973; Moore, 1987; Kilburn and Lopes, 1991), although it is often unclear whether these estimates refer to velocity at the flow front or within the central channel. Borgia *et al*. (1983) describe the flow front as the most active zone of the flow because it is the conditions at the flow

front that influence the construction of marginal levees, the formation of debris, morphological changes in the flow deposit, and the direction of the flow path. Following the work of Borgia *et al*. (1983), Kilburn and Lopes (1991) propose that the downflow reduction in flow velocity observed in the channel zone of some basaltic lavas is due to conditions at the flow front, and that these conditions therefore determine the mean rate of flow advance. Based on this hypothesis, Kilburn and Lopes (1991) determine that the Jeffreys equation can be used to calculate a general estimate of the mean daily flow front velocity. However, Kilburn and Lopes (1991) note that this method does not take into account long time-scale deviations in steady-state flow front velocity that can occur at both the early and final stages of flow emplacement. Kilburn and Lopes (1991) developed a method correcting for potential velocity fluctuations, which takes into account the difference in time and length of flow emplacement during steady rates of flow advance and the final length and emplacement time of the flow. However, well-constrained emplacement duration data are required to use this method, which limits its use as a method for forecasting flow behaviour. Therefore, where flow emplacement data is not well-constrained the Jeffreys equation appears to be the best method for determining mean rates of flow front velocity.

Mean lava flow velocity (V_e) of the 1954 lavas was calculated using the Jeffreys equation (Kilburn and Lopes, 1991, Equation 3, p.19,724), in which flow velocity is a function of bulk density, gravitational acceleration, underlying slope angle, viscosity and mean flow depth. The equation is intended to represent mean flow front velocity and is based on the assumption that velocity at the flow front remains at a constant steady state throughout the duration of flow emplacement, and that short-term fluctuations in effusion rate at the vent do not affect velocity conditions at the flow front. Laminar flow, constant vertical and lateral velocity throughout the flow, and Newtonian behaviour of lava within the hot interior of the frontal flow zone are also assumed (Kilburn and Lopes, 1991).

Velocity calculations are based on average bulk density (ρ) (Table 4.3), total viscosity (η_T) over the temperature range 950 to 1150°C (Table 4.2), mean flow depths of 2.5 and 3 m and a range of underlying slope angles applicable to the 1954 lavas (Table 2.1). The constant *b* (see Appendix C.1) is given a value of 3

for these calculations because the flow deposit widths of the 1954 lavas are much greater than their depths (after Kilburn and Lopes, 1991).

Mean Flow Velocity

Calculated mean lava flow velocity values (V_e m s^{-1}) for the 1954 lavas are presented in Table 4.6. Mean flow velocity ranges from 0.02 to 6.8 m s^{-1} (73 to 24,500 m h^{-1}) at 3 m flow depth and 0.01 to 4.7 m s^{-1} (51 to 17,000 m h^{-1}) at 2.5 m depth. Lava flow velocity is strongly dependent on temperature, with a 99% decrease in velocity from 1150 to 950°C at both mean flow depth values and at each of the underlying slope angles. Flow depth has a less marked effect on velocity, although still relatively significant, at ~ 30% reduction in velocity with 0.5 m reduced flow depth. Underlying slope angle has a significant effect on velocity with an approximate 80% decrease in velocity between calculated values for 53° and 9° slope angles. However, the effect of underlying slope angle on velocity is greater on gentler slopes than on steep slopes; for example, velocity decreases by ~ 50% between 19° and 9° slope angles, whereas between 53° and 42° slope angles the decrease in velocity is 16%.

The calculated mean flow velocity values for the 1954 lavas are considerably higher than flow front velocities reported by Naranjo *et al.* (1992) during the first two days of emplacement duration of the 1988-1990 andesite lava on Lonquimay volcano, which are in the range of ~ 0.02 to 0.007 m s^{-1} (~ 25 to 65 m h^{-1}). Conversely, Lipman and Banks (1987) reported mean flow velocities of 15 to 5.2 m s^{-1} over the first ~ 3 km distance from the vent for the basaltic 1984 Mauna Loa lava flows, markedly higher than the calculated flow velocity values for the 1954 lavas, although flow temperatures for the Mauna Loa lavas are in the range of 1,070 to 1,140°C. The calculated flow velocity of the 1954 lavas at 950°C appears to be reasonably comparable with measured flow velocities of the 1975 Mount Etna lavas, with a range of 0.005 to 0.15 m s^{-1} (Pinkerton and Sparks, 1976). Additionally, calculated flow velocity at temperatures > 950°C, would result in a flow emplacement duration of ~ 4 minutes to 1½ hours for the longest of the 1954 lava flows (30th June) when compared with measured flow length. Given the disparity of calculated flow velocity with measured final flow length it

Table 4.6 Mean flow velocity values[1] (V_e) (m s^{-1} and m h^{-1}) calculated for the 1954 lavas over the temperature range 950-1150°C at mean flow deposit depths of 3 m and 2.5 m and for a range of underlying slope angles associated with the 1954 lava flow deposits.

		Mean Flow Depth = 3 m								Mean Flow Depth = 2.5 m							
Slope angle[2]		**9°**	**14°**	**19°**	**28°**	**37°**	**39°**	**42°**	**53°**	**9°**	**14°**	**19°**	**28°**	**37°**	**39°**	**42°**	**53°**
Temp (℃)	**η_T (Pa S)**	**Velocity (V_e)** (m s^{-1}) and ***(m h^{-1})***								**Velocity (V_e)** (m s^{-1}) and ***(m h^{-1})***							
950	10902	0.02	0.03	0.04	0.06	0.08	0.08	0.09	0.10	0.01	0.02	0.03	0.04	0.05	0.06	0.06	0.07
		73	***113***	***152***	***219***	***280***	***293***	***312***	***372***	***51***	***78***	***105***	***152***	***195***	***204***	***216***	***258***
1000	3037	0.07	0.11	0.15	0.22	0.28	0.29	0.31	0.37	0.05	0.08	0.11	0.15	0.19	0.20	0.22	0.26
		262	***405***	***544***	***785***	***1,006***	***1,052***	***1,119***	***1,336***	***182***	***281***	***378***	***545***	***699***	***731***	***777***	***927***
1050	1008	0.22	0.34	0.46	0.66	0.84	0.88	0.94	1.12	0.15	0.24	0.32	0.46	0.58	0.61	0.65	0.78
		788	***1,219***	***1,640***	***2,365***	***3,032***	***3,171***	***3,371***	***4,024***	***547***	***846***	***1,139***	***1,642***	***2,106***	***2,202***	***2,341***	***2,794***
1100	385	0.57	0.89	1.19	1.72	2.20	2.30	2.45	2.92	0.40	0.61	0.83	1.19	1.53	1.60	1.70	2.03
		2,061	***3,187***	***4,289***	***6,185***	***7,928***	***8,291***	***8,815***	***10,521***	***1,431***	***2,213***	***2,978***	***4,295***	***5,506***	***5,757***	***6,122***	***7,306***
1150	166	1.33	2.06	2.77	4.00	5.13	5.36	5.70	6.81	0.93	1.43	1.93	2.78	3.56	3.72	3.96	4.73
		4,799	***7,421***	***9,987***	***14,402***	***18,461***	***19,305***	***20,526***	***24,499***	***3,333***	***5,154***	***6,936***	***10,001***	***12,820***	***13,406***	***14,254***	***17,013***

[1] Velocity calculated using the Jeffreys equation (Kilburn and Lopes,1991) and is based on average density (ρ), and the total viscosity values (η_T) obtained from the Llewellin and Manga (2005) model (Table 4.2).

[2] Range of slope angles based on minimum underlying slope angles of the 18th August (F), 30th June (Bn), and 29th July (E) lavas (9°, 14°, 28°); average underlying slope angles for the six lava flow deposits visited in the field [4th June (A), 30th June (B), 14th July (Dc), 29th July (E), 18th August (F), 16th September (G)] (Table 2.1), and average underlying slope angle for the top 200 m section of the cone (53°) (Appendix A.2).

is unlikely that the 1954 basaltic andesite a'a lavas would reach velocities similar to those calculated for temperatures > 950°C. If the Jeffreys equation is a valid method for determining mean lava flow velocity it may therefore be reasonable to infer an eruption temperature of ~ 950°C for the 1954 lavas. However, the reported fire-fountaining associated with the 1954 lava flows (Gregg, 1956) may have resulted in some degree of cooling of the lava between the time of extrusion from the vent and the activation of flow advance. This implies that either the eruption temperature of the 1954 lava was greater than 950°C and that the lava cooled to this approximate temperature before propagation away from the vent, or that eruption temperature was ~ 950°C and that either no cooling, or minimal cooling occurred before the activation of flow advance. Thus, assuming a lava temperature of 950°C during the initial stages of flow advance, mean flow velocity for the 1954 lavas can be inferred at a range of 0.06 to 0.09 m s^{-1} (219 to 312 m h^{-1}) at 3 m flow depth, and 0.04 to 0.06 m s^{-1} (152 to 216 m h^{-1}) at 2.5 m flow depth, based on average underlying slope angles of 28° to 42°.

Gregg (1956) recorded flow velocities of ~ 0.08 m s^{-1} (304 m h^{-1}) during the early emplacement stages of the 30th June (BnL) lava flow on the steep upper cone slope, comparable with the calculated velocity at 950°C temperature on a 42° slope at 3 m flow depth. However, as this lava flow advanced further downslope, reported velocity decreased to 0.004 m s^{-1} (~ 14 m h^{-1}) over a 15° slope, while the flow velocity of the 18th August lava flow was recorded approximately 1400 m downflow from the crater rim at 0.003 m s^{-1} (~ 9 m h^{-1}) over a 20° slope (Gregg, 1956). These observed values are seven to 12 times lower than the calculated velocity values at 950°C over 14° and 19° slope angles respectively, implying that the lavas were considerably cooler (and more viscous) once they reached the lower slopes of the cone.

4.4.2 Effusion Rate and Flow Emplacement Duration

Models and Assumptions

Mean effusion rate is commonly calculated as a function of mean flow velocity, and flow deposit width and depth (e.g. Hulme and Fielder, 1977; Baloga *et al.*,

1995; Harris and Rowland, 2001). Hulme and Fielder (1977) used theoretical models and experimental data to show that flow width and depth are related to effusion rate, underlying slope angle, and rheological properties of the lava. Similarly, Harris and Rowland (2001) found a significant relationship between effusion rate and channel depth. Pinkerton and Wilson (1994) examined the relationship between flow length and effusion rate and noted that emplacement duration, slope angle and flow depth, as well as effusion rate, have a strong influence on the length of lava flows. Thus if flow length and effusion rate is known, the duration of flow emplacement can also be estimated.

Mean effusion rate was determined using the Hulme and Fielder (1977, p.228) model, and subsequent flow emplacement duration calculated by rearranging the Pinkerton and Wilson (1994, p. 110) model, based on calculated effusion rates. Effusion rate is given as a function of flow width, depth and velocity, and emplacement duration as a function of flow length and depth, effusion rate and underlying slope angle. Effusion rate and emplacement duration was calculated for each of the six lava flows visited in the field, using measured flow length, estimated mean flow width and depth, and average underlying slope angle for each of the lava flow deposits (Table 2.1), and the mean flow velocities (V_e) derived from the Kilburn and Lopes (1991) model at 950°C (Table 4.6). Effusion rate and emplacement duration was also calculated for a ± 10 m estimated error margin for mean flow width, and ± 0.5 m error margin for mean flow depth.

Effusion Rate and Flow Emplacement Duration

Calculated effusion rates and subsequent flow emplacement duration for six of the 1954 lavas are given in Table 4.7. Effusion rate ranges from 7.1 to 35 $m^3 s^{-1}$ at the measured mean flow depth for each of the flow deposits, and 3.6 to 20.3 $m^3 s^{-1}$ at mean flow depth minus 0.5 m, equating to ~ 40% reduction in effusion rate with 0.5 m reduced flow depth. A ± 10 m error in estimated mean flow width produces ± 7 to 20% difference in effusion rate at both of the mean flow depths calculated for each of the flow deposits.

Table 4.7 Effusion rate (E_f) ($m^3 s^{-1}$) and flow emplacement duration (hrs) calculated for six of the 1954 lavas using the models of Hulme and Fielder (1997) and Pinkerton and Wilson (1994) respectively.

Flow Deposit	L (m)	W (m)	Ave α (°)	H (m)	V_e[1] ($m\ s^{-1}$)	E_f[2] ($m^3\ s^{-1}$)	Duration[3] (hrs)	H (m)	V_e[1] ($m\ s^{-1}$)	E_f[2] ($m^3\ s^{-1}$)	Duration[3] (hrs)
4th June (A)	1400	80	42	3	0.09	20.8	1.5	2.5	0.06	12.0	2.0
		(± 10 m)				(2.6)	(0.1)			(1.5)	(0.2)
30th June (BnL)	2350	100	37	3	0.08	23.4	3.2	2.5	0.05	13.5	4.2
		(± 10 m)				(2.3)	(0.2)			(1.4)	(0.3)
14th July (Dc)	1550	90	39	3	0.08	22.0	1.8	2.5	0.06	12.7	2.4
		(± 10 m)				(2.4)	(0.1)			(1.4)	(0.2)
29th July (E)	1350	60	37	3.5	0.11	22.3	1.6	3	0.08	14.0	2.0
		(± 10 m)				(3.7)	(0.2)			(2.3)	(0.2)
18th August (F)	1900	100	28	3	0.06	18.2	3.3	2.5	0.04	10.5	4.4
		(± 10 m)				(1.8)	(0.2)			(1.1)	(0.3)
16th Sept (G)	1200	50	39	2.5	0.06	7.1	2.4	2	0.04	3.6	3.4
						(1.4)	(0.3)			(0.7)	(0.4)

[1] Velocity values (V_e) calculated at 950°C for each of the 1954 lavas for their respective average underlying slope angles and mean flow depths (H) ± 0.5 m for each of the lava flow deposits except 18th August (± 1 m) using the Kilburn and Lopes (1991) model (Table 4.6).

[2] Effusion rate calculated using the Hulme and Fielder (1977) model based on mean flow width (W) ± 10 m, mean flow depth (H) and mean flow velocity (V_e) for each of the 1954 lavas.

[3] Eruption duration calculated using Pinkerton and Wilson (1994) based on measured flow length (L), mean flow depth (H), average underlying slope angle and calculated effusion rates for each flow deposit.

Calculated flow emplacement duration times range from ~ 1.5 to 3.3 hours at the measured mean flow depth for each of the flow deposits, increasing to ~ 2 to 4.4 hours at mean flow depth minus 0.5 m. A ± 10 m difference in mean flow width gives an error margin of 0.1 to 0.4 hours over the two mean flow depth values calculated for each of the lavas, which equates to ~ 4 to 11% difference in flow emplacement duration with 10 m difference in mean flow width. These calculated flow emplacement duration times are considerably lower than expected, and are between 30 to 40 hours less than the emplacement times reported by Gregg (1956) for the 30th June (BnL) and 18th August (F) lava flows.

4.4.3 Comparison with Reported 1954 Lava Flow Emplacement Data

Although the documented accounts of the flow emplacement duration of the 1954 lavas (Gregg, 1956) are not well constrained, enough information is available for three of the lava flows [4th June (A), 30th June (Bn), 18th August (F)] to enable a reasonable estimate of the duration time for these flows. The mean flow velocity of these lavas can therefore be estimated as a function of flow length over emplacement duration. Table 4.8 presents documented and estimated values of flow velocity and emplacement duration for these three lavas based on the recorded observations of Gregg (1956).

The 4th June (A) lava flow is reported to have travelled approximately one-third of the distance down the length of the underlying 1949 lava flow deposit (therefore approximately 550 m) three hours after overflowing from the crater rim (Gregg, 1956), giving an estimated initial flow velocity of ~ 0.05 m s^{-1}. This lava flow is reported to have almost reached its full length by the evening of the same day (Gregg, 1956); therefore, assuming that 'evening' refers to ~ 6 pm and that the flow was ~ 100 m short of its final length, the 4th June (A) lava is estimated to have travelled a further ~ 750 m over the next seven hours, giving an estimated flow velocity of ~ 0.03 m s^{-1}. Overall, the 4th June (A) lava flow travelled approximately 1300 m from the crater rim over ~ 10 hours, giving an estimated mean flow velocity of ~ 0.03 m s^{-1} for most of its flow length. The 4th June (A) lava is reported to have stopped moving by the following day (Gregg, 1956), although the exact time of flow cessation is not known; however, if the lava

Table 4.8 Estimated flow velocity and emplacement duration of three 1954 lavas based on recorded observations (Gregg, 1956).

Flow Deposit	Time of observation	Hours between observations	Flow Velocity (m h^{-1})	Flow Velocity (m s^{-1})	Distance advanced (m)
4th June (A)	11am*	3	183	0.051	550†
Overtopped crater rim at 8:15 am*	6pm	7	107	0.030	750
	9pm	3	36	0.010	100
	Total	***13***	***Ave***	***0.030***	**L=1400**
30th June (Bn-L)	6pm	2	304	0.084*	608
Overtopped crater rim ~ 4pm*	10am	16	97	0.027	1557†
	1am	12.8	14.4	0.004*	185
	Total	***31***	***Ave***	***0.038***	**L=2350**
18th August (F)	5am*	4	365	0.101	1460†
Overtopped crater rim at 1 am*	12:45pm*	8	9	0.003*	86
	2pm*	25	9	0.003*	270
	1 am	11	9	0.003	118
	Total	***48***	***Ave***	***0.027***	**L=1934**

* Actual time/flow velocity documented by Gregg (1956).
† Distance from crater rim estimated from documented locations (Gregg, 1956).

continued to advance with a velocity of 0.03 m s^{-1}, the final ~ 100 m of its flow length would have been reached within the next hour. The underlying slope angle of the 4th June (A) lava reduces to 27° over the last 200 m of its flow length (average of 44° over the first ~ 1200 m length) thus flow velocity is likely to have been reduced. Therefore, assuming up to a two-thirds reduction in flow velocity over the final 100 m of its flow length (i.e. ~ 0.01 m s^{-1}) would increase the emplacement time for the final 100 m to approximately three hours. The 4th June lava can therefore be estimated to have an emplacement duration of ~ 11 to 13 hours, with a maximum of ~ 17 hours if the time of the 'evening' observation is one hour later (i.e. 7 pm), and the flow was 200 m short of its final flow length at this time. An overall average flow velocity of 0.03 m s^{-1} for the entire flow length gives an emplacement duration of 13 hours.

The emplacement duration of the northern of the two 30th June lavas (BnL) is less well documented, with the lava known to have overtopped the crater rim at ~ 4 pm and was reported to be advancing downslope at ~ 0.084 m s^{-1} (304 m h^{-1}) by the evening of the same day (Gregg, 1956). Again, assuming that 'evening' refers to ~ 6 pm, the flow is estimated to have travelled ~ 600 m from the crater rim over a period of two hours at the reported flow velocity. The following day

(1st July) the 30th June (BnL) lava was reported to have reached close to the base of the cone and continued to slowly advance at ~ 0.004 m s^{-1} (~14 m h^{-1}) (Gregg, 1956). Although the exact distance travelled from the crater rim and the time of the observations on the 1st July are not documented, Gregg (1956) reports that the lava had branched into several smaller lobes at the time of the observation. Emplacement duration and flow velocity can therefore be estimated by assuming that the flow had reached ~ 1400 m.a.s.l. elevation (the approximate elevation where the southern lobe, BnL-S, bifurcates into the six elongated distal lobes described in Chapter 2, Section 2.3.2), and that the time of this observation occurred at ~ 10 am on the 1st July. The 30th June (BnL) lava flow is therefore estimated to have travelled a further ~ 1,550 m from the evening of the previous day over a period of ~ 16 hours, giving a flow velocity of ~ 0.027 m s^{-1} for this time period and an overall flow velocity for most of the flow length of ~ 0.05 m s^{-1}. The final stopping time of the 30th June (BnL) lava is not documented, except that it had ceased to advance by the 2nd July (Gregg, 1956). Assuming the lava continued to advance at the slower velocity of 0.004 m s^{-1}, the final ~ 180 m of the flow length would be emplaced over ~ 13 hours. Therefore a mean flow velocity for the 30th June lava for its entire flow length is ~ 0.038 m s^{-1} with a total emplacement duration of ~ 31 hours.

The 18th August (F) lava flow is reported to have reached the Pukekaikiore Saddle at 5 am, four hours after overtopping the crater rim (Gregg, 1956). Assuming the level of the Pukekaikiore Saddle refers to ~ 1600 m.a.s.l., the 18th August lava is estimated to have travelled approximately 1460 m over the first four hours of emplacement, giving an initial flow velocity of 0.1 m s^{-1}. At 12:45 pm (eight hours after reaching the saddle) the 18th August lava had a reported velocity of ~ 0.003 m s^{-1} (~ 9 m h^{-1}), and by 2 pm on the following day (19th August) (i.e. 33 hours after reaching the saddle) the lava, travelling at the same speed, had reached a point approximately 300 m around the southern side of Pukekaikiore (Gregg, 1956). Assuming that flow velocity slowed considerably upon reaching the Pukekaikiore Saddle (based on evidence from pre-existing topographical features and the morphology and surface features of the 18th August lava flow deposit described in Chapter 2 and discussed further in Chapter 5), the 18th August lava advancing at 0.003 m s^{-1} would have travelled a further ~ 86 m between 5 am and

12:45 pm on the 18th August, and an additional ~ 270 m by 2 pm on the 19th August. This relates to a total distance of ~ 1,800 from the crater rim and is consistent to within ~ 50 m of the reported position of the flow front at that time (Gregg, 1956). Assuming the lava continued to advance at ~ 0.003 m s^{-1} for the last ~ 117 m of its final flow length, stopping time would be another ~ 11 hours, giving a final flow emplacement duration of ~ 48 hours and a mean flow velocity of 0.028 m s^{-1}.

The estimated mean flow velocity of the 4th June (A) lava (0.03 m s^{-1}) is ~ 50 to 65% lower than those calculated using the Jeffreys equation (Kilburn and Lopes, 1991) for the average underlying slope angle (42°) of the 4th June lava at 2.5 and 3 m mean flow depths. However, the initial flow velocity (0.05 m s^{-1}) over the first three hours of emplacement is relatively similar (~ 15% lower) to those calculated using the Jeffreys equation for a 42° underlying slope angle at 2.5 m mean flow depth. Similarly, the estimated mean flow velocity of the northern 30th June (BnL) lava (0.038 m s^{-1}) is ~ 30 to 50% lower than calculated velocity for the average underlying slope angle of 37° at 2.5 and 3 m mean flow depths, although the initial reported flow velocity of 0.084 m s^{-1} is consistent with calculated flow velocity for mean flow depth of 3 m at 37° slope angle. The estimated mean flow velocity of the 18th August (F) lava (0.027 m s^{-1}) is ~ 30 to 50% lower than that estimated using the Jeffreys equation for an average underlying slope angle of 28°, however, the estimated initial flow velocity (0.1 m s^{-1}) over the first four hours of emplacement is fairly consistent with calculated values at 3 m flow depth and an underlying slope angle of 42°. The average underlying slope angle of this flow, from the crater rim to ~ 1,700 m.a.s.l. elevation is ~ 41°. The Jeffreys equation therefore appears to be relatively comparable with initial flow velocities on steeper slopes and at higher temperatures, but the difference between calculated and estimated flow velocities based on reported data suggests that the Jeffreys equation does not appear to reflect the effect of reduced velocity and cooling on the gentler slopes.

The estimated flow emplacement duration times for these three lavas are considerably greater than those calculated using the Pinkerton and Wilson (1994)

model for the same flows (Table 4.7). This is possibly due to the higher mean velocity values derived from the Jeffreys equation which are used in the calculations. However, recalculating effusion rate and emplacement duration using the Hulme and Fielder (1977) and Pinkerton and Wilson (1994) models at the lower estimated flow velocities presented in Table 4.8 still results in much lower emplacement duration times (Table 4.9) than those estimated using the documented accounts of Gregg (1956). For example, at the estimated mean flow velocity of 0.03 m s^{-1}, the 4th June lava with a mean flow depth of 3 m would be emplaced in 3.1 hours (± 0.3 hours with a 10 m difference in mean flow width), approximately 10 hours less than the estimated emplacement duration time. Similarly, the Pinkerton and Wilson (1994) model underestimates the estimated emplacement duration of the 30th June (BnL) lava by ~ 26 hours, and the 18th August (F) lava by ~ 42 hours. Table 4.9 presents the estimated emplacement duration of the six 1954 lavas as a function of estimated mean flow velocity and measured flow deposit length (estimated duration[4] column). An estimate of effusion rate calculated as a function of flow deposit volume and the estimated emplacement duration times gives effusion rates of ~ 2.5 to 6.4 m^3 s^{-1} (Table 4.9), which are ~ 1 to 5.6 m^3 s^{-1} lower than those calculated using the Hulme and Fielder (1977) model and based on the estimated flow velocities. Emplacement duration has also been recalculated using the Pinkerton and Wilson (1994) model and based on these newly estimated effusion rates (Table 4.9); however, although calculated emplacement duration increases by ~ 20 to 50%, emplacement duration times remain ~ 6 to 35 hours less than those estimated by estimated mean flow velocity.

4.5 FLOW SURFACE COOLING

4.5.1 Grätz Number

Methods and Assumptions

Guest *et al*. (1987) suggest that, in the absence of topographical barriers, lava flows cease to advance when either the supply of lava to the flow front is terminated, or cooling of the lava increases viscosity and yield strength to the point where further flow advance is prevented. The role of cooling on the

Table 4.9 Effusion rate ($m^3 s^{-1}$) and flow emplacement duration (hours) for six 1954 lavas recalculated using the Hulme and Fielder (1977) and Pinkerton and Wilson (1994) models, and based on the estimated mean flow velocities in Table 4.8.

Flow Deposit	L (m)	W (m)	Ave α (°)	V_e (m s^{-1})[1]	Mean Flow Depth (m)	Calculated E_f[2] ($m^3 s^{-1}$)	Calculated Duration[3] (hrs)	Estimated Duration[4] (hrs)	Flow volume (m^3)	Estimated E_f[5] ($m^3 s^{-1}$)	Calculated duration[6] (hrs)
4th June (A)	1400	80	42	0.03	3	7.2	3.1	13	183,000	3.9	4.65
		(± 10 m)				(0.9)	(0.3)				
30th June (BnL)	2350	100	37	0.038	3	11.4	5.1	31	718,200	6.4	7.50
		(± 10 m)				(1.1)	(0.4)				
14th July (Dc)	1550	90	39	0.03	3	8.1	3.5	**14**	264,000	**5.1**	4.70
		(± 10 m)				(0.9)	(0.3)				
29th July (E)	1350	60	37	0.03	3.5	6.3	3.7	**12.5**	210,000	**4.7**	4.54
		(± 10 m)				(1.1)	(0.5)				
18th August (F)	1900	100	28	0.027	3	8.1	5.7	48	425,000	2.5	12.38
		(± 10 m)				(0.8)	(0.4)				
16th Sept (G)	1200	50	39	0.03	2.5	3.8	3.7	**11**	110,000	**2.8**	4.46
		(± 10 m)				(0.8)	(1)				

[1] Estimated mean flow velocity based on documented velocity and flow emplacement duration for the 4th June (A), 30th June (BnL), and 18th August (F) lavas (Table 4.8). A mean flow velocity of 0.03 m s^{-1} is assumed for the 14th July (Dc), 29th July (E), and 16th September (G) lavas.
[2] Effusion rate calculated using the Hulme and Fielder (1977) model and based on estimated mean flow velocities.
[3] Flow emplacement duration calculated using the Pinkerton and Wilson (1994) model and based on newly calculated effusion rates in previous column.
[4] Estimated flow emplacement duration for the 4th June (A), 30th June (BnL) and 18th August (F) lavas based on documented accounts (Table 4.8). Emplacement duration for the 14th July (Dc), 29th July (E) and 16th September (G) lavas (bold type) is estimated as a function of mean flow velocity (0.03 m s^1) and measured flow deposit length.
[5] Effusion rate estimated as a function of flow volume (Table 2.1) over estimated emplacement duration.
[6] Flow emplacement duration calculated using the Pinkerton and Wilson (1994) model and the estimated effusion rates in previous column.

cessation of lava flow advancement has been quantified by several researchers (e.g. Pinkerton and Sparks, 1976; Hulme and Fielder, 1977; Guest *et al*., 1987; Pinkerton and Wilson, 1994) using the Grätz number: a dimensionless number that characterises the ability of the lava to conduct heat from the internal core to the exterior surfaces of the advancing lava flow, and thus the rate at which the advancing flow is cooling (Pinkerton and Wilson, 1994). The Grätz number can therefore be used to predict the factors that control the maximum distance travelled by a single lava flow unit from the source vent, that is, whether flow advancement ceased as a result of cooling of the lava (cooling-limited) or as a result of termination of the lava supply at the source (volume-limited) (Parfitt and Wilson, 2008).

A Grätz (G_z) number has been calculated for each of the six lava flows using the Pinkerton and Sparks (1976) model, in which G_z is a function of measured flow deposit length, mean flow deposit depth, mean flow velocity, and thermal diffusivity. Mean flow velocity values are derived from both the calculated values using the Jeffreys equation for lavas at 950°C (Table 4.6) and the estimated values based on the documented accounts of Gregg (1956) (Tables 4.8 and 4.9), and at the relevant mean underlying slope angle for each of the six lavas (Table 2.1). A thermal diffusivity value of 10^{-6} (m^2 s^{-1}) is used after Griffiths and Fink (1993). The duration required for G_z to reach 300 and 100 is also calculated for each of these lavas using the Pinkerton and Wilson (1994) model, based on mean flow deposit width and depth, and thermal diffusivity. As with previous rheology calculations, the use of mean flow deposit dimensions assumes constant flow width and depth throughout the length of the flow.

Grätz Numbers

Grätz (G_z) numbers for the six 1954 lava flows calculated using the Pinkerton and Sparks (1976) model, are presented in Table 4.10. At the higher flow velocities derived from the Jeffreys equation (Table 4.6), G_z values range between ~ 1000 to 3500 at measured flow depth and ~ 450 to 1900 at measured flow depth minus 0.5 m. However, at the lower estimated mean flow velocities based on documented accounts (Table 4.9), G_z is markedly reduced, with a range of ~ 540

to 970 at measured flow depth and ~ 370 to 500 at measured flow depth minus 0.5 m. There is little difference in the Grätz numbers calculated for a ± 10 m difference in flow width, with ± 0.5 to 7% difference calculated. Empirical data suggests that flow advancement ceases when G_z reaches ~ 300 to 100 when surface cooling is the major limitation on further advancement (Pinkerton and Sparks, 1976; Hulme and Fielder, 1977; Pinkerton and Wilson, 1994). Therefore, if the velocities calculated using the Jeffreys equation apply to the 1954 lavas, calculated G_z values (i.e. > 300) suggest the maximum length of these flows was controlled by a limited volume supply rather than cooling. Similarly, at the lower estimated flow velocities of the 1954 lavas, although the G_z values are markedly lower they remain > 300 at both mean flow depths, which also implies that the lengths of these six 1954 lavas were volume-limited rather than cooling-limited.

However, calculating the duration required for G_z to reach between 300 and 100 for each of the six lavas (Table 4.10) shows that G_z reaches 300 at between ~ 21 to 40.5 hours for each of the six lavas at measured mean flow depths, reducing to ~ 14 to 30 hours at mean flow depths minus 0.5 m. The time required for G_z to reach 100 increases to ~ 63 to 121 hours at mean flow depths, and ~ 41 to 91 hours when mean flow depth is reduced by 0.5 m. If the critical G_z number representing the point at which cooling is the limiting factor determining flow length is 300, the 30th June (BnL) and 18th August (F) lavas can be inferred as cooling-limited flows because G_z reaches 300 at approximately the same time as the estimated flow emplacement duration of the 30th June (BnL) lava, and in less time than the estimated emplacement duration of the 18th August (F) lava, at both mean flow depths calculated. The estimated emplacement duration of the remaining four lavas [4th June (A), 14th July (Dc), 29th July (E), 16th September (G)] is less than the time required for G_z to reach 300, suggesting that these lavas were limited by volume. However, the time required for each of the lavas to reach a G_z of 100 is considerably greater than the estimated emplacement duration for each of these lavas, at both of the mean flow depths calculated.

Table 4.10 Calculated Grätz (G_z) numbers for six 1954 lavas based on flow deposit dimensions and mean flow velocity using the Pinkerton and Sparks (1976) model. The estimated time required for G_z to reach 300 and 100 is also given, calculated using the Pinkerton and Wilson (1994) model, and is based on flow deposit dimensions and thermal diffusivity of the lava.

Flow Deposit	L (m)	W (m)	H[1] (m)	Ve[3] (m s^{-1})	G_z	Ve[4] (m s^{-1})	G_z	G_z=300 T (hrs)	G_z=100 T (hrs)	H[2] (m)	Ve[3] (m s^{-1})	G_z	Ve[4] (m s^{-1})	G_z	G_z=300 T (hrs)	G_z=100 T (hrs)
4th June (A)	1400	80	3	0.087	2068	0.03	717	31.0	92.9	2.5	0.060	1010	0.03	504	21.8	65.3
30th June (BnL)	2350	100	3	0.078	1124	0.038	549	31.4	94.3	2.5	0.054	548	0.038	385	22.0	66.1
14th July (Dc)	1550	90	3	0.081	1771	0.03	653	31.2	93.7	2.5	0.057	863	0.03	458	21.9	65.7
29th July (E)	1350	60	3.5	0.106	3435	0.03	972	40.5	121.5	3	0.078	1883	0.03	726	30.2	90.7
18th August (F)	1900	100	3	0.061	1085	0.03	536	31.4	94.3	2.5	0.042	528	0.03	376	22.0	66.1
16th Sept (G)	1200	50	2.5	0.057	1069	0.03	567	21.0	63.0	2	0.036	446	0.03	370	13.7	41.1

[1] Represents mean flow depth as estimated in the field (Table 2.1).
[2] Represents mean flow depth minus 0.5 m.
[3] Mean flow velocity values calculated using the Kilburn and Lopes (1991) model (Table 4.6).
[4] Estimated mean flow velocity values based on documented accounts by Gregg (1956) (Table 4.9).

4.5.2 Surface Cooling and Crust Strength

Models and Assumptions

Lyman and Kerr (2006) expanded on the theoretical models of Griffiths and Fink (1993) to obtain empirical data on the relationship between surface cooling and lava flow dynamics. Following earlier experimental work (Lyman *et al*., 2005) Lyman and Kerr (2006) modelled the behaviour of lava released instantaneously from a reservoir of a given volume and its subsequent emplacement along a sloping surface. Five dynamic flow regimes were identified:

1. Inertial slumping of the lava moving at constant velocity proximal to the source vent,
2. Horizontal viscous regime with small volumes of basaltic lavas, which may occur in place of slumping on horizontal surfaces or gentle slopes,
3. Sloping viscous regime follows either slumping or horizontal regime in lavas with no internal yield strength,
4. Sloping viscoplastic regime occurs either immediately, or following the slumping regime in lavas with an internal yield strength,
5. Surface crust strength regime occurs where the strength of the growing surface crust eventually stops the downslope lava flow, regardless of volume.

The spreading regime of the lava depends on the initial reservoir volume and its internal yield strength, while the stopping time, final flow length and final flow depth of the lava is controlled either by the surface crust strength or the internal yield strength of the lava (Lyman *et al*., 2005; Lyman and Kerr, 2006). The Lyman and Kerr (2006) models show that lavas emplaced on a sloping surface with no internal yield strength will spread in the sloping viscous regime (SVs) and are stopped by the surface crust strength regime (CrS); whereas lavas with an internal yield strength will spread in the sloping viscoplastic regime (SVp) and are stopped either by the surface crust strength regime or by the internal yield strength of the lava (YSL). In both scenarios, and depending on the initial reservoir volume, the lava may initially spread in the inertial slumping regime (Sl) as a result of gravitational forces. Lyman and Kerr (2006) found a good correlation between their experimental data and theoretical models when applied to

hypothetical Hawaiian lavas with no yield strength, and Mount Etna lavas with internal yield strength, determining that their models can be used to predict flow spreading behaviour and therefore the final flow length of lavas.

Kerr and Lyman (2007) applied these predictive spreading regime models to the 1988-1990 andesite lava flow of Lonquimay volcano, by comparing the known propagation of the lava flow over time with the predicted flow spreading behaviour of the sloping viscous (assuming no internal yield strength) and surface crust strength regimes. Their study showed that the sloping viscous regime considerably overestimated the flow spreading behaviour of the lava, whereas the surface crust strength regime accurately predicted flow propagation, confirming that the spreading behaviour of this lava was controlled by the strength of the cooling surface crust. Lyman and Kerr (2007) also produced a model predicting the volume of lava erupted over time, based on an exponentially decreasing eruption rate. In a comparison with the estimated volume of lava erupted during emplacement of the Lonquimay lava flow Kerr and Lyman (2007) found that their model corresponded well to known data, particularly after the first ~ 100 days of the eruption duration.

The Lyman and Kerr (2006) theoretical flow spreading regime models (equations 1, 2, 5, 9, 10, 15, 21, 24, pp. 2-3) are based on lavas emplaced over relatively low average slope angles (3 and 10°), and with higher viscosity and yield strength values than those associated with the 1954 lavas. Therefore, to assess the effect of greater slope angle and lower viscosity and yield strength values on the behaviour and predictability of these flow spreading regimes, the flow spreading behaviour of a lava with the same rheological properties as the 1954 lavas is determined for the instantaneous release of two fixed reservoir volumes (small, 10 m^3 and large, 1000 m^3, after Lyman and Kerr, 2006) over underlying slope angles of 10° and 42°. Flow spreading behaviour is calculated using average bulk lava density (ρ) (Table 4.3), thermal diffusivity (10^{-6} m^2 s^{-1}), gravitational acceleration (9.8 m s^{-2}), total viscosity (η_T) of the 1954 lavas at 950°C (Table 4.2), internal yield strength (25 Pa) at maximum crystal abundance and average mean particle diameter and

shape factor values based on the Pinkerton and Stevenson (1992) model (Table 4.4), and assumes a surface crust strength of 10^6 Pa.

The propagation of three of the 1954 lava flows [4th June (A), 30th June (BnL), 18th August (F)] is plotted as a function of flow length over time, based on the flow velocities and emplacement times estimated from documented accounts (Table 4.8), and compared with the predicted spreading behaviour of the lavas in the sloping viscous (SVs), sloping viscoplastic (SVp) and surface crust strength (CrS) regimes to determine which of these regimes (if any) controls the spreading behaviour of these lavas. An order of magnitude for the surface crust strength of these lavas is estimated using Lyman and Kerr (2006, equation 30, p.6), based on estimated flow deposit volume (Table 2.1), gravitational acceleration, average bulk density, thermal diffusivity (10^{-6} m^2 s^{-1}), measured flow length (Table 2.1) and estimated emplacement duration (Table 4.8) of each lava. The estimated volume of lava erupted during emplacement of these three 1954 lavas, is also compared with the predictive model of Kerr and Lyman (2007, equation 2, p.6) to determine trends in the eruption rate associated with these lavas. The estimated volume is based on estimated flow length over time, assuming constant flow width and depth.

Effect of Slope on Theoretical Flow Spreading Models

Fig. 4.2 compares each of the flow spreading regimes (except the horizontal viscous regime) for the two reservoir volumes of lava emplaced over 10° and 42° slope angles. At 10° slope angle, the small volume of lava with no internal yield strength spreads immediately in the sloping viscous regime without initially slumping due to gravity (the pink line lies beneath the blue line) (Fig. 4.2a), whereas the large volume spreads initially in the inertial slumping regime for ~ 40 seconds before transition to the sloping viscous regime (the blue line initially lies beneath the pink line and crosses the path of the pink line at ~ 40 seconds) (Fig. 4.2b). If the lava has a yield strength of 25 Pa, the small volume spreads immediately in the sloping viscoplastic regime (the orange line lies beneath the blue line) (Fig. 4.2a), although this regime follows similar behaviour to the inertial slumping regime, whereas with the large reservoir volume, the lava

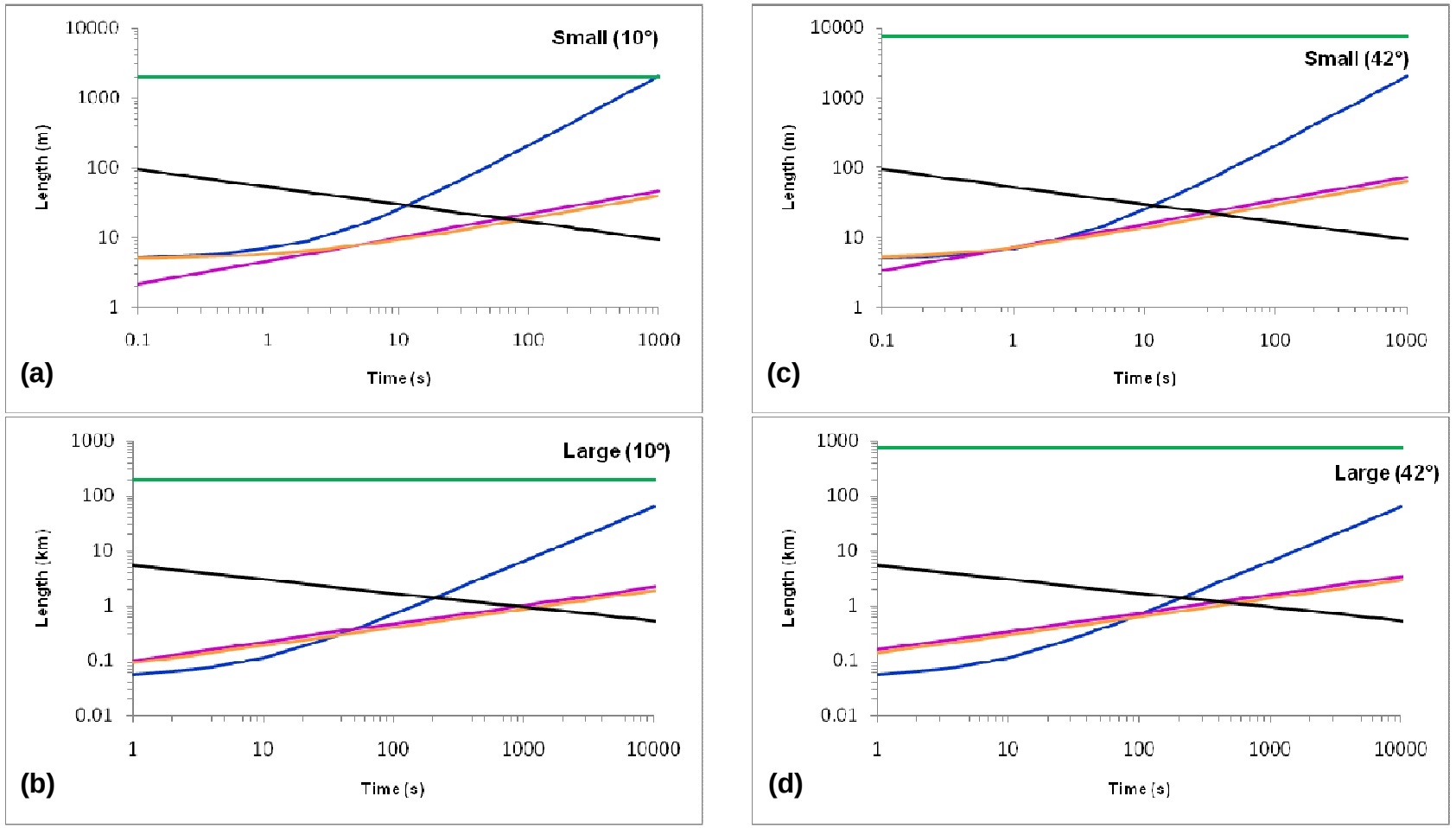

Fig. 4.2 Flow length plotted as a function of time for the instantaneous release of lava with a fixed volume (small, 10 m^3; large, 1000 m^3) over a 10° and 42° sloping surface. Flow spreading is shown for the inertial slumping regime (blue line), the sloping viscous regime (pink line), the sloping viscoplastic regime (orange line), and the surface crust strength regime (black line). The yield strength limit of the lava (green line) represents the maximum length at which the lava will flow with an internal yield strength of 25 Pa. Note difference in length scale between small (m) and large (km) volume flows.

spreads initially in the slumping regime before transition to the sloping viscoplastic regime at ~ 40 seconds (the blue line initially lies beneath the orange line and crosses the path of the orange line at ~ 40 seconds) (Fig. 4.2b). At both reservoir volumes there is little apparent difference between the spread of the lava in the sloping viscous regime (no internal yield strength) and the sloping viscoplastic regime (an internal yield strength of 25 Pa). However, after 1000 seconds the sloping viscoplastic regime flow is ~ 6.5 m shorter than the sloping viscous regime flow with the small reservoir volume, and ~ 128 m shorter with the large reservoir volume. The low yield strength value therefore appears to have a significant effect on the spreading behaviour of the lava, although a surface crust strength of 10^6 Pa stops the flow well before it reaches its internal yield strength limit (green line), that is, the length at which a lava with an internal yield strength of 25 Pa will cease to flow due to its internal yield strength without the effect of surface cooling. With the small reservoir volume, the growing surface crust stops flow spreading in both the sloping viscous regime and the sloping viscoplastic regime at ~ 70 seconds, and with the large volume the flow is stopped by the surface crust at ~ 1000 seconds.

The effect of increasing the underlying slope angle to 42° on flow spreading is shown in Figs. 4.2c, d. Initial spreading of the lava in the inertial slumping regime remains controlled by reservoir volume as with the gentler slope angle, although the transition time from the slumping regime to the sloping viscous and sloping viscoplastic regimes is approximately double at this higher slope angle (~ 80 seconds). The difference in flow length between the sloping viscous and sloping viscoplastic regimes increases to 10 m with the small volume reservoir and to ~ 200 m with the large volume reservoir after 1000 seconds. In the sloping viscous regime the flow length of the small volume reservoir increases by 26 m between the 10 and 42° slope angle at 1000 seconds, and the large volume by 570 m. Similarly, in the sloping viscoplastic regime, the 42° slope angle gives a flow length 24 m longer with the small volume reservoir, and ~ 500 m longer with the large volume reservoir. Slope angle therefore has a significant effect on flow spreading in both regimes and the small yield strength of the lava continues to have a small effect on flow spreading at the higher slope angle. Increasing the

slope angle has a major effect on the yield strength limit of the lavas, increasing from 2 to ~ 8 km with the small volume reservoir and from 200 km to ~ 800 km with the large volume reservoir. The increased slope angle also effects the time at which the flow is stopped by the surface crust, decreasing the time to ~ 35 seconds with the small volume, and to ~ 400 seconds with the large volume reservoir. The small volume of lava is stopped at ~ 5 m greater distance than with the lower slope angle, while the large volume lava is stopped at approximately the same distance as the lower slope angle.

Flow Spreading Behaviour of Three 1954 Lavas

The estimated propagation of the three 1954 lava flows [4th June (A), northern 30th June (BnL), 18th August (F)] is plotted as a function of time and compared with the predicted spreading behaviour of the lavas in the sloping viscous regime (no internal yield strength) and the sloping viscoplastic regime at two yield strength values (25 and 2500 Pa), assuming lava viscosity at the value calculated for the 1954 lavas at 950°C (i.e. 19092 Pa s) (Fig. 4.3). Both spreading regimes greatly over estimate flow propagation of each of the three lava flows by several kilometres. The sloping viscoplastic regime at the greater yield strength value (2500 Pa) more closely predicts flow propagation towards the final stages of emplacement for each of the lavas, with a final predicted flow length ~ 2 to 5 km shorter than the predicted length of the lower yield strength lava, although predicted length remains 5 to 16 km greater than measured flow lengths.

Increasing viscosity by 10^2 and 10^3 Pa s gives a closer approximation of actual flow propagation for both spreading regimes (Fig. 4.4), although neither regime accurately predicts flow propagation for the entire length of the lava. For example in Fig. 4.4a, the sloping viscous regime at a viscosity 10^2 times greater than calculated viscosity more accurately predicts propagation of the 4th June (A) lava for the initial three hours of emplacement, while the final three hours of emplacement is more closely predicted by the sloping viscoplastic regime at both yield strength values. Similarly, the sloping viscous regime at a viscosity 10^3 times greater than calculated viscosity more accurately predicts propagation of the 30th June (BnL) lava for the initial ~ 18 hours of emplacement, with the sloping

viscoplastic regime more accurately predicting the final three to four hours of emplacement at the two yield strength values (Fig. 4.4b). The 18th August (F) lava is more accurately predicted by the sloping viscous regime when viscosity is increased by 10^2 Pa s for the initial four hours of emplacement, although flow propagation is greatly overestimated by both spreading regimes at this viscosity for the remainder of the flow. However, increasing the viscosity by 10^3 Pa s, gives a closer prediction of flow propagation towards the final 12 to 14 hours of emplacement with both spreading regimes.

Interestingly, as viscosity is increased, the difference in flow length predicted by the sloping viscoplastic regime at the two yield strength values decreases. For example, increasing viscosity by 10^2 Pa s results in ~ 100 to 300 m difference in predicted flow length between the two yield strength values, compared to 2 to 5 km difference at the calculated viscosity value of 10902 Pa s (Figs.4.4a, c). This difference decreases further to ~ 60 to 70 m when viscosity is increased by 10^3 Pa s (Fig. 4.4b). The sloping viscoplastic regime at the greater yield strength value with viscosity increased by 10^3 Pa s is not shown for the 18th August (F) lava (Fig. 4.4c) because at the scale shown the predicted flow spreading patterns at both yield strength values follow the same path.

Calculated surface crust strengths for the 4th June (A) and 18th August (F) lavas are 3.5×10^5 and 3.4×10^5 Pa respectively, and 7.9×10^5 Pa for the 30th June (Bn) lava (Table 4.11). These values are within the range of the ~ 10^4 Pa surface crust strength estimated by Blake and Bruno (2000) for basaltic to intermediate composition lavas, the ~ 1 MPa (10^6 Pa) crust strength estimated for fractured silicic domes (e.g. Iverson, 1990), and ~ 2 MPa for the 1988-90 Lonquimay andesite lava flow (Kerr and Lyman, 2007). Fig. 4.5 compares predicted flow spreading in the surface crust strength regime at these calculated crust strength values with estimated flow propagation and the sloping viscous and sloping viscoplastic regimes assuming calculated viscosity of the 1954 lavas (10902 Pa s).

Fig. 4.3 (next page) Comparison of estimated flow propagation over time of three 1954 lavas (blue triangles) with predicted flow spreading in the sloping viscous regime (pink line) and the sloping viscoplastic regime at two yield strength values (solid orange line = 25 Pa; dashed orange line with diamonds = 2500 Pa). Flow spreading in each predicted regime assumes the calculated total viscosity (η_T) of the 1954 lavas at 950°C (10902 Pa s). A, 4th June (A) lava; B, northern 30th June (Bn) lava; C, 18th August (F) lava.

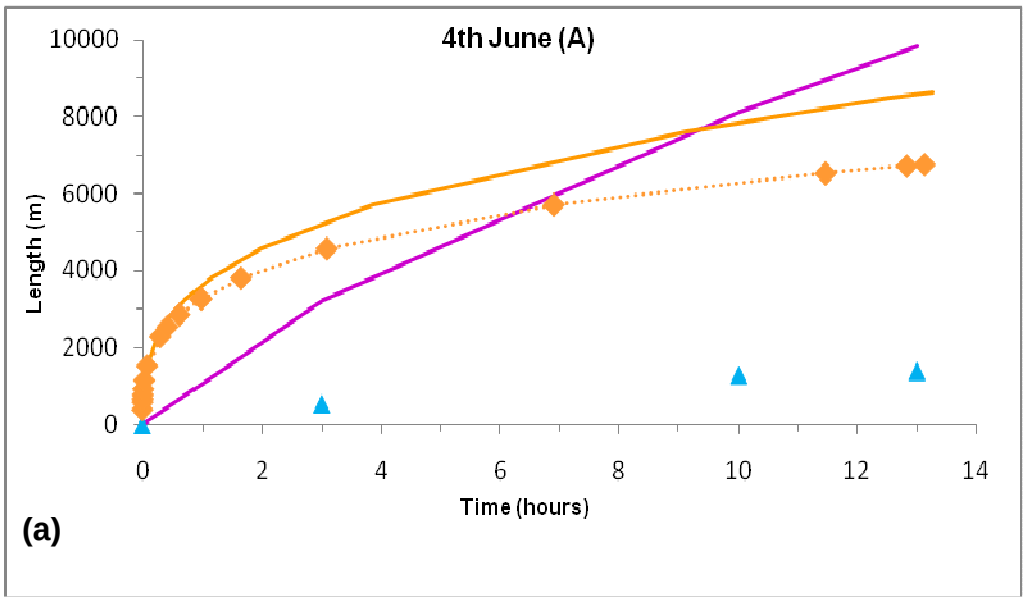
4th June (A)
Length (m)
Time (hours)
0
2000
4000
6000
8000
10000
0
2
4
6
8
10
12
14

(a)

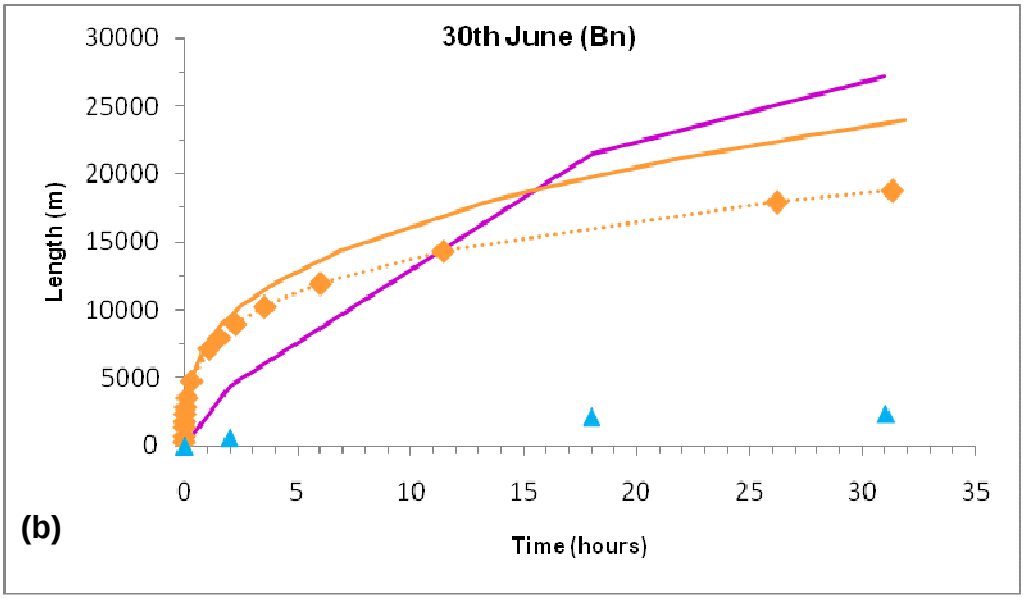
30th June (Bn)
Length (m)
Time (hours)
0
5000
10000
15000
20000
25000
30000
0
5
10
15
20
25
30
35

(b)

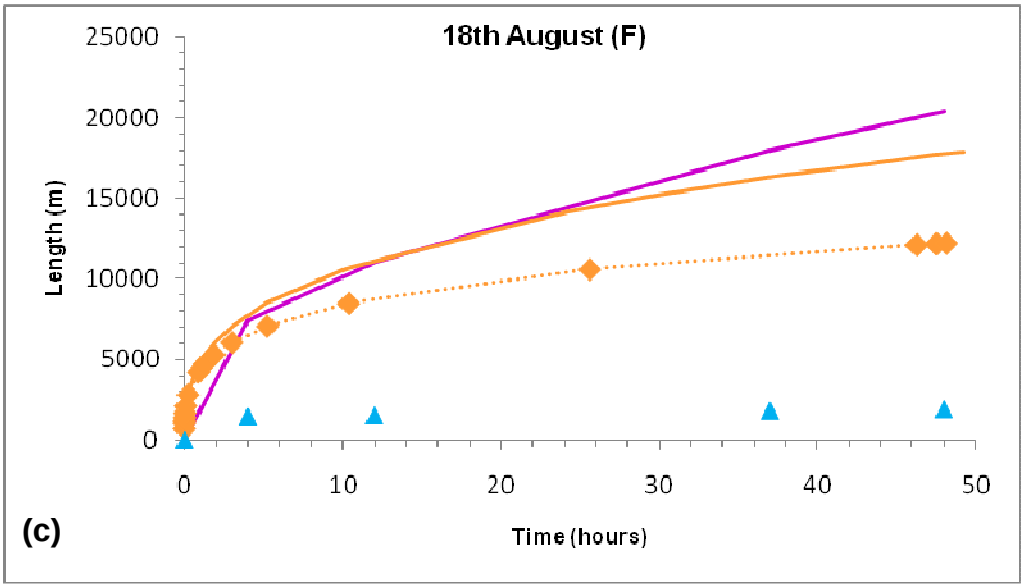
18th August (F)
Length (m)
Time (hours)
0
5000
10000
15000
20000
25000
0
10
20
30
40
50

(c)

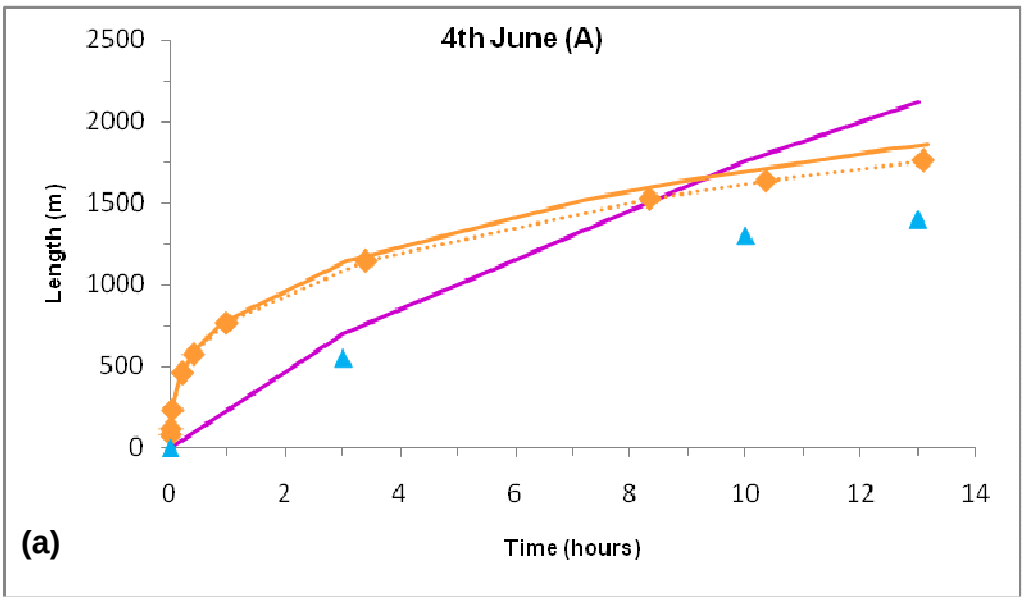
4th June (A)
Length (m)
Time (hours)
(a)

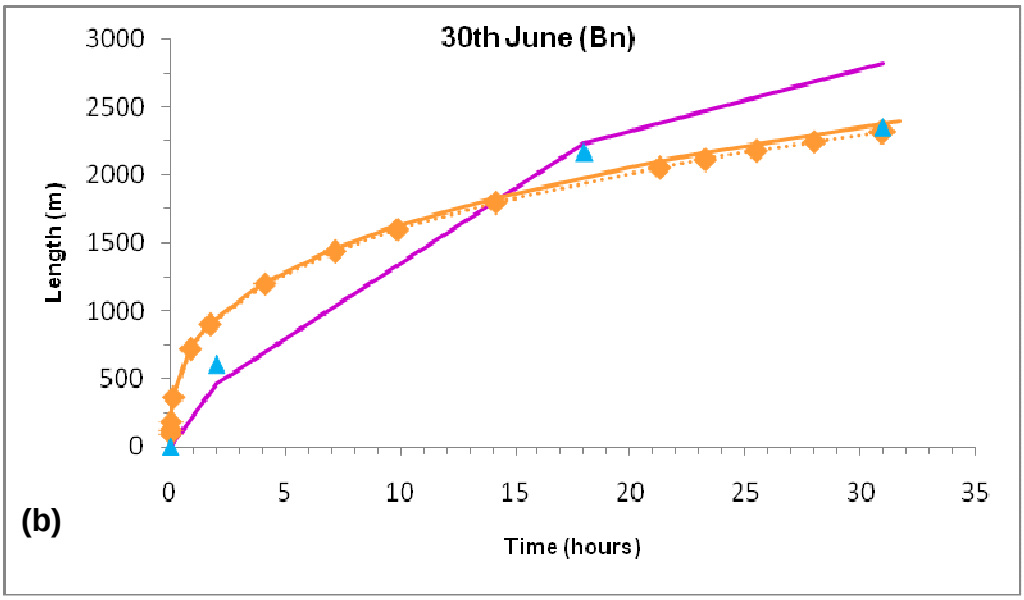
30th June (Bn)
Length (m)
Time (hours)
(b)

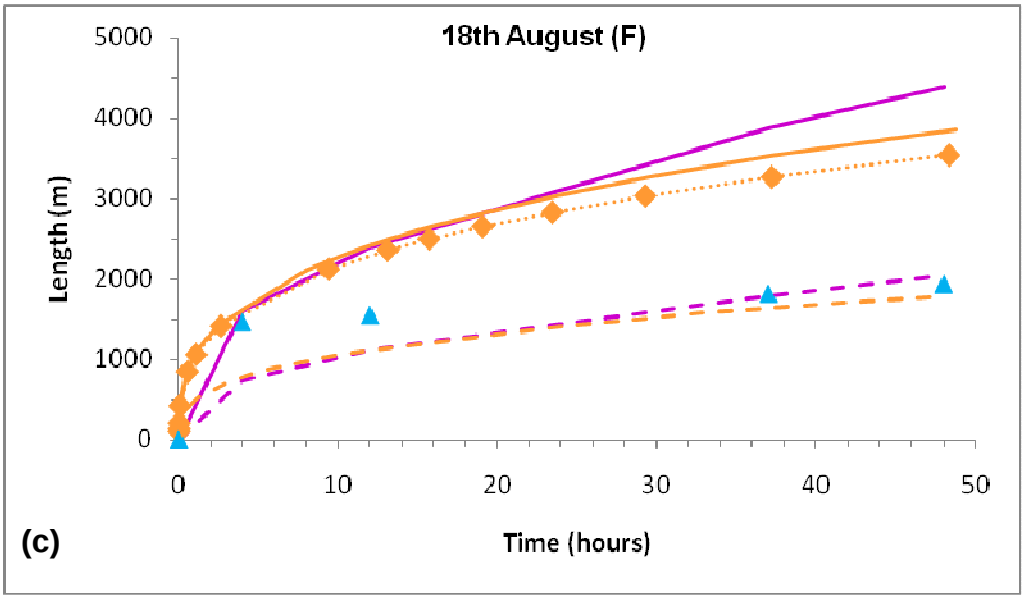
18th August (F)
Length (m)
Time (hours)
(c)

Table 4.11 Surface crust strength (CrS) and calculated final flow front height of three of the 1954 lavas in the surface crust strength regime comparison of measured flow front height with final flow front height for three of the 1954 lavas based on Lyman and Kerr (2006).

Flow Deposit	CrS[1] (Pa)	Final flow front height[1] (m)	CrS[2] (Pa)	Final flow front height[2] (m)	Measured flow front height (m) (Table 2.1)
4th June (A)	3.5 x 10^5	1.6	10^6	2.8	3.5
			$10^{6.5}$	4.9	
30th June (BnL)	7.9 x 10^5	3	10^6	3.5	3.2 to 4
18th August (F)	3.4 x 10^5	2.3	10^6	3.8	4.5

[1] Surface crust strength estimated for each lava based on measured flow deposit length and estimated volume (Table 2.1) and emplacement duration (Table 4.8). Final flow front height calculated as a function of surface crust strength and emplacement duration and denotes the maximum height at which the surface crust of a given strength can prevent further flow advance.
[2] Greater magnitudes of surface crust strength and corresponding final flow front heights.

At these viscosity values, the surface crust strength more accurately predicts flow propagation for each of the lavas for their entire flow length, although the crust strength regime slightly overestimates flow length of the 18th August (F) lava during the initial stages of emplacement.

However, comparison of predicted flow spreading under the surface crust strength regime at calculated crust strength values with the sloping viscous and sloping viscoplastic regimes at the higher viscosity values (i.e. viscosity increased by 10^2 and 10^3 Pa s) (Fig. 4.6) shows a less accurate fit of the surface crust strength regime than appeared in Fig. 4.5. In Fig. 4.6a, the sloping viscous regime with viscosity increased by 10^2 Pa s slightly more accurately predicts the initial stages of flow emplacement for the 4th June (A) lava than the surface crust strength regime, although the surface crust strength regime more closely predicts flow propagation for the remainder of the flow length, and accurately predicts flow propagation for the final three to four hours of emplacement. Conversely, the sloping viscous regime with viscosity increased by 10^3 Pa s much more accurately predicts flow propagation of the 30th June (Bn) lava for the first 18 hours of emplacement, with the surface crust strength regime only predicting flow length accurately for the last approximately half hour of emplacement (Fig. 4.6b). Similarly, the surface crust strength regime considerably overestimates flow

Fig. 4.4 (previous page) Comparison of estimated flow propagation over time of the three 1954 lavas (blue triangles) with predicted flow spreading at higher viscosities in the sloping viscous regime (pink curves) and the sloping viscoplastic regime at two yield strength values (solid orange line = 25 Pa; dashed orange line with diamonds = 2500 Pa). A, 4th June (A) lava at η_T x 10^2 Pa s; B, northern 30th June (Bn) lava at η_T x 10^3 Pa s; C, 18thAugust (F) lava solid lines and fine dashed line with diamonds at η_T x 10^2 Pa s, coarse dashed lines at η_T x 10^3 Pa s.

propagation of the 18th August (F) lava for most of its flow length, with the sloping viscous regime with viscosity increased by 10^2 Pa s more accurately predicting the initial two to four hours of emplacement, although the surface crust strength regime accurately predicts the final two hours of flow emplacement (Fig. 4.6c)

Fig. 4.7 compares predicted flow spreading of the surface crust strength regime at the greater surface crust strength value of 1 MPa (10^6 Pa) with the calculated surface crust strength regime for each of the three lavas and the sloping viscous and sloping viscoplastic regimes at greater viscosities. At this greater surface crust strength, flow spreading is more accurately predicted for the initial three to four hours emplacement of the 4th June (A) and 18th August (F) lavas (Figs. 4.7a,c), although the remainder of flow propagation is considerably underestimated by this crust strength. Conversely, the greater crust strength overestimates flow spreading of the 30th June (BnL) lava for the first ~18 hours of emplacement and underestimates flow propagation for the remainder of the flow duration.

These results suggest that surface cooling was not the major control on flow propagation for most of the flow emplacement of these three lavas, although depending on the strength of the surface crust the final stages of emplacement may have been controlled by some extent by surface cooling. However, the ability of the surface crust to cease further advance of the lava flow is dependant on the depth of the surface crust relative to the total depth of the lava at the flow front. The surface crust depth at the flow front grows diffusively as a function of the thermal diffusivity of the lava and emplacement duration (Griffiths and Fink, 1993). Lyman and Kerr (2006, equation 23, p.3) use this as the basis for calculating the maximum depth at which the flow front is held back by the surface crust of a given strength. Table 4.11 gives the calculated surface crust strength of each of the three 1954 lavas based on the estimated final stopping time of each flow and compares the measured flow front depth with the calculated maximum

Fig. 4.5 (next page) Comparison of estimated flow propagation over time of three 1954 lavas (blue triangles) with predicted flow spreading in the sloping viscous regime (pink line), the sloping viscoplastic regime at two yield strength values (solid orange line = 25 Pa; dashed orange line with diamonds = 2500 Pa) and the surface crust regime based on calculated surface crust strength of each of the lavas. Flow spreading in the sloping viscous and sloping viscoplastic regimes assumes the calculated total viscosity (η_T) of the 1954 lavas at 950°C (10902 Pa s). A, 4th June (A) lava. Crust strength = 3.5×10^5 Pa; B, northern 30th June (Bn) lava. Crust strength = 7.9×10^5 Pa; C, 18th August (F) lava. Crust strength = 3.4×10^5 Pa.

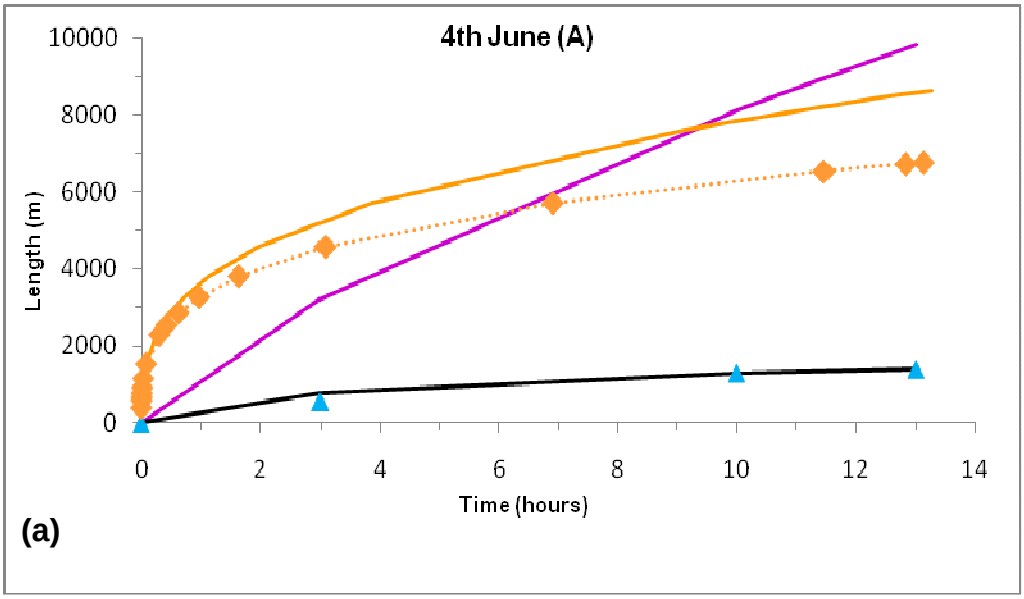
4th June (A)
Length (m)
Time (hours)
0
2000
4000
6000
8000
10000
0
2
4
6
8
10
12
14

(a)

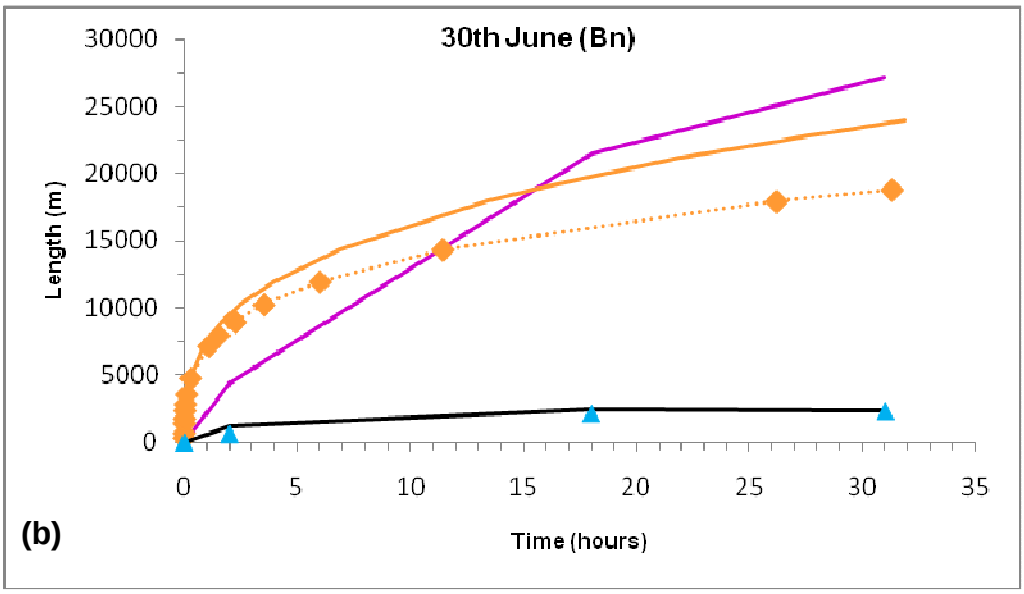
30th June (Bn)
Length (m)
Time (hours)
0
5000
10000
15000
20000
25000
30000
0
5
10
15
20
25
30
35

(b)

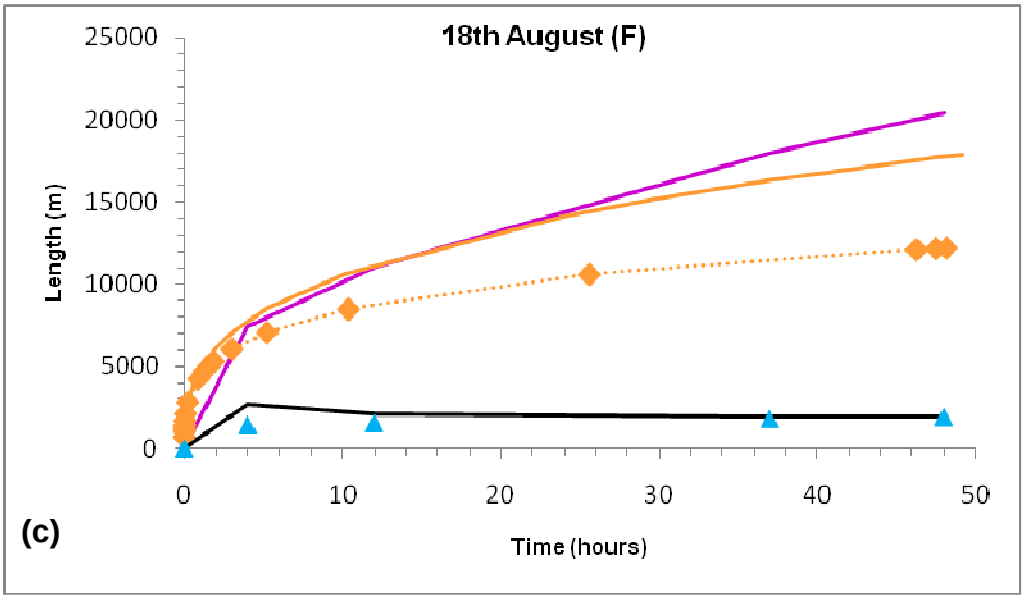
18th August (F)
Length (m)
Time (hours)
0
5000
10000
15000
20000
25000
0
10
20
30
40
50

(c)

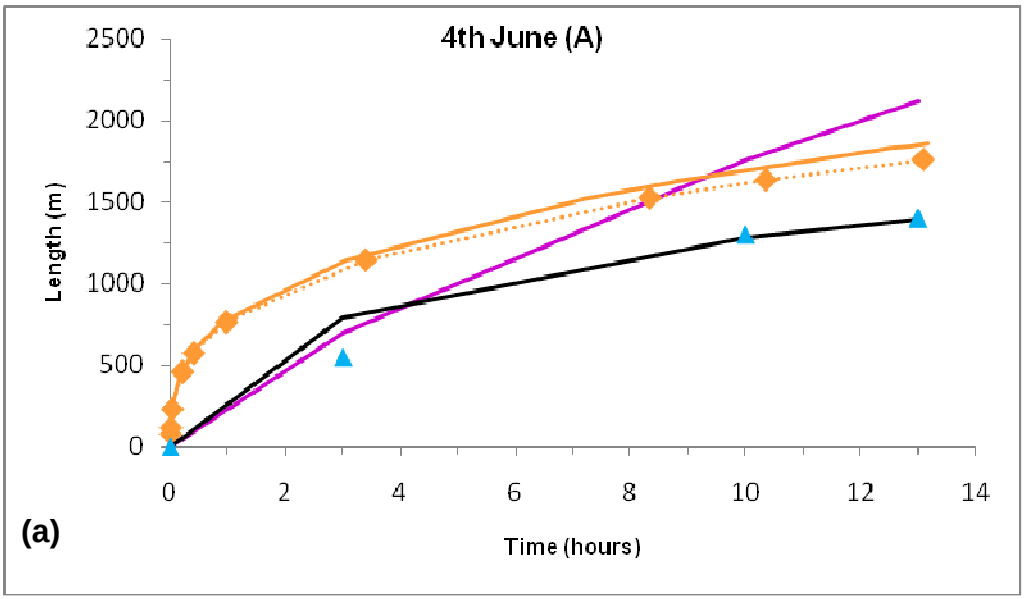
4th June (A)
Length (m)
Time (hours)
(a)

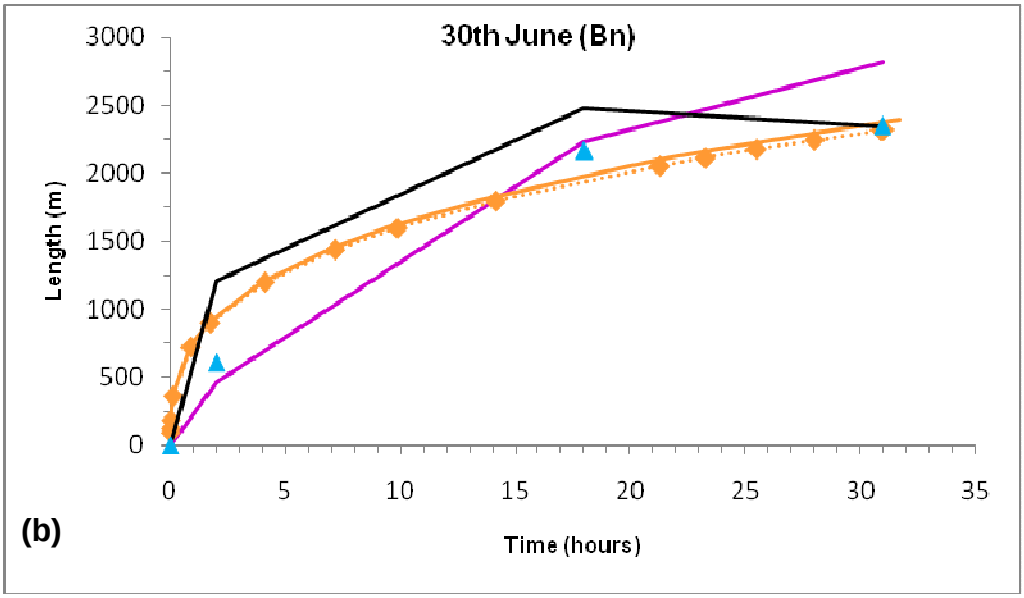
30th June (Bn)
Length (m)
Time (hours)
(b)

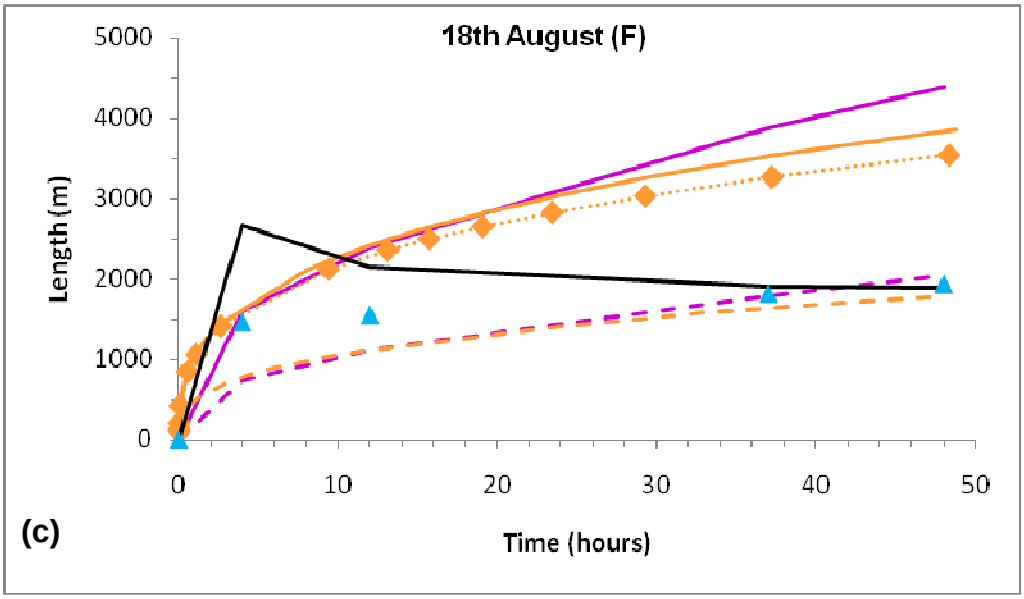
18th August (F)
Length (m)
Time (hours)
(c)

flow front depths at which the strength of the surface crust can effectively prevent further flow advance. At calculated surface crust strength values, the strength of the surface crusts of the 4th June (A) and 18th August (F) lavas would be able to prevent further flow advance at depths approximately 2 m less than the measured flow front heights of these two flow deposits. However, the calculated surface crust strength of the 30th June (BnL) lava would be able to prevent further advance of this lava at ~ 0.2 to 0.8 m less than the measured flow front heights of this flow. Increasing the surface crust strength by 0.5 to 1 order of magnitude (i.e. to between 10^6 to $10^{6.5}$ Pa) would enable the surface crust to prevent further flow advancement at depths comparable to the measured flow front heights of each of these lavas.

Predicted Effusion Rate Trends For Three 1954 Lavas

The estimated erupted volume of lava for each of the three 1954 lavas is plotted as a function of time and compared with the predicted volume erupted assuming a steady effusion rate, and the predicted volume assuming an exponentially decreasing eruption rate over time (Fig. 4.8). The estimated volume erupted during the 4th June (A) lava appears to more closely follow the predicted pattern of a steady eruption rate, although the estimated volume erupted over time is greater than the predicted volume (Fig. 4.8a). However, there does appear to be a slight decrease in eruption rate over the emplacement duration of this lava. Conversely, the estimated erupted volumes of the 30th June (BnL) and 18th August (F) lavas appear to more closely follow the predicted pattern of an exponentially decreasing eruption rate. Although this predicted volume considerably overestimates erupted volume during the initial two hours of the 30th June (BnL) lava, the decreasing discharge rate pattern of the estimated volume is reasonably comparable with the predicted model (Fig. 4.8b). Similarly, the predicted volume for an exponentially decreasing eruption rate during the initial four hours of the 18th August (F) lava is greater than the estimated volume, however the steadily

Fig. 4.6 (previous page) Comparison of estimated flow propagation over time of three 1954 lavas (blue triangles) with predicted flow spreading at higher viscosities in the sloping viscous regime (pink line), the sloping viscoplastic regime at two yield strength values (solid orange line = 25 Pa; dashed orange line with diamonds = 2500 Pa) and the surface crust regime based on calculated surface crust strength of each of the lavas. A, 4th June (A) lava at η_T x 10^2 Pa s; crust strength = $3.5x10^5$ Pa; B, northern 30th June (Bn) lava at η_T x 10^3 Pa s; crust strength = $7.9x10^5$ Pa; C, 18th August (F) lava solid lines and fine dashed line with diamonds at η_T x 10^2 Pa s, coarse dashed lines at η_T x 10^3 Pa s; crust strength = $3.4x10^5$ Pa.

decreasing eruption rate evident for the remainder of the flow compares well with the predicted model (Fig. 4.8c).

Kerr and Lyman (2007) found that their prediction model for the volume erupted with an exponentially decreasing eruption rate underestimated the actual volume erupted during the first ~ 100 days of the Lonquimay lava flow, but accurately predicted the volume erupted for the remainder of the flow emplacement duration (330 days). Kerr and Lyman (2007) note that the higher than predicted volume of lava erupted during the first 100 days of the Lonquimay eruption was primarily due to changes in vent geometry over the initial stages of the eruption, and argue that, excluding other factors controlling eruption rate, their model is valid for predicting lava volumes for exponentially decreasing eruption rates. Therefore, the overestimation of erupted volume during the first two to four hours of emplacement of the 30th June (BnL) and 18th August (F) lavas suggests that discharge rate may have been relatively variable during the initial stages, although it appears to have stabilised thereafter into a steadily decreasing discharge rate. The difference in the pattern of estimated volume erupted over time between the three 1954 lavas also suggests that discharge rates were variable between lava flows as well as during the emplacement of individual lavas.

Fig. 4.7 (next page) Comparison of estimated flow propagation over time of three 1954 lavas (blue triangles) with predicted flow spreading at higher viscosities in the sloping viscous regime (pink line), the sloping viscoplastic regime at 2500 Pa yield strength (dashed orange line with diamonds) and the surface crust regime at the calculated surface crust strength (solid black lines) of each of the lavas and at a surface crust strength of 10^6 Pa (dashed black lines). A, 4th June (A) lava at η_T x 10^2 Pa s; calculated crust strength = $3.5x10^5$ Pa; B, northern 30th June (Bn) lava at η_T x 10^3 Pa s; calculated crust strength = $7.9x10^5$ Pa; C, 18th August (F) lava solid lines and fine dashed line with diamonds at η_T x 10^2 Pa s, coarse dashed lines at η_T x 10^3 Pa s; calculated crust strength = $3.4x10^5$ Pa. Note: the sloping viscoplastic regime at higher viscosity and with an internal yield strength of 25 Pa is not shown.

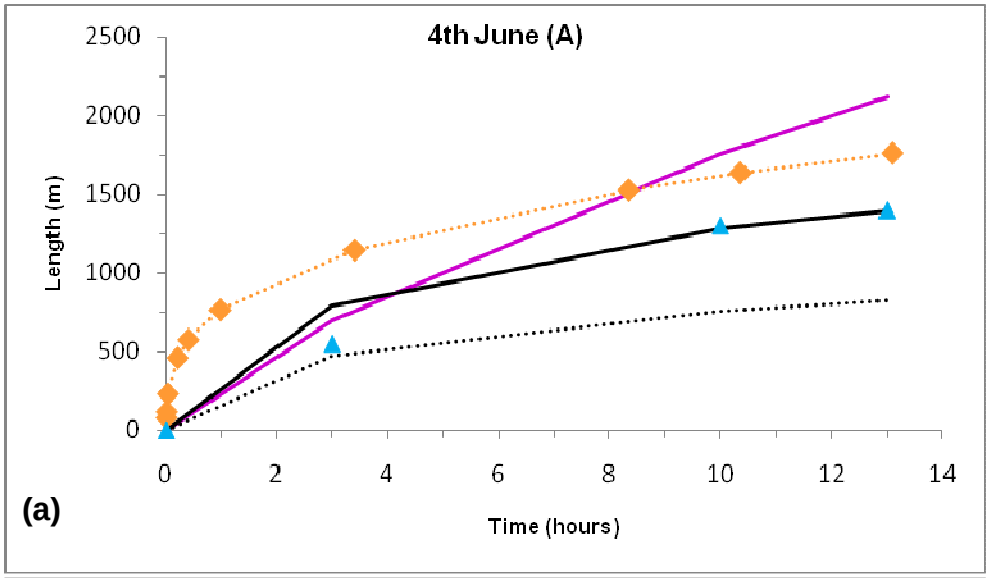
4th June (A)
Length (m)
2500
2000
1500
1000
500
0
0
2
4
6
8
10
12
14
Time (hours)
(a)

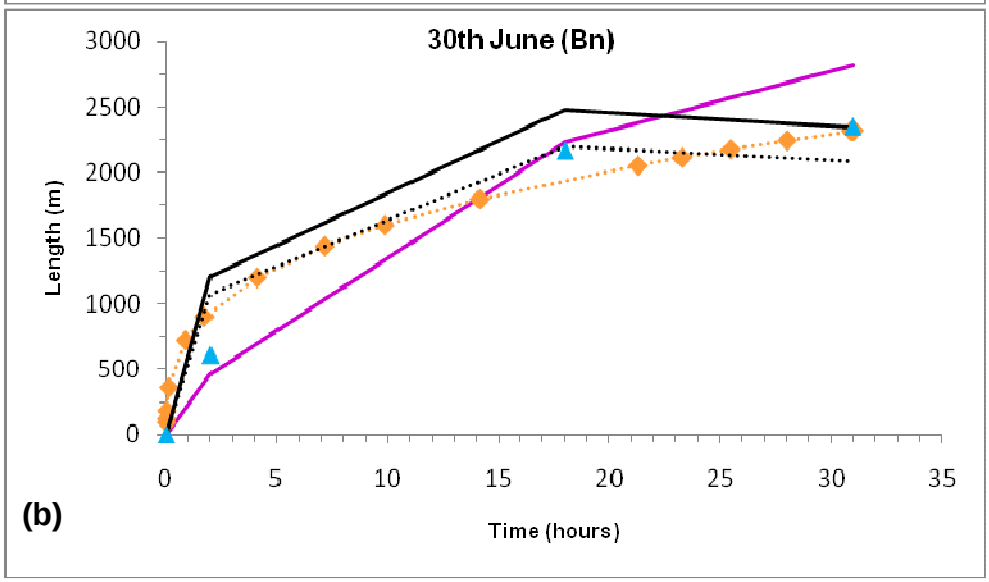
30th June (Bn)
Length (m)
3000
2500
2000
1500
1000
500
0
0
5
10
15
20
25
30
35
Time (hours)
(b)

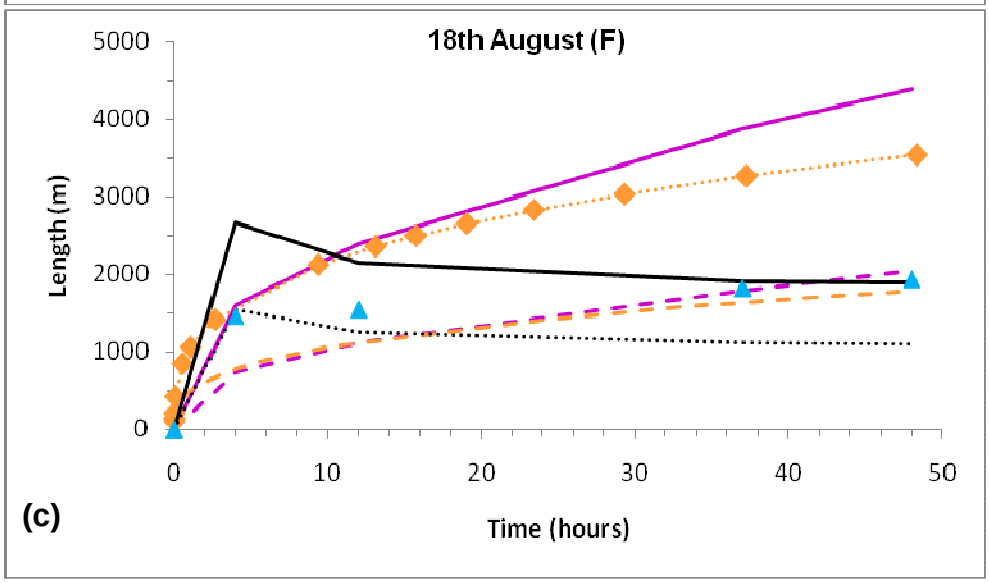
18th August (F)
Length (m)
5000
4000
3000
2000
1000
0
0
10
20
30
40
50
Time (hours)
(c)

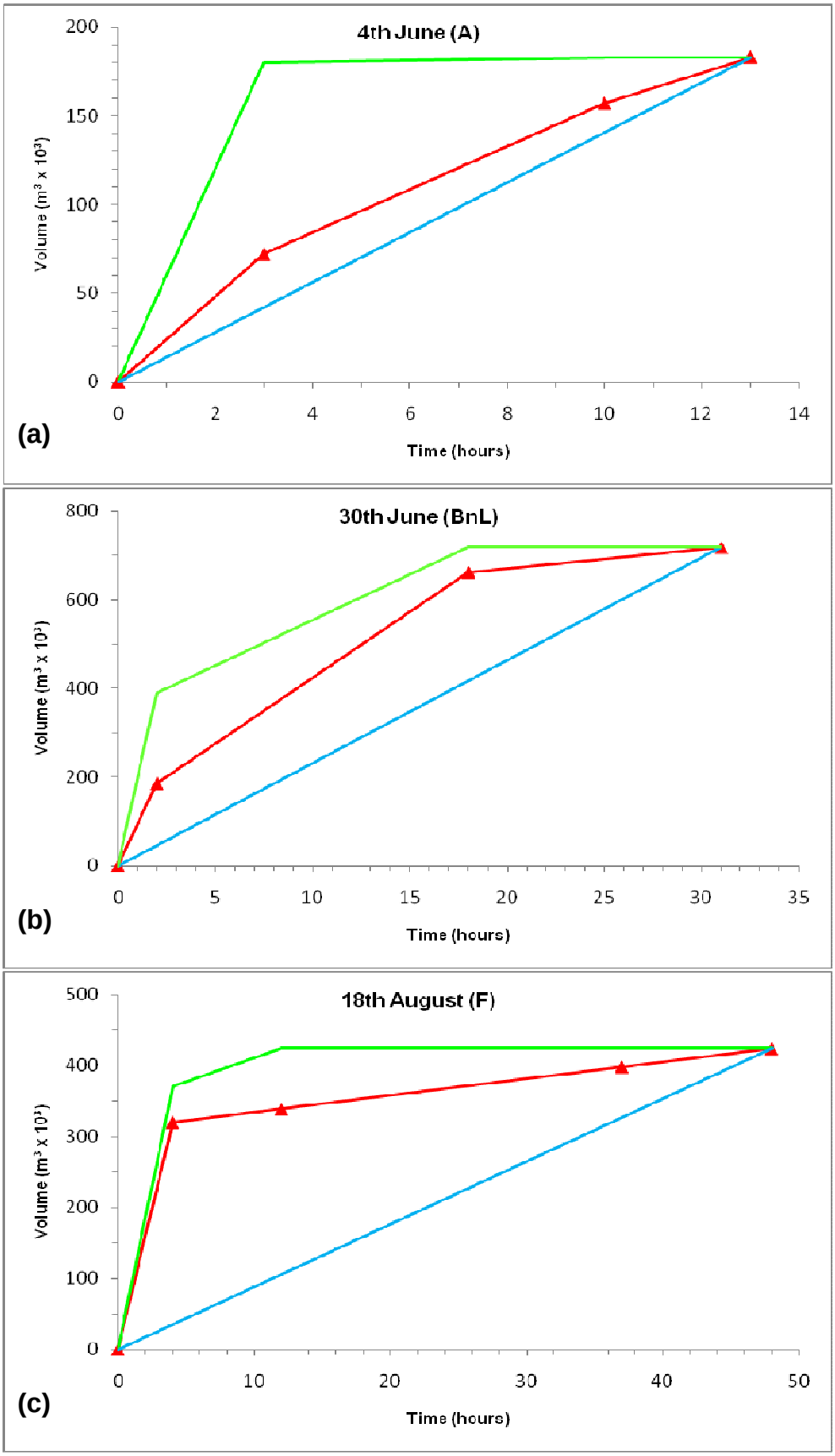

Fig. 4.8 Comparison of the estimated volume of the three 1954 lavas erupted as a function of time (red line with triangles) with calculated volume erupted during a steady rate of effusion (blue line) and with an exponential decrease in effusion rate over time (green line) using the Lyman and Kerr (2007) model. A, 4th June (A) lava; B, northern 30th June (Bn) lava; C, 18th August (F) lava.

CHAPTER 5

Discussion

5.1 INTRODUCTION

Understanding the processes that determine the propagation, growth and geometry of lava flows, particularly the controls on final flow length, are essential when assessing the potential hazard posed by the lava flow to humans, property and the environment (Borgia and Linneman, 1990). The aim of this chapter is use the data presented in previous chapters to determine the factors controlling the growth of the 1954 lavas and to ascertain how the information presented here can be employed to determine the behaviour of future lava flows at Mount Ngauruhoe. The role of rheological properties, eruption conditions, and environmental controls in determining the dynamics of lava flow emplacement are discussed, and an interpretation of these processes in relation to the 1954 lavas is given. A model for the emplacement dynamics specific to the 1954 lava flows is proposed and used to infer the emplacement behaviour of previous Mount Ngauruhoe lava flows. Implications for the behaviour of future lava flow events at Mount Ngauruhoe and potential monitoring and flow behaviour prediction measures are suggested. Field locations referred to in this chapter are underlined in parentheses, and are shown in either Fig. 2.5 or Appendix D.1.

5.2 RHEOLOGICAL & ENVIRONMENTAL CONTROLS ON LAVA FLOW MORPHOLOGY, GEOMETRY & TEXTURE

5.2.1 Controls on Lava Flow Morphology

Lava Flow Field Morphology

Borgia and Linneman (1990) relate the large-scale morphological characteristics of a lava flow field to its emplacement conditions by distinguishing the difference between a *unit* flow and a *composite* flow. The former is described as a finite

quantity of lava that is emplaced during a single, continuous phase of effusion, maintaining fluid continuity along its entire length as it moves downhill away from the vent. Conversely, composite flows are made up of more than one individual flow unit that traverse the same flow path as the original flow unit and are emplaced over short periods of time. As composite flows evolve, each flow unit adds a new layer of lava to the marginal levees. Similarly, Kilburn and Lopes (1991) suggest that under the simplest of conditions an effusive episode will produce a single *arterial* flow, which is characterised by stationary lateral margins and a central channel zone along which lava flows from the vent to the flow front. *Compound* flows are formed where new arterial flows propagate from existing arterial flows under conditions where, for example, the existing flow bifurcates around topographical barriers, or lateral flow margins are breached or overflowed by hot lava from within the channel. Compound flows are generally formed when effusive activity continues after the original arterial flow has stopped moving. Growth of the compound flow continues either by simple thickening of the existing flow as new lava accumulates beneath the surface of the cooled crust, superpositioning of a new discrete arterial flow on top of the cooled arterial flow, widening, or lengthening of the initial arterial flow due to breaching or overflow of the cooled flow margins. Walker (1972) observed that single *unit* or *arterial* flows typically result from high effusion rates, whereas *compound* or *composite* flows form due to the slow effusion of low viscosity lava. Using polyethylene glycol wax (PEG) experiments, Blake and Bruno (2000) confirmed Walker's (1972) observations, finding that the growth of a compound flow is primarily due to the combined effects of effusion rate, initial lava viscosity and eruption duration, and hence the volume of material erupted. The importance of eruption duration lies in the time required for a cooled, surface crust to form. With sufficient time and providing effusive activity continues at the source vent, the mechanical strength of the cooled crust prevents further spreading of the lava, resulting in the breakout of hot lava from the interior through the cooled margins and thus propagating a new flow.

The first map of the 1954 lavas (Gregg, 1956) is based on eyewitness accounts of the eruption, in which individual lava flows are known to have been emplaced on specific dates, thereby inferring that the 1954 lava flow field is composed of a

collection of single, discrete, unit (or arterial) flows. However, the multiple lobes of the 30th June (B) lava flow and the small 'breakout' lobe on the southern margin of the 18th August (F) lava flow deposit (Fig. 2.5) more closely conform to the compound flow morphology described by Kilburn and Lopes (1991). Furthermore, because the proximal margins of individual flow deposits are not clearly identifiable either on aerial photograph analysis or *in situ*, and with the exception of the 4th June (A) and northern-most 14th July (Da) lava flows, the 1954 lavas appear as a single, broad lava flow deposit (Fig. 5.1); thus, if the emplacement history of these lavas was unknown the overall planimetric form of the flow field could be described as a compound flow. Additionally, using the description of Kilburn and Lopes (1991), the emplacement of several of the 1954 lavas over earlier 1954 flow deposits [e.g. the 8-13th July (C), middle 14th July (Db), and 29th July (E) lavas overlie the 30th June (B) flow deposit] would also render classification of the 1954 lavas as a compound flow. However, based on Borgia and Linneman's (1990) composite flow classification, the emplacement of new lava flows over the preceding original arterial flow would occur within a few days, whereas there is eight to 29 days between the emplacement of the underlying lava flows and the superpositioned flow deposits. Vigorous fire-fountaining activity at the vent is also reported to have been intermittent during the 1954-55 eruption (Gregg, 1956), indicating that the lava flows are more likely to have been the product of individual effusive episodes. It is therefore primarily due to documented eyewitness accounts that the 1954 lava flow field can be classified as a collection of individual, discrete flow units, suggesting that the flow field evolved as a result of intermittent effusive episodes characterised by high effusion rates.

Unit Lava Flow Morphology

Most of the 1954 lava flow deposits display simple, relatively straight and narrow planimetric forms, with the exception of the 30th June (B) and 18th August (F) lavas which are distinguished by the multiple lobes of the former, and the s-shaped deposit of the latter (Fig. 2.5). These distinct morphological features occur at the medial to distal regions of the two flow deposits, while the proximal regions are comparable to the simple straight planimetric form displayed by the

remaining 1954 lavas. This implies that the factors influencing individual lava flow morphology may have changed with increasing distance from the vent. The planimetric form of the individual 1954 lava flow deposits were controlled to a large degree by the factors controlling the physical dimensions of each flow deposit, discussed in the following sections.

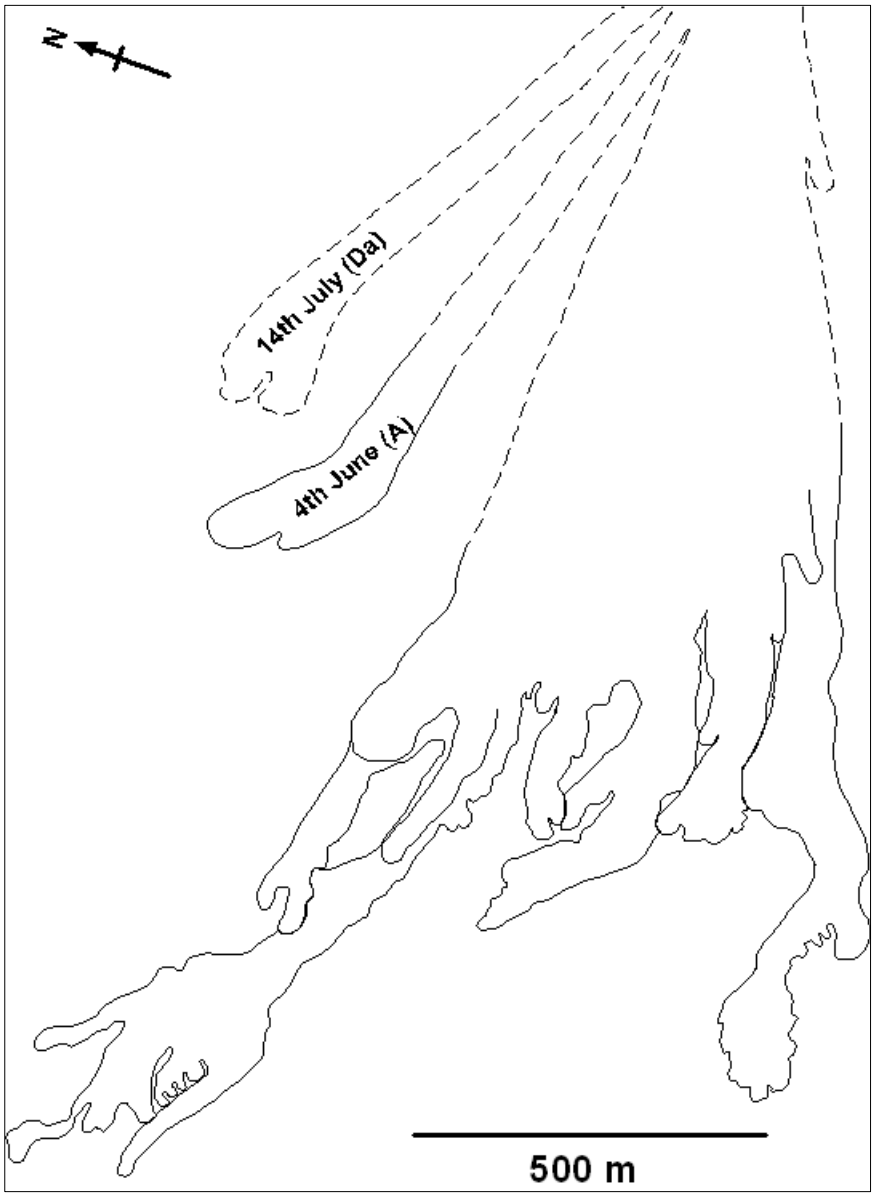

Fig. 5.1 Planimetric form of the 1954 lava flow field as it would appear if the dates of emplacement for individual flow units were unknown. Solid line represents clearly defined flow margins. Dashed line denotes inferred flow margins of the flow field.

5.2.2 Controls on Lava Flow Width and Depth

Yield Strength

Hulme (1974) proposed that the extent of lateral spreading and thinning of a lava flow is controlled by the yield strength of the lava and theorised that lavas must behave as isothermal Bingham fluids because a Newtonian fluid would continue to spread laterally until either pre-existing topographical barriers or the surface tension of the lava restricted further spreading; in the latter case resulting in an extremely thin flow deposit. Additionally, Hulme (1974) discounted cooling of the lava as a controlling factor because lava flows tend to reach a fixed width and depth shortly after propagation begins, reducing the time available for the cooled surface to gain the strength required to prevent lateral spreading. Therefore, in the absence of confining topographical features, Hulme (1974) theorised that lava flow width and depth are dependant on effusion rate, underlying slope angle and the rheological properties of the lava, predicting that there is a critical flow depth at which the yield strength of the lava exceeds the shear stress at the base of the flow. Below this critical flow depth longitudinal flow (i.e. downstream flow) does not occur, resulting in a zone of stationary lava. Because lava flows typically reduce in depth towards the outer flow margins (Rossi, 1997), the flowing lava is bounded on either side by these stationary lava zones, which develop into levees, thus preventing further lateral spread. This fixed flow width is maintained throughout the remainder of the flow length providing effusion rate and slope angle remain unchanged (Hulme, 1974). Based on this premise, Hulme (1974) found that levee height is proportional to yield strength and is therefore an indication of lava flow depth during emplacement.

Hulme's (1974) theory has commonly been used as the basis for modelling lava flow rheology and emplacement (e.g. Dragoni *et al*., 1986; Fink and Zimbelman, 1990; Moore *et al*., 1992; Stevenson *et al*., 1994a; Fink and Griffiths, 1998). However, the yield strength values for the 1954 lavas calculated using the Hulme (1974) model (Table 4.5) are significantly greater than the values derived using the Pinkerton and Stevenson (1992) model (Table 4.4) and reported laboratory measurements for basaltic andesite lavas (e.g. Pinkerton and Norton, 1995). The use of lava flow deposit dimension parameters to calculate yield strength is known

to produce values up to several orders of magnitude greater than laboratory measurements of melt yield strength (e.g. Moore *et al*., 1978; Hupert *et al.*, 1982; Fink and Zimbelman, 1990). Dragoni *et al*. (1986) observed that the Hulme (1974) model overestimates yield strength in relatively narrow flow deposits where flow depth is considerably greater than the expected critical flow depth due to greater basal friction. Similarly, Sparks *et al*. (1975) showed that because width and depth are assumed to remain constant throughout the length of the flow, the Hulme (1974) model considerably overestimates yield strength in situations where there are significant downflow width and depth variations. The use of mean flow width and depth values in calculating the yield strength of the 1954 lavas may therefore explain the large discrepancy between yield strength values derived using the Hulme (1974) model and those derived using the Pinkerton and Stevenson (1992) model.

Although the margins of individual 1954 lava flow deposits proximal to the crater rim are not clearly identifiable, Gregg's (1956) map implies that downflow width generally remains constant from the crater rim throughout the length of the flow deposit in all except the three longest lavas [30th June (B), 14th July (Dc), 18th August (F)]. Additionally, in a contemporary photograph of the 1954 eruption (Fig. 5.2), the proximal zones of these three lava flow deposits appear to retain relatively constant flow widths from the crater rim over the steeper slopes of the cone, with flow width variations only occurring towards the medial and distal regions of these flow deposits. Thus, the use of mean flow width values to calculate rheological parameters should be reasonably valid for most of the 1954 lava flows.

The mean flow depth values used in the yield strength calculations are based on multiple measurements of *in situ* lateral flow margin depths, although these were recorded at medial to distal locations of the 1954 lava flow deposits relative to the crater rim (Fig. 2.5 and Appendix D.1) and may not reflect the depth of the proximal regions of these flow deposits. In analogue experiments using PEG wax emplaced over a range of slope gradients Gregg and Fink (2000) found little variation in depth along flow length at any slope angle, although PEG flows emplaced on slopes > 40° were generally thinner than those emplaced on

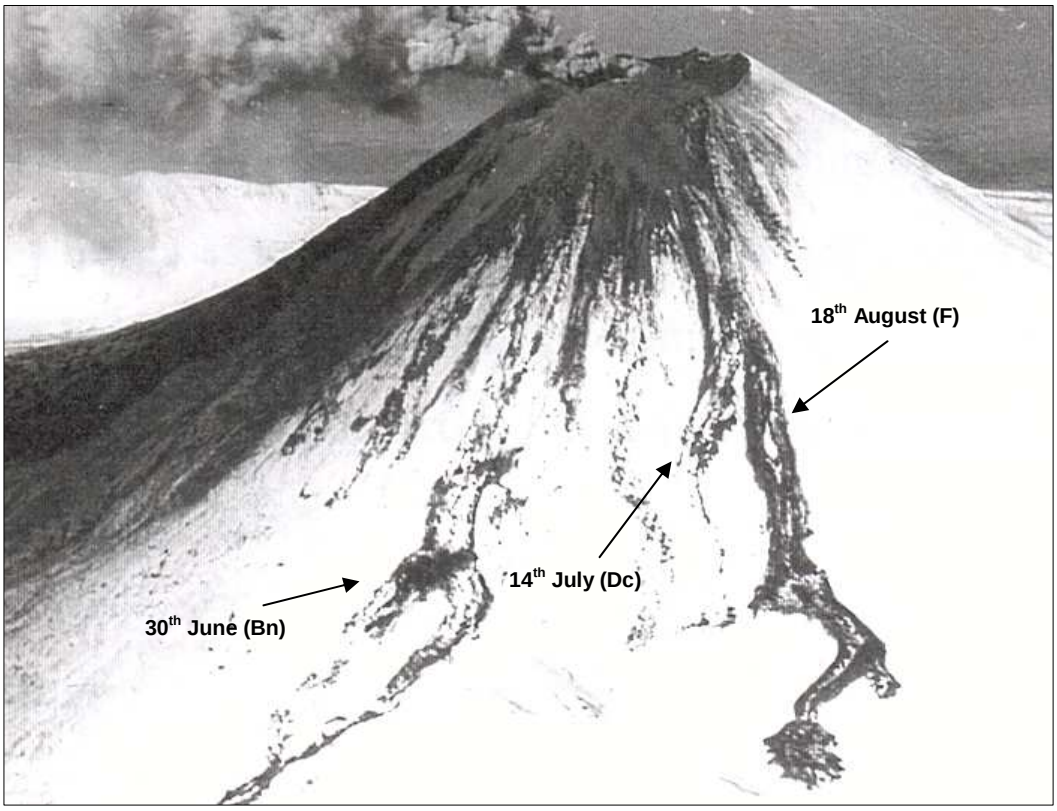

Fig. 5.2 Recently emplaced lavas of the 1954 eruption on the north-western slopes of Mount Ngauruhoe. Flow width appears relatively constant from the crater rim for most of the flow deposit length. Proximal deposits are partially covered by ash. Photographed on 3rd September 1954 (Gregg, 1956).

shallower slopes. However, these experimental PEG flows were emplaced over surfaces with a constant slope angle, whereas there are considerable local slope angle variations underlying the 1954 lavas. Baloga *et al*. (1995) observed that the 1801 Hualalai lava flow, emplaced over an average ~ 6° slope, increased in depth from ~ 2 to 3 m near the source vent to ~ 5 to 8 m deep 15 km downflow. The marginal levees of the 18th August (F) lava flow deposit display a marked downflow increase in height, from ~2 to 3 m depth near the front of the 16th September (G) lava flow deposit (F38) to ~ 8 to 12 m depth at the medial zone (F1b) (Fig. 2.5 and Appendix D.1), suggesting that some flow thickening occurred during the emplacement of this flow deposit with distance from the source vent. Therefore, if thickening of the 1954 lava flows did occur between the proximal regions on the steep upper slopes and the medial to distal regions on shallower slopes, it is possible that the high yield strength values derived using the Hulme (1974) model may be due to an overestimation of the mean flow depth values (2.5 to 3.5 m) for the 1954 lavas. However, assuming a reduced mean flow depth of

0.5 m and an average underlying slope angle of 28° the Hulme (1974) model gives a minimum yield strength of ~ 6 x 10^3 Pa, which is over two orders of magnitude greater than the yield strength values derived using the Pinkerton and Stevenson (1992) model and is at the higher end of the possible range of basaltic andesite yield strength values (i.e. ~ 10 to 10^3 Pa) inferred from published yield strength values of basaltic and rhyolitic lavas (e.g. Pinkerton and Sparks, 1978; Moore *et al*., 1992; Stevenson *et al*., 1994a; Pinkerton and Norton, 1995; Fink and Griffiths, 1998). Alternatively, if the low yield strength value derived using the Pinkerton and Stevenson (1992) model (~ 25 Pa) is more representative of the 1954 lavas, according to Hulme (1974) lateral flow spreading would cease at the unrealistically low critical flow depth of ~ 0.1 to 0.5 cm, depending on underlying slope angle.

The problem in comparing the yield strength values derived using the morphology-based model of Hulme (1974) and the Pinkerton and Stevenson (1992) petrography-based model is in the basic principles of the models themselves. Hulme's (1974) model was developed as a means to determine the factors controlling the lateral spread of lava and uses yield strength as a parameter to calculate the critical depth at which a lava flow will cease to spread. Conversely, the Pinkerton and Stevenson (1992) model is intended to quantify the yield strength of quenched lava using the principle that yield strength develops in a lava when neighbouring crystals within the melt form a bridging network. If both models are equally valid they should produce similar yield strength values, whereas the large discrepancy between the values derived using these two models suggests that either one or both of the models may not be reliable methods for quantifying the yield strength of the 1954 lavas. However, there may be other explanations for the inconsistency of these models. For example, if the lava flow deposits thicken downflow with decreasing slope angle, then, assuming a lower mean flow depth value than that used, the Hulme (1974) model may more accurately reflect the yield strength of the 1954 lavas than the Pinkerton and Stevenson (1992) model, particularly those flow deposits with little apparent variation in downflow width. Conversely, the 1954 lavas may have initially ceased to spread laterally at low critical flow depths of ~ 1 cm or less, consistent with the low yield strength of the Pinkerton and Stevenson (1992) model, but

variations in effusion rate and/or slope angle may have increased the depth of the flow deposit during later stages of emplacement when the flow margins had cooled sufficiently to prevent further lateral spread. Alternatively, yield strength may not have been the primary control on flow width and depth, which would also support the lower value derived from Pinkerton and Stevenson (1992). Instead, lava flows may have been confined close to the vent by pre-existing topographic features no longer evident because they have been subsequently covered by more recent eruption deposits. The existence of partially confining ridges adjacent to some 1954 lava flow deposits on the lower slopes (e.g. Fig. 2.30), and the high-relief remnant lava flow deposits present near the summit on the south-eastern section of the cone (Fig. 5.3) support this hypothesis. Other factors, for example effusion rate, slope angle, velocity or viscosity may have had a greater control on flow width and depth than yield strength, therefore the low values derived using the Pinkerton and Stevenson (1992) model may more accurately reflect the yield strength of the lavas. Alternatively, the low Pinkerton and Stevenson (1992) values may represent the initial yield strength of the 1954 lava during the early stages of flow emplacement, while the higher values derived using the Hulme (1974) model may reflect the yield strength of the cooling lava towards the distal flow margins, implying that yield strength increased over time.

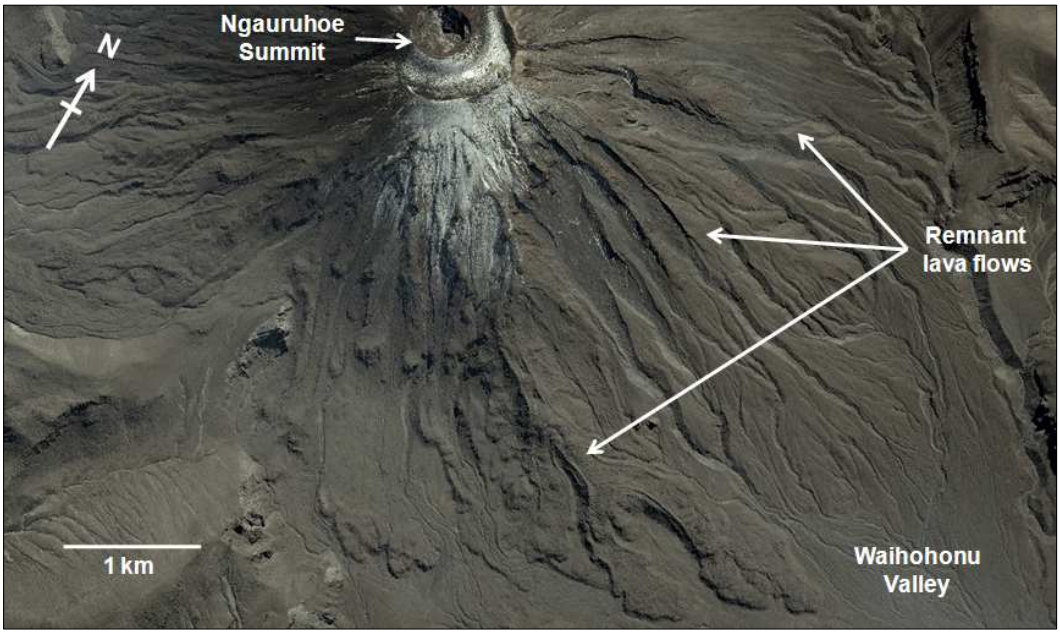

Fig. 5.3 Aerial photograph showing the high relief of remnant lava flow deposits near the crater rim on the south-eastern flanks of Mt Ngauruhoe. Aerial photograph courtesy of GNS Science, Wairakei.

This final point is supported by laboratory measurements in which yield strength significantly increased as lava cooled below its liquidus (e.g. McBirney and Murase, 1984; Fink and Zimbelman, 1990). Fink and Zimbelman (1990) calculated an exponential downflow increase in yield strength, by up to two orders of magnitude, over the length of the 1983 Pu'u O'o lavas; although yield strength was calculated using the Hulme (1974) model and the Pu'u O'o lavas extend for much greater distances from the vent (~ 5 to 8 km) than the 1954 lavas. Crown and Peiterson (1995) suggest that the effects of cooling and crystallisation during downflow emplacement changes the properties of the lava, including yield strength, and may in turn result in changes to the downslope dimensions of the lava flow. Fink and Zimbelman (1990) propose that, in addition to surface cooling and crystal growth, localised basal stresses due to underlying surface roughness may also contribute to downflow yield strength changes. Crown and Peiterson (1995) also suggest that downflow thickness of the flow deposit would be inversely related to slope angle if yield strength remained constant throughout the length of the flow, whereas neither Crown and Peiterson (1995) or Gregg and Fink (2000) found any significant correlation between slope angle and flow thickness in their experimental research. Changes in yield strength may therefore be due to the mechanical strength of a cooling, solidifying surface crust and/or the internal strength of an expanding framework of crystals as cooling promotes new crystal growth.

There is considerable evidence for continued crystal growth during lava flow emplacement. For example, Lipman *et al*. (1985) showed that degassing of volatiles during lava flow emplacement rapidly undercools the melt, promoting crystal growth. Guilbaud *et al*. (2007) noted that the relatively large abundance of groundmass crystals (~ 20 to 40% volume) in the 1783-84 Laki lavas resulted in a significant increase in the downflow yield strength and viscosity of the lava. The ability of microlites to grow during flow emplacement was demonstrated by Crisp and Baloga (1994), who measured a 15 to 25% increase in microlite abundance over a period of 100 to 230 minutes during the emplacement of the 1984 Mauna Loa lava flow. Although the yield strength values of the 1954 lavas derived using the Pinkerton and Stevenson (1992) model are based on the abundance, size and shape of crystals within quenched lava samples, and should therefore reflect the

yield strength of the cooled lava, the abundance and size of smaller phenocrysts (< 0.1 mm) and groundmass microlites was not accounted for. The groundmass of the 1954 lavas is dominated by abundant microlites, with minimal quantities of interstitial glass (Fig. 3.13E). Given that groundmass accounts for ~ 40 to 60% volume of the whole rock (Table 3.1), and with microlite crystals accounting for ≳ 90% of the groundmass, it is possible that some microlite growth occurred during flow emplacement, which may have increased the downflow yield strength (and viscosity) of the 1954 lavas.

There appears to be compelling evidence that the yield strength of the 1954 lavas may have increased downflow, which suggests relatively low values of yield strength during initial flow emplacement and may explain the discrepancy between the values derived using the Hulme (1974) and Pinkerton and Stevenson (1992) models. This implies that yield strength is unlikely to have been the major control on flow width and depth during the early stages of flow emplacement although it may have had more influence downflow as the lava cooled and yield strength increased.

Effusion Rate and Underlying Slope Angle

Changes in the downflow dimensions of lava flows (i.e. width and depth) reflect temperature- and/or time-dependant variations in both eruption processes and the rheological properties of the lava, as well as responses of the lava to the underlying slope gradient and topography (Crown and Peiterson, 1995). Hulme (1974) suggests that changes in flow width are more directly related to slope angle than to effusion rate, in that flow width is inversely proportional to slope, whereas large increases in effusion rate may either only slightly increase flow width, or have no effect on flow width if previously constructed marginal levees have cooled sufficiently to confine the flow channel within a fixed position. A reduction in effusion rate may also result in the construction of new levees inside the original levees, and therefore channel width rather than total flow width is reduced (Hulme, 1974). Similarly, Gregg and Fink (2000) found in PEG analogue experiments that average flow width increased with decreasing slope angle in all simulated flow situations, although they also found that high effusion rates tended

to generate wider flow deposits than low effusion rates, even on steep slopes. Conversely, Crown and Peiterson (1995; 1996), suggest that cyclical widening and narrowing of lava flow deposits may reflect episodes of surging and waning effusion rates, although the authors also attribute other factors, for example, a decrease in flow velocity or an increase in lava viscosity, as controls on downflow width variation.

As previously noted, although most of the 1954 lavas display relatively constant flow widths throughout their lengths, the three longest flow deposits [30th June (Bn), southern-most 14th July (Dc), 18th August F)] show a greater variation in downflow width towards their medial and distal zones. For example, the southern lower lobe (BnL-S) of the 30th June Bn lobe group narrows in width beyond the distal end of the northern lower lobe (BnL-N) (Bn15), followed by significant widening further downflow (Bn16) (Fig. 2.5). The southern-most 14th July (Dc) lava maintains a relatively constant width throughout most of its length, but widens considerably over the final ~ 200 m of the deposit length (Figs. 2.5, 2.25). The 18th August (F) lava flow deposit displays the greatest downflow variation in width, with significant widening of the deposit to the east of Pukekaikiore ridge, followed by marked narrowing of the deposit as it extends around the southern end of the ridge, and subsequent widening at the flow front (Fig. 2.5). These episodes of widening may therefore reflect the response of each of the lava flows to changes in effusion rate and/or slope angle; however, the relatively uniform flow width of these and the remaining 1954 lava flow deposits on the steeper slopes of the cone suggests that slope angle, rather than effusion rate may be the major control on flow width variations. Additionally, localised widening of each of these lava flow deposits coincides with a marked decrease in slope angle to almost horizontal gradients. For example, both the distal region of the 14th July (Dc) lava and the medial zone of the 18th August (F) lava to the east of Pukekaikiore ridge rest on a gentle ~ 9° slope, while the subsequent narrowing of the latter flow deposit in the distal zone coincides with an increase in slope angle to 16°.

Widening of lava flow deposits at regions of markedly reduced slope angle is consistent with the findings of Arpa *et al.* (2008) who observed that the

accumulation of lava at the slope break formed the widest segment of each of the 2006 Mayon basaltic andesite lavas. However, Crown and Peiterson (1995) demonstrated that the width and depth of the 1983-84 basaltic Pu'u O'o lavas were insensitive to 6 to 12 m scale (or larger) changes in the topography, although these lavas are compositionally more mafic than the 1954 lavas and were emplaced over much lower average slope gradients (~ 1 to 7°). If slope angle rather than effusion rate controlled the width of the 1954 lavas, the ability of these lavas to spread laterally on shallower slopes after a relatively long distance of sustained flow width suggests that yield strength may have been considerably lower than the values derived using the Hulme (1974) model. It also implies that the lateral flow margins had not cooled sufficiently to prevent lateral spreading. Widening of the 18th August (F) lava on the eastern side of the Pukekaikiore ridge is predominantly taken up by the width of the northern levee, whereas the central flow channel width remains relatively constant (Figs. 2.4A, 2.5), confirming that cooling of the flow margins may have been insufficient to prevent lateral spreading.

It appears that the main influence on flow deposit width of the 1954 lavas near the source vent was either pre-existing topographical features or effusion rate. However, in the absence of topographic obstacles, slope gradient appears to have had greater control on flow width both over the steeper slopes of the upper cone and over shallower slope gradients near the base of the cone. Yield strength may have increased to some extent downflow but the ability of the lava to spread laterally with distance from the vent suggests that yield strength may have remained relatively low.

5.2.3 Controls on Lava Flow Length

The distance that lava flows extend from their source vent poses the greatest potential hazard during effusive eruptions; therefore understanding the factors that control lava flow length enables the development of predictive flow behaviour models to determine the extent of this hazard. The constraints on lava flow length have been well-debated (e.g. Walker, 1973; Malin, 1980; Guest *et al.*, 1987; Pinkerton and Wilson, 1994; Calvari and Pinkerton, 1998). Lava flows are

generated under conditions where the yield strength of the lava is less than both the gravitational force and the degree of shear stress at the base of the lava (Borgia *et al*., 1983). However, it is the factors controlling the ability of the lava to spread longitudinally, and thus the cessation of further flow advance, that determine the final length of the flow.

Lava Viscosity

Lava viscosity is known to increase downstream during flow emplacement, for example, the viscosity of the 1984 Mauna Loa lavas is estimated to have increased by several orders of magnitude during five days of flow advance (Crisp *et al*., 1994). Similarly, Fink and Zimbelman (1990) estimated that the viscosity of the 1983 Pu'u O'o lava increased exponentially by up to three orders of magnitude over the distance of the flow, although these viscosity estimates were based on a rearrangement of the Jeffreys equation rather than on the geochemical composition of the lava. As demonstrated in Chapter 4, lava viscosity is highly dependant on temperature, increasing rapidly with relatively small decreases in temperature. For example, the total viscosity calculated for the 1954 lavas more than triples in value between 1000 and 950°C (Table 4.2), thus downflow cooling alone will have a marked effect on the viscosity of the melt. Additionally, a relatively small reduction in volatile content (e.g. from 0.4 to 0.02% volume) has a significant effect on the viscosity of the 1954 lavas (Fig. 4.1), thus, if degassing occurs during flow emplacement, viscosity would markedly increase.

Crystal abundance has also been shown to have a significant effect on the viscosity of the 1954 lavas (Table 4.2), with suspension viscosity increasing by 400% with a 50% increase in crystal abundance (from 27 to 41% volume). The Pinkerton and Stevenson (1992) model used to calculate the suspension viscosity of the 1954 lavas is based on the principle that lava is unable to flow when the volume of crystals in the melt is greater than the critical crystal abundance value ($Ø_{max}$) of 60% volume. The maximum crystal abundance of the 1954 lavas (41%) was determined from quenched lava samples, therefore it appears that this critical abundance was not reached and that suspension viscosity had no control on the length of the 1954 lavas. However, phenocryst modal abundance analysis did not

include the groundmass microlite population, and, as discussed in the previous section, it is possible that microlite growth may have occurred during flow emplacement increasing overall crystal abundance. Therefore, if microlites are included in the phenocryst population, the total crystal abundance of the quenched 1954 lavas would be > 60%, suggesting that crystal growth during flow emplacement may have had a significant impact on lava viscosity, which would ultimately prevent the continued downflow advance of the lavas. However, Pinkerton and Stevenson (1992) note that the $\emptyset_{max}$ value of 60% only gives a reasonable approximation of the critical abundance at which lava will cease to advance, thus it is possible that lavas may be able to advance at crystal concentrations greater than 60%.

The physical presence of vesicles is known to have a marked effect on lava viscosity; although, depending on the ratio between the internal strength of the bubble and the external viscous stress of the melt, vesicle abundance may either increase or decrease lava viscosity (Llewellin and Manga, 2005). In the case of the 1954 lavas, because the majority of vesicles are either spheroid or ellipsoid in shape the internal vesicle strength was assumed to be greater than the external viscous stress, therefore an increase in vesicle abundance would result in an increased lava viscosity (Table 4.2). There is strong evidence that volatile exsolution continues during lava flow emplacement, resulting in a downflow decrease in vesicularity. For example, Lipman and Banks (1987) noted a vesicularity decrease in the 1984 Mauna Loa a'a lavas, from > 85% near the vent to < 20% at 10 to 15 km distance from source. The high vesicle abundance at the vent significantly decreased the apparent viscosity of the lava due to thin, easily deformable vesicle walls, thus, as vesicularity reduced downflow, apparent viscosity increased (Lipman and Banks, 1987). Similarly, Cashman *et al*. (1994) reported a downflow decrease in vesicularity of the 1983 Kilauea lavas with increasing distance from the vent.

Vesicle abundance of the 1954 lavas was determined from quenched samples of lava collected at medial to distal locations of the flow deposits and is assumed to reflect lava vesicularity towards the final stages of flow emplacement after

degassing has occurred. It is therefore possible that vesicle abundance was significantly greater on eruption, implying that lava viscosity was high at the vent and decreased downflow as vesicle abundance reduced with degassing. In contrast, statistical analysis of bulk lava flow deposit vesicularity suggests that vesicle abundance significantly increased downflow during emplacement of the 18th August (F) lava (Table 3.3). However, these results are based on quantitative analysis of a small number of samples (n = 100) collected at one proximal and one distal site on the flow deposit and may not be fully representative of the degassing processes that may have occurred during flow emplacement. Additionally, although there is a statistically significant difference in vesicularity between the two sample sites ($P = 0.39^{-4}$), vesicle abundance increased by only 4% volume, which would result in a reasonably small increase (~ 10%) in lava viscosity. The 1984 Mauna Loa and 1983 Kilauea lavas are more mafic in composition, and were emplaced over much greater distances and duration times (Lipman and Banks, 1987; Cashman *et al*., 1994) than the 1954 lavas. The relatively higher SiO_2 composition of the 1954 lavas may have reduced the ease with which volatiles could escape during flow emplacement, while the downflow increase viscosity subsequent to cooling and crystallisation may also have prohibited volatile exsolution. Thus, it is possible that either vesicle abundance did not decrease sufficiently downflow to affect viscosity, or that the combined effect of cooling and crystallisation on lava viscosity negated any decrease in viscosity caused by a downflow reduction in vesicle abundance. Alternatively, vesicle abundance may have initially increased during flow emplacement as volatiles exsolved from the melt, but the relatively short emplacement duration of the 1954 lava flows resulted in quenching of the lava before volatiles could completely escape and thus reduce vesicle abundance. Assuming that the viscous shear rate remained lower than the internal strength of the bubbles, this would have resulted in an increase in viscosity as vesicle abundance increased.

Velocity

The rate at which a lava flow advances away from the source vent may not necessarily in itself influence its final length, in that flow rate affects the length of time the lava takes to reach a certain distance from the vent rather than the ability

of the lava to reach that distance. However, the time required for a lava flow to reach any given distance influences the cooling rate of the lava, thus lava flows with high velocities are able to advance to a greater distance from the vent before the surface of the lava starts to cool than those with low velocities (Gregg and Fink, 2000). Flow velocity is highly dependant on both the underlying slope angle and the viscosity of the lava. For example, the calculated velocity of the 1954 lavas decreases by 99% when temperature is reduced from 1150 to 950°C (Table 4.6), demonstrating the marked effect increasing lava viscosity has on flow velocity. This results in a continuous feedback effect where cooling of the lava increases viscosity, resulting in a reduction in flow velocity, which in turn increases the cooling rate of the lava. In addition, the strong dependence of slope angle on flow velocity compounds this feedback effect. Flow velocity reduces with decreasing slope angle, with relatively small gradient changes on gentler slopes having a much greater effect on velocity than the same gradient change on steeper slopes. For example, the calculated velocity of the 1954 lavas decreased by 16% with an 11° reduction in slope angle from 53°, and decreased by 50% with a 10° reduction in slope from 19° (Table 4.6). Thus, as the underlying slope angle of the 1954 lavas decreased, flow velocity would have significantly decreased and the cooling rate increased. Although the calculated velocity values (Table 4.6) derived using the Jeffreys equation are considerably greater than the reported velocities of the 1954 lavas (Table 4.8), the marked reduction in the reported velocity of the 30th June (B) lava flow, from ~ 300 m h^{-1} over the steep upper slopes of the cone, to ~ 14 m h^{-1} on the lower, shallow slopes (Gregg, 1956) supports these findings.

The relationship between lava viscosity and flow velocity combine to influence the duration of lava flow emplacement, controlling the cooling rate of the lava, and may therefore be a secondary control determining the final length of the flow.

Effusion Rate

Walker (1973) proposed that effusion rate is the most important factor controlling flow length, particularly in cases where high effusion rates result in proportionally lower cooling rates over distance compared with low effusion rates. Similarly,

Franzetta and Romano (1984) suggest that the length of the 1983 Mount Etna lava was controlled by short-term fluctuations in effusion rate. Although Malin (1980) found a poor relationship between flow length and effusion rate in Hawaiian lavas, on a re-evaluation of the data presented by both Walker (1973) and Malin (1980), Pinkerton and Wilson (1994) found that the relationship between effusion rate and flow length proposed by Walker (1973) is valid for non-tube-fed (i.e. channelised) lavas emplaced over $\gtrsim$ 30 to 48 hours. Similarly, Calvari and Pinkerton (1998) observed a strong correlation between flow length and effusion rate for many of the channel-fed Mount Etna lavas, while the flow field formed during the 1991-93 Mount Etna eruption reached a distance 3 km further than predicted by this relationship due to the development of tube-fed rather than channel-fed flow emplacement systems. Gregg and Fink (2000) also found that flow length generally increased with increased effusion rate and slope angle in PEG analogue experiments, although depending on other parameters (e.g. cooling rate, viscosity, temperature) high effusion rates also occasionally produced much shorter flow lengths.

There is no evidence for the development of lava tubes during the emplacement of the 1954 lavas, and all but the 30th June (Bn) and 18th August (F) lavas are estimated to have been emplaced in less than 30 hours; therefore, the relationship proposed by Pinkerton and Wilson (1994) should only apply to these two lavas. However, the use of calculated effusion rate values to determine flow emplacement duration using the Pinkerton and Wilson (1994) model significantly underestimates duration time for all of the 1954 lavas compared to reported duration times (Table 4.8) at both the calculated (Table 4.7) and estimated mean flow velocities (Table 4.9). As with yield strength calculations, mean flow width and depth values are used to calculate effusion rate and emplacement duration, which may account for the discrepancies in calculated versus documented flow duration times. Alternatively, effusion rate may not have been the main factor controlling the length of the 1954 lavas, although effusion rate does appear to have a direct influence on the cooling rate of lava, which may subsequently influence the final flow length.

Volume

Guest *et al*. (1987) proposed that lava flows cease to advance because they are either volume-limited, cooling-limited, or are obstructed by pre-existing topographical barriers. Volume-limited lavas advance until the supply of lava from the source vent is terminated, after which flows may either cease to advance immediately, or move forward at diminishing velocity as un-cooled lava in the central flow channel continues to advance towards the flow front (Borgia *et al*., 1983). In the latter case this results in drained or partially drained flow channels bounded by abandoned levees, a feature typically seen in many of the Pu'u O'o lavas (Pinkerton and Wilson, 1994). The 18th August (F) lava is the only 1954 flow deposit to display evidence of channel drainage (Fig. 2.28), suggesting that the length of this flow alone was controlled by the supply of lava from the source vent. Conversely, the absence of drained flow channels within the remaining 1954 lava flow deposits implies that either they ceased to advance immediately once lava supply was terminated, or that their final length was limited by cooling rather than volume. The Grätz numbers (G_z) derived from the Pinkerton and Sparks (1976) model for six of the 1954 lavas (Table 4.10) are significantly greater than the critical G_z defining cooling-limited flow lengths (300 to 100), indicating that the length of each of these lavas was controlled by volume. In contrast, the Pinkerton and Wilson (1994) model determined that the two longest 1954 lavas [30th June (Bn) and 18th August (F)] would reach a G_z of 300 in less time than the estimated emplacement duration of these two flows (Table 4.10), implying that these flow lengths were limited by cooling rather than by volume and conflicting with the evidence indicated by the drained flow channel of the 18th August (F) lava flow deposit. However, if the length of cooling-limited lava flows are defined by the lower critical G_z of 100, then none of the six 1954 lavas would have reached the critical G_z within their estimated emplacement duration, indicating that each of their flow lengths were limited by volume.

These conflicting results may be due to the use of mean flow deposit dimensions (width and depth), which, as discussed previously, may not accurately reflect the dimensions of the 1954 lavas. In particular, the mean depth of the 18th August (F) lava was difficult to quantify due to the drained proximal zone flow channel, the

elevated marginal levees, and the markedly lower central flow channel surface of the medial zone. Additionally, the basis for the critical Grätz number (300 to 100) is derived entirely from empirical data for basaltic lavas (e.g. Pinkerton and Sparks, 1976; Hulme and Fielder, 1977; Pinkerton and Wilson, 1994), with no supporting analogue or mathematical data. Therefore, it is possible that the calculated Grätz numbers do not accurately reflect the role of cooling- versus volume-limiting factors in controlling the lengths of the 1954 lavas. Alternatively, although the estimated emplacement duration for each of the 1954 lavas is based on a combination of reported flow velocities, and the time and distance of flow advance from the vent (Gregg, 1956), there is some degree of ambiguity in these estimates, which may account for the contradiction between the calculated Grätz numbers derived from the Pinkerton and Sparks (1976) and Pinkerton and Wilson (1994) models for the 30th June (B) and 18th August (F) lavas.

Surface Cooling

With the cooling-limited lavas defined by Guest *et al*. (1987), effusive activity and lava flow advance continues for a sufficient enough time to allow significant cooling of the flow surface and lateral margins to occur. Although cooling increases lava viscosity and yield strength, it also promotes the growth of a chilled crust on the flow surface. As the mechanical strength of the cooling crust increases the flow front thickens, reducing flow velocity to zero, and thereby prohibiting further flow advance even if the supply of lava from the source vent continues. Consequently, this will either result in flow thickening throughout a significant portion of the flow length, superposition of a new lava flow on top of the earlier cooled flow deposit, episodes of overspill or breakout of hot lava from the interior core of the flow through the cooled levees or flow front (boccas) Guest *et al*. (1987).

The effects of cooling on lava viscosity and yield strength have already been discussed; however, more recent research has focused on the role of surface cooling and the mechanical strength of a cooled surface crust in determining emplacement dynamics, morphology, and the final length of the flow (e.g. Griffiths and Fink, 1993; Lyman *et al*., 2005; Lyman and Kerr, 2006; Kerr and

Lyman, 2007). In most lava flows, cooling during flow emplacement is confined to a thin, partially solid, partially brittle carapace on the top surface of the flowing lava which deforms in response to flow conditions (Griffiths and Fink, 1993). Griffiths and Fink (1993) use the example of pillow lava formation, in which at irregular, short-lived intervals hot lava breaks through the otherwise strong, rapidly chilled crust, to show that a cooled, solidified surface crust plays a dynamic role in controlling the spread of lava. The presence of a surface crust will act to insulate the interior core of the lava flow from radiative heat loss, except where fractures in the crust expose the inner core to significant heat loss (Baloga *et al*., 1995). Insulation of the flow interior prevents rapid cooling of the lava, minimising any significant downflow changes to lava viscosity and yield strength, although this will primarily depend on the growth rate and integrity of the surface crust. Borgia and Linneman (1990) suggest that by continually modifying the distribution of lateral and vertical shear stress within the lava flow, the cooled surface crust actively controls dynamic flow processes, including flow front velocity, levee formation, and the formation of pressure ridges on the flow surface. Additionally, Kilburn (1993) attributes the 'healing' time of crust fractures to the manner of flow advance. For example, slow healing times reduce the strength of the crust and its ability to influence the behaviour of the flowing lava beneath the crust, resulting in a steady rate of flow advance largely governed by the dynamics of the flow interior. Conversely, relatively fast healing times result in varying degrees of crust integrity and strength, and, because a strong solid crust restricts the advance of the underlying hot lava, the flow rate fluctuates between alternating episodes of fractured and solid crust over time; thus flow advance is dominated by crustal resistance.

Griffiths and Fink (1993) determined that where effusion rates are high and/or cooling rates are low, a large solid crust forms at a greater distance from the vent than with low effusion rates and high rates of cooling. They conclude that the cooled surface crust is the dominant factor in ceasing further flow advance when the crust reaches a critical thickness; which occurs when "the ratio of crust thickness near the flow front to flow length is greater than the ratio of the crust's yield stress to the basal shear stress exerted on the bulk of the flow" (Griffiths and Fink, 1993, p701). The depth of the surface crust at the flow front grows

diffusively as a function of time and the thermal diffusivity of the lava (Griffiths and Fink, 1993), although a thin chilled crust may develop on the surface of the flow channel within tens of minutes to a few hours Crisp and Baloga (1990). Therefore, a combination of effusion rate, duration of effusive activity, and flow emplacement duration are the major controls on the growth and strength of the surface crust and its subsequent ability to control flow advance.

Using the Lyman and Kerr (2006) theoretical flow spreading models, Kerr and Lyman (2007) demonstrated that the strength of the surface crust was the dominant factor determining the final length of the 1988-90 Lonquimay lava flow. However, the Lonquimay lava is andesitic in composition (~ 58 wt. % SiO2), and, because of a very low crystal content (< 1%), was determined to have had no internal yield strength. The Lonquimay lava flow advanced for ~ 330 days with an overall mean flow velocity of ~ 33 m h^{-1}, and a flow front velocity range of ~ 152 to 1.3 m h^{-1} (Naranjo *et al*., 1992; Kerr and Lyman, 2007). The relatively low mean flow velocity and long flow emplacement duration would have enabled the growth of a well-chilled, strong surface crust, which would subsequently have had a major influence on flow advance. In comparison, the 1954 basaltic andesite lavas are less silicic in composition, and were emplaced over considerably shorter duration times (~ 2 to 48 hours) and at greater estimated mean flow velocities (~ 100 m h^{-1}) than the Lonquimay lava; thus, the rate of cooling and subsequent strength of the cooling surface crust would be significantly lower.

Based on the predictive models of Lyman and Kerr (2006) and Kerr and Lyman (2007), propagation of the three longest 1954 lavas [4th June (A), northern 30th June (Bn), 18th August (F)] is more closely predicted by a spreading regime in which surface crust strength is the dominant factor, than by viscous or viscoplastic flow spreading behaviour (Figs. 4.5 to 4.7). However, the predicted surface crust strength regime generally overestimates flow propagation up to the final two to six hours of emplacement, strongly suggesting that surface cooling was not the dominant factor limiting flow advance; although the surface crust may have developed enough strength to limit flow length in the final stages of emplacement. The estimated propagation patterns of these three 1954 lavas over time are derived from reported flow velocities and relatively ambiguous estimates of the distances

the lavas had reached from the vent (Gregg, 1956). Therefore, depending on the degree of accuracy in these estimates, it is possible that actual flow propagation may more closely resemble the predicted pattern of the surface crust strength regime. However, the duration and flow velocities of the initial stages of flow advance over the steep upper slopes of the cone, and the subsequent reduction in flow velocity on shallower slopes is reasonably well constrained for the 4th June (A) and 18th August (F) lavas, and it is during these initial stages of flow advance that the predicted spreading of these flows in the surface crust strength regime is most greatly overestimated. Additionally, the *in situ* measured flow front depths of the three 1954 lava flow deposits are significantly greater than the maximum depth at which the calculated surface crust strength of each lava flow could effectively prohibit further flow advance (Table 4.11); conflicting with the apparent correspondence of predicted flow spreading in the surface crust strength regime with the estimated flow propagation pattern during the final stages of flow emplacement (Figs. 4.5 to 4.7).

The Lyman and Kerr (2006) surface crust strength model assumes that a solid, unfractured crust grows during flow propagation; whereas, if the crust is fractured its strength, and therefore ability to control flow advance, would be compromised. The markedly autobrecciated deposits of the 1954 lavas (e.g. Figs. 3.1 to 3.3) indicates that flow surfaces were highly fractured, possibly throughout the duration of flow emplacement. However, if the strength of the surface crust was lower than the calculated values for each of the three 1954 lavas (Table 4.11), the surface crust strength model should underestimate, rather than overestimate flow propagation because flow advance should theoretically be faster without the constraining influence of a strong surface crust. Interestingly, the predicted spreading behaviour of lava with a greater crust strength value (10^6 Pa) does underestimate flow propagation of the 4th June (A) and 18th August (F) lavas for most of their flow lengths (Fig. 4.7); although at this crust strength flow advance is more accurately predicted during the initial stages of flow emplacement. Thus, it is possible that a cooling surface crust with a strength of ~ 10^6 Pa initially controlled flow advance, but that subsequent fracturing reduced crust strength, diminishing its ability to influence continued flow propagation. However, the *in situ* measured flow front depths are more comparable to the maximum depth at

which this greater surface crust strength could effectively prohibit flow advance (Table 4.11), implying that the surface crust maintained its strength throughout the length of the flow, which is not reflected in the predicted propagation models for this crust strength. Additionally, the high flow velocities reported on the steep upper slopes of the cone would result in slow cooling rates, precluding the development of a surface crust strength of this magnitude during the early stages of flow emplacement. Furthermore, a crust strength of 10^6 Pa is more comparable to the surface crust strength of fractured silicic domes (Iverson, 1990), and is two orders of magnitude greater than the expected crust strength of basaltic to andesitic lavas (Blake and Bruno, 2000). It therefore seems unlikely that surface crust strength was the main factor controlling the length of these lavas.

Another limitation of the Lyman and Kerr (2006) flow spreading prediction models is that in analogue experiments PEG/kaolin slurries were released instantaneously, and therefore the models assume a rapid but steady effusion rate. In modelling the 1988-90 Lonquimay lava, Kerr and Lyman (2007) expanded the model equations to incorporate the effect of an exponentially decreasing effusion rate. This technique was not applied to the predictive 1954 lava flow spreading regime models because the available data suggests that effusion rate did not decrease exponentially over flow emplacement duration. Instead, assuming both the estimated flow propagation patterns (Figs. 4.5 to 4.7) and estimated flow deposit volumes (Table 2.1) are reasonably accurate, effusion rate appears to have been relatively high, although variable, during the early stages of flow emplacement, followed by a steadily decreasing rate for the remainder of the flow emplacement duration (Fig 4.8). A relatively unsteady effusion rate during the early stages of flow emplacement would account for the overestimation of flow propagation predicted by the surface crust strength model, indicating that the length of the 1954 lavas was more likely to have been limited by lava supply (i.e. volume) rather than by surface cooling.

The volume- and cooling-limited flow morphologies described by Guest *et al*. (1987) are comparable to the Kilburn and Lopes' (1991) classification of arterial and compound flows, with volume-limited lava flow morphology coinciding with that of arterial lava flows, and cooling-limited lavas akin to compound lava flow

morphology. In agreement with the factors controlling the development of arterial and compound flows (Walker, 1972; Blake and Bruno, 2000), Guest *et al*. (1987) conclude that short duration, high effusion rates tend to produce volume-limited flows, whereas low effusion rates over long durations are more likely to produce cooling-limited lavas. Although, most of the 1954 lava flow deposits do not display evidence of flow channel drainage, the morphological characteristics of the 1954 lavas are otherwise consistent with those of volume-limited lavas, implying that final flow length was predominately limited by the cessation of lava supply rather than by cooling of the lava, and supporting the previous evidence for high effusion rates.

5.2.4 Controls on Lava Flow Surface Features and Textures

Lava Flow Surface Features

Pinkerton and Sparks (1976) observed that prominent levee and channel morphologies developed in the 1975 Mount Etna lavas at relatively higher rates of effusion (e.g. > 0.002 $m^3 s^{-1}$) than those with less pronounced levees and channels. This is a considerably lower effusion rate than those calculated for the 1954 lavas (Tables 4.7, 4.9), therefore it should be expected that all of the 1954 lava flow deposits would display channel and levee morphologies. As this is not the case, the implication is that either the calculated effusion rates for the 1954 lavas are markedly overestimated by the Hulme and Fielder (1977) model or that effusion rate is not the major control on the development of channel and levee morphologies.

Gregg and Fink (2000) observed in PEG analogue experiments that at any given slope angle, effusion and cooling rates were the two major controls on the development of flow surface features. Four distinct morphologies, characterised by different rates of effusion and surface cooling developed during these simulations. For example, at the lowest effusion rate and highest cooling rate, the PEG deposits formed morphologies comparable with pillow lavas, while rifted and folded flow morphologies developed at progressively increasing effusion rates and decreasing cooling rates. In folded flow morphologies, the surface of the deposit developed a series of folds perpendicular to the downstream flow

direction, with the distance between each fold (wavelength) typically consistent on all slope gradients. Although slope angle did not control fold wavelength, surface folding occurred at increasingly greater distances from the source vent with increasing slope angle. Additionally, fold sets tended not to span the entire flow channel width on shallow slopes (~ 10° or less); instead, two or more fold sets developed across the channel width, which were separated by a linear zone of uncooled liquid. At the highest effusion rate and lowest cooling rate PEG flows formed levee and channel morphologies, although in some cases of very high effusion rate and very low cooling rate, flow deposits showed no evidence of solidification at the lateral margins. Folding of the flow channel surface also tended to develop on leveed flows advancing over horizontal surfaces, while small lobes or pillows often formed at PEG flow margins on shallow slopes (≤ 30°) associated with lower flow velocities (Gregg and Fink, 2000).

The surface features of the 18th August (F) lava flow deposit are comparable to the leveed flow morphologies described by Gregg and Fink (2000). For example, the elevated marginal levees and drained central flow channel in the proximal zone of the flow deposit (Fig. 2.28), while the multi-toed nature of the flow front (Fig. 2.34) may correlate to the lobe or pillow morphologies associated with shallow slopes and low velocities. Additionally, the low-elevation ridges observed within the central flow channel of the medial zone (Fig. 2.29A) coincide with a marked reduction in slope angle from an average of ~ 38° to ~ 9°; comparable to the multiple surface fold sets that developed within Gregg and Fink's (2000) leveed PEG flow deposits on shallower slopes. The similarity of these features with the morphologies described by Gregg and Fink (2000) implies that this lava flow was emplaced under conditions of both high effusion rate and low cooling rate, although the surface folding and multi-lobate flow front morphologies appear to be simply the response of the lava to the reduced slope angle.

Fink and Fletcher (1978) proposed that surface folding occurs due to the compressional force imposed on the flow surface when flow front velocity is reduced compared to upstream flow velocity. A reduction in flow front velocity may be caused by increased viscosity due to cooling, the development of a brittle

surface crust, or a topographic obstacle. A marked reduction in slope angle will also significantly reduce flow front velocity, which is consistent with the relationship between slope angle and the development of surface folding observed by Gregg and Fink (2000). Gregg *et al*. (1998) agree that surface crust deformation is the result of compressional force, adding that fold wavelength is a function of both the extent and duration of applied compressive stress. Thus, relatively small fold wavelengths and amplitudes form initially but may be superimposed by a second generation of folds with greater wavelengths and amplitudes if compression continues over a long period of time, and/or the magnitude of compressional stress increases. Additionally, Fink and Fletcher (1978) suggest that for folding to occur, the viscosity gradient of the lava must decrease rapidly from the flow surface to depth, thus cooling of the lava surface also influences folding. Fold wavelength therefore depends primarily on the ratio of the viscosity at the surface to that of the interior of the flow. Gregg *et al*. (1998) also suggest that fold wavelength may be proportional to crust thickness, which in turn is controlled in part by lava composition, due to the relationship between viscosity and velocity on cooling rates. Therefore fold wavelength will vary between lavas of different compositions, and will be small in basaltic lavas relative to silicic lava flows (Gregg *et al*., 1998).

The highly autobrecciated surface of the 1954 lava flow deposits precludes evidence of the first generation, small wavelength and amplitude fold sets, more typically found on ropey pahoehoe flow surfaces (Fink and Fletcher, 1978; Gregg *et al*., 1998). The fold wavelengths on the surface of the 18th August (F) lava flow deposit range from 7 to 21 m on the northern fold set, and 5 to 13 m on the southern fold set, averaging ~ 12 and 9 m respectively (Table 2.2). Although fold amplitude is more difficult to quantify, trough depths typically range from 0.5 to 3.7 m, trending towards greater depths on the leeward side of each fold, particularly within the southern fold set (Table 2.2). These surface folds appear to involve a large proportion of the flow channel depth, with the base of some troughs possibly extending to the substrate in places, suggesting that either the surface crust at this location was relatively deep and/or that compressional forces were relatively large. As well as coinciding with a marked reduction in slope angle, the surface folds of 18th August (F) flow deposit may also be associated

with the presence of the southern end of the Pukekaikiore ridge immediately downflow from the position of the folds. Flow front velocity is known to have reduced markedly from ~ 360 m h^{-1} to ~ 9 m h^{-1} once the flow front had reached the Pukekaikiore Saddle (Gregg, 1956), therefore, the combination of the slope break and the topographical obstacle created by the Pukekaikiore ridge may have acted to both reduce flow velocity and apply considerable compressional stress to the flow surface as new lava continued to flow downslope at high velocity behind the flow front.

Levee and channel flow surface morphologies are also consistent with the conditions under which single, arterial lava flows (Kilburn and Lopes, 1991) and volume-limited lavas (Guest *et al*., 1987) are formed, i.e. high effusion rates over a relatively short duration. Although these features are not evident on the remaining 1954 lava flow deposits, the lack of solidified flow margins at very high effusion rates and very low cooling rates in Gregg and Fink's (2000) PEG analogue experiments may explain the apparent absence of channel and levee features at these flow deposits. Conversely, Borgia *et al*. (1983) suggest that levee formation coincides with a lateral increase in basal shear stress from the flow centre to the outer flow margin, and thus, if frictional forces at the flow base/ground-surface interface are low, lateral shear stress gradients cannot develop and the lava will propagate by sliding *en masse* as a single entity, precluding the construction of lateral levees. Propagation of lava flows by sliding generally occurs on steep slope gradients, for example, there is evidence of flow sliding in some pre-historic Arenal volcano lavas emplaced down slopes of ~ 35 to 38° (Borgia *et al*., 1983). The proximal zone of 1954 lavas were emplaced over an average underlying slope of ~ 44° over the first ~ 400 m, which may suggest that the flows initially propagated by sliding downslope. However, as discussed in the following section, the low basal friction and shear stress rates associated with sliding of the lava would preclude the development of the autobrecciated surface textures characteristic of the 1954 lavas.

A combination of effusion rate, slope gradient and duration of lava supply appear to be the major controls on the development of morphological surface features,

although cooling, increased viscosity and topographical barriers may also have some influence in the development of these features.

Lava Flow Surface Textures

The medial to distal regions of the 1954 lava flow deposits are characterised by markedly autobrecciated a'a surface textures (e.g. Figs. 3.1 to 3.3). Hobden (1997) notes that the majority of Ngauruhoe lavas display a'a textures throughout the length of the flow deposits; although the author also observed a textural transition from pahoehoe to a'a on the surfaces of some thin, pre-historic Ngauruhoe lavas on the upper slopes of the cone. Thus, although there is no evidence of pahoehoe surface textures at the medial to distal regions of the 1954 lava flow deposits, such a transition may have occurred proximal to the vent.

The factors contributing to the transition of basaltic lavas from pahoehoe to a'a surface textures have been well debated (e.g. Hulme, 1974; Peterson and Tilling, 1980; Kilburn, 1990; Kilburn, 1993; Kilburn and Guest, 1993). Hulme (1974) attributes the ratio of surface tension to yield strength as the primary control on the development of the autobrecciated textures typical of a'a lavas. Surface tension keeps the lava flow surface smooth, acting to restore distorted surfaces when surface tension exceeds yield strength. Where yield strength is greater than surface tension, distorted surfaces cannot be restored, resulting in fragmentation of the cooling surface (Hulme, 1974). However, other researchers propose that shear stress has a greater control on surface fracturing than tensile stress. For example, Kilburn (1990) suggests that the structure of the lava flow surface is dependant on both the rheological resistance to flow advance and the degree of shear stress the flow surface encounters. Thus a surface crust that is able to deform without fracture until its strength exceeds the shear stress remains intact; whereas, when shear stress is considerably greater than the strength of the crust, the surface crust fragments forming a'a flow surface textures. Deformation of the cooling surface crust results from crustal resistance to the flow advance of the underlying, hot lava (Kilburn, 1993; 2004). Kilburn (1990) also demonstrated that in Mount Etnean lavas pahoehoe and a'a surface textures often develop at the same time across the width of a flow channel. Thus the differences in shear rate

across the flow channel are the main conditions promoting the development of the two textures; with pahoehoe textures forming in regions of low shear rates and a'a textures at regions of high shear rates, for example at the lateral margins of the central flowing channel (Kilburn and Guest, 1993). Therefore, for autobrecciation to occur throughout the flow deposit, high shear stress rates must exist on a large-scale across the entire width and length of the flow surface.

Kilburn and Guest (1993) suggest that downflow changes in surface texture (i.e. from pahoehoe to a'a) reflect the influence of both surface rupture and cooling processes on the lava because, as the surface crust fails, fresh hot lava is brought to the surface to cool. Continued surface cooling promotes crustal thickening downward towards the hot interior of the flow so that, although the core is thermally insulated by the crust, the new material brought the surface is increasingly cooler downflow as the depth of the surface crust increases. Therefore, larger fragments of surface crust are fractured resulting in the observed transitional changes from pahoehoe to cauliflower a'a to rubbly a'a textures with distance downflow. Additionally, the rate at which surface crust fractures can heal has a significant influence on the development of a'a surface textures. Thus a combination of high deformation and low cooling rates leads to a slow healing rate and subsequent widespread crustal fracture (Kilburn, 1993).

Guilbaud *et al*. (2007) observed that the downflow increase in yield strength and viscosity of the 1783-84 Laki lavas may have contributed to the rubbly appearance of the pahoehoe surface of these lavas. Similarly, Peterson and Tilling (1980) note that viscosity, shear stress and the rate of shear strain are the dominant factors controlling the pahoehoe-a'a transition, and suggest that as viscosity increases, the critical value of shear deformation rate for the pahoehoe-a'a transition to occur decreases. However, the evidence presented previously strongly suggests that both the yield strength and cooling rate of the 1954 lavas was relatively low. Additionally, although it has been demonstrated that the viscosity of the 1954 lavas increased downflow, there is no evidence of a textural transition within the medial to distal regions of the flow deposits, where the greatest increase in viscosity would have occurred.

External factors, such as sudden changes in slope angle, flow direction, channel width or obstacles within the channel can also promote surface crust fracturing by disrupting the streamline of the flow (Crisp and Baloga, 1994), and therefore contributing to the distribution of different shear stress rates within the flow. For example, pahoehoe lava is commonly observed to change abruptly to a'a when the flow encounters a marked increase in slope angle (Peterson and Tilling, 1980). Similarly, Ball *et al*. (2008) observed that widespread crustal fracture occurred on steeper slopes due to gravitational stretching and tearing of the crust during emplacement of recent Kilauean lavas. Kilburn (2004) demonstrated that the pahoehoe-a'a transition is directly related to slope angle, flow depth and velocity, in that as slope angle decreases, the maximum flow depth and velocity at which textural transition occurs increases. The development of a'a surface textures requires conditions of persistent failure, which are ultimately related to the relative thickness of the flow interior and the surface crust. Additionally, there is a maximum velocity at any given slope angle at which lavas can maintain a pahoehoe flow surface, which increases as slope angle decreases. Therefore, a'a surface textures will develop under conditions of high velocity and slope angle and at relatively shallow flow depths (Kilburn, 2004). Gregg and Fink (2000) demonstrated in analogue experiments that for any given effusion and cooling rate, there is a critical slope angle beyond which the surface crust of the PEG flow deposits become continually disrupted due to gravitational force. Additionally, Pinkerton and Sparks (1976) observed that the a'a surface textures of the 1975 Mount Etna lavas tended to be associated with high effusion rates, whereas low effusion rates resulted in the formation of pahoehoe surface textures.

The relationship between high rates of strain and autobrecciation may also be confirmed by the work of Anderson *et al*. (1998) who found that high strain rates and associated rapid effusion rate promoted marked crustal fracture of silicic lavas, resulting in the generation of relatively small block/clast sizes at or near the source vent compared to the larger slabs produced by lower effusion and strain rates. Thus the distribution patterns of block and clast sizes along lava flow deposits will reflect the conditions of shear stress and deformation during flow emplacement (Anderson *et al*., 1998). The distribution of clast sizes observed within the 1954 lava flow deposits is strongly suggestive of variable shear stress

rates within the lava flow. For example, at the lateral margins of the flow deposits clast sizes are relatively small and uniform and individual clasts consistently display sub-rounded morphologies, indicating relatively high shear stress rates (Fig. 3.2). Conversely, large, irregular-shaped clasts and a wider range of clast sizes are prevalent on near the centre of flow channel surfaces (Fig. 3.3A), suggesting lower shear stress rates in this region of the flow.

Although the combination of high effusion rate and low cooling rate over steep slopes appear to contribute to the formation of a'a surface textures, according to Gregg and Fink (2000) these conditions would preclude the development of the prominent levee and channel morphology of the 18th August (F) lava flow deposit. It appears, therefore that the combined effect of steep slope gradients and high shear stress rates were the dominant factors controlling the development of a'a surface textures on the 1954 lavas.

5.3 1954 LAVA FLOW EMPLACEMENT DYNAMICS

It has been demonstrated that a range of parameters can influence the morphology, geometry and texture of lava flows, both as dominant and as contributory controls. The diversity in length, morphology and surface features of the 1954 lava flow deposits suggest that the controls on flow emplacement may have differed for each of these lavas. However, flow deposit characteristics of individual lavas at relatively equidistant regions from the crater rim are reasonably comparable, for example flow width changes occur at approximately the same distance from the vent in both the 14th July (Dc) and 18th August (F) flow deposits. This suggests that emplacement of each of the 1954 lava flows was controlled by the same conditions at any given distance from the vent, and that it was the dominant controls on flow emplacement that changed with distance from the vent. This scenario is particularly relevant to the rheological properties of the 1954 lavas, i.e. viscosity and yield strength, which, given the relatively homogeneous geochemical composition between individual flow deposits, are assumed to have been the same for all of the 1954 lava flows, at least initially. Consequently, the changes in rheological properties as the lava flows cooled should result in an increased influence on flow emplacement as the lavas advanced to greater

distances from the vent. The flow emplacement dynamics of the 1954 lavas can therefore be related to specific zones of increasing distance from the crater rim, i.e. proximal, medial and distal zones, characterised by both the pre-existing environmental conditions and the dominant constraints on flow emplacement within each zone (Fig. 5.4).

5.3.1 1954 Lava Flow Genesis

Effusion rate appears to have been one of the major controls on the flow morphology, geometry, and surface features and textures of the 1954 lavas. However, much of the supporting research is generally related to the direct, quiescent effusion of lava from a source vent or fissure onto the receiving surface on which the flows are emplaced. Conversely, the effusive activity of the 1954-55 Mount Ngauruhoe eruption was associated with intermittent, vigorous fire-fountaining episodes, producing both lava flows and a scoria cone at the vent (Gregg, 1956), which may have contributed significantly to the emplacement dynamics of the 1954 lava flows.

Fire-fountain Dynamics

Fire fountains produce a variety of deposits, the structure and nature of which is dependant on effusion rate and volatile content of the magma. Volatile content is considered to be the dominant factor determining the height of most fire-fountains in basaltic eruptions (Head and Wilson, 1989), although vent dimensions and architecture are also contributing factors. For example, in theory, given the same vent conditions, effusion rate and conduit pressure gradients, a volatile-free basaltic magma would produce a small fire-fountain in the range of centimetres to tens of centimetres in height; whereas a basaltic magma containing ~ 0.4 wt.% exsolved volatiles is expected to produce a fountain ~ 200 m height (Head and Wilson, 1989). The volatile content of the 1954 lavas was estimated at ~ 0.4 wt.%, and episodes of continuous fire-fountaining were reported to reach heights of ~ 300 m, with some fragments reaching ~ 760 m height (Gregg, 1956), suggesting that either volatile content was greater than estimated, or that the vent diameter was less than the 3 to 6 m theorised by Head and Wilson (1989); although

additionally this theory applies to basaltic lava, therefore the marginally greater silicic composition of the 1954 lavas may also have influenced fountain height.

The nature of the deposits produced by fire-fountaining activity is controlled by two factors: the local temperature of individual clasts on deposition, and the clast accumulation rate, both of which are strongly dependant on gas content and effusion rate. Volatile content controls the degree of fragmentation of the magma as it leaves the vent and therefore clast size range and distribution within the fountain. This in turn determines the density, and hence opacity of the fountain and therefore the temperature and cooling rate gradient within the fountain structure (Fig. 5.5). Therefore, at a fixed effusion rate, increasing volatile content acts to decrease clast size and enable wider dispersal of the clasts, thus density and opacity are reduced, cooling rates increase, and temperature decreases. Conversely, at a constant volatile content, the clast size and dispersal pattern is fixed but increasing effusion rate leads to increased clast density and therefore increased clast temperature and decreased cooling rates (Head and Wilson, 1989).

The nature of the deposit formed during fire-fountain events is determined by the relationship between the temperature of individual clasts on deposition and the rate of clast accumulation. Clast temperature and accumulation rate are determined by the distance that clasts are deposited from the vent, which is primarily controlled by fountain height, so that clast temperature and accumulation rate decrease with increasing deposition distance from the vent. The majority of clasts remain within the centre of the fountain structure (zone 1, Fig. 5.5), settling at the fountain base at high rates of accumulation. This rapid accumulation of hot, fluid clasts either inhibits or significantly reduces cooling rates, leading to coagulation of individual clasts to form either a lava pond at the base of the fountain or an immediately advancing lava flow. Additionally, ponded lava may also eventually overflow the lower elevation sites on the crater rim to form a lava flow. At lower temperatures (but not completely chilled), rapid accumulation rates produce welded spatter deposits, whereas low rates of

Fig. 5.4 (next page) Summary diagram indicating the primary and other controlling factors on 1954 lava flow emplacement processes within zones characterised by increasing distance from the vent.

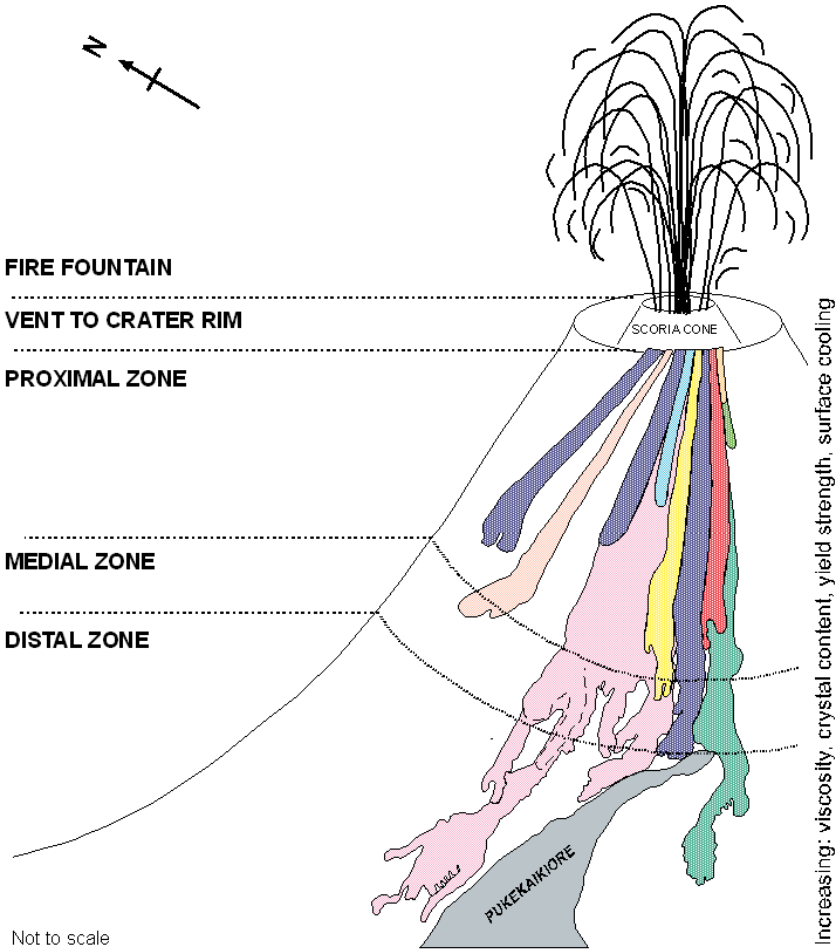

Increasing: viscosity, crystal content, yield strength, surface cooling

Decreasing: temperature, volatiles, velocity, slope angle

FLOW PROCESSES	PRIMARY CONTROLS	OTHER CONTROLS
Fire-fountaining	Effusion rate Volatile content	Conduit/vent architecture
Directional flow emplacement	Crater floor slope/topography Scoria cone wall breach	Asymmetric fountain profile
Single, unit flows	Effusion rate & duration	
Constant flow width maintained	Slope angle	Effusion rate
Surface autobrecciation	Basal shear stress due to slope angle, velocity	Low yield strength
Flow cessation	Termination of lava supply	Low viscosity & yield strength
Flow channel drainage	Termination of lava supply	Slope angle, velocity, low viscosity
Flow widening & thickening	Slope angle Reduced velocity	Topography Compressional stress Low yield strength
Flow bifurcation & multiple lobe formation	Topography	
Surface folding (18th August lava)	Compressional stress	Surface cooling
Flow cessation	Termination of lava supply	Reduced velocity Increased viscosity
Flow narrowing Multiple lobe formation	Topography	Slope angle
Flow front widening	Slope angle	Low yield strength
Flow cessation	Termination of lava supply	Reduced velocity Increased viscosity

4th June (A) | 30th June (B) | 8-13th July (C) | 14th July (D) | 29th July (E) | 18th Aug (F) | 16th Sept (G) | 18th Sept (H) | 26th Sept (I)

accumulation results in relatively plastic, poorly-welded scoria and spatter accretions. Accumulation of cold clasts at any rate produces an accretion of brittle scoria, resulting in the formation of unwelded scoria and spatter bombs. The overall fire-fountain structure is typically symmetrical, although depending on wind velocity and direction the fountain may develop an asymmetrical profile, with smaller, cooled clasts preferentially distributed downwind of the fountain, while coarse, cooled clasts persist on the upwind side of the fountain structure (Head and Wilson, 1989).

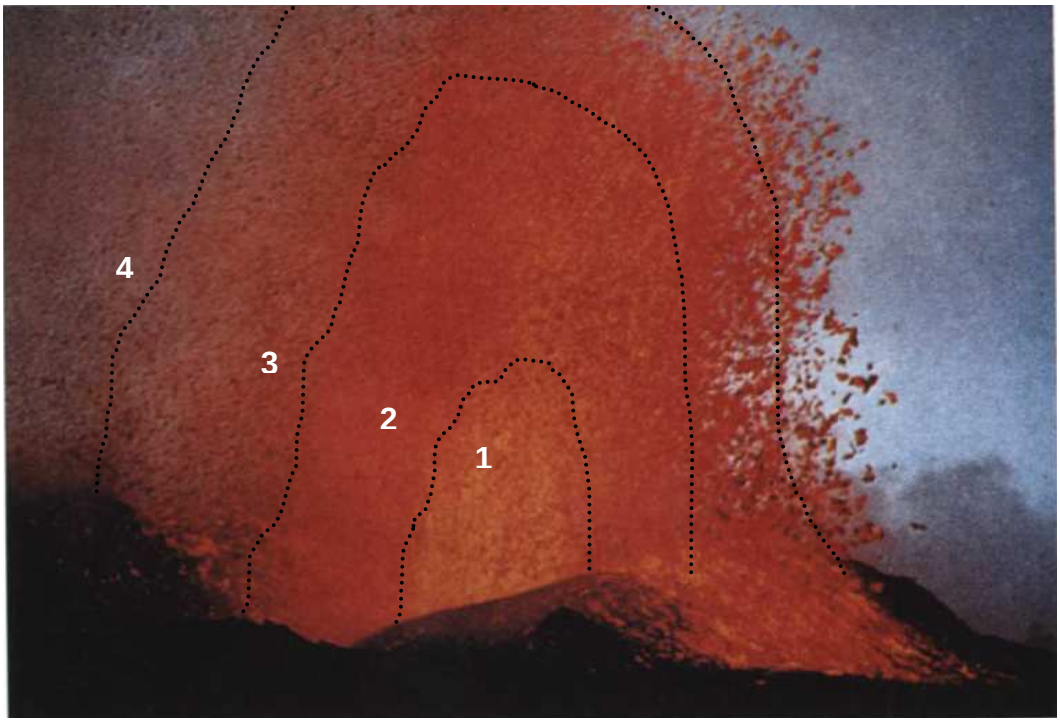

Fig. 5.5 Fire-fountain in Hawaii showing thermal and clast density gradients (dashed lines denote gradient boundaries) within the fire-fountain structure. Clast density, opacity and temperature decrease, cooling rates increase, and clast accumulation rate decreases from zone 1 to zone 4. Adapted from Head and Wilson (1989).

1954-55 Scoria Cone Construction

Construction of the 1954-55 scoria cone on the summit of Mount Ngauruhoe is reported to have begun with an episode of vigorous fire-fountaining on the 4th June 1954 (coinciding with emplacement of the first of the 1954 lava flows), which formed a broad, intact dome of accumulated scoria in the south-western sector of the main summit crater. By the 30th June (coinciding with emplacement of the second lava flow) the scoria cone was estimated to have grown to ~ 30 m

height above the original crater floor, but had formed a horseshoe-shape around the vent due to a breach in the western wall. By the 19th August the scoria cone had grown to approximately 6 m lower than the eastern rim of the original crater, and completely encircled the vent, although a shallow breach remained in the western wall. A secondary vent was observed on the western rim of the scoria cone in early September, with continued lateral and vertical growth of the cone to ~ 6 m higher than the pre-existing eastern rim by 17th September. By the end of October the scoria cone had covered the original north-western crater rim, integrating the sloped wall of the scoria cone with the main slopes of the mountain (Gregg, 1956). Pyroclastic deposits, including lapilli, ash and agglutinated spatter produced during the 1974-75 Ngauruhoe eruption have subsequently been added to this scoria cone (Krippner, 2009).

There is considerable lateral and vertical variation in the nature of the 1954-55 scoria cone deposits, ranging from non-welded, brittle scoria to densely welded and/or agglutinated spatter deposits, with some evidence of both fluidal and angular clast morphologies embedded within these (Krippner, 2009). The vertical variability in the nature of these scoria cone deposits indicates that clast temperature and accumulation rates varied throughout the 1954-55 eruption, suggesting changes in fire-fountain height due to fluctuating effusion rates. Additionally, lateral changes in the degree of welding and agglutination strongly suggest an asymmetric fountain structure, where hotter clasts preferentially accumulated to one side of the vent, which also agrees with the observed horseshoe shape of the cone during the early stages of the eruption. Asymmetry may have been due to either wind direction and velocity or possibly the architecture of the upper conduit and vent.

1954 Lava Flow Activation

Sumner (1998) distinguishes between the formation of *spatter-fed* and *clastogenic* lava flows, although both originate with the accumulation of coalesced fire-fountain deposits. Spatter-fed lavas form due to the complete coalescence of the accumulated clasts and are texturally indistinguishable from lavas that effuse directly from the source vent. Conversely, clastogenic lavas may be generated

from either an accumulation of partially coalesced clasts, or by the sudden failure and subsequent slumping of the agglutinated spatter deposits within the scoria cone wall. Clastogenic lavas are texturally distinguished by the preservation of individual remnant clasts within the bulk lava flow deposit, with typically only the deformed, stretched or flattened outline of the original clast remaining. Although there is no evidence of remnant clasts within the medial to distal 1954 lava flow deposits, these may be present within the proximal regions of the flow deposits. However, the slope of the pre-existing crater floor and the potentially asymmetric structure of the fire-fountain indicate that the 1954 lavas were probably generated from completely coalesced lava, either directly following accumulation, or as overflow of ponded lava.

The lava flows emplaced during June and early July 1954 most likely formed due to the coalescence of rapidly accumulated lava at the base of the fire-fountain. It is reasonable to assume that these early lavas may have propagated almost immediately, initially due to the absence of accumulated scoria deposits which could block their flow path, and later due to the breach in the western wall of the growing scoria cone. Additionally, the original summit crater floor slopes downwards in a north-westerly to westerly direction (Figs. 1.4D, F), promoting flow advance away from the vent. The breach in the western wall of the scoria cone appears to have been partially infilled sometime towards the end of July to the middle of August, suggesting that the later 1954 lavas, i.e. end of July to end of September, were generated in a different manner. Flow activation of these lavas may have occurred in several ways, for example, coalesced clasts may have accumulated within the scoria cone crater until the ponded lava overtopped the lower walls of the cone on the western rim. Alternatively, changes in effusion rate may have increased fountain height and clast density so that the rapid accumulation of hot clasts occurred on the crater rim of the scoria cone and the lava flows generated from this point. Similarly, an asymmetrical fountain structure would also result in clast accumulation on the rim of the scoria cone.

The sloping crater floor, the breach in the scoria cone wall, and a potentially asymmetrical fire-fountain also appear to have directed the emplacement of the 1954 lavas on the north-western to western slopes of Ngauruhoe. However, with

the exception of the northern and middle 14th July (Da and Db) lava flow deposits, there is a general trend of successive southward emplacement of the 1954 lavas. The distribution of lateral scoria deposit variations indicates changes in the directional focus of the fire-fountaining (Krippner, 2009), and therefore possibly the symmetry of the fountain structure during the course of the 1954-55 eruption, which may have been controlled by either wind direction and velocity, or conduit and vent architecture. Fire-fountaining with a directional focus that moved progressively southward would explain the chronological emplacement pattern of the 1954 lavas, except that not all of the lava flows were emplaced immediately adjacent to the southern margin of preceding flow deposits. Some lava flows [i.e. northern 30th June (Bn), 8-13th July (C), 29th July (E), 16th September (G), 26th September (I)] were emplaced over earlier, cooled flow deposits, while the northern and middle of the three 14th July (Da and Db) lava flows were emplaced to the north of preceding lava flow deposits (Fig. 2.5). Emplacement of lava flows over earlier flow deposits may suggest that the underlying flow deposits were not thick enough to direct newly propagating lava flows towards separate flow paths. Alternatively, a deep pond of coalesced lava may have formed at the base of the fire-fountain enabling new lava flows to propagate over the top of the underlying flow deposits. Although the 8-13th July (C), 29th July (E), 16th September (G) and 26th September (I) lava flow deposits overlie preceding lavas, each of these flows also follow the general southerly trend relative to each other (Fig. 2.5), suggesting that the combined thickness of two superpositioned flow deposits probably precluded propagation of a third lava flow over the same flow path, instead directing subsequent lava flows towards the south.

The three lava flows emplaced on the 14th July (Da, Db, Dc) do not conform to the successively southward flow emplacement trend, with one flow deposit (Da) emplaced to the north of the 4th June (A) lava flow deposit, another flow (Db) emplaced to the south of the 4th June (A) lava flow deposit and overlying the 30th June (Bn) lava, and the third flow (Dc) emplaced immediately adjacent to the southern margin of the 30th June (Bs) flow deposit (Fig. 2.5). Because all three lava flows were observed to be advancing downslope simultaneously (Gregg, 1956) it is unlikely that an asymmetrical fire-fountain structure could have directed the emplacement path of all three of these lavas. Additionally, if flow

path direction was controlled solely by the scoria cone wall breach, the activity on the 14th July would be expected to have produced a large volume, single unit lava flow. Therefore it is possible that the three 14th July (Da, Db, Dc) lavas were each activated under different conditions. For example, an asymmetric fire-fountain would enable lava accumulation at both the fountain base, and to a lesser extent at some distance from the vent along the inclined axis of the asymmetric fountain. Thus, the southern-most of the three 14th July lavas (Dc), which does conform to the southward trend of successive flow emplacement, was probably generated by the accumulation of coalesced lava at the fountain base, and the flow path therefore directed by a combination of the scoria cone wall breach and the depth of the preceding lava flow deposits. Conversely, the two northern 14th July flows (Da, Db) may have propagated following the accumulation of directional fire-fountain spatter deposits on the north-western rim of the scoria cone and thus their flow paths would have been controlled primarily by the location of accumulated spatter and the slope angle of the scoria cone wall. Because of the fundamental nature of the fire-fountain structure (Fig. 5.5), the volume of accumulated clasts at the base of the fire-fountain would have been greater than that accumulated at greater distance from the vent on the scoria cone wall, which is reflected in the significantly shorter flow deposit lengths of the two northern 14th July (Da, Db) flow deposits compared to the southern (Dc) flow deposit (Fig. 2.5, Table 2.1).

5.3.2 Proximal Zone Lava Flow Emplacement

The proximal zone of the 1954 lava flow field extends from the source vent to ~ 1660 m elevation (a.s.l.) and is characterised by the relatively gentle slopes of the pre-existing summit crater floor and the much steeper slopes of the main Ngauruhoe cone. All of the 1954 lava flow deposits display comparable morphological characteristics within this zone and six lava flows [8-13th July (C), 14th July (Da, Db), 16th September (G), 18th September (H), 26th September (I)] terminated in this zone.

Much of the evidence previously presented indicates that high effusion rates were a major control on the emplacement dynamics, and therefore the flow deposit characteristics of the 1954 lavas, for example, intermittent episodes of high

effusion rate controlled the development of single unit, arterial flows, as opposed to a compound flow field. The majority of the 1954 lavas were probably generated by the overflow of ponded lava, which implies a time interval between the effusion of lava at the vent and the activation of lava flow advance. Thus, any time-lag between clast accumulation and the generation of a lava flow would potentially reduce the influence of effusion rate on the early stages of advance of the overflowing lava. However, the time interval would depend on the rate of clast accumulation which is directly controlled by effusion rate, therefore the high effusion rates implied by the 1954 lava flow deposit characteristics would result in rapid clast accumulation at the base of the fire-fountain structure and a relatively short time interval between ponding and lava flow activation. Additionally, a rapid clast accumulation rate would minimise the cooling rate of the coalesced fragments, thereby maintaining lava temperature and viscosity at similar values to those on eruption of the lava from the vent, and contributing to the high flow velocity rates reported during the early stages of flow emplacement.

The initial width of the newly propagating lavas may have been constrained by either the slope gradient and topography of the pre-existing crater floor, or the width of the breach in the scoria cone wall. Alternatively, if the lava flows were generated from an accumulated spatter pile on the rim of the scoria cone, rather than overflow of ponded lava [e.g. after 19th August when the scoria cone wall breach was blocked, or the two northern 14th July (Da, Db) lavas], the outer margins of the spatter pile may have cooled sufficiently before lava flow genesis that the flow width was determined by the cooling diameter of the accumulated spatter. Lava flow width remained relatively constant after reaching the crater rim and therefore may have already been fixed prior to reaching this point. Conversely, if flow width was not fixed until the lavas overtopped the crater rim, and assuming that the initial yield strength of the lavas was relatively low and had no significant effect on lateral flow spreading, the combination of high effusion rate and steep slope gradient was the major control in determining flow width. Alternatively, it is possible that newly propagating lava flows were constrained by pre-existing topographical features on the main slopes of the cone (Fig. 5.3).

The combination of high effusion rate, high temperature and low viscosity enabled the lavas to reach the crater rim rapidly following activation from the vent, again minimising cooling time. On reaching the crater rim, the steep gradient of the main slopes of the cone became a major controlling factor in the emplacement of these lavas. Slope gradient and low lava viscosity were the main controls on flow velocity during the early stages of flow emplacement, and subsequently the cooling rate of the lava. The combination of slope gradient and high flow velocity contributed to the high shear stresses within the lava flows, resulting in high deformation rates compounded by the low yield strength of the lava. Additionally, high effusion rates promoted slow healing times, and subsequent widespread crustal fracture, enabling an autobrecciated a'a surface to develop during the very early stages of flow emplacement. The combination of steep slope gradient and high effusion rate are considered to be a major controlling factor determining the development of marginal levees, although the absence of these features at all but the 18th August (F) lava flow deposit implies that even higher effusion rates were associated with the emplacement of the remaining 1954 lavas. However, Hobden (1997) suggests that the lateral levee structures of some earlier Ngauruhoe lavas were not constructed during flow emplacement but are the cooled flow margins abandoned by the drainage of the central flow channel towards the distal flow front. Similarly, Gregg (1956) observed that marginal levees developed on several of the 1954 lavas following partial collapse of the cooling central flow channel surface. The drained central flow channel in the proximal zone of the 18th August (F) lava flow supports Hobden's (1997) proposal, although there is no evidence of channel drainage at the remaining 1954 lava flow deposits. Alternately, the low-elevation marginal levees observed within the medial to distal regions of the northern 30th June (Bn) and southern 14th July (Dc) flow deposits are compatible with the partial collapse of a central flow channel as observed by Gregg (1956). In either scenario, effusion rate and slope gradient would not therefore be the major controlling factor on levee formation, rather flow margin cooling rate and depth (related to the degree of basal sheer stress) would determine the development of cooled flow margins; thus, either the cessation of lava supply, or surface cooling rate would determine the presence or absence of elevated marginal levees.

Six of the 1954 lava flows ceased to advance in the proximal zone [8-13th July (C), 14th July (Da and Db), 16th September (G), 18th September (H), 26th September (I)], controlled primarily by the termination of lava supply from the vent, rather than by cooling. The steep slope gradient and subsequent high flow velocities associated with these lavas indicates short emplacement duration times of ~ 0.5 to 7 hours, assuming flow velocities comparable to those reported during the early stages of the 4th June (A), 30th June (B) and 18th August (F) lavas (0.05 to 0.1 m s^{-1}, Table 4.8). In particular, the final two 1954 lavas [18th (H) and 26th September (I)] were emplaced within ~30 to 120 minutes, minimising cooling time and implying low lava viscosity and yield strength throughout the duration of flow emplacement. Given the steep slope gradient, it may be expected that these lava flows would continue to advance after the termination of supply from the vent. Although there is no evidence of channel drainage on these flow deposits, the proximal zones of these lava flows are obscured by later eruptive deposits, therefore it possible that some channel drainage did occur.

5.3.3 Medial Zone Lava Flow Emplacement

The medial zone of the 1954 lava flow field extends from ~ 1660 to 1580 m elevation (a.s.l.) and is characterised by a marked reduction in slope angle and the presence of prominent topographic features, including Pukekaikiore ridge and various low-elevation ridges and depressions. The 4th June (A), 14th July (Dc) and 29th July (E) lavas terminated within this zone, while the morphological and surface feature characteristics of the 30th June (B) and 18th August (F) lavas differ significantly in this zone relative to their respective proximal zone sections.

Two lava flow deposits [14th July (Dc) and 18th August (F)] display significant widening in this zone, which may indicate an increase in effusion rate. Although there was potentially some variability in effusion rate during the emplacement of each of the 1954 lavas, there is no evidence of flow widening within the proximal zone, suggesting that variations in effusion rate were associated with longer effusive episodes and therefore the longer length lavas. However, it is unlikely that a significant increase in effusion rate occurred on two separate occasions to coincide with both the 14th July (Dc) and 18th August (F) lavas reaching the same

distance from the vent. The increased width of these two lava flow deposits is directly correlated to the marked overall reduction in slope gradient within the medial zone, indicating that underlying slope angle remained a major control on the emplacement dynamics of the 1954 lavas.

As with the proximal zone, slope angle was the major control on the rate of flow advance as flow front velocity reduced in response to the shallower slope gradient in the medial zone, promoting an increase in lava viscosity and cooling rate; although any associated increase in the yield strength of the lava was insufficient to prevent lateral flow spreading of the 14th July (Dc) and 18th August (F) lavas. The formation of the short, sub-lobes observed at the lateral margins of the 30th June (Bs3) and 14th July (Dc12) may reflect a reduction in flow velocity as the lavas reached the medial zone (Figs. 2.19 and 2.25 respectively). Additionally, lava upstream from the flow front would have continued to advance at higher flow velocities on the steep proximal zone slopes resulting in a decreasing downstream velocity gradient. Consequently, high rates of compressional stress developed behind the advancing flow front resulting in significant flow widening and some thickening at the flow front. Although there is no significant increase in the width of the 4th June (A), and 29th July (E) lavas where they extend into this zone, the reduction in underlying slope gradient is less marked at the distal margins of these two deposits. For example the final ~ 100 m of the 4th June (A), and ~ 50 m of the 29th July (E) lavas were emplaced on slopes of ~ 27 and 24° respectively, whereas the widening of the 14th July (Dc) and 18th August (F) lava flow deposits coincides with a more significant reduction in slope angle to ~ 14 to 9°. Thus, the effect of reducing slope angle on flow velocity was considerably less for the 4th June (A) and 29th July (E) lavas, resulting in a smaller downflow velocity gradient and lower rates of compressional stress at the flow front.

High compressional stress rates controlled the development of surface folding within the flow channel of the 18th August (F) lava flow (Fig. 2.29A) once this lava reached the medial zone. However, although the low-relief ridges and shallow depressions on the surface of the widened distal end of the 14th July (Dc) lava flow deposit (Fig. 2.25) also coincide with reduced slope angle and the subsequent reduction in flow front velocity, these ‘folds’ are generally orientated

in a downflow direction, rather than the perpendicular to flow stream orientation that usually characterises compression-induced surface folding. Additionally, there is no evidence of surface folding of the 30th June (B) lava flow deposit within the medial zone, although this lava was also subject to a reduction in flow front velocity on reaching this zone. Therefore, although the compressional stress induced by a decrease in slope angle and flow front velocity facilitated flow widening of both the 14th July (Dc) and 18th August (F) lavas, the magnitude of compressive stress was too low to initiate the formation of the folded channel surface at the latter flow deposit.

Widening of the 18th August (F) lava primarily occurs on the northern margin of the flow deposit within the medial zone, with the southern margin maintaining a relatively straight path from the proximal zone (Fig. 2.5). The southern margin is confined by a pre-existing ridge (Figs. 2.4A, 2.30) in this zone preventing lateral spread to the south, whereas the northern margin remains unconfined. Additionally, because the height of Pukekaikiore ridge reduces markedly towards its southern distal end, on reaching the base of the ridge the southern margin of the advancing flow encountered a lower-elevation section of the ridge than the northern margin. Consequently, considerably greater rates of compressional stress developed at the northern section of the flow front, compared to the southern section, before the flow front thickened sufficiently to enable continued advance over the top of the higher-elevation section of the ridge. Subsequently, the high compressional stress at the northern section of the flow front promoted flow widening behind the flow front on the northern margin.

Surface folding of the 18th August (F) lava flow developed ~ 100 m upstream from the distal end of Pukekaikiore ridge, while the reported reduction in flow front velocity also coincided with the lava reaching this ridge (Gregg, 1956). Furthermore, Gregg (1956) reports that on reaching Pukekaikiore ridge the flow front thickened over the following eight hours to ~ 15 m height, while only advancing forward a further ~ 80 m in this time. However, the distinct southerly dip in the flow surface elevation at this point (Fig.2.29A) indicates that the lava inundated the distal end of Pukekaikiore ridge. Flow advance was therefore initially obstructed by the increased elevation of Pukekaikiore ridge for several

hours before the increased flow depth enabled the lava to overtop the distal end of the ridge, resulting in high rates of compressional stress. However, the ability of the lava to overcome this obstacle suggests that insufficient cooling took place to promote the development of surface folding during the initial stages of flow obstruction. It is more likely that surface cooling took place, to some extent, following the reduction in flow front velocity and prior to the flow inundating the ridge. However, significant surface cooling did not take place until the later stages of emplacement following upstream channel drainage in the proximal zone and subsequent infilling of the channel downstream on the lower slopes of the medial zone. With the cessation of lava supply, flow velocity would have further decreased, reducing the ability of the remainder of the lava to overtop the ridge. This lava pooled immediately upstream from the ridge, promoting surface cooling and the development of surface folds as the final vestiges of lava continued to compress against the ridge base.

The width of the 30th June (B) lava flow deposit also appears to increase at the distal boundary of the proximal zone, although in the absence of well-delineated lateral flow margins the extent of flow widening is unclear. Evidence of further widening of the 30th June (B) lava flow in response to the reduced slope gradient of the medial zone is precluded by the sub-division of this lava into multiple lobes. Additionally, there is no significant widening of individual lobes associated with the reduction in slope angle. Instead both the formation and subsequent width of individual lobes was predominantly controlled by pre-existing topographic features; typically the ridges and depressions formed by the remnant levees and channels of pre-historic lava flows. For example, the lower southern Bn lobe (BnL-S) is confined by the kipuka on the northern margin (Bn39) and by a low-elevation ridge on the southern margin (Bn38a) (Fig. 2.5).

The upper lobes overlying the northern 30th June (Bn39, Bn40a) and the southern 14th July (Dc14) lava flow deposits (Fig. 2.5) may indicate variable effusion rates during the emplacement of these lavas. These superimposed lobes were neither mapped as separately dated flow deposits by Gregg (1956) nor described in previous studies of Mount Ngauruhoe lava flows (e.g. Hobden, 1997; Hobden and Houghton, 2000), therefore they are assumed to have been emplaced during the

same dated, effusive episode that generated their respective underlying flow deposits. The reasonably well-defined contact between underlying flow deposits and superimposed lobes may imply a significant time interval between the deposition of each correlated flow deposit, which allowed sufficient cooling of the underlying flow deposit to prevent amalgamation of the two flow deposits. Additionally, the considerably shorter lengths of the upper lobes compared to those of their related underlying lava flows suggests that either significantly greater viscosity, yield strength and/or cooling of the surface restricted further flow advance, or that the supply of lava from the vent ceased relatively quickly following activation of the overlying lobes at the vent. The latter scenario implies waning effusion rates during emplacement of the underlying flow unit followed by a brief surge in effusion rate towards the end of the fire-fountaining episode which generated the overlying lobe deposit. Alternately, the superpositioned lobes may not be associated with their respective underlying flow deposits and instead represent discrete arterial flow units produced during different effusive episodes on unknown dates during the 1954-55 eruption event. In this case, it is therefore possible that channel drainage may have occurred in the proximal regions of the underlying flows following termination of lava supply, but the subsequent emplacement of these superpositioned lobes either infilled or obscured the drained channels.

The 4th June (A), 14th July (Dc), 29th July (E) lava flows ceased to advance in the medial zone as a result of termination of lava supply at the vent. The 4th June (A) and 29th July (E) lavas show no evidence of channel drainage although both of these lavas were emplaced over earlier lava flow deposits. The increased basal friction created by the underlying autobrecciated lava flow deposits may have inhibited further flow advance once flow velocity reduced on the shallower slopes of the medial zone and lava supply ceased. Although there is no evidence of a drained flow channel on the proximal slopes of the 14th July (Dc) lava flow deposit, the shallow central flow channel evident towards the distal margin of the flow deposit behind the flow front (Fig. 2.25) may indicate the onset of some channel drainage. The southern section of the 14th July (Dc) flow front reaches, and partially abuts the base of the eastern face of Pukekaikiore ridge (Figs. 2.5, 2.26), although there is no significant flow thickening of this section of the flow,

while the main face of the flow front terminates ~ 10 to 50 m before reaching the ridge base (Figs. 2.19, 2.25); thus flow advance was not obstructed, or redirected by this ridge. Final flow length was therefore controlled primarily by cessation of lava supply at the vent, although the lava probably continued to advance after the supply was terminated until the flow reached the shallow slopes of the medial zone. The subsequent reduction in flow velocity, increased viscosity and lateral spread of the flow front contributed to the cessation of further flow advance just as the southern margin of the flow reached the base of Pukekaikiore ridge.

5.3.4 Distal Zone Lava Flow Emplacement

The distal zone of the 1954 lava flow field extends from ~ 1580 m elevation (a.s.l.) to the distal end of the northern 30th June (Bn) lava flow deposit (1350 m elevation a.s.l.). The two longest 1954 lavas [30th June (B), 18th August (F)] extend into and terminate in this zone. Each of these flow deposits displays markedly different morphological characteristics relative to their respective proximal and medial sections and to each other.

Northern 30th June (Bn) Lava Flow

As with the medial section of the northern 30th June (Bn) lava, individual lobe width in the distal zone is partially controlled by pre-existing topographic features, although, in the absence of these obstacles, slope angle remains the major control. For example, on reaching the distal zone the northern margin of the lower southern lobe (BnL-S) initially remains confined by the high-elevation kipuka around which the northern 30th June lava (Bn) bifurcated upstream (Fig. 2.5), while subsequent lateral spreading of the northern margin coincides with the discontinuation of this obstacle at the western end of the kipuka (Bn39a).

Significant additional widening of this lobe occurs further downflow (Bn16, Fig. 2.5), although the reduction in slope gradient is relatively minor (from 19 to 16°). However, this section of the lower southern BnL-S lobe was emplaced over a wide, flat-topped ridge, which appears to be the remains of an undrained, pre-historic lava flow deposit. Thus, the combined discontinuation of confining topographic obstacles and the presence of downward sloping surfaces

perpendicular to the advancing lava facilitated bi-lateral spreading of the BnL-S lobe as the lava advanced freely down either side of this underlying ridge. The increase in flow width indicates that the yield strength of the lava at this distance from the vent was insufficient to prevent lateral flow spread, although, as a relatively high yield strength would be required to preclude the spread of lava down the higher gradient of the lateral ridge slopes, this does not necessarily imply that no increase in yield strength occurred. The advancing lobe reached this point approximately 12 to 14 hours after flow activation, thus lava viscosity and cooling rates would be significantly increased, supported by the reported reduction in flow velocity (Table 4.8), potentially resulting in some increase in yield strength.

The multiple, localised variations in slope gradient and orientation associated with the margins of this underlying ridge were the primary control on the formation and dimensions of the elongated lobes at the distal margin of the lower southern (BnL-S) lobe deposit (Fig. 2.5-inset). For example, the southern section of this lobe advanced down the southwest-facing slopes of the ridge forming three separate lobes (distal lobes 1, 2 and 3, Fig. 2.12), whereas the middle section (distal lobe 4) continued to advance along the length of the ridge top and subsequently flowed down the steep slope at the distal end of the ridge (Fig. 2.5). The width of these individual distal lobes was primarily controlled by the presence or absence of confining topography, for example the narrow width of distal lobe 1 is the result of flow confinement by the base of the southwest-facing ridge slope on the northern margin and the base of the main Pukekaikiore massif at the southern margin (Fig. 2.12A). Each of the distal lobes encountered a marked increase in the local underlying surface gradient on reaching the lateral or distal sloping margins of the underlying ridge, which may have facilitated a small increase in flow velocity on these slopes. However, these distal lobes were emplaced ~ 20 to 30 hours following generation of the lava at the vent; consequently, the associated increase in lava viscosity with cooling may have prevented any significant increase in flow velocity. Additionally, the flow front of distal lobes 1 and 4 ceased to advance on relatively steep slopes compared to the surface gradient underlying the upstream section of these lobes, with slope angle increasing from ~ 4° to ~ 20°, indicating that a significant amount of cooling and

the associated increase in lava viscosity may have prohibited further flow advance. Thus, although the termination of lava supply at the vent contributed to final flow length, local topography, slope angle and increased lava viscosity played a major role in the cessation of flow advance.

Southern 30th June (Bs) Lava Flow

The southern-most lobe of the southern 30th June (Bs) lava extends a short distance into the distal zone, terminating at ~ 1540 m elevation (a.s.l.). The flow path of this lobe changed direction towards the north as it reached the distal zone (Fig. 2.19), coinciding with the southern margin of the lobe reaching the base of the eastern face of the main Pukekaikiore massif. However, there is minimal contact between the southern flow margin and the base of the eastern Pukekaikiore face (Fig. 2.20A), and no evidence of flow thickening or compressional stress-induced folding (Fig. 2.20), indicating that this high-elevation obstacle did not primarily control the flow path of the southern Bs lobe. The distinct ridge crest underlying the central flow channel of this deposit in the medial zone appears to mimic the flow path of the southern Bs lobe (Fig. 2.22), while the northern margin of the southern Bs lobe is emplaced down the northwest-facing slope of this underlying ridge (Fig. 2.18). As with the lower northern BnL-S lobe, the southern Bs lobe therefore appears to have been emplaced along the flat-topped remnant of a pre-historic lava flow deposit, and the orientation of this ridge top and its sloping margins controlled the flow path of the southern Bs lobe. Because the northern section of the southern Bs lobe was directed down the northwest-facing slope of the underlying ridge, the volume of lava reaching the base of the eastern face of Pukekaikiore at the southern margin was reduced, minimising the development of compressional stress as the lobe reached this obstacle. Additionally, the lateral spread of the northern margin down the underlying ridge slope precludes a significant increase in the yield strength of the lava. The front of the southern Bs lobe reaches but does not come into contact with the base of a relatively high-elevation ridge perpendicular to the flow front (Figs. 2.5, 2.21), therefore flow advance was not obstructed by this obstacle. The gentle slope of the underlying surface (~ 10°) of this lobe indicates a significant reduction in flow velocity, thus the combination of lava supply cessation at the

vent and the increase in cooling rates and viscosity associated with decreased flow velocity controlled the final length of this lobe deposit.

18th August (F) Lava Flow

The distal zone of the 18th August (F) lava flow is characterised by significant narrowing of the flow deposit upon reaching the distal zone and subsequent widening of the flow towards the flow front. Flow narrowing coincides with an increase in slope angle to ~ 16° to the west of the distal end of Pukekaikiore ridge; however, there is also evidence of flow confinement by pre-existing topography. For example, the southern margin of the flow is emplaced along the top of and down the south-facing slope of a pre-existing ridge (Fig. 2.32), while the northern margin is initially confined by the distal end of Pukekaikiore ridge. Additionally, the marked decrease in levee height of both margins behind the flow front (Fig. 2.33) implies that the northern margin of the flow was also emplaced over a pre-existing ridge whose distal end coincides with that of the ridge underlying the southern flow margin. Thus, as the lava advanced beyond the distal end of Pukekaikiore ridge, the flow was either confined between two adjacent pre-existing ridges, or as with the southern lower BnL-S lobe, the flow was emplaced along the top of a single pre-existing ridge, directing the flow path of the lava.

The construction of secondary levees within the central flow channel of this zone (Fig. 2.31) may indicate a marked reduction in effusion rate at the vent, signifying the final stages of this effusive episode. Alternatively, the outer levees may represent the initial advance of the lava flow following inundation of the distal end of Pukekaikiore ridge, which were subsequently abandoned as the lava behind the flow front lost momentum due to obstruction of the flow by the ridge end. Whereas, the secondary, inner levees may represent a second influx of lava as the proximal flow channel drained, increasing compressional stress of the lava ponded upstream from the ridge which allowed another surge of lava to overtop the ridge end. However, with the cessation of lava supply at the vent, this second influx would have occurred at reduced velocity and reduced volume, thus the width of the flowing lava would be narrower than the original flow, resulting in new cooled flow margins within the earlier margins.

The small 'break-out' lobe on the southern margin outer levee (Figs. 2.4A, 2.5) is comparable to those described by Kilburn and Lopes (1991) and Blake and Bruno (2000) in which the cooled marginal levee is breached by hot lava from the central flow channel during the formation of compound flows, consequently implying that cooling of the lava was the main control on flow emplacement in this zone. However, this is contradicted by the drained proximal flow channel in the proximal zone and by the formation of the secondary levees. Alternatively, this lobe may have formed in response to a small dip in the underlying ridge-top elevation, promoting a small surge of lava to advance down the south-facing slopes of the ridge.

Widening of the flow front of this lava coincides with another marked reduction in slope angle to ~ 9°. The flow front also formed a series of small lobes or toes as a result of the low flow velocity associated with this reduced slope angle. Additionally, this lava flow reached its final flow length ~ 48 hours following activation of the flow at the vent, thus lava viscosity increased significantly, although again the ability of the lava to spread laterally at this distance from the vent and after the long duration of flow emplacement indicates that yield strength remained relatively low.

5.3.5 Summary of the Controls on 1954 Lava Flow Emplacement

Large-scale and localised variations in slope gradient was the primary environmental factor governing the flow emplacement dynamics of the 1954 lavas, although pre-existing topographic features contributed to flow direction, dimensions and subsequent morphology in the medial to distal regions of the lava flow field. Slope angle was the major control on flow velocity, which in turn influenced cooling rates and lava viscosity with distance from the vent. The relatively low initial viscosity of the 1954 lavas due to eruption temperature, geochemical composition and volatile content contributed to the initially high velocities of the 1954 lavas on the steeper slopes. A continuous feedback effect between flow velocity, lava viscosity and cooling rates had a slightly stronger influence on flow dynamics towards the medial and distal regions of the longer lava flows, contributing to the final flow length of these lavas. Slope angle and

flow velocity were also the main controls on basal shear stress rates, resulting in highly autobrecciated flow deposits extending throughout flow depth. Effusion rate contributed to the activation of lava flow advance and initial cooling rates, while effusion duration and subsequent lava supply were the main factors contributing to final flow length of the 1954 lavas. The relatively short-lived emplacement duration of each of the 1954 lavas precluded the development of a strong surface crust.

5.4 EMPLACEMENT OF PREVIOUS NGAURUHOE LAVAS

Pre-historic and early historic Ngauruhoe lavas display a wider range of flow deposit dimensions, volume and morphological features than those of the 1954 lavas. Hobden *et al*. (2002) identified five chronostratigraphic groups of lava flows deposited over the c. 2.5 ka history of Mount Ngauruhoe (Fig. 1.4), distinguished by their geochemical and isotopic composition. There is a generalised trend of decreasing flow deposit length between the older chronostratigraphic groups, particularly groups 1 and 3 (c. 2.5 ka to pre-1870), and the newer groups, 4 and 5 (pre-1870 to 1975), indicating that larger volumes of material erupted during pre-historic flow emplacement and may imply different controls on flow emplacement processes. The oldest group of lavas (group 1) extended ~ 3 to 5 km from the vent, along the Mangatepopo and Waihohonu Valley floors, while the group 2 and 3 lavas extended ~ 2 to 4 km from the vent. Group 4 and 5 lavas extend at most ~ 2.5 km from the vent, and did not reach the valley floors (Hobden *et al*., 2002). Many of the pre-historic flow deposits display evidence of a drained central flow channel towards their medial to distal regions (Hobden, 1997), indicating both rapid effusion rates of large volumes of lava over a relatively short duration and a final flow length controlled by the cessation of lava supply.

The generally decreasing trend in flow length over time implies increasing lava viscosity with successive effusive episodes. However, geochemical and isotope analysis indicates that there is no simple linear trend in the evolution of magma at Mount Ngauruhoe and that individual eruption episodes are associated with mixing of numerous, small, short-lived batches of magma and crustal

contaminants within a complex plumbing system beneath the vent. Ngauruhoe lavas range in composition from basaltic andesite to andesite, with most chronostratigraphic lava groups displaying a narrow range of SiO_2 composition (e.g. groups 1 and 2, 54.2 to 55.9 wt.% SiO_2; groups 3 and 4, 57.2 to 58.6 wt.% SiO_2), while the historic lavas of group 5 display the widest SiO_2 composition range (54.8 to 58.2 wt.% SiO_2) (Hobden *et al*., 2002). Consequently, lava viscosity varied between successive chronostratigraphic lava groups; however, although it can be assumed that viscosity of the group 3 and 4 andesitic lavas would have been greater than the 1954 lavas, this did not prohibit flow length reaching greater distances from the vent than the 1954 lavas.

Eruption style during emplacement of early Ngauruhoe lavas is unknown, therefore lava flows may have been generated by quiescent outpouring of lava directly from a vent or fissure, or by the accumulation of spatter-fed deposits. Additionally, the gradient of the underlying slope of the proximal regions of early Ngauruhoe lavas is also unknown, thus flow velocity can not be estimated. However, although flow dimensions are considerably greater, the generally morphological trend of drained central flow channels strongly suggests that emplacement processes were controlled by the same factors in all Ngauruhoe lavas.

5.5. MONITORING AND PREDICTING FUTURE NGAURUHOE LAVA FLOW BEHAVIOUR

Assuming no change in vent architecture or scoria cone morphology, future lava flows may arise either from overflow of ponded lava within the current scoria cone or the accumulation of fire-fountain spatter deposits on the rim of the cone. In the former case, the low elevation of the north-western scoria cone rim would direct future lava flows along similar flow paths to the 1954 lavas, whereas in the latter case, flow paths will primarily depend on the fire-fountain profile and the location of the accumulated spatter pile on the scoria cone rim. Lava viscosity is determined by magma composition and eruption temperature; however, it is likely that rapid flow velocities would still develop in lava flows of andesitic composition due to initial emplacement over the steep proximal slopes. Cooling

rate and final flow length will depend on the rate and duration of effusive episodes, which will also determine the development of either single arterial or compound flows. Therefore, if a future eruption is dominated by intermittent, short-lived, rapid effusive episodes, a series of single, arterial, volume-controlled lavas will evolve. Conversely, significant changes in magma composition, volatile content or magma chamber dynamics may result in the slow effusion of lava over a longer time interval, producing compound, cooling-limited lava flows. However, the previous eruptive history of Ngauruhoe indicates that future effusive activity is more likely to be comparable to the eruption style observed during the 1954-55 eruption event, therefore the controls on future flow behaviour will be similar to these lavas.

Predicting the final flow length of volume-limited lavas is problematic because termination of lava supply cannot be easily forecast and flow emplacement duration is relatively short-lived. However, accurate measurement of effusion rate and fire-fountain dynamics (where applicable) to identify trends in effusion rate and duration would assist in predicting the final stages of effusion. Additionally, measured flow front velocity and associated underlying slope gradient can be used to estimate lava viscosity and thus model the continued advance and behaviour of the flow. It may be possible to directly measure active lava flows *in situ* at increasing distances from the vent, which would enable an estimation of cooling rate and thus greater accuracy of flow behaviour models. Predicting the behaviour of cooling-limited lavas is generally less problematic, partly because emplacement duration is usually longer, enabling more comprehensive data collection and allowing more time to estimate flow behaviour. Additionally, many of the recently developed predictive flow behaviour models have been designed to assess the effect of surface cooling on flow behaviour.

The hazards posed by future lava flow events at Mount Ngauruhoe are relatively low, compared to overseas volcanoes, because the surrounding slopes are neither densely inhabited nor cultivated for agriculture. However, the region is popular with trampers and sightseers and, depending on the velocity and distance of flow advance from the vent, future lava flows may pose some hazard to these and to scientists and DOC employees monitoring the eruption. The generation of future

lava flows at Mount Ngauruhoe would provide invaluable data regarding the emplacement processes of basaltic andesite to andesite composition lavas emplaced over steep slopes, enabling assessment, validation and refinement of current predictive flow models.

CHAPTER 6

Summary and Conclusions

6.1 SUMMARY

Mount Ngauruhoe is a young, basaltic andesite to andesite, composite volcano and the most recently active cone of the Tongariro Volcanic Centre. Historic eruptions have displayed a diverse range of eruption styles and eruption products. The penultimate eruption of 1954-55 was the last lava flow producing event, in which approximately 17 spatter-fed lava flows were emplaced on the north-western flanks of the cone. Of these, 11 lava flow deposits have been previously mapped and six clearly identified in the field. The 1954 lava flow deposits generally display similar morphological characteristics on the steep upper slopes of the cone, with variations in flow morphology, dimensions and surface features occurring towards the medial to distal margins of the flow deposits emplaced on shallower slopes. These a'a lavas are typically highly autobrecciated, and display a large-scale trend in clast-size and morphological distribution across the width of the flow deposits. Smaller, sub-rounded clasts are generally concentrated at the outer flow margins and large, sub-angular to irregular clasts dominate central flow channel surfaces and flow front margins.

The 1954 lavas are porphyritic, olivine-bearing, medium-K, calc-alkaline basaltic andesites with a narrow SiO_2 composition range (55.15 to 55.64 wt. % SiO_2), consistent with the findings of previous studies, with an average crystal and vesicle abundance of 27% and 23% respectively. There are no trends in petrographic or geochemical composition between successively emplaced lava flows, indicating that all the 1954 lavas derived from a single, homogeneous magmatic source, with no apparent evolution in physical and chemical properties during the course of the eruption. Rheological properties of individual lava flows are thus assumed to be comparable at the time of flow activation.

The calculated total viscosity of the 1954 lavas includes crystal and vesicle abundance and is highly dependant on eruption temperature and cooling rates, with a range of 10^2 to 10^4 Pa s at 1150 to 950°C. Yield strength was difficult to quantify but is assumed in this study to be relatively low (~ 25 Pa). Viscosity and yield strength are expected to have increased to some extent during flow advance as the lavas cooled, depending primarily on the cooling rate and emplacement duration of individual lava flows. The calculated mean flow velocity range is 0.04 to 0.09 m s^{-1}, assuming 950°C lava temperature and is reasonably comparable with the estimated mean flow velocities (0.03 to 0.04 m s^{-1}) based on eye-witness reports. The velocity calculation model shows a significant reduction in flow velocity over shallow slopes, consistent with the reported reduction in flow velocities at these locales. Effusion rate could not be definitively quantified but morphological flow deposit characteristics indicate intermittent, short-duration episodes of high effusion rates. Grätz numbers used to determine the controls on flow cessation gave conflicting results but generally indicate that the run-out distances of the lavas were volume-limited. Comparison of documented and predictive flow propagation patterns indicate that cooling of the lava flow surface was not a major control on either flow advance or cessation of the 1954 lavas.

6.2 CONCLUSIONS

The morphological, geometric and textural characteristics of the 1954 lava flow deposits represent the various processes involved during their emplacement and are characterised by:

- Discrete, single unit lava flows directed down the north-western and western slopes of the cone.
- Straight flow paths proximal to the crater rim with bifurcation, multiple lobe formation and variable/diverted flow path directions occurring at medial to distal regions.
- Relatively constant flow width and depth of individual flows proximal to the crater rim, with increasing variability occurring at medial to distal regions.
- Autobrecciation of flow surfaces.

- Marginal levee development and drainage of central flow channels proximal to the crater rim and partially or fully infilled flow channels at medial to distal regions.
- Compression-induced folding of flow channel surfaces.
- Variable length flow deposits with distal margins emplaced on a range of underlying slope gradients.

The emplacement dynamics of the 1954 lavas can be determined by comparing rheological and flow behaviour models, flow deposit characteristics and documented accounts of the eruption. Three main factors primarily governed the processes involved during lava flow emplacement:

❖ ***Effusion rate:*** Intermittent, high rates of effusion determined fire-fountain dynamics and subsequent lava flow generation, producing at least 11 discrete lava flow units directed in part by an asymmetric fire-fountain profile. The duration of each effusive episode primarily controlled flow emplacement duration and the subsequent cessation of flow advance.

❖ ***Rheological Properties:*** Rheological properties played a major role in the proximal zone, where low viscosity and yield strength promoted high flow velocity and low cooling rates. The relatively short emplacement duration of most of the lavas precluded significant downflow changes to their rheological properties. Viscosity increases associated with reduced flow velocity on shallow slopes is indicated but yield strength did not increase sufficiently to prevent lateral spread of the lava in the medial and distal zones.

❖ ***Topography:*** Emplacement dynamics were primarily controlled by the gradient and localised variations in slope angle at all distances from the vent. Slope angle was the major control on flow velocity and flow width and depth and contributed to the distribution of shear stress associated with autobrecciation of the lava. The marked reduction in flow front

velocity associated with shallow slopes, promoted an increase in cooling rate and lava viscosity. Localised variations in slope angle contributed to the planimetric form of lavas in the medial and distal zones. Pre-existing topographic features in the medial to distal zones also strongly controlled the flow path and subsequent flow deposit morphology, and was the major control on the development of compression-induced surface folding.

The emplacement dynamics of future Ngauruhoe lava flows will be comparable to the 1954 lavas if similar eruption conditions i.e. intermittent, high effusion rate, short-duration fire-fountaining, and magma composition prevail, enabling the development of well-constrained flow behaviour prediction models. Due to the broad compositional range of previous Ngauruhoe lavas, the viscosity and yield strength of future lavas may significantly differ from the 1954 lavas. Consequently the rheological properties of future lavas may exert a greater control on emplacement dynamics. However, future lavas will be subject to the same topographic conditions, on any sector of the cone, and slope gradient, particularly proximal to the vent, will remain a major controlling factor in emplacement dynamics.

This study has effectively incorporated the flow deposit characteristics of the 1954-55 Ngauruhoe lavas with existing numerical models to quantify flow rheology and emplacement processes. This is the first study relating to intermediate lavas in New Zealand and offers a basis for approaching future flow behaviour studies of intermediate lavas at other composite volcanoes.

REFERENCES

Allen, L.R. 1949. The eruption of Ngauruhoe. February-March 1949, *New Zealand Science Review*, 7, 180-183.

Anderson, S.W., Stofan, E.R., Plaut, J.J., Crown, D.A. 1998. Block size distributions on silicic lava flow surfaces: Implications for emplacement conditions. *Geological Society of America Bulletin*, 110, 1258-1267.

Arpa, M.C.B., Laguerta, E.P., Perez, J.S., Villacorte, E.U., Maximo, R.P.R., Dela Cruz, E., Ayuson, J.R.C. 2008. Morphology, flow front advance and volume of the active lava flow from the 2006 eruption of Mayon Volcano, Philippines. *Geophysical Research Abstracts*, 10, EGU2008-A-01544.

Bagdassarov, N. Sh., Dingwell, D.B. 1992. A rheological investigation of vesicular rhyolite. *Journal of Volcanology and Geothermal Research*, 50, 307-322.

Ball, M., Pinkerton, H., Harris, A.J.L. 2008. Surface cooling, advection and the development of different surface textures on active lavas on Kilauea, Hawaii. *Journal of Volcanology and Geothermal Research*, 173, 148-156.

Baloga, S., Spudis, P.D., Guest, J.E. 1995. The dynamics of rapidly emplaced terrestrial lava flows and implications for planetary volcanism. *Journal of Geophysical Research*, 100, 24,509-24,519.

Barberi, F., Carapezza, M.L., Valenza, M., Villari, L. 1993. The control of lava flow during the 1991-1992 eruption of Mount Etna. *Journal of Volcanology and Geothermal Research*, 56, 1-34.

Battey, M.H. 1949. The recent eruption of Ngauruhoe. *Records of the Auckland Institute and Museum*, 3, 387-409.

Bebbington, M.S., Lai, C.D. 1996. Statistical analysis of New Zealand volcanic occurrence data. *Journal of Volcanology and Geothermal Research*, 74, 101-110.

Bibby, H. M., Caldwell, T G., Davey, F. J., Webb, T. H. 1995. Geophysical evidence on the structure of the Taupo Volcanic Zone and its hydrothermal circulation. *Journal of Volcanology and Geothermal Research*, 68, 29-58.

Blake, S., Bruno, B.C. 2000. Modelling the emplacement of compound lava flows. *Earth and Planetary Science Letters*, 184, 181-197.

Booth, B., Self, S. 1973. Rheological features of the 1971 Mount Etna lavas. *Philosophical Transactions of the Royal Society of London,* Series A, 274, 99-106.

Borgia, A., Linneman, S.R. 1990. On the mechanisms of lava flow emplacement on volcano growth: Arenal, Costa Rica. *In:* Fink, J.H. (Ed). *Lava Flows and Domes: Emplacement Mechanisms and Hazard Implications,* IAVCEI Proceedings in Volcanology 2, Springer-Verlag, New York, 249pp.

Borgia, A., Linneman, S., Spencer, D., Moralis, L.D., Andre, J.B. 1983. Dynamics of lava flow fronts, Arenal Volcano, Costa Rica. *Journal of Volcanology and Geothermal Research*, 19, 309-329.

Calvari, S., Pinkerton, H. 1998. Formation of lava tubes and extensive flow field during the 1991-1993 eruption of Mount Etna. *Journal of Geophysical Research*, 103, 27,291-27,301.

Cashman, K.V., Mangan. M.T., Newman, S. 1994. Surface degassing and modifications to vesicle size distributions in Kilauea basalt. *Journal of Volcanology and Geothermal Research*, 61, 45-68.

Cashman, K., Thornber, C., Kauahikaua, J. 1999. Cooling and crystallisation of lava in open channels, and the transition of pahoehoe lava to a'a. *Bulletin of Volcanology*, 61, 306-323.

Chan, D., Powell, R.L. 1984. Rheology of suspensions of spherical particles in a Newtonian and non-Newtonian fluid. *Journal of Non-Newtonian Fluid Mechanics*, 15, 165-179.

Cole, J.W. 1978. Andesites of the Tongariro Volcanic Centre, North Island, New Zealand. *Journal of Volcanology and Geothermal Research*, 3, 121-153.

Crisp, J., Baloga, S. 1994. Influence of crystallization and entrainment of cooler material on the emplacement of basaltic aa lava flows. *Journal of Geophysical Research*, 99, 11,819-11,831.

Crisp, J., Cashman, K.A., Bonini, J.A., Hougen, S.B., Pieri, D.C. 1994. Crystallisation history of the 1984 Mauna Loa lava flow. *Journal of Geophysical Research*, 99, 7177-7198.

Crown, D.A., Peiterson, M.N. 1995. Downflow morphologic variations in Hawaiian and Martian lava flows [abs.]. *Lunar and Planetary Science Conference* XXVI, 299-300.

Crown, D.A., Peiterson, M.N. 1996. Downflow morphologic variations in Hawaiian lava flows: Implications for modelling planetary lava flow emplacement [abs.]. *Lunar and Planetary Science Conference* XXVII, 271-272.

Dragoni, M. 1993. Modelling the rheology and cooling of lava flows. *In*: Kilburn, C.R.J., Luongo, G. (eds), *Active Lavas*, UCL Press, London, pp 235-261.

Dragoni, M., Bonafede, M., Boschi, E. 1986. Downslope flow models of a Bingham liquid: implications for lava flows. *Journal of Volcanology and Geothermal Research*, 30, 305-325.

Favalli, M., Chirico, G.D., Papale, P., Pareschi, M.T., Boschi, E. 2009. Lava flow hazard at Nyiragongo volcano, D.R.C. 1. Model calibration and hazard mapping. *Bulletin of Volcanology*, 71, 363-374.

Fink, J.H., Fletcher, R.C. 1978. Ropy pahoehoe: Surface folding of a viscous fluid. *Journal of Volcanology and Geothermal Research*, 4, 151-170.

Fink, J.H., Griffiths, R.W. 1998. Morphology, eruption rates, and rheology of lava domes: Insights from laboratory models. *Journal of Geophysical Research*, B, 103, 527-545.

Fink, J.H., Zimbelman, J. 1990. Longitudinal variations in rheological properties of lavas: Pu'u O'o basalt flows, Kilauea volcano, Hawaii. *In:* Fink, J.H. (Ed). *Lava Flows and Domes: Emplacement Mechanisms and Hazard Implications*, IAVCEI Proceedings in Volcanology 2, Springer-Verlag, New York, 249pp.

Franzetta, G., Romano, R. 1984. The 1983 Etna eruption: event chronology and morphological evolution of the lava flow. *Bulletin of Volcanology*, 47, 1079-1096.

Gay, E.C., Nelson, P.A., Armstrong, W.P. 1969. Flow properties of suspensions with high solids concentrations. *American Institute of Chemical Engineers Journal*, 15, 815-822.

Gill, J.B. 1981. *Orogenic Andesites and Plate Tectonics*. Springer-Verlag, Berlin. 390 pp.

Giordano, D., Dingwell, D.B. 2003. Non-Arrhenian multicomponent melt viscosity: a model. *Earth and Planetary Science Letters*, 208, 337-349.

Giordano, D., Romano, C. Dingwell, D.B. Poe, B., Behrens, H. 2004. The combined effects of water and fluorine on the viscosity of silicic magmas. *Geochimica et Cosmochimica Acta*, 68, 5,159-5,168.

Giordano, D., Russell, J.K., Dingwell, D.B. 2008. Viscosity of magmatic liquids: a model. *Earth and Planetary Science Letters*, 271, 123-134.

Graham, I.J., Cole, J.W., Briggs, R.M, Gamble, J.A., Smith, I.E.M. 1995. Petrology and petrogenesis of volcanic rocks from the Taupo Volcanic Zone: a review. *Journal of Volcanology and Geothermal Research*, 68, 59-87.

Gregg, D.R. 1956. Eruption of Ngauruhoe 1954-1955. *New Zealand Journal of Science and Technology*, B37, 675-688.

Gregg, D.R. 1960. *The Geology of the Tongariro Subdivision*. New Zealand Geological Survey, Bulletin n.s. 40, Wellington, New Zealand.

Gregg, T.K.P., Fink. J.H. 2000. A laboratory investigation into the effects of slope on lava flow morphology. *Journal of Volcanology and Geothermal Research*, 96, 145-159.

Gregg, T.K.P., Fink, J.H., Griffiths, R.W. 1998. Formation of multiple fold generations on lava flow surfaces: Influence of strain rate, cooling rate, and lava composition. *Journal of Volcanology and Geothermal Research*, 80, 281-292.

Griffiths, R.W., Fink, J.H. 1993. Effects of surface cooling on the spreading of lava flows and domes. *Journal of Fluid Mechanics*, 252, 667-702.

Guest, J.E., Kilburn, C.R.J., Pinkerton, H., Duncan, A.M. 1987. The evolution of lava flow-fields: observations of the 1981 and 1983 eruptions of Mount Etna, Sicily. *Bulletin of Volcanology*, 49, 527-540.

Guilbaud, M.-N., Blake, S., Thordarson, T., Self, S. 2007. Role of syn-eruptive cooling and degassing on textures of lavas from the AC 1783-1784 Laki eruption, South Iceland. *Journal of Petrology*, 48, 1265-1294.

Harris, A.J.L., Rowland, S.K. 2001. FLOWGO: a kinematic thermo-rheological model for lava flowing in a channel. *Bulletin of Volcanology*, 63, 20-44.

Head, J.W., Wilson, L. 1989. Basaltic pyroclastic eruptions: Influence of gas-release patterns and volume fluxes on fountain structure, and the formation of cinder cones, spatter cones, rootless flows, lava ponds and lava flows. *Journal of Volcanology and Geothermal Research*, 37, 261-271.

Hess, K.U., Dingwell, D.B. 1996. Viscosities of hydrous leucogranitic melts: a non-Arrhenian model. *American Mineralogist*, 81, 1,297-1,300.

Hobden, B.J. 1997. Modelling magmatic trends in time and space: eruptive and magmatic history of Tongariro volcanic complex, New Zealand. PhD Thesis, University of Canterbury, Christchurch.

Hobden, B.J., Houghton, B.F., Davidson, J.P., Weaver. S.D. 1999. Small and short-lived magma batches at composite volcanoes: time windows at Tongariro volcano, New Zealand. *Journal of the Geological Society, London*, 156, 865-868.

Hobden, B.J. Houghton, B.F. 2000. Geology of the Tongariro Volcanic Traverse. *In*: Price, R.C., Gamble, J.A., Hobden, B.J. (eds). 2000. *State of the Arc 2000: Guidebook for field excursions on Ruapehu and Tongariro Volcanoes*, The Royal Society of New Zealand.

Hobden, B.J., Houghton, B.F., Nairn, I.A. 2002. Growth of a young, frequently active composite cone: Ngauruhoe volcano, New Zealand. *Bulletin of Volcanology*, 64, 392-409.

Hoover, S.R., Cashman, K.V., Manga, M. 2001. The yield strength of sub-liquidus basalts – experimental results. *Journal of Volcanology and Geothermal Research*, 107, 1-18.

Houghton, B. F., Wilson, C. J. N., McWilliams, M. O., Lanphere, M. A., Weaver, S. D., Briggs, R. M., Pringle, M. S. 1995. Chronology and dynamics of a large silicic magmatic system: Central Taupo Volcanic Zone, New Zealand. *Geology*, 23, 13-16.

Hui, H., Zhang, Y. 2007. Toward a general viscosity equation for natural anhydrous and hydrous silicate melts. *Geochimica et Cosmochimica Acta*, 71, 403-416.

Hulme, G. 1974. The interpretation of lava flow morphology. *Geophysical Journal of the Royal Astronomical Society*, 39, 361-383.

Hulme, G., Fielder, G. 1977. Effusion rates and rheology of lunar lavas. *Philosophical Transactions of the Royal Society of London*, A285, 227-234.

Huppert, H.E., Shepherd, J.B., Sigurdsson, H., Sparks, R.S.J. 1982. On lava dome growth, with application to the 1979 lava extrusion of the Soufriere of St Vincent. *Journal of Volcanology and Geothermal Research*, 14, 199-222.

Iverson, R.M. 1990. Lava domes modelled as brittle shells that enclose pressurized magma, with application to Mount St Helens. *In:* Fink, J.H. (Ed). *Lava Flows and Domes: Emplacement Mechanisms and Hazard Implications*, IAVCEI Proceedings in Volcanology 2, Springer-Verlag, New York, 249pp.

Johnson, A.M. 1970. *Physical Processes in Geology*. Freeman, Cooper and Company, San Francisco, 577pp.

Kerr, R.C., Lister, J.R. 1991. The effects of shape on crystal settling and the rheology of magmas. *Journal of Geology*, 99, 457-467.

Kerr, R.C., Lyman, A.W. 2007. Importance of surface crust strength during the flow of the 1988-1990 andesite lava of Lonquimay Volcano, Chile. *Journal of Geophysical Research*, B,112, B03209, doi: 10.1029/2006JB004522.

Kilburn, C.R.J. 1990. Surface of aa flow-fields on Mount Etna, Sicily: Morphology, rheology, crystallisation and scaling phenomena. *In:* Fink, J.H. (Ed). *Lava Flows and Domes: Emplacement Mechanisms and Hazard Implications*, IAVCEI Proceedings in Volcanology 2, Springer-Verlag, New York, 249pp.

Kilburn, C.R.J. 1993. Lava crusts, aa flow lengthening and the pahoehoe-aa transition. *In:* Kilburn, C.R.J., Luongo, G. (eds). *Active Lavas: Monitoring and Modelling*, UCL Press, London, 374pp.

Kilburn, C.R.J. 2000. Lava flows and flow fields. *In*: Sigurdsson, H. *Encyclopedia of Volcanoes*, Academic Press, San Diego.

Kilburn, C.R.J. 2004. Fracturing as a quantitative indicator of lava flow dynamics. *Journal of Volcanology and Geothermal Research*, 132, 209-224.

Kilburn, C.R.J., Lopes, R.M.C. 1991. General patterns of flow field growth: a'a and blocky lavas. *Journal of Geophysical Research*, B, 96, 19,721-19,732.

Kilburn, C.R.J., Guest, J.E. 1993. Aa lavas of mount Etna, Sicily. *In:* Kilburn, C.R.J., Luongo, G. (eds). *Active Lavas: Monitoring and Modelling*, UCL Press, London, 374pp.

Krieger, I.M., 1972, Rheology of monodispersed lattices. *Advances in Colloid and Interface Sciences*, 3, 111-136.

Krippner, J.B. 2009. Ngauruhoe inner crater volcanic processes of the 1954-1955 and 1974-1975 eruptions. MSc Thesis, University of Waikato, Hamilton, New Zealand.

Lipman, P.W., Banks, N.G. 1987. A'a flow dynamics, Mauna Loa 1984. *In*: Decker, R.W., Wright, T.L, Stauffer, P.H. (eds). *Volcanism in Hawaii*, USGS Professional Paper 1350, 1,527-1,568.

Lipman, P.W., Banks, N.G., Rhodes, J.M. 1985. Degassing-induced crystallisation of basaltic magma and effects on lava flow rheology. *Nature*, 317, 604-607.

Llewellin, E.W., Manga, M. 2005. Bubble suspension rheology and implications for conduit flow. *Journal of Volcanology and Geothermal Research*, 143, 205-217.

Lyman, A.W., Kerr, R.C. 2006. Effect of surface solidification on the emplacement of lava flows on a slope. *Journal of Geophysical Research*, B,111, B05206, doi: 10.1029/2005JB004133.

Lyman, A.W., Kerr, R.C., Griffiths, R.W. 2005. The effects of internal rheology and surface cooling on the emplacement of lava flows. *Journal of Geophysical Research*, B,110, B08207, doi: 10.1029/2005JB003643.

Malin, M.C. 1980. Lengths of Hawaiian lava flows. *Geology*, 8, 306-308.

Manga, M., Loewenberg, M. 2001. Viscosity of magmas containing highly deformable bubbles. *Journal of Volcanology and Geothermal Research*, 105, 19-24.

Manga, M. Castro, J., Cashman, K., Loewenberg, M. 1998. Rheology of bubble-bearing magmas. *Journal of Volcanology and Geothermal Research*, 87, 15-28.

Marsh, B.D. 1981. On the crystallinity, probability of occurrence, and rheology of lava and magma. *Contributions to Mineralogy and Petrology*, 78, 85-98.

Marsh, B.D. 1987. Magmatic processes. *Reviews of Geophysics*, 25, 1043-1053.

McBirney, A.R., Murase, T. 1984. Rheological properties of magmas. *Annual Review of Earth and Planetary Sciences*, 12, 337-357.

McDonough, W.F., Sun, S.-s., Ringwood, A.E., Jagoutz, E., Hofmann, A.W. 1992. Potassium, rubidium and cesium in the Earth and Moon and the evolution of the mantle of the earth. *Geochimica et Cosmochimica Acta*, 56, 1001-1012.

Moore, H.J., Arthur, D.W.G., Schaber, G.G. 1978. Yield strengths of flows on the Earth, Mars and Moon. *Proceedings of the Lunar and Planetary Science Conference*, 9, 3351-3378.

Moore, H.J. 1987. Preliminary estimates of the rheological properties of 1984 Moana Loa lava. *US Geological Survey Professional Paper*, 1350, 1569-1588.

Moore, H.J., Plaut, J.J., Schenk, P.M., Head, J.W. 1992. An unusual volcano on Venus. *Journal of Geophysical Research*, E, 97, 13,479-13,493.

Naranjo, J.A., Sparks, R.S.J., Stasiuk, M.V., Moreno, H., Ablay, G.J. 1992. Morphological, structural and textural variations in the 1988-1990 andesite lava of the Lonquimay volcano, Chile. *Geological Magazine*, 129, 657-678.

Ngauruhoe Erupts. 2003. Video recording from an original film by David Branagan, Folkus Video, Wellington.

Pal, R. 2003. Rheological behaviour of bubble-bearing magmas. *Earth and Planetary Science Letters*, 207, 165-179.

Parfitt, E.A., Wilson, L. 2008. *Fundamentals of Physical Volcanology*, Blackwell, Malden, MA. 330 pp.

Patterson, D.B. and Graham, I.J. 1988. Petrogenesis of andesitic lavas from Mangatepopo Valley and Upper Tama Lake, Tongariro Volcanic Centre, New Zealand. *Journal of Volcanology and Geothermal Research*, 35, 17- 29.

Peterson, D.W., Tilling, R.I. 1980. Transition of basaltic lava from pahoehoe to aa, Kilauea volcano, Hawaii: Field observations and key factors. *Journal of Volcanology and Geothermal Research*, 7, 271-293.

Peterson, D.W., Tilling, R.I. 2000. Lava Flow Hazards. *In*: Sigurdsson, H. *Encyclopedia of Volcanoes*, Academic Press, San Diego.

Pinkerton, H., Sparks, R.S.J. 1976. The 1975 sub-terminal lavas, Mount Etna: a case history of the formation of a compound lava field. *Journal of Volcanology and Geothermal Research*, 1, 167-182.

Pinkerton, H., Sparks, R.S.J. 1978. Field measurements of the rheology of lava. *Nature*, 276, 383-85.

Pinkerton, H., Stevenson, R.J. 1992. Methods of determining the rheological properties of magmas at sub-liquidus temperatures. *Journal of Volcanology and Geothermal Research*, 53, 47-66.

Pinkerton, H., Wilson, L. 1994. Factors controlling the lengths of channel-fed lava flows. *Bulletin of Volcanology*, 56, 108-120.

Pinkerton, H., Norton, G. 1995. Rheological properties of basaltic lavas at sub-liquidus temperatures: laboratory and field measurements on lavas from Mount Etna. *Journal of Volcanology and Geothermal Research*, 68, 307-323.

Price, R.C., Gamble, J.A., Smith, I.E.M., Stewart, R.B., Eggins, S., Wright, I.C. 2005. An integrated model for the temporal evolution of andesites and rhyolites and crustal development in New Zealand's North Island. *Journal of Volcanology and Geothermal Research*, 140, 1-24.

Rollinson, H. 1993. *Using Geochemical Data: evaluation, presentation, interpretation.* Longman Scientific and Technical, Harlow, England. 352 pp.

Rossi, M.J. 1997. Morphology of the 1984 open-channel lava flow at Krafla volcano, northern Iceland. *Geomorphology*, 20, 95-112.

Rowland, J.V., Sibson, R.H. 2001. Extensional fault kinematics within the Taupo Volcanic Zone, New Zealand: soft-linked segmentation of a continental rift system. *New Zealand Journal of Geology & Geophysics*, 44, 271-283.

Ryerson, F.J., Weed, H.C., Piwinski, A.J. 1988. Rheology of subliquidus magmas 1. Picritic compositions. *Journal of Geophysical Research*, 93, 3421-3436.

Saar, M., Manga, M., Cashman, K.V., Fremouw, S. 2001. Numerical models of the onset of yield strength in crystal-melt suspensions. *Earth and Planetary Science Letters*, 187, 367-379.

Shaw, H.R., Wright, T.L., Peck, D.L., Okamura, R. 1968. The viscosity of basaltic magma: an analysis of field measurements in Makaopuhi lava lake, Hawaii. *American Journal of Science*, 226, 225-264.

Shaw, H.R., 1969, Rheology of basalt in the melting range. *Journal of Petrology*, 10, 510-535.

Shaw, H.R. 1972. Viscosities of magmatic silicate liquids: an empirical method of prediction. *American Journal of Science*, 272, November, 870-893.

Sparks, R.S.J. 1992. Magma generation on the earth. *In*: Brown, G.C., Hawkesworth, C.J., Wilson, R.C.L. (eds). *Understanding the Earth*, Cambridge University Press, Cambridge. 551pp.

Sparks, R.S.J., Pinkerton, H., Hulme, G. 1975. Classification and formation of lava levees on Mount Etna, Sicily. *Geology*, 4, 269-271.

Stein, D.J., Spera, F.J. 1992. Rheology and microstructure of magmatic emulsions-theory and experiments. *Journal of Volcanology and Geothermal Research*, 49, 157-174.

Stevenson, R. 1989. Physical volcanology, emplacement history and inferred viscosity of two rhyolites. PhD Thesis, University of Waikato, Hamilton, New Zealand.

Stevenson, R.J., Hodder, A.P.W., Briggs, R.M. 1994a. Rheological estimates of rhyolite lava flows from the Okataina Volcanic Centre, New Zealand. *New Zealand Journal of Geology & Geophysics*, 37, 211-221.

Stevenson, R.J., Briggs, R.M., Hodder, A.P.W. 1994b. Physical volcanology and emplacement history of the Ben Lomond rhyolite lava flow, Taupo Volcanic Centre, New Zealand. *New Zealand Journal of Geology & Geophysics*, 37, 345-358.

Stewart, R.B., Price, R.C., Smith, I.E.M. 1996. Evolution of high-K arc magma, Egmont volcano, Taranaki, New Zealand: evidence from mineral chemistry. *Journal of Volcanology and Geothermal Research*, 74, 275-295.

Sumner, J.M. 1998. Formation of clastogenic lava flows during fissure eruption and scoria cone collapse: the 1986 eruption of Izu-Oshima Volcano, eastern Japan. *Bulletin of Volcanology*, 60, 195-212.

Walker, G.P.L. 1972. Compound and simple lava flows and flood basalts. *Bulletin of Volcanology*, 35, 579-590.

Walker, G.P.L. 1973. Lengths of lava flows. *Philosophical Transactions of the Royal Society of London*, A274, 107-118.

Whittington, A., Richet, P., Holtz, F. 2000. Water and the viscosity of depolymerised aluminosilicicate melts. *Geochimica et Cosmochimica Acta*, 64, 3,725-3,736.

Wilson, C.J.N., Houghton, B., McWilliams, M., Lanphere, M., Weaver, S., Briggs, R. 1995. Volcanic and structural evolution of Taupo Volcanic Zone, New Zealand – A review. *Journal of Volcanology and Geothermal Research, 68*, 1-28.

Zhang, Y., Xu, Z., Liu, Y., 2003. Viscosity of hydrous rhyolitic melts inferred from kinetic experiments, and a new viscosity model. *American Mineralogist*, 88, 1741–1752.

Zhou, J.Z.Q., Fang, T., Luo, G., Uhlerr, P.H.T. 1995. Yield stress and maximum packing fraction of concentrated suspensions. *Rheologica Acta*, 34, 544-561.

Appendix A

Flow Deposit Geometry & Field Location Descriptions

A.1 Aerial photograph of the north-western sector of Ngauruhoe

Recent lavas and pyroclastic flows show as darker deposits. Aerial photograph courtesy of GNS Science, Wairakei.

A.2 Topographic Map of the North-Western Sector of Ngauruhoe Cone with 1954 Lava Flow Deposits Shown

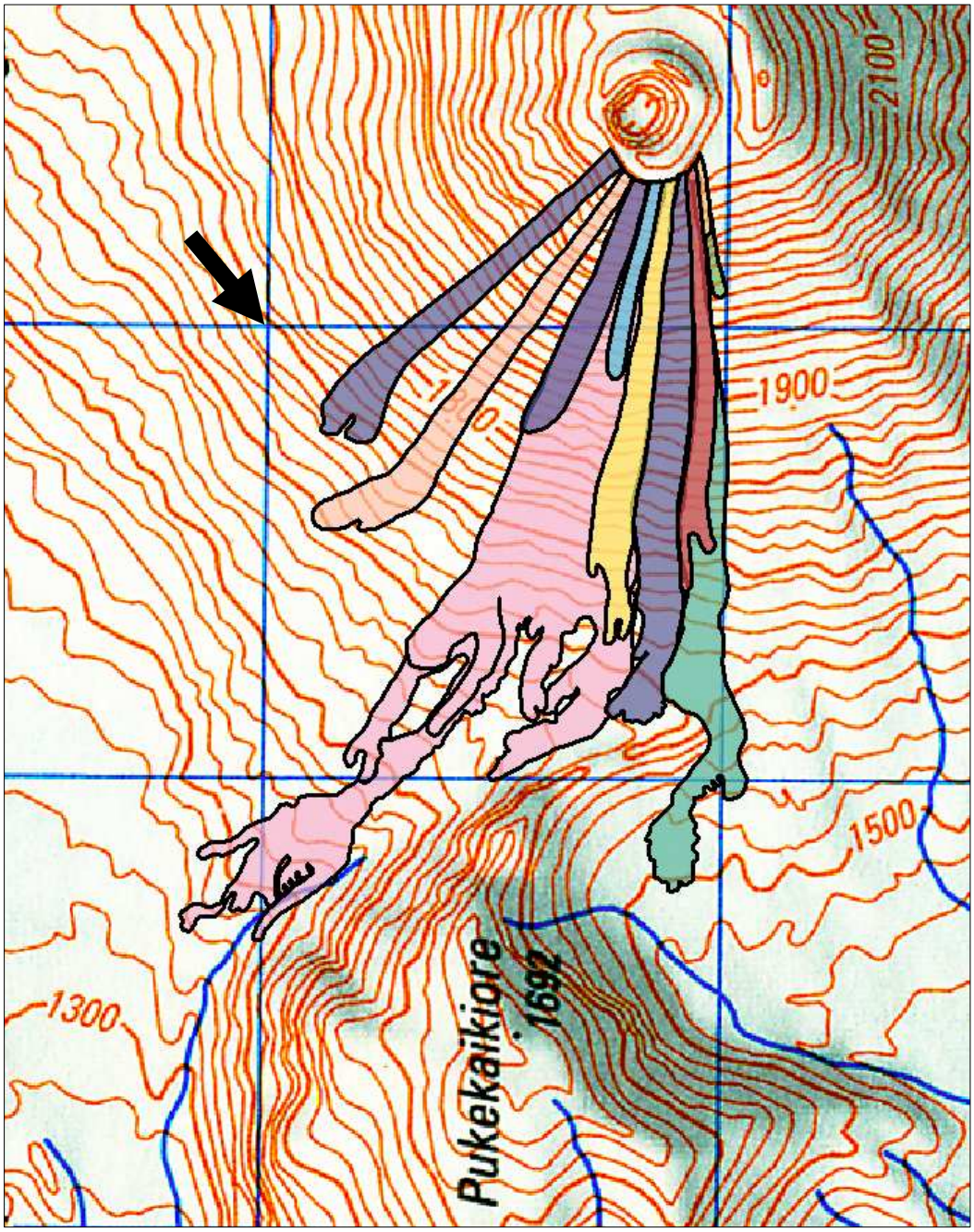

Black arrow points to grid reference: T19 370250 using NZMS260 series topographic map. Central blue grid represents 1 km distance. Flow deposit colours match those in Figs. 2.4, 2.5 and Appendix A.4.

A.2.1 Calculations for underlying slope angle & flow deposit length for each of the 1954 lavas

4th June (A)				8-13th July (C)			
Contour line	**Distance between contour lines (m)**	**Slope Angle (°)**	**Length (m)**	**Contour line**	**Distance between contour lines (m)**	**Slope Angle (°)**	**Length (m)**
2140	126	53	209.4	2140	126	53	209.4
2040	132	49	201.2	2040	149	42	200.5
1940	155	40	202.3	1940	149	42	200.5
1840	121	56	216.4	1915	34	47	49.9
1740	172	36	212.6				
1680	115	31	134.2				
1590	195	27	218.9				
Average (°)		**42**		**Average (°)**		**46**	
Total Length (m)			**1395**	**Total Length (m)**			**660**

29th July (E)				18th August (F)			
Contour line	***Distance between contour lines (m)***	**Slope Angle (°)**	**Length (m)**	**Contour line**	**Distance between contour lines (m)**	**Slope Angle (°)**	**Length (m)**
2140	*138*	46	198.7	2140	172	36	212.6
2040	*138*	46	198.7	2040	126	53	209.4
1940	*149*	42	200.5	1940	149	42	200.5
1840	*132*	49	201.2	1840	178	34	214.7
1740	*195*	31	227.5	1740	172	36	212.6
1640	*207*	29	236.7	1640	218	27	244.7
1610	*92*	19	97.3	1600	167	14	172.1
				1560	149	16	155.0
				1520	149	16	155.0
				1500	126	9	127.6
				1495	29	9	29.4
Average (°)		**37**		**Average (°)**		**27**	
Total Length (m)			**1360**	**Total Length (m)**			**1934**

18th Sept (H)				26th Sept (I)			
Contour line	**Distance between contour lines (m)**	**Slope Angle (°)**	**Length (m)**	**Contour line**	**Distance between contour lines (m)**	**Slope Angle (°)**	**Length (m)**
2140	184	33	219.4	2140	172	36	212.6
2040	132	49	201.2				
Average (°)		**41**		**Average (°)**		**36**	
Total Length (m)			**421**	**Total Length (m)**			**213**

16th Sept (G)			
Contour line	**Distance between contour lines (m)**	**Slope Angle (°)**	**Length (m)**
2140	172	36	212.6
2040	129	51	205.0
1940	155	40	202.3
1840	178	34	214.7
1740	172	36	212.6
1660	144	34	173.7
Average (°)		**39**	
Total Length (m)			**1221**

30th June (B)-Bn Lobe Group

Northern Upper Lobe (BnU-N)				Southern Upper Lobe (BnU-S)				Northern Lower Lobe (BnL-N)			
Contour line	**Distance between contour lines (m)**	**Slope Angle (°)**	**Length (m)**	**Contour line**	**Distance between contour lines (m)**	**Slope Angle (°)**	**Length (m)**	**Contour line**	**Distance between contour lines (m)**	**Slope Angle (°)**	**Length (m)**
2140	121	56	216.4	2140	126	53	209.4	2140	121	56	216.4
2040	149	42	200.5	2040	149	42	200.5	2040	149	42	200.5
1940	149	42	200.5	1940	149	42	200.5	1940	149	42	200.5
1840	149	42	200.5	1840	161	38	204.3	1840	149	42	200.5
1740	172	36	212.6	1740	167	37	209.1	1740	172	36	212.6
1640	230	26	255.9	1640	201	30	232.1	1640	230	26	255.9
1560	218	22	235.1	1580	210	17	219.6	1540	276	21	295.6
				1525	178	18	187.2	1500	155	15	160.5
								1485	63	14	64.9
Average (°)		**38**		**Average (°)**		**35**		**Average (°)**		**33**	
Total Length (m)			**1522**	**Total Length (m)**			**1663**	**Total Length (m)**			**1807**

30th June (B)-Bn Lobe Group

Southern Lower Distal Lobe 1 (BnL-S-1)				Southern Lower Distal Lobe 2 (BnL-S-2)				Southern Lower Distal Lobe 3 (BnL-S-3)			
Contour line	**Distance between contour lines (m)**	**Slope Angle (°)**	**Length (m)**	**Contour line**	**Distance between contour lines (m)**	**Slope Angle (°)**	**Length (m)**	**Contour line**	**Distance between contour lines (m)**	**Slope Angle (°)**	**Length (m)**
2140	126	53	209.4	2140	126	53	209.4	2140	126	53	209.4
2040	149	42	200.5	2040	149	42	200.5	2040	149	42	200.5
1940	149	42	200.5	1940	149	42	200.5	1940	149	42	200.5
1840	161	38	204.3	1840	161	38	204.3	1840	161	38	204.3
1740	167	37	209.1	1740	167	37	209.1	1740	167	37	209.1
1640	201	30	232.1	1640	201	30	232.1	1640	201	30	232.1
1540	310	19	327.9	1540	310	19	327.9	1540	310	19	327.9
1440	374	16	389.1	1440	379	15	392.4	1440	414	14	426.7
1400	155	15	160.5	1420	52	23	56.5	1420	69	17	72.2
1370	138	13	141.6	1400	80	14	82.4	1400	63	19	66.6
								1385	40	22	43.1
Average (°)		**31**		**Average (°)**		**31**		**Average (°)**		**30**	
Total Length (m)			**2275**	**Total Length (m)**			**2115**	**Total Length (m)**			**2192**

30th June (B)-Bn Lobe Group

Southern Lower Distal Lobe 4 (BnL-S-4)				Southern Lower Distal Lobe 5 (BnL-S-5)				Southern Lower Distal Lobe 6 (BnL-S-6)			
Contour line	**Distance between contour lines (m)**	**Slope Angle (°)**	**Length (m)**	**Contour line**	**Distance between contour lines (m)**	**Slope Angle (°)**	**Length (m)**	**Contour line**	**Distance between contour lines (m)**	**Slope Angle (°)**	**Length (m)**
2140	126	53	209.4	2140	126	53	209.4	2140	126	53	209.4
2040	149	42	200.5	2040	149	42	200.5	2040	149	42	200.5
1940	149	42	200.5	1940	149	42	200.5	1940	149	42	200.5
1840	161	38	204.3	1840	161	38	204.3	1840	161	38	204.3
1740	167	37	209.1	1740	167	37	209.1	1740	167	37	209.1
1640	201	30	232.1	1640	201	30	232.1	1640	201	30	232.1
1540	310	19	327.9	1540	310	19	327.9	1540	310	19	327.9
1440	414	14	426.7	1440	414	14	426.7	1460	270	17	282.3
1400	149	16	155.0	1400	149	16	155.0	1400	247	14	254.6
1385	63	14	64.9	1380	92	13	94.4	1370	69	26	76.8
				1350	80	22	86.3				
Average (°)		**31**		**Average (°)**		**30**		**Average (°)**		**32**	
Total Length (m)			**2230**	**Total Length (m)**			**2346**	**Total Length (m)**			**2197**

30th June (B)-Bs Lobe Group

Southern Lobe				Middle Lobe				Northern Lobe			
Contour line	**Distance between contour lines (m)**	**Slope Angle (°)**	**Length (m)**	**Contour line**	**Distance between contour lines (m)**	**Slope Angle (°)**	**Length (m)**	**Contour line**	**Distance between contour lines (m)**	**Slope Angle (°)**	**Length (m)**
2140	138	46	198.7	2140	138	46	198.7	2140	126	53	209.4
2040	138	46	198.7	2040	138	46	198.7	2040	149	42	200.5
1940	149	42	200.5	1940	149	42	200.5	1940	149	42	200.5
1840	132	49	201.2	1840	132	49	201.2	1840	164	38	208.1
1740	195	31	227.5	1740	195	31	227.5	1740	161	38	204.3
1640	207	29	236.7	1640	207	29	236.7	1640	190	32	224.0
1600	144	16	149.8	1600	144	16	149.8	1580	207	17	216.5
1540	356	10	361.5	1560	167	14	172.1	1560	86	13	88.3
Average (°)		**34**		**Average (°)**		**34**		**Average (°)**		**34**	
Total Length (m)			**1774**	**Total Length (m)**			**1585**	**Total Length (m)**			**1552**

4th July (Da)				14th July (Db)				14th July (Dc)			
Contour line	**Distance between contour lines (m)**	**Slope Angle (°)**	**Length (m)**	**Contour line**	**Distance between contour lines (m)**	**Slope Angle (°)**	**Length (m)**	**Contour line**	**Distance between contour lines (m)**	**Slope Angle (°)**	**Length (m)**
2140	126	53	209.4	2140	121	56	216.4	2140	115	60	230
2040	144	44	200.2	2040	149	42	200.5	2040	126	53	209
1940	144	44	200.2	1940	149	42	200.5	1940	152	41	201
1840	167	37	209.1	1840	149	42	200.5	1840	152	41	201
1740	161	38	204.3	1820	46	26	51.2	1740	195	31	227
1660	138	35	168.5					1640	178	34	215
								1580	253	14	261
Average (°)		**42**		**Average (°)**		**42**		**Average (°)**		**39**	
Total Length (m)			**1192**	**Total Length (m)**			**869**	**Total Length (m)**			**1545**

A.3 Flow Deposit Volumes

A.3.1 Surface Area Grids

4th June (A) and 30th June (B) Lavas

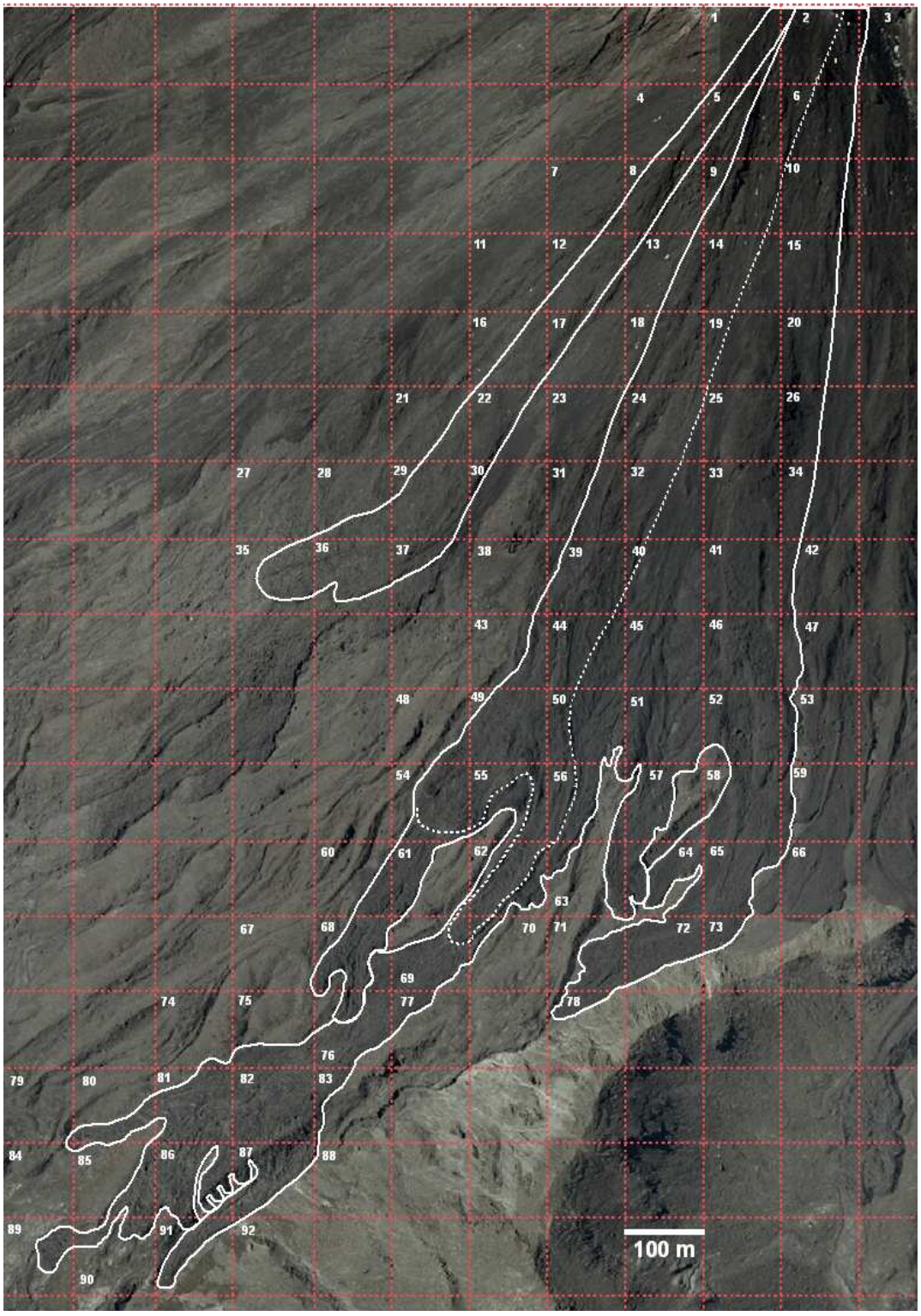

Each grid square represents 100 m^2 surface area. Grid squares in which lava flow deposit is present are numbered. The surface area of each numbered square relevant to individual lava flow deposits are given in A.3.2

8th-13th July(C), 14th July (Da, Db, Dc), 18th September (H) and 26th September (I) Lavas

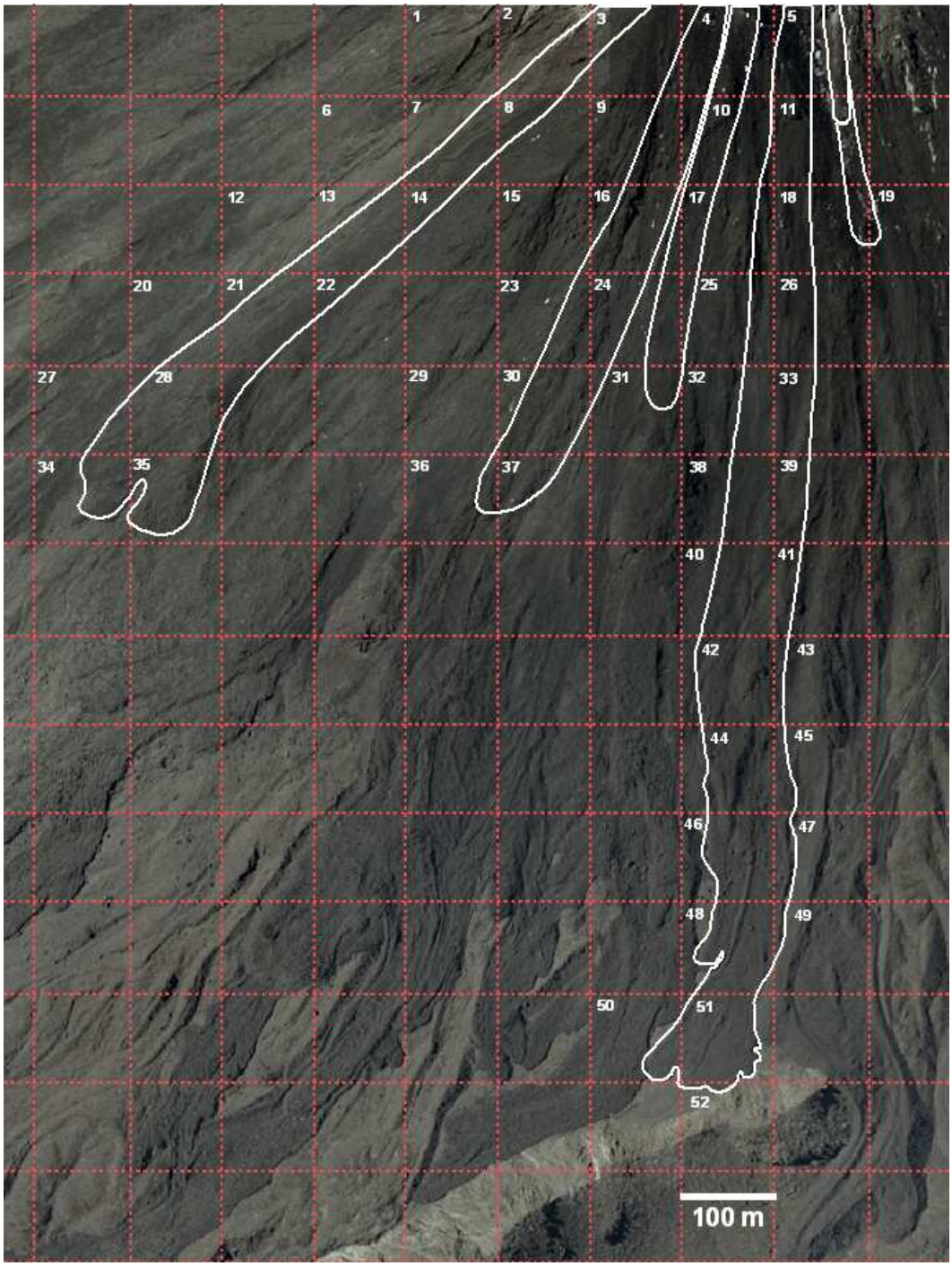

29th July (E), 18th August (F) and 16th September (G) Lavas

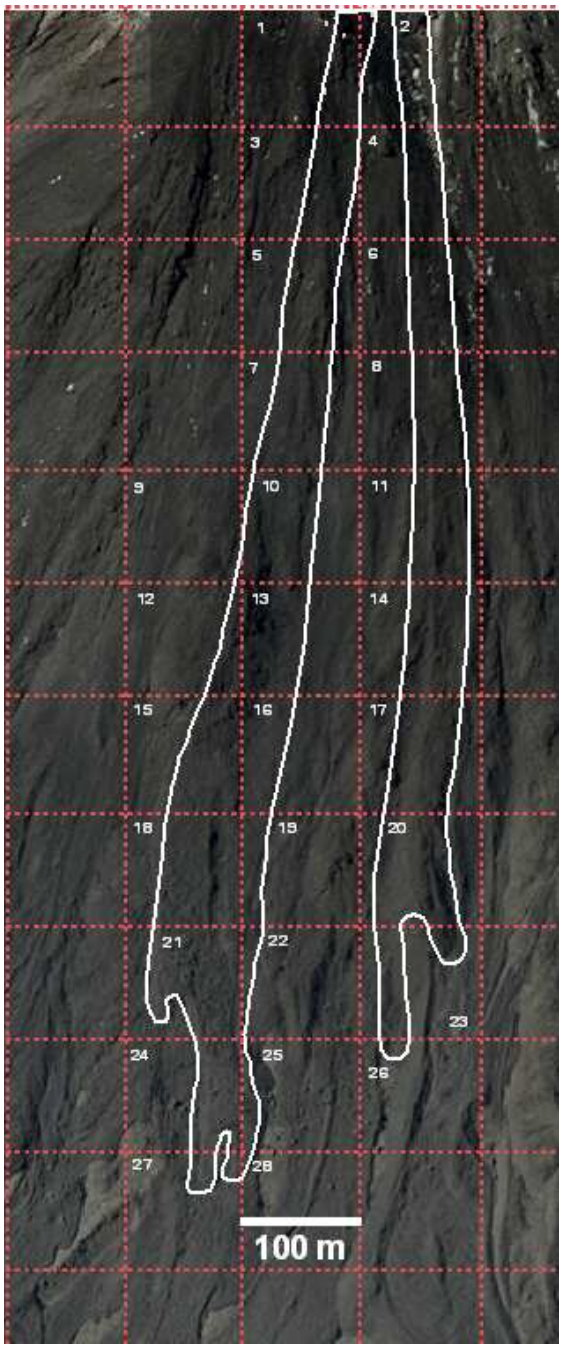

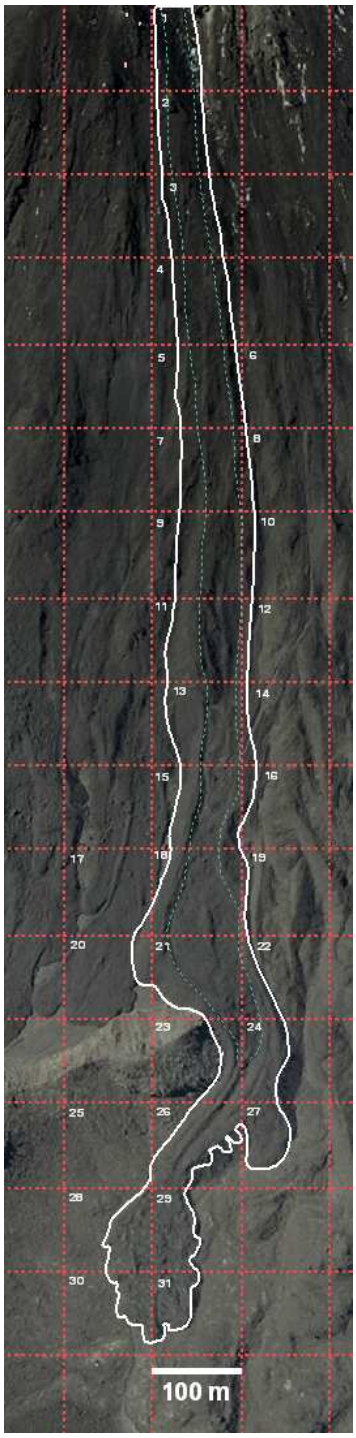

A.3.2 Estimated Surface Area and Volume of 1954 Lava flow Deposits

4th June (A)

Grid square no.	Flow deposit coverage (%)	Surface Area (m^2)	3 m flow depth Vol (m^3)	2 m flow depth Vol (m^3)
1	33	3300	9900	6600
2	4	400	1200	800
4	23	2300	6900	4600
5	22	2200	6600	4400
7	7	700	2100	1400
8	46	4600	13800	9200
11	1	100	300	200
12	55	5500	16500	11000
13	5	500	1500	1000
16	48	4800	14400	9600
17	22	2200	6600	4400
21	25	2500	7500	5000
22	55	5500	16500	11000
28	26	2600	7800	5200
29	85	8500	25500	17000
30	8	800	2400	1600
35	43	4300	12900	8600
36	75	7500	22500	15000
37	27	2700	8100	5400
	TOTAL	**61,000**	**183,000**	**122,000**
	error	**± 3,800**	**± 11,400**	**7,600**

14th July (Da)

Grid square no.	Flow deposit coverage (%)	Surface Area (m^2)	3 m flow depth Vol (m^3)	2 m flow depth Vol (m^3)
2	45	4500	13500	9000
3	21	2100	6300	4200
6	1	100	300	200
7	46	4600	13800	9200
8	20	2000	6000	4000
12	6	600	1800	1200
13	61	6100	18300	12200
14	18	1800	5400	3600
20	16	1600	4800	3200
21	67	6700	20100	13400
22	14	1400	4200	2800
27	16	1600	4800	3200
28	93	9300	27900	18600
34	32	3200	9600	6400
35	58	5800	17400	11600
	TOTAL	**51,400**	**154,200**	**102,800**
	error	**± 3,000**	**± 9,000**	**± 6,000**

14th July (Db)

Grid square no.	Flow deposit coverage (%)	Surface Area (m^2)	3 m flow depth Vol (m^3)	2 m flow depth Vol (m^3)
3	8	800	2400	1600
4	34	3400	10200	6800
9	44	4400	13200	8800
10	13	1300	3900	2600
15	2	200	600	400
16	60	6000	18000	12000
23	36	3600	10800	7200
24	41	4100	12300	8200
29	1	100	300	200
30	78	7800	23400	15600
31	5	500	1500	1000
36	13	1300	3900	2600
37	31	3100	9300	6200
	TOTAL	**36,600**	**109,800**	**73,200**
	error	**± 2,600**	**± 7,800**	**± 5,200**

Surface area error margin assumed at 2% estimation error per grid square (=200 m^3 each square) and total surface area error for each flow obtained by multiplying this by the number of gird squares covered by each flow deposit.
Total surface area error is then multiplied by flow depth to give a volume error correlated to surface area error.
The total error for each flow (Table 2.1) is given by a 2% surface area error and a 1 m flow depth error and is calculated by adding the difference between the volume of the two flow depths to the volume error value of the greater flow depth e.g. 4th June flow total error = 11,400 + (183,000 – 122,00) = 72,400

8-13th July (C),18th Sept (H),

Grid square no.	8-13th July Flow deposit coverage (%)	Surface Area (m^2)	3 m flow depth Vol (m^3)	2 m flow depth Vol (m^3)
4	30	3000	9000	6000
10	30	3000	9000	6000
16	9	900	2700	1800
17	50	5000	15000	10000
24	37	3700	11100	7400
25	7	700	2100	1400
31	14	1400	4200	2800
	TOTAL	**17,700**	**53,100**	**35,400**
	error	**± 1,400**	**± 4,200**	**± 2,800**
	18th Sept (H)		**2.5 m flow depth**	**1.5 m flow depth**
5	20	2000	5000	3000
11	21	2100	5250	3150
18	15	1500	3750	2250
19	3	300	750	450
	TOTAL	**5,900**	**14,750**	**8,850**
	error	**± 800**	**± 2,000**	**± 1,200**

16th September (G), 26th September (I)

Grid square no.	Flow deposit coverage (%)	Surface Area (m^2)	2.5 m flow depth Vol (m^3)	1.5 m flow depth Vol (m^3)
2	28	2800	7000	4200
4	28	2800	7000	4200
6	33	3300	8250	4950
8	40	4000	10000	6000
11	48	4800	12000	7200
14	50	5000	12500	7500
17	49	4900	12250	7350
20	58	5800	14500	8700
23	28	2800	7000	4200
26	3	300	750	450
	TOTAL	**36,500**	**91,250**	**54,750**
	error	**± 2,000**	**± 5,000**	**± 3,000**
	26th Sept (I)		**2.5 m flow depth**	**1.5 m flow depth**
5	20	2000	5000	3000
11	6	600	1500	900
	TOTAL	**2,600**	**6,500**	**3,900**
	error	**± 400**	**± 1,000**	**± 600**

18th August (F) (continues on next page-see footnotes)

Grid square no.	Flow deposit coverage (%)				Surface Area (m^2)				Flow depth (m)			Volume (m^3)		
	N Levee	S Levee	Channel -no fill	Channel -fill	N Levee	S Levee	Channel -no fill	Channel -fill	N Levee	S Levee	Channel -fill	N Levee	S Levee	Channel -fill
1	10	10	25	0	1000	1000	2500	0	1	1	0	1000	1000	0
2	10	10	30	0	1000	1000	3000	0	1	1	0	1000	1000	0
3	12	10	29	0	1200	1000	2900	0	2	2	0	2400	2000	0
4	11	11	36	0	1100	1100	3600	0	3	2	0	3300	2200	0
5	18	11	33	0	1800	1100	3300	0	4	2.5	0	7200	2750	0
6	0	1	0	0	0	100	0	0	0	2.5	0	0	250	0
7	25	7	37	0	2500	700	3700	0	6	2.5	0	15000	1750	0
8	0	7	0	0	0	700	0	0	0	2.5	0	0	1750	0
9	27	0	45	0	2700	0	4500	0	8	0	0	21600	0	0
10	0	13	0	0	0	1300	0	0	8	3	0	0	3900	0
11	24	2	55	0	2400	200	5500	0	8	3	0	19200	600	0
12	0	7	0	0	0	700	0	0	0	3	0	0	2100	0
13	36	7	36	0	3600	700	3600	0	8	3	0	28800	2100	0
14	0	8	0	0	0	800	0	0	0	3	0	0	2400	0
15	21	11	42	0	2100	1100	4200	0	8	5	0	16800	5500	0
16	0	8	0	0	0	800	0	0	0	5	0	0	4000	0
17	3	0	0	0	300	0	0	0	8	0	0	2400	0	0
18	21	14	0	57	2100	1400	0	5700	8	5	6	16800	7000	34200
19	0	2	0	0	0	200	0	0	0	5	0	0	1000	0
20	12	0	0	0	1200	0	0	0	8	0	0	9600	0	0
21	41	1	0	50	4100	100	0	5000	7	6	6	28700	600	30000
22	0	8	0	14	0	800	0	1400	0	6	6	0	4800	8400

Grid square no.	Flow deposit coverage (%)				Surface Area (m^2)				Flow depth (m)			Volume (m^3)		
	N Levee	S Levee	Channel -no fill	Channel -fill	N Levee	S Levee	Channel -no fill	Channel -fill	N Levee	S Levee	Channel -fill	N Levee	S Levee	Channel -fill
23	25	0	0	6	2500	0	0	600	7	0	6	17500	0	3600
24	0	35	0	10	0	3500	0	1000	0	5.5	6	0	19250	6000
25	1				100				4	0	0	400	0	0
26	57				5700				4.6	5.5	0	26220	0	0
27	35				3500				0	6	0	0	0	0
28	43				4300				4			17200	0	0
29	45				4500				4			18000	0	0
30	28				2800				4			11200	0	0
31	30				3000				4			12000	0	0
											Total	276320	65950	82200
											Overall Total			**424,470**

Surface area of each lateral flow margin (north and south levee) and central flow channel estimated separately
Levee heights and flow channel depths variable throughout deposit therefore flow depth in each grid estimated separately
Full width of the flow deposit in the distal zone is included in the northern levee column
Error margin not calculated due to variable flow depths/levee heights but a 2% surface area error = ± 18,600m^3

14th July (Dc)

Grid square no.	Flow deposit coverage (%)	Surface Area (m^2)	3 m flow depth Vol (m^3)	2 m flow depth Vol (m^3)
4	1	100	300	200
5	37	3700	11100	7400
10	15	1500	4500	3000
11	40	4000	12000	8000
17	22	2200	6600	4400
18	40	4000	12000	8000
25	31	3100	9300	6200
26	42	4200	12600	8400
32	38	3800	11400	7600
33	40	4000	12000	8000
38	51	5100	15300	10200
39	33	3300	9900	6600
40	67	6700	20100	13400
41	21	2100	6300	4200
42	83	8300	24900	16600
43	11	1100	3300	2200
44	25	2500	7500	5000
45	17	1700	5100	3400
46	72	7200	21600	14400
47	21	2100	6300	4200
48	73	7300	21900	14600
49	5	500	1500	1000
50	18	1800	5400	3600
51	75	7500	22500	15000
52	3	300	900	600
	TOTAL	**88,100**	**264,300**	**176,200**
	error	**± 5,000**	**± 15,000**	**± 10,000**

29th July (E)

Grid square no.	Flow deposit coverage (%)	Surface Area (m^2)	3.5 m flow depth Vol (m^3)	2.5 m flow depth Vol (m^3)
1	28	2800	9800	7000
2	4	400	1400	1000
3	38	3800	13300	9500
5	43	4300	15050	10750
7	46	4600	16100	11500
9	1	100	350	250
10	57	5700	19950	14250
12	20	2000	7000	5000
13	51	5100	17850	12750
15	51	5100	17850	12750
16	33	3300	11550	8250
18	70	7000	24500	17500
19	20	2000	7000	5000
21	71	7100	24850	17750
22	6	600	2100	1500
24	41	4100	14350	10250
25	10	1000	3500	2500
27	10	1000	3500	2500
28	1	100	350	250
	TOTAL	**60,100**	**210,350**	**150,250**
	error	**± 3,800**	**± 13,300**	**± 9,500**

30th June (B)-main flow before division into lobe groups (see A/XVII)

Grid square no.	Flow deposit coverage (%)	Surface Area (m^2)	3 m flow depth Vol (m^3)	2 m flow depth Vol (m^3)
1	7	700	2100	1400
2	95	9500	28500	19000
3	6	600	1800	1200
5	45	4500	13500	9000
6	90	9000	27000	18000
8	2	200	600	400
9	85	8500	25500	17000
10	80	8000	24000	16000
13	35	3500	10500	7000
14	100	10000	30000	20000
15	70	7000	21000	14000
18	76	7600	22800	15200
19	100	10000	30000	20000
20	63	6300	18900	12600
23	17	1700	5100	3400
24	100	10000	30000	20000
25	100	10000	30000	20000
26	50	5000	15000	10000
31	52	5200	15600	10400
32	100	10000	30000	20000
33	100	10000	30000	20000
34	34	3400	10200	6800
38	3	300	900	600
39	92	9200	27600	18400
40	100	10000	30000	20000
41	100	10000	30000	20000
42	18	1800	5400	3600
43	31	3100	9300	6200
44	100	10000	30000	20000
45	100	10000	30000	20000
46	100	10000	30000	20000
47	24	2400	7200	4800
48	11	1100	3300	2200
49	93	9300	27900	18600
50	98	9800	29400	19600
51	99	9900	29700	19800
52	95	9500	28500	19000
53	19	1900	5700	3800
	TOTAL	**249,000**	**747,000**	**498,000**
	error	**± 7,600**	**± 22,800**	**± 15,200**
	HALF TOTAL	**124,500**	**373,500**	**249,000**

30th June (BnU)

Grid square no.	Flow deposit coverage (%)	Surface Area (m^2)	9 m flow depth Vol (m^3)	8 m flow depth Vol (m^3)
1	7	700	6300	5600
2	61	6100	54900	48800
5	45	4500	40500	36000
6	25	2500	22500	20000
9	79	7900	71100	63200
10	1	100	900	800
13	35	3500	31500	28000
14	57	5700	51300	45600
18	76	7600	68400	60800
19	22	2200	19800	17600
23	17	1700	15300	13600
24	89	8900	80100	71200
31	52	5200	46800	41600
32	48	4800	43200	38400
38	3	300	2700	2400
39	90	9000	81000	72000
40	10	1000	9000	8000
43	31	3100	27900	24800
44	60	6000	54000	48000
48	11	1100	9900	8800

30th June (BnL)

Grid square no.	Flow deposit coverage (%)	Surface Area (m^2)	3 m flow depth Vol (m^3)	2 m flow depth Vol (m^3)
54	69	6900	20700	13800
55	87	8700	26100	17400
56	61	6100	18300	12200
57	3	300	900	600
60	20	2000	6000	4000
61	44	4400	13200	8800
62	79	7900	23700	15800
63	13	1300	3900	2600
67	1	100	300	200
68	77	7700	23100	15400
69	66	6600	19800	13200
70	12	1200	3600	2400
74	3	300	900	600
75	31	3100	9300	6200
76	73	7300	21900	14600
77	16	1600	4800	3200
79	2	200	600	400
80	24	2400	7200	4800
81	87	8700	26100	17400
82	100	10000	30000	20000

30th June (Bs)

Grid square no.	Flow deposit coverage (%)	Surface Area (m^2)	3 m flow depth Vol (m^3)	2 m flow depth Vol (m^3)
57	57	5700	17100	11400
58	83	8300	24900	16600
59	86	8600	25800	17200
63	25	2500	7500	5000
64	88	8800	26400	17600
65	77	7700	23100	15400
66	2	200	600	400
71	42	4200	12600	8400
72	68	6800	20400	13600
73	19	1900	5700	3800
78	14	1400	4200	2800
	TOTAL	**56,100**	**168,300**	**112,200**
	error	± 2,200	± 6,600	± 4,400
TOTAL (Bs)		180,600	541,800	361,200

30th June (BnU) cont'd

Grid square no.	Flow deposit coverage (%)	Surface Area (m^2)	9 m flow depth Vol (m^3)	8 m flow depth Vol (m^3)
49	93	9300	83700	74400
50	30	3000	27000	24000
54	54	5400	48600	43200
55	61	6100	54900	48800
56	31	3100	27900	24800
61	2	200	1800	1600
62	40	4000	36000	32000
63	1	100	900	800
69	9	900	8100	7200
70	4	400	3600	3200
	TOTAL	**114,400**	**1,029,600**	**915,200**
	error	± 6,000	± 54,000	± 48,000

30th June (BnL) cont'd

Grid square no.	Flow deposit coverage (%)	Surface Area (m^2)	3 m flow depth Vol (m^3)	2 m flow depth Vol (m^3)
83	21	2100	6300	4200
84	1	100	300	200
85	33	3300	9900	6600
86	88	8800	26400	17600
87	70	7000	21000	14000
88	1	100	300	200
89	18	1800	5400	3600
90	17	1700	5100	3400
91	31	3100	9300	6200
92	1	100	300	200
	TOTAL	**114,900**	**344,700**	**229,800**
	error	± 6,000	± 18,000	± 12,000
TOTAL (Bn)		**353,800**	**1,747,800**	**1,394,000**

Error margins are calculated by assuming a 2% error in surface area estimation per grid square (= 200 m^2 each square), multiplying this by the number of squares covered by the flow deposit and adding the difference between the two total values given for flow depths (i.e. assuming a 1 m error in flow depth)

Volumes on page A/XV are for the entire width of the main flow deposit before the flow divides into lobe groups
The total for each lobe group (i.e. Bn and Bs assumes half of the total of the main flow each)
The upper (BnU) lobes were calculated separately due to much greater flow deposit depths
The total volume for 30th June (B) is the combined totals for Bn, BnU, and Bs

TOTAL 30TH JUNE (B) FLOW
2,289,600 m^3

A.4 List of field site locations and brief descriptions with relevant GPS coordinates

Flow Deposit	Site No.	Site Description	GPS-coordinates	Flow Depth (m)	Comments
4th June	A1	southern margin	E2736593/N6224694	3.0	overlying 1949 flow deposit
	A2	southern margin	E2736557/N6224698	1.5	extended lobe to south-? 1949 flow deposit
30th June	Bn3	southern margin BnL-S downflow from BnU-S lobe front		3 to 4	deep flow channel
	Bn4	southern margin Bm lobe	E2736319/N6224407	1-2	
	Bn5	lobe front Bm lobe			
	Bn6	northern margin BnL-S-1 lobe	E2735678/N6225044	4.0	BnL-S-3 lobe meets northern margin-no overlap
	Bn9	BnL-S-1 lobe front		2.0	lobe front rests on steep underlying slope
	Bn12	southern margin BnL-S-4 lobe		5 - 5.5	
	Bn16	southern margin at top of underlying ridge	E2735865/N6224857	1.5	Flow widens and spills down ridge slope.
	Bn18	southern margin, part way down ridge slope		0.4 - 1.3	thin veneer of lava emplaced on ridge slope
	Bn19	BnL-S-4 lobe front	E2735662/N6225120	4-5	several large boulders within shallow flow channel
	Bn20	southern margin BnL-S-5 lobe		0.9-2.2	inner wall depth greater than outer wall depth
	Bn21	flow channel BnL-S-4 lobe	E2735762/N6225091		large, dense boulders in central flow channel
	Bn22	southern margin BnL-S-6 lobe		2.9	
	Bn23	northern margin BnL-S-5 lobe		1.5	flow emplaced over low-elevation, steep ridge slope
	Bn24	BnL-S-5 lobe front	E2735640/N6225241	3.5	
	Bn26	BnL-S-6 lobe front	E2735786/N6225201	3.0	
	Bn30	southern margin BnL-S-1 lobe		1.7	flow diverted into stream valley adjacent to Pukekaikiore
	Bn30	southern margin BnL-S-1 lobe		1.7	flow diverted into stream valley adjacent to Pukekaikiore
	Bn34a	southern margin BnL-S-4 lobe	E2735742/N6224992	1.5	BnL-S-2 & BnL-S-3 divided by small kipuka on ridge top
	Bn35	western margin BnL-S-2		2.9	flow emplaced on steep ridge slope & meets BnL-S-1 margin-no contact
	Bn37a	southern margin BnL-S, small lobe extending from margin	E2736130/N6224541	2.5	

Flow Deposit	Site No.	Site Description	GPS-coordinates	Flow Depth (m)	Comments
	Bn38a	southern margin BnL-S, adjacent to BnU-S lobe front		2.0	deep flow channel, outer levee wall height low
	Bn39a	western end of kipuka between BnL-N & BnL-S	E2736224/N6224733		
	Bn40a	northern margin BnL-N adjacent to BnU-N lobe front		2.0	
	Bn40b	BnL-N lobe front		2.5	lobe front forked, southern fork emplaced over BnL-S lobe surface
	Bs2	northern margin, northern lobe	E2736319/N6224407	1-1.5	shallow flow channel, overlain by a small secondary lobe
	Bs3	southern margin, southern lobe	E2736162/N6224249	3	sub-lobe extends out from margin of main flow
	Bs7	southern margin, southern lobe	E2736067/N6224296	2-3.5	flow margin diverted at base of Pukekaikiore-no contact
	Bs9	southern margin, southern lobe		1.8	flow margin alongside but no contact with base of Pukekaikiore
	Bs9a	**southern margin, southern lobe**	**E2736018/N6224422**	**0.5 - 0.7**	**flow margin fully abuts base of Pukekaikiore**
	Bs10	southern margin, southern lobe		2.9	outer wall of flow margin obscured by Pukekaikiore slopes
	Bs11	southern lobe front, western end	E2735966/N6224525	3-3.5	lobe front rests on gentle slope ~ 10°
	Bs14	southern lobe front		3.5	multiple toe formation at lobe front
	Bs15	southern lobe front	E2736038/N6224490	3.5	multiple toe formation at lobe front
	Bs16	southern lobe front	E2736067/N6224487	3.7	multiple toe formation at lobe front
	Bs18	southern lobe front, eastern end	E2736082/N6224450	3.5	multiple toe formation at lobe front
	Bs22	northern margin, southern lobe		3.5	southern and middle lobes emplaced down ridge slopes, lobes divide on ridge top
	Bs25	lobe front, middle lobe	E2736120/N6224394	3.2	lobe front partially overlain by northern lobe front
	Bs26	lobe front, middle lobe			overlying northern lobe front ~ 1 m higher than middle lobe
	Bs27	lobe front, northern lobe		3-3.5	northern lobe front divided into two toes at flow front
	Bs29	lobe front, northern lobe	E2736114/N6224417	4-6	
	Bs30	northern margin, northern lobe		2	flow margin confined by low-elevation ridge slope
	Bs31	southern margin, southern lobe		2	overlain by 29th July lava and block and ash deposit, also close to 14th July (Dc) margin so this section of flow unknown

Flow Deposit	Site No.	Site Description	GPS-coordinates	Flow Depth (m)	Comments
14th July	Dc2	flow front, second of 5 multiple flow front toes		6	front of toe just abuts the base of Pukekaikiore
	Dc4	flow front, first flow front toe, southern end		3	no contact with the base of Pukekaikiore
	Dc5	flow front, first flow front toe, northern end	E2763090/N6224188	4.8	flow front emplaced on gentle ~9° slope-several met res before base of Pukekaikiore
	Dc7	southern margin	E2736309/N6224093	3.7 - 3.8	low-elevation levee and shallow flow channel
	Dc8	southern margin			small lobe emplaced between 14th July and 18th August flows-no clear flow margins upstream
	Dc9	northern flow front	E2736116/N6224252	3.5	contact with southern margin, southern Bs lobe, no overlap, contact minimal
	Dc10a	northern margin		4-5	contact with southern margin, southern Bs lobe, no overlap, contact minimal
	Dc12	northern margin, sub-lobe front	E2736225/N6224192	6	sub-lobe extends along northern margin, low-elevation levee divides from main flow
	Dc12a	northern margin		2	contact with southern margin, southern Bs lobe, no overlap, contact minimal
	Dc13	northern margin	E2763393/N6224185	2 - 2.2	no clear delineation of flow margins of this or 30th June lava upstream from this locale
	Dc14	northern margin, upper-lobe front		3.5 - 4	distinct lobe deposit overlying main flow channel
29th July	E1	southern margin	E2736302/N6224198	5.0	overlies 30th June lava, no distinct contact between flow surfaces
	E1a	flow surface, southern margin			block and ash flow overlies lava
	E2	flow front, southern fork	E2736281/N6224429	4.8	flow front divided into angular fork
18th August	F1	northern margin	E2736116/N6224058		abuts tightly against Pukekaikiore ridge
	F1b	northern margin		8-12	
	F3	central flow channel	E2736259/N6224055	0	drained flow channel upstream from this local, crest top within the middle of the flow channel, folded surface
	F9	southern margin	E2736291/N6224004	1.6	
	F10	southern margin		2.8	flow margin follows path of adjacent ridge-no contact
	F12	southern margin	E2736062/N6223934	7.5	flow margin contacts with base of adjacent ridge
	F13	southern margin		5.5	underlying slope angle increases markedly

Flow Deposit	Site No.	Site Description	GPS-coordinates	Flow Depth (m)	Comments
	F17	southern margin		5.5	flow margin emplaced along the top of an underlying ridge with some oversplii down ridge slopes
	F20	flow front, southern toe	E2735740/N6224079	3.8	distal end of flow broad and multiple toes formed
	F21	flow front, longest toe	E2735725/N6224134	5	
	F22	northern margin of flow front	E2735743/N6224134	5	
	F27	northern margin, small toe	E2735813/N6224166	3.6	
	F28	northern margin, small toe		7	
	F31	northern margin		6	levee height reduces markedly before spreading out towards distal end, southern levee also markedly reduced at same place
16th Sept	G1	flow front	E2736477/N6224032		distal end of flow emplaced down the south-facing inside wall of the 18th August northern levee
	G2	flow front		1 - 1.5	no clear delineation between G and F flow surfaces or margins
	G2a	flow surface before emplacement down F flow levee			

A complete list of field sites, including more comprehensive descriptions and flow deposit dimensions is given in Appendix D

Appendix B

Rock Sample Analyses

B.1 List of Rock Samples and Analyses Undertaken (see notes p. BIII)

U o W Number	Sample no. (this study)	Flow Deposit	Comments/reason for analysis	Thin Section			Polished section	Petrographic Description	Point count	Gas Pycnometer Analysis	XRF	Photos
				WR	Z	X						
W20090330	A1	4th June	Southern margin	●			●	●	●		●	
W20090331	A2*	4th June	Either A or 1949 flow deposit	●				●	●		●	
W20090332	Bn6-4	30th June								●		
W20090333	Bn17-1	30th June										●
W20090334	Bn19	30th June								●		
W20090335	Bn20-2	30th June								●		
W20090336	Bn21-1a	30th June										●
W20090337	Bn25	30th June										●
W20090338	Bn26	30th June	Lobe front (BnL-S-6)	●				●	●		●	
W20090339	Bn27	30th June					●					
W20090340	Bn38	30th June	Lobe front (BnU-S)	●				●	●		●	
W20090341	Bn40	30th June								●		
W20090342	Bs3-1	30th June	Southern Bs lobe-very crystalline texture		●	●		●	●			
W20090343	Bs3-2	30th June		●				●	●		●	
W20090344	Bs8-1	30th June										●
W20090345	Bs8-2	30th June	SW margin, southern BS lobe		●	●		●	●			
W20090346	Bs11-1	30th June	Southern Bs lobe front-dense inner core, no vesicles		●	●		●	●		●	
W20090347	Bs11-2	30th June	Southern Bs lobe front-highly vesicular		●			●	●			

U o W Number	Sample no. (this study)	Flow Deposit	Comments/reason for analysis	Thin Section			Polished section	Petrographic Description	Point count	Gas Pycnometer Analysis	XRF	Photos
				WR	Z	X						
W20090348	Bs27	30th June								●		
W20090349	Bs31*	30th June	Either B, E or Dc flow	●	●	●		●	●		●	
W20090350	Bs32*	30th June	Either B, E or Dc flow	●	●	●		●	●		●	
W20090351	Dc1-2	14th July										●
W20090352	Dc2-1	14th July								●		
W20090353	Dc3-1	14th July								●		
W20090354	Dc6	14th July	Flow front	●			●	●	●		●	
W20090355	Dc8-1*	14th July	Small lobe between Dc & F (possibly G flow)	●				●	●		●	
W20090356	Dc8-2*	14th July	Small lobe between Dc & F (possibly G flow)	●				●	●		●	
W20090357	Dc8-3	14th July	Southern margin	●				●	●			
W20090358	Dc13	14th July	Northern margin	●				●	●			
W20090359	Dc14*	14th July	Overlying lobe	●				●	●		●	●
W20090360	E1-1	29th July	Southern margin	●				●	●			
W20090361	E2	29th July	Flow front	●			●	●	●		●	
W20090362	F2	18th Aug								●		
W20090363	F10	18th Aug	Southern levee		●	●		●	●			
W20090364	F13	18th Aug	Southern levee		●			●	●			
W20090365	F15-1	18th Aug	Flow front-dense inner core, no vesicles				●	●		●	●	

U o W Number	Sample no. (this study)	Flow Deposit	Comments/reason for analysis	Thin Section			Polished section	Petrographic Description	Point count	Gas Pycnometer Analysis	XRF	Photos
				WR	Z	X						
W20090366	F15-2	18th Aug	Flow front-highly vesicular		●	●		●	●			
W20090367	F20	18th Aug	Flow front		●	●		●	●			
W20090368	F21	18th Aug	Flow front	●			●	●	●		●	
W20090369	G1*	16th Sept	Base of G flow-possibly F flow	●				●	●		●	
W20090370	G2	16th Sept	Flow front	●			●	●	●		●	
W20090371	G3*	16th Sept		●					●		●	
W20090372	Z1	1949	Southern margin	●				●	●		●	

UoW Number refers to University of Waikato sample library number
Sample Numbers allocated in this study correlate to field location numbers (Fig. 2.5 or Appendix D.1)
*** Denotes samples collected from locations where the date-specific flow deposit cannot be clearly established**
WR = thin section made from whole rock sample incorporating both the inner and outer zones (Z & X) of the sample within the same thin section
Z & X = thin sections made from the same whole rock sample, with each one either representing the outer scoreaceous zone (X), or the inner, less vesicular zone (X)
Polished sections are uncovered and used to identify opaque mineral components
Photos refers to photographs used as figures

B.2 Gas Pycnometer Results and Vesicularity Calculations

Sample no.	Zone (size)	Sample block dimensions L (mm)	W (mm)	D (mm)	VOL (mm^3)	VOL (cm^3)	Wt (g)	$(100*(density_{pow}-density_t))/density_{pow}$ DENSITY$_{POW}$ (g/cm^3)	DENISTY$_T$ (g/cm^3)	TOTAL VES (%)	$(100*(density_{pow}-density_{pyc}))/density_{pow}$ DENSITY$_{pyc}$ (g/cm^3)	VES ISOLATED (%)	v_t-v_i VES CON (%)
Bn6-4	O	20.71	16.74	16.44	5700	5.70	14.07	2.8670	2.4686	13.89	2.7795	3.05	10.84
Bn6-4	I (s)	20.80	15.84	16.75	5519	5.52	12.75	2.8652	2.3103	19.37	2.7806	2.95	16.41
Bn6-4	I (m)	35.93	28.28	27.96	28410	28.41	66.83	2.8786	2.3523	18.28	2.8307	1.66	16.62
Bn19	O	20.43	16.72	15.38	5254	5.25	10.34	2.8672	1.9682	31.36	2.7230	5.03	26.33
Bn19	I (s)	20.55	16.43	16.14	5449	5.45	11.95	2.8534	2.1929	23.15	2.7708	2.89	20.25
Bn19	I (m)	35.70	27.43	28.43	27840	27.84	62.60	2.9106	2.2486	22.75	2.8426	2.34	20.41
Bn20-2	I (s)	20.77	16.68	16.09	5574	5.57	8.15	2.8860	1.4621	49.34	2.7225	5.67	43.67
Bn20-2	I (m)	35.32	27.85	28.23	27769	27.77	45.64	2.9017	1.6436	43.36	2.8464	1.91	41.45
Bn40	O	20.78	16.09	15.20	5082	5.08	11.37	2.8683	2.2373	22.00	2.8169	1.79	20.21
Bn40	I (s)	20.06	16.89	16.04	5435	5.43	12.92	2.8630	2.3774	16.96	2.7968	2.31	14.65
Bn40	I (m)	33.65	24.52	29.39	24250	24.25	57.07	2.8912	2.3534	18.60	2.8443	1.62	16.98
Bs27	O	20.41	16.24	16.70	5535	5.54	12.43	2.8569	2.2456	21.40	2.8111	1.60	19.80
Bs27	I (s)	20.52	16.70	16.32	5593	5.59	11.90	2.8542	2.1278	25.45	2.8120	1.48	23.97
Bs27	I (m)	35.37	28.25	27.01	26988	26.99	57.73	2.8920	2.1391	26.04	2.8285	2.20	23.84
Dc2-1	O	20.77	16.67	16.46	5699	5.70	11.83	2.8589	2.0758	27.39	2.8100	1.71	25.68
Dc2-1	I (s)	20.21	15.63	16.77	5297	5.30	10.39	2.8764	1.9614	31.81	2.8122	2.23	29.58
Dc2-1	I (m)	32.94	27.62	28.49	25920	25.92	52.21	2.9012	2.0143	30.57	2.8502	1.76	28.81
F2	I (s)	19.74	16.41	16.65	5393	5.39	11.89	2.8576	2.2045	22.85	2.8190	1.35	21.50
F2	I (m)	35.22	27.63	28.12	27364	27.36	**59.78**	2.8938	2.1846	24.51	2.8404	1.85	22.66
Dc3-1	I (s)	19.59	16.62	16.39	5336	5.34	8.62	2.8611	1.6153	43.54	2.8167	1.55	41.99
Dc3-1	I (m)	35.59	26.93	28.06	26894	26.89	50.12	2.9083	1.8636	35.92	2.8584	1.72	34.20
							Ave	**2.8768**		**27.0732**			**24.7557**

Gas Pycnometer results and vesicularity calculation table-notes

- Block sample zone refers to sample taken from outer (O) scoriaceous zone or inner (I) less vesicular zone; size refers to small (s) or medium (m) block sizes as discussed in Chapter 3.

- $Density_T$ refers to the whole sample block density and is calculated by: weight/volume.

- $Density_{POW}$ and $Density_{pyc}$ refer to the powdered sample density and bulk density excluding exposed vesicles respectively, both values measured by the gas pycnometer.

- The formulas for calculating total vesicularity, isolated vesicle abundance and connected vesicle abundance are given.

- The average $Density_{POW}$ value shown is used to represent whole rock density in rheological calculations (Chapter 4) and therefore assumes a bubble-free melt.

B.3 Quantitative Bulk Flow Deposit Vesicularity Data

Autoclast size & vesicularity data collected at the proximal flow zone site (F38), 18th August flow

	Grid 1-Lower Right				Grid 2-Lower Left				Grid 3-Upper Left				Grid 4-Upper Right			
Clast No.	Clast D (cm)	Vesicle D (mm)	Abundance I (%)	Abundance O (%)	Clast D (cm)	Vesicle D (mm)	Abundance I (%)	Abundance O (%)	Clast D (cm)	Vesicle D (mm)	Abundance I (%)	Abundance O (%)	Clast D (cm)	Vesicle D (mm)	Abundance I (%)	Abundance O (%)
1	20	10	12	40	16	< 1	15	40	18	10	20	N/A	25	1	7	35
2	10	?	3	40	12	1	10	35	15	< 1	7	35	10	2	10	30
3	14	?	1	35	11	< 0.5	5	35	8	?	7	35	9	5	15	30
4	9	< 1	20	40	8	3	5	40	10	1	7	40	11	2	20	N/A
5	35	5	25	30	10.5	7	15	30	8.5	1	5	35	23	0.5	5	40
6	12	?	7	35	11.5	2	15	35	12.5	?	< 1	40	13	7	20	30
7	14	2	10	40	12	6	15	40	11	1	5	35	10	0.5	3	25
8	12	2	15	40	8	1	7	35	12	< 0.5	7	40	13	1	7	30
9	15	3	12	30	7	< 0.5	10	35	8	9	29	49	8	0.5	3	40
10	10	5	25	N/A	13	4	20	40	7.5	1	7	35	14	8	25	40
11	16	2	7	40	24	< 0.5	5	35	10	5	10	35	12	2	10	40
12	16	< 1	10	35	11	7	15	35	9	< 0.5	15	40	15	0.5	1	40
13	18	4	15	35	10.5	10	15	40	7	?	< 1	35	12	0.5	7	35
14	24	3	12	40	14	< 1	7	35	12.5	3	20	N/A	19	10	12	40
15	17	3	7	30	11	2	10	30	8	5	15	N/A	18	0.5	< 1	35
16	12	1	5	30	7.5	2	15	40	11	< 1	3	40	8	4	15	35
17	11	5	15	40	15.5	?	3	40	8.5	25	25	N/A	10	0.5	5	35
18	14	< 1	7	35	20	2	7	40	10	1	3	30	17	1	7	40
19	7	< 1	5	30	15	2	7	40	10	2	12	35	30	1	7	40
20	11	1	12	40	6	< 0.5	5	35	7	5	15	N/A	13	5	15	35
21	14	< 1	5	40	60	< 0.5	7	35	12	< 0.5	10	35	10	6	20	40
22	17	5	15	40	13	2	20	40	9.5	1	10	35	14	0.5	1	40
23	27	2	12	40	24	2	5	30	14	< 0.5	7	35	24	0.5	7	35
24	12	1	15	40	14	1	10	40	13	1	7	35	10	1	7	35
25	10	< 1	7	40	8.5	?	1	30	16	<1	7	40	13	0.5	3	40

D = maximum diameter; I = inner clast zone; O = outer clast zone. N/A = no outer scoriaceous zone present.

Autoclast size and vesicularity data collected at the frontal flow zone site (F39), 18th August flow

Clast No.	Grid 1-Lower Right				Grid 2-Lower Left				Grid 3-Upper Left				Grid 4-Upper Right			
	Clast	Vesicle	Abundance		Clast	Vesicle	Abundance		Clast	Vesicle	Abundance		Clast	Vesicle	Abundance	
	D (cm)	D (mm)	I (%)	O (%)	D (cm)	D (mm)	I (%)	O (%)	D (cm)	D (mm)	I (%)	O (%)	D (cm)	D (mm)	I (%)	O (%)
1	7	2	20	40	8.5	5	20	N/A	6.5	< 0.5	10	35	6.5	2	3	35
2	9	3	10	40	9.5	< 0.5	15	30	7.5	1	15	35	9.5	< 0.5	5	40
3	9	< 0.5	15	40	13	1	15	40	10	< 0.5	5	30	8.5	3	15	40
4	8.5	10	20	40	10	4	20	35	10	1	10	40	5	< 0.5	7	35
5	7	< 0.5	15	30	8.5	< 0.5	7	40	9.5	8	10	35	8	1	7	40
6	4.5	1	15	40	9.5	1	10	40	7	2	12	35	5.5	< 0.5	10	35
7	10	2	15	40	6.5	2	15	35	15.5	2	15	35	7.5	2	20	40
8	10	1	15	40	9	6	20	35	11	1	10	40	10	3	10	40
9	11	3	10	40	11	8	20	40	7	2	15	40	10	7	25	35
10	8	< 0.5	15	35	10	7	15	40	9	< 0.5	7	40	8.5	10	25	40
11	9	6	25	30	6.5	1	5	30	6.5	2	7	35	13	8	20	35
12	14	1	10	40	11	5	20	35	8.5	3	15	30	7	3	15	35
13	9.5	< 0.5	15	30	10	4	15	35	7.5	< 0.5	5	35	10	1	15	40
14	10	< 0.5	15	40	14	8	15	40	11	5	10	35	7	< 0.5	5	35
15	11	< 0.5	5	40	10	< 0.5	15	35	8.5	4	10	35	7	2	20	40
16	9	< 0.5	15	40	10.5	2	10	35	7	1	7	40	10	< 0.5	15	35
17	7	< 0.5	15	40	10.5	< 0.5	15	40	10	2	5	40	7	< 0.5	7	35
18	11	5	15	40	8	< 0.5	14	40	18	7	25	40	8	< 0.5	10	40
19	11	2	15	35	7	4	20	40	4.5	6	10	35	5	< 0.5	7	35
20	11	10	15	35	6.5	2	5	35	6.5	5	15	35	3.5	1	10	30
21	8	8	20	35	6.5	1.5	10	40	6.5	4	20	40	7.5	1	10	30
22	7.5	4	15	35	8	2	20	35	8.5	4	15	30	6	< 0.5	7	35
23	9	< 0.5	20	35	11	2	15	30	5.5	8	15	35	7.5	4	20	40
24	8.5	1	10	40	11	1	7	40	6.5	5	15	35	8	< 0.5	25	40
25	10.5	10	20	40	8.5	8	20	30	8.5	< 0.5	5	35	5.5	< 0.5	15	30

D = maximum diameter; I = inner clast zone; O = outer clast zone. N/A = no outer scoriaceous zone present.

APPENDIX C

Rheology & Flow Behaviour Model Equations

C.1 Symbols Used In Rheology Equations

Table C.1 Symbols used in rheology equations and their definitions. Symbols are arranged in order of the equation they are first used in.

Symbol	Definition	Symbol	Definition
η	Viscosity (Pa s)	σ_{sd}	Geometric standard
s	Characteristic slope for a given multicomponent mixture	H	Mean flow depth (m)
T	Temperature (Kelvin)	α	Underlying slope angle (°)
c_T	Constant value = 1.50	W	Mean flow width (m)
c_η	Constant value = 6.40	V_e	Velocity (m s^{-1})
X_i	Mole fraction of oxides in the melt	E_f	Effusion rate (m^3 s^{-1})
Si	SiO_2	t	Time (seconds)
Al	Al_2O_3	L	Measured flow length (m)
FM	$\sum X_i$ of Fe_2O_3, FeO, MnO and MgO (Shaw, 1972)	*Gz*	Gräetz number
CT	$\sum X_i$ of TiO_2 and CaO (Shaw, 1972)	d_e	Equivalent diameter (m)
NK	$\sum X_i$ of Na_2O and K_2O (Shaw, 1972)	κ	Thermal diffusivity (m^2 s^{-1})
H	H_2O	L_o	Initial reservoir length (m)
A, B, C, D	Fitting parameters that vary linearly with the mole fraction of major element components in the melt (Hui and Zhang, 2007; Giordano *et al.*, 2008)	C_{sl}	Constant value = 0.46
a_i	Constant fitting parameter (Hui and Zhang, 2007, Table C.2)	Δρ	Density difference between the lava and the ambient air (kg m^{-3})
b_i	Constant fitting parameter (Hui and Zhang, 2007, Table C.2) (Giordano *et al.*, 2008, Table C.3)	H_o	Initial reservoir height (m)
c_i	Constant fitting parameter (Hui and Zhang, 2007, Table C.2) (Giordano *et al.*, 2008, Table C.3)	C_{vs}	Constant value = 1.31
d_i	Constant fitting parameter (Hui and Zhang, 2007, Table C.2)	q	Fluid volume per unit channel width (m^3)
η_s	Viscosity of the suspension	L_y	Theoretical limit of an isothermal yield strength flow on a slope (m)
η_1	Viscosity of the liquid phase	σ_o	Internal yield strength of lava (Pa s) (equivalent to $\boldsymbol{\tau_y}$)
R	Inverse of the maximum concentration which can be attained by the crystals ($R=1/\phi_{max}$).	H_y	Final static height of an isothermal yield strength flow on a slope (m)
ø	Crystal or bubble concentration (volume fraction)	$\mathcal{T}$	Timescale of a viscoplastic flow on a slope (s)
ϕ_{max}	Maximum concentration which can be attained by crystals in the melt	h	Height of the flow at any given point along the flow length (m)
η_o	Differential viscosity at low strain rate	L*	Final flow length (m)
η_{inf}	Differential viscosity at high strain rate	C_c	Constant value = 1
η_v	Bubble-suspension viscosity	H^*	Final flow height (m)
τ_y	Yield strength (Pa s)	σ_c	Surface crust strength (Pa s)
ρ	Density of the melt (kg m^{-3})	t*	Final stopping time of the flow
g	Gravitational acceleration (m s^{-2})	V (t)	Volume of lava erupted at time t (m^3)
D_p	Mean particle diameter (μm)	V_f	Final erupted volume (m^3)
ξ	Shape factor defined as the ratio of the surface area of a sphere of equivalent volume to the surface area of the particle		

C.2 Viscosity Equations

C.2.1 Temperature and Major Oxide Composition

1. *Shaw (1972, Eq. 3, p. 873):*

$$\ln \eta = s\left(\frac{10^4}{T}\right) - c_T s + c\eta$$

The slope (s) is calculated by:

$$s = \frac{\left((6.7X_{Si})X_{Al}\right) + \left((3.4X_{Si})X_{FM}\right) + \left((4.5X_{Si})X_{CT}\right) + \left((2.8X_{Si})X_{NK}\right) + \left((2X_{Si})X_{H}\right)}{(1 - X_{Si})}$$

2. *Hui and Zhang (2007, Eq.11, p. 412):*

$$\log \eta = A + \frac{B}{T} + \exp\left(C + \frac{D}{T}\right)$$

Fitting parameters *A*, *B*, *C* and *D* are calculated using:

$$\log \eta = \left(\sum_i a_i X_i\right) + \frac{(\sum_i b_i X_i)}{T} + exp\left(\left(\sum_i c_i X_i\right) + \frac{(\sum_i d_i X_i)}{T}\right)$$

The values for fitting parameters a_i, b_i, c_i and d_i are given in the table below.

Table C.2 Fitting parameters for Hui and Zhang (2007) viscosity equation.

Oxides	a_i	$b_i \times 10^3$	c_i	$d_i \times 10^3$
SiO_2	-6.83	18.14	0.00	2.16
TiO_2	-170.79	248.93	0.00	-143.05
[a] Al_2O_{3ex}	-14.71	32.61	21.73	-22.10
(Fe,Mn)O	0.00	0.00	-61.98	38.56
MgO	-18.01	25.96	-105.53	110.83
CaO	-19.76	22.64	-69.92	67.12
[b] $(Na,K)_2O_{ex}$	34.31	-68.29	-85.67	58.01
P_2O_5	0.00	0.00	0.00	384.77
H_2O	159.26	-48.55	-432.22	513.75
[c] $(Na,K)AlO_2$	-8.43	16.12	-3.16	0.00
[d] Z	-140.38	38.84	332.01	-404.97
[e] e_1	185.80	0.00	0.00	0.00

[a] = (X_{Al2O3} + X_{Na2O} + X_{K2O}) - (2(X_{Na2O}+X_{K2O}))
[b] = (X_{Na2O} + X_{K2O} - X_{Al2O3}) if (X_{Na2O} + X_{K2O} > X_{Al2O3}); otherwise = 0
[c] = 2(X_{Na2O} + X_{K2O})
[d] = (X_{H2O})^(1/(1+(e_1/T_K))
[e] Constant

3. *Giordano et al. (2008, Eq. 1, p.125):*

$$\log \eta = A + \frac{(\sum_i b_i X_i)}{(T - (\sum_i c_i X_i))}$$

A is a constant (- 4.55), and b_i and c_i are fitting parameters whose values are given in the table below.

Table C.3 Fitting parameters for Giordano *et al*. (2008) viscosity equation.

Oxides	b_i values	Oxides	c_i values
$SiO_2 + TiO_2$	159.6	SiO_2	2.75
Al_2O_3	-173.3	TA[b]	15.7
$FeO(T) + MnO + P_2O_5$	72.1	FM[c]	8.3
MgO	75.5	CaO	10.2
CaO	-39	NK[d]	-12.3
$Na_2O + V$[a]	-84.1	ln(1+V)	-99.5
$V + \ln(1+H_2O)$	141.5	$(Al_2O_3 + FM + CaO - {}_2O_5) * (NK+V)$	0.3
$(SiO_2 + TiO_2)(FM)$	-2.43		
$(SiO_2+TA+P_2O_5)(NK+H_2O)$	-0.91		
$(Al_2O_3)(NK)$	17.6		

[a] $\Sigma(H_2O + F_2O_{-1})$
[b] $\Sigma(TiO_2 + Al_2O_3)$
[c] $\Sigma(FeO(T) + MnO + MgO)$
[d] $\Sigma(Na_2O + K_2O)$

C.2.2 Crystal and Bubble Content

1. *Einstein-Roscoe Equation (Pinkerton and Stevenson, 1992, Eq. 1, p. 49):*

$$\eta_s = \eta_l (1 - R\phi)^{-2.5}$$

2. *Differential Viscosity at Low Strain Rate (Gay et al., 1969, Eq.17, p.817):*

$$\eta_o = \eta_l \left(\frac{\phi_{max}}{\phi_{max} - \phi} \right)^{2.5}$$

3. *Differential Viscosity at High Strain Rate (Gay et al., 1969, Eq.19, p.817):*

$$\eta_{inf} = \eta_l \exp\left\{ \left[2.5 + \left(\frac{\phi}{\phi_{max} - \phi} \right)^{0.48} \right] \frac{\phi}{\phi_{max}} \right\}$$

4. *Minimum Bubble Viscosity (Llewellin and Manga, 2005, Eq.7, p. 210):*

$$\eta_v = (1 - \phi)^{-1}$$

5. *Maximum Bubble Viscosity (Llewellin and Manga, 2005, Eq.9, p. 210):*

$$\eta_v = 1 + 9\phi$$

C.2.3 Yield Strength

1. *Pinkerton and Stevenson (1992, Eq. 3, p. 53):*

$$\tau_y = 1.26\rho g\left(\frac{D_p}{\phi_{\max} - \phi}\right)\left(\frac{\phi_{\max}}{1 - \phi_{\max}}\right)^2 \frac{1}{\xi^{1.5}\sigma_{sd}^2}$$

2. *Hulme (1974, Eq.14, p.364):*

$$\tau_y = \rho g H \sin\alpha$$

3. *Orowan (1949) Equation-Moore et al. (1992, Eq. 1, p. 13,488):*

$$\tau_y = \frac{\rho g H^2}{W}$$

C.2.4 Velocity, Effusion Rate and Eruption Duration

1. *Velocity (Jeffreys Equation) (Kilburn and Lopes (1991, Eq. 3, p.19724):*

$$V_e = \frac{\rho g H^2 \sin\alpha}{b\eta_T}$$

where the constant b = 3

2. *Effusion Rate (Hulme and Fielder,1977, p. 228):*

$$E_f = WHV_e$$

3. *Eruption Duration (Pinkerton and Wilson, 1994, p. 110):*

$$t = \left(\frac{L}{\left(1.32E_f^{0.47}\alpha^{0.51}H^{-0.34}\right)}\right)^{\frac{1}{0.71}}$$

C.2.5 Gräetz Number

1. *Pinkerton and Sparks (1976, p 181.):*

$$G_z = \frac{V_e d_e^2}{\kappa L}$$

where d_e is calculated by Pinkerton and Wilson (1994, p. 112):

$$d_e = \frac{2W\mathrm{H}}{(W + \mathrm{H})}$$

2. *Pinkerton and Wilson (1994, Eq.6, p. 112):*

$$G_z = \frac{d_e^2}{\kappa t}$$

C.2.6 Surface Crust Strength

1. *Inertial Slumping Regime (Lyman and Kerr, 2006, Eq.1, p.2):*

$$\boldsymbol{L = L_0 + C_{sl}\left[\frac{g\Delta\rho}{\rho} H_0\right]^{\frac{1}{2}} t}$$

2. *Sloping Viscous Flow Regime (Lyman and Kerr, 2006, Eq. 5, p.2):*

$$\boldsymbol{L = C_{vs}\left[\frac{g\Delta\rho \sin\alpha q^2 t}{\eta_T}\right]^{\frac{1}{3}}}$$

3. *Internal Yield Strength Limit (Lyman and Kerr, 2006, Eq. 10, p.2):*

$$\boldsymbol{L_y = \frac{q g\Delta\rho \sin\alpha}{\sigma_0}}$$

4. *Sloping Viscoplastic Regime-final static height of a flow with yield strength (Lyman and Kerr, 2006, Eq. 9, p. 2):*

$$H_y = \frac{\sigma_0}{g\Delta\rho\sin\alpha}$$

5. *Sloping Viscoplastic Regime-timescale of viscoplastic flow on a slope (Lyman and Kerr, 2006, Eq. 15, p. 3):*

$$\mathcal{T} = \frac{2q\eta_T}{\mathrm{g}\Delta\rho H_y^3 \sin\alpha}$$

6. *Sloping Viscoplastic Regime –time at which height (h) occurs (Lyman and Kerr, 2006, Eq. 21, p. 3):*

$$t = \mathcal{T}\left(\frac{H_y}{h - H_y}\right) - \left(\frac{H_y}{H_0 - H_y}\right) + \left(\frac{H_y}{h}\right) - \left(\frac{H_y}{H_0}\right) + 2\ln\left(1 - \frac{H_y}{h}\right) - 2\ln\left(1 - \frac{H_y}{H_0}\right)$$

7. *Sloping Viscoplastic Regime-length at time (t) and height (h) (Lyman and Kerr, 2006, Eq. 2, p. 2):*

$$L = \frac{q}{h}$$

8. *Crust Strength Regime (Lyman and Kerr,2006, Eq. 24, p.3):*

$$L^* = C_c\left[\frac{\mathrm{g}\Delta\rho}{\sigma_c}\right]^{\frac{1}{2}} q(\kappa t)^{-0.25}$$

9. *Crust Strength Regime (Lyman and Kerr,2006, Eq. 23, p.3):*

$$H^* = \frac{1}{C_c}\left[\frac{\sigma_c}{\mathrm{g}\Delta\rho}\right]^{\frac{1}{2}} (\kappa t)^{\frac{1}{4}}$$

10. *Surface Crust Strength (Lyman and Kerr, 2006, Eq. 30, p.6):*

$$\sigma_c = \frac{g\Delta\rho q^2}{(L^*)^2(\kappa t^*)^{0.5}}$$

C.2.7 Eruption Rate

Kerr and Lyman (2007, Eq. 6, p.2):

$$V(t) = V_f\left(1 - \exp^{-\frac{t}{\mathcal{T}}}\right)$$

C.3 Mean Diameter, Shape Factor & Geometric Standard Calculations

Method:

- 50 intact (or mostly intact) plagioclase and orthopyroxene crystals selected randomly along cross-sectional transects of six thin sections using a petrographic microscope
- Length (L) and width (W) of each crystal recorded and width measurement also assumed to equal depth (D)
- Mean diameter (D_p) calculated as the average crystal length of the 300 measurements
- The surface area of each crystal (XSA) was calculated by:

$$(4 * (L * W) + (2 * (W * D)$$

and is equivalent to:

$$4pi\ r^2$$

- Crystal volume (Vol) was calculated by:

$$LWD$$

and is equivalent to:

$$(4/3)\ pi\ r^3$$

- The radius (r) of a sphere with an equivalent volume to the crystal is calculated by:

$$(Vol/4/3/pi)^{1/3}$$

- And the surface area of the sphere (SSA) is given by:

$$4pi(r^2)$$

- The ratio of the sphere surface area to the crystal surface area is calculated:

$$SSA/XSA$$

- The shape factor (ξ) is obtained as the average surface area ratio of the 300 crystals

- The geometric standard deviation (σ_{sd}) is obtained by sorting crystal length data into size class intervals and determining the frequency and cumulative frequency of each class size. The 50^{th} and 15.87^{th} percentile clast sizes were determined and the cumulative frequency (CF) of those clast sizes used to determine geometric standard by:

$$\frac{CF\ 50th\ Percentile}{CF\ 15.87th\ percentile}$$

- Raw data for these calculations are given in the following tables.

Sample No	L (mm)	W (mm)	D (mm)	XSA (mm^2)	Xal Vol (mm^3)	r (mm)	SSA (mm^2)	Ratio
A1	0.225	0.125	0.125	0.144	0.004	0.09434	0.112	0.78
	0.225	0.175	0.175	0.219	0.007	0.11807	0.175	0.80
	0.15	0.05	0.05	0.035	0.000	0.04474	0.025	0.72
	0.175	0.125	0.125	0.119	0.003	0.08676	0.095	0.80
	0.15	0.075	0.075	0.056	0.001	0.05863	0.043	0.77
	0.3	0.175	0.175	0.271	0.009	0.12995	0.212	0.78
	0.375	0.125	0.125	0.219	0.006	0.11186	0.157	0.72
	0.55	0.2	0.2	0.520	0.022	0.17385	0.380	0.73
	0.225	0.1	0.1	0.110	0.002	0.08130	0.083	0.75
	0.375	0.175	0.175	0.324	0.011	0.13998	0.246	0.76
	0.15	0.075	0.075	0.056	0.001	0.05863	0.043	0.77
	0.5	0.175	0.175	0.411	0.015	0.15407	0.298	0.72
	0.3	0.125	0.125	0.181	0.005	0.10384	0.135	0.75
	0.375	0.2	0.2	0.380	0.015	0.15302	0.294	0.77
	0.2	0.1	0.1	0.100	0.002	0.07817	0.077	0.77
	0.325	0.25	0.25	0.450	0.020	0.16929	0.360	0.80
	0.375	0.225	0.225	0.439	0.019	0.16552	0.344	0.78
	0.275	0.15	0.15	0.210	0.006	0.11391	0.163	0.78
	0.3	0.175	0.175	0.271	0.009	0.12995	0.212	0.78
	0.375	0.175	0.175	0.324	0.011	0.13998	0.246	0.76
	0.35	0.2	0.2	0.360	0.014	0.14954	0.281	0.78
	0.275	0.2	0.2	0.300	0.011	0.13799	0.239	0.80
	0.125	0.075	0.075	0.049	0.001	0.05517	0.038	0.78
	0.275	0.175	0.175	0.254	0.008	0.12624	0.200	0.79
	0.3	0.125	0.125	0.181	0.005	0.10384	0.135	0.75
	0.525	0.425	0.425	1.254	0.095	0.28294	1.005	0.80
	0.175	0.125	0.125	0.119	0.003	0.08676	0.095	0.80
	0.3	0.175	0.175	0.271	0.009	0.12995	0.212	0.78
	0.275	0.1	0.1	0.130	0.003	0.08693	0.095	0.73
	0.5	0.275	0.275	0.701	0.038	0.20825	0.545	0.78
	0.6	0.275	0.275	0.811	0.045	0.22130	0.615	0.76
	0.175	0.1	0.1	0.090	0.002	0.07477	0.070	0.78
	0.225	0.2	0.2	0.260	0.009	0.12906	0.209	0.80
	0.25	0.175	0.175	0.236	0.008	0.12229	0.188	0.80
	0.375	0.275	0.275	0.564	0.028	0.18921	0.450	0.80
	0.275	0.15	0.15	0.210	0.006	0.11391	0.163	0.78
	0.175	0.075	0.075	0.064	0.001	0.06172	0.048	0.75
	0.175	0.125	0.125	0.119	0.003	0.08676	0.095	0.80
	0.275	0.1	0.1	0.130	0.003	0.08693	0.095	0.73
	0.35	0.15	0.15	0.255	0.008	0.12344	0.191	0.75
	0.65	0.225	0.225	0.686	0.033	0.19882	0.497	0.72
	0.375	0.2	0.2	0.380	0.015	0.15302	0.294	0.77
	0.275	0.125	0.125	0.169	0.004	0.10087	0.128	0.76
	0.375	0.25	0.25	0.500	0.023	0.17756	0.396	0.79
	0.25	0.125	0.125	0.156	0.004	0.09772	0.120	0.77
	0.175	0.125	0.125	0.119	0.003	0.08676	0.095	0.80
	0.3	0.15	0.15	0.225	0.007	0.11726	0.173	0.77
	0.15	0.1	0.1	0.080	0.002	0.07102	0.063	0.79
	0.25	0.125	0.125	0.156	0.004	0.09772	0.120	0.77
	0.25	0.15	0.15	0.195	0.006	0.11034	0.153	0.78

Sample No	L (mm)	W (mm)	D (mm)	XSA (mm^2)	Xal Vol (mm^3)	r (mm)	SSA (mm^2)	Ratio
XBs11-1	0.375	0.125	0.125	0.219	0.006	0.11186	0.157	0.72
	0.25	0.075	0.075	0.086	0.001	0.06951	0.061	0.70
	0.425	0.2	0.2	0.420	0.017	0.15954	0.320	0.76
	0.375	0.15	0.15	0.270	0.008	0.12631	0.200	0.74
	0.6	0.25	0.25	0.725	0.038	0.20768	0.542	0.75
	0.3	0.1	0.1	0.140	0.003	0.08949	0.101	0.72
	0.125	0.05	0.05	0.030	0.000	0.04210	0.022	0.74
	0.3	0.1	0.1	0.140	0.003	0.08949	0.101	0.72
	0.225	0.075	0.075	0.079	0.001	0.06711	0.057	0.72
	0.625	0.25	0.25	0.750	0.039	0.21052	0.557	0.74
	0.3	0.075	0.075	0.101	0.002	0.07387	0.069	0.68
	0.425	0.15	0.15	0.300	0.010	0.13169	0.218	0.73
	0.45	0.1	0.1	0.200	0.005	0.10243	0.132	0.66
	0.2	0.1	0.1	0.100	0.002	0.07817	0.077	0.77
	0.25	0.1	0.1	0.120	0.003	0.08421	0.089	0.74
	0.45	0.15	0.15	0.315	0.010	0.13423	0.226	0.72
	0.3	0.15	0.15	0.225	0.007	0.11726	0.173	0.77
	0.5	0.25	0.25	0.625	0.031	0.19543	0.480	0.77
	0.375	0.2	0.2	0.380	0.015	0.15302	0.294	0.77
	0.175	0.075	0.075	0.064	0.001	0.06172	0.048	0.75
	0.375	0.15	0.15	0.270	0.008	0.12631	0.200	0.74
	1	0.3	0.3	1.380	0.090	0.27805	0.971	0.70
	0.425	0.1	0.1	0.190	0.004	0.10050	0.127	0.67
	0.325	0.15	0.15	0.240	0.007	0.12043	0.182	0.76
	0.75	0.175	0.175	0.586	0.023	0.17637	0.391	0.67
	0.4	0.125	0.125	0.231	0.006	0.11429	0.164	0.71
	0.4	0.125	0.125	0.231	0.006	0.11429	0.164	0.71
	0.3	0.125	0.125	0.181	0.005	0.10384	0.135	0.75
	0.375	0.25	0.25	0.500	0.023	0.17756	0.396	0.79
	0.225	0.075	0.075	0.079	0.001	0.06711	0.057	0.72
	0.15	0.05	0.05	0.035	0.000	0.04474	0.025	0.72
	0.3	0.15	0.15	0.225	0.007	0.11726	0.173	0.77
	0.375	0.125	0.125	0.219	0.006	0.11186	0.157	0.72
	0.425	0.15	0.15	0.300	0.010	0.13169	0.218	0.73
	0.5	0.15	0.15	0.345	0.011	0.13903	0.243	0.70
	0.375	0.125	0.125	0.219	0.006	0.11186	0.157	0.72
	0.375	0.125	0.125	0.219	0.006	0.11186	0.157	0.72
	0.875	0.375	0.375	1.594	0.123	0.30860	1.196	0.75
	0.35	0.125	0.125	0.206	0.005	0.10931	0.150	0.73
	0.35	0.15	0.15	0.255	0.008	0.12344	0.191	0.75
	0.25	0.1	0.1	0.120	0.003	0.08421	0.089	0.74
	0.25	0.125	0.125	0.156	0.004	0.09772	0.120	0.77
	0.25	0.1	0.1	0.120	0.003	0.08421	0.089	0.74
	0.325	0.15	0.15	0.240	0.007	0.12043	0.182	0.76
	0.425	0.1	0.1	0.190	0.004	0.10050	0.127	0.67
	0.375	0.125	0.125	0.219	0.006	0.11186	0.157	0.72
	0.25	0.075	0.075	0.086	0.001	0.06951	0.061	0.70
	0.225	0.1	0.1	0.110	0.002	0.08130	0.083	0.75
	0.225	0.125	0.125	0.144	0.004	0.09434	0.112	0.78
	0.4	0.1	0.1	0.180	0.004	0.09849	0.122	0.68

Sample No	L (mm)	W (mm)	D (mm)	XSA (mm2)	Xal Vol (mm3)	r (mm)	SSA (mm2)	Ratio
Dc6	0.5	0.25	0.25	0.625	0.031	0.19543	0.480	0.77
	0.175	0.1	0.1	0.090	0.002	0.07477	0.070	0.78
	0.125	0.075	0.075	0.049	0.001	0.05517	0.038	0.78
	0.525	0.275	0.275	0.729	0.040	0.21167	0.563	0.77
	0.45	0.175	0.175	0.376	0.014	0.14876	0.278	0.74
	0.175	0.125	0.125	0.119	0.003	0.08676	0.095	0.80
	0.2	0.1	0.1	0.100	0.002	0.07817	0.077	0.77
	0.2	0.1	0.1	0.100	0.002	0.07817	0.077	0.77
	0.875	0.25	0.25	1.000	0.055	0.23551	0.697	0.70
	0.275	0.125	0.125	0.169	0.004	0.10087	0.128	0.76
	0.45	0.175	0.175	0.376	0.014	0.14876	0.278	0.74
	0.425	0.2	0.2	0.420	0.017	0.15954	0.320	0.76
	0.175	0.1	0.1	0.090	0.002	0.07477	0.070	0.78
	0.275	0.175	0.175	0.254	0.008	0.12624	0.200	0.79
	0.275	0.1	0.1	0.130	0.003	0.08693	0.095	0.73
	0.4	0.15	0.15	0.285	0.009	0.12906	0.209	0.73
	0.125	0.075	0.075	0.049	0.001	0.05517	0.038	0.78
	0.475	0.15	0.15	0.330	0.011	0.13667	0.235	0.71
	0.3	0.15	0.15	0.225	0.007	0.11726	0.173	0.77
	0.325	0.15	0.15	0.240	0.007	0.12043	0.182	0.76
	0.375	0.125	0.125	0.219	0.006	0.11186	0.157	0.72
	0.425	0.125	0.125	0.244	0.007	0.11662	0.171	0.70
	0.15	0.075	0.075	0.056	0.001	0.05863	0.043	0.77
	0.65	0.2	0.2	0.600	0.026	0.18381	0.424	0.71
	0.625	0.15	0.15	0.420	0.014	0.14976	0.282	0.67
	0.25	0.125	0.125	0.156	0.004	0.09772	0.120	0.77
	0.375	0.125	0.125	0.219	0.006	0.11186	0.157	0.72
	0.625	0.175	0.175	0.499	0.019	0.16597	0.346	0.69
	0.35	0.125	0.125	0.206	0.005	0.10931	0.150	0.73
	0.375	0.175	0.175	0.324	0.011	0.13998	0.246	0.76
	0.55	0.125	0.125	0.306	0.009	0.12709	0.203	0.66
	0.2	0.075	0.075	0.071	0.001	0.06453	0.052	0.73
	0.4	0.2	0.2	0.400	0.016	0.15634	0.307	0.77
	0.2	0.1	0.1	0.100	0.002	0.07817	0.077	0.77
	0.375	0.2	0.2	0.380	0.015	0.15302	0.294	0.77
	0.35	0.1	0.1	0.160	0.004	0.09420	0.111	0.70
	0.45	0.25	0.25	0.575	0.028	0.18869	0.447	0.78
	0.375	0.125	0.125	0.219	0.006	0.11186	0.157	0.72
	0.5	0.175	0.175	0.411	0.015	0.15407	0.298	0.72
	0.3	0.1	0.1	0.140	0.003	0.08949	0.101	0.72
	0.5	0.2	0.2	0.480	0.020	0.16842	0.356	0.74
	0.125	0.075	0.075	0.049	0.001	0.05517	0.038	0.78
	0.375	0.15	0.15	0.270	0.008	0.12631	0.200	0.74
	0.75	0.3	0.3	1.080	0.068	0.25263	0.802	0.74
	0.45	0.25	0.25	0.575	0.028	0.18869	0.447	0.78
	0.4	0.175	0.175	0.341	0.012	0.14303	0.257	0.75
	0.25	0.125	0.125	0.156	0.004	0.09772	0.120	0.77
	0.55	0.125	0.125	0.306	0.009	0.12709	0.203	0.66
	0.55	0.175	0.175	0.446	0.017	0.15905	0.318	0.71
	0.4	0.15	0.15	0.285	0.009	0.12906	0.209	0.73

Sample No	L (mm)	W (mm)	D (mm)	XSA (mm2)	Xal Vol (mm3)	r (mm)	SSA (mm2)	Ratio
E1-1	0.55	0.25	0.25	0.675	0.034	0.20174	0.511	0.76
	0.15	0.075	0.075	0.056	0.001	0.05863	0.043	0.77
	0.4	0.15	0.15	0.285	0.009	0.12906	0.209	0.73
	0.25	0.125	0.125	0.156	0.004	0.09772	0.120	0.77
	0.425	0.15	0.15	0.300	0.010	0.13169	0.218	0.73
	0.75	0.275	0.275	0.976	0.057	0.23839	0.714	0.73
	0.375	0.15	0.15	0.270	0.008	0.12631	0.200	0.74
	0.575	0.2	0.2	0.540	0.023	0.17645	0.391	0.72
	0.15	0.075	0.075	0.056	0.001	0.05863	0.043	0.77
	0.25	0.125	0.125	0.156	0.004	0.09772	0.120	0.77
	0.15	0.1	0.1	0.080	0.002	0.07102	0.063	0.79
	0.325	0.125	0.125	0.194	0.005	0.10665	0.143	0.74
	0.3	0.125	0.125	0.181	0.005	0.10384	0.135	0.75
	0.25	0.1	0.1	0.120	0.003	0.08421	0.089	0.74
	0.275	0.125	0.125	0.169	0.004	0.10087	0.128	0.76
	0.175	0.1	0.1	0.090	0.002	0.07477	0.070	0.78
	0.35	0.15	0.15	0.255	0.008	0.12344	0.191	0.75
	0.425	0.175	0.175	0.359	0.013	0.14595	0.268	0.75
	0.175	0.1	0.1	0.090	0.002	0.07477	0.070	0.78
	0.8	0.2	0.2	0.720	0.032	0.19698	0.487	0.68
	0.325	0.1	0.1	0.150	0.003	0.09190	0.106	0.71
	0.15	0.075	0.075	0.056	0.001	0.05863	0.043	0.77
	0.25	0.1	0.1	0.120	0.003	0.08421	0.089	0.74
	0.15	0.075	0.075	0.056	0.001	0.05863	0.043	0.77
	0.6	0.25	0.25	0.725	0.038	0.20768	0.542	0.75
	0.225	0.1	0.1	0.110	0.002	0.08130	0.083	0.75
	0.575	0.175	0.175	0.464	0.018	0.16142	0.327	0.71
	0.325	0.175	0.175	0.289	0.010	0.13346	0.224	0.77
	0.575	0.15	0.15	0.390	0.013	0.14566	0.266	0.68
	0.375	0.125	0.125	0.219	0.006	0.11186	0.157	0.72
	0.425	0.175	0.175	0.359	0.013	0.14595	0.268	0.75
	0.175	0.1	0.1	0.090	0.002	0.07477	0.070	0.78
	0.3	0.175	0.175	0.271	0.009	0.12995	0.212	0.78
	0.425	0.15	0.15	0.300	0.010	0.13169	0.218	0.73
	0.275	0.125	0.125	0.169	0.004	0.10087	0.128	0.76
	0.2	0.125	0.125	0.131	0.003	0.09071	0.103	0.79
	0.225	0.125	0.125	0.144	0.004	0.09434	0.112	0.78
	0.25	0.15	0.15	0.195	0.006	0.11034	0.153	0.78
	0.125	0.075	0.075	0.049	0.001	0.05517	0.038	0.78
	0.25	0.125	0.125	0.156	0.004	0.09772	0.120	0.77
	0.35	0.125	0.125	0.206	0.005	0.10931	0.150	0.73
	0.275	0.125	0.125	0.169	0.004	0.10087	0.128	0.76
	0.45	0.15	0.15	0.315	0.010	0.13423	0.226	0.72
	0.25	0.125	0.125	0.156	0.004	0.09772	0.120	0.77
	0.775	0.325	0.325	1.219	0.082	0.26940	0.912	0.75
	0.65	0.2	0.2	0.600	0.026	0.18381	0.424	0.71
	0.75	0.25	0.25	0.875	0.047	0.22371	0.629	0.72
	0.225	0.125	0.125	0.144	0.004	0.09434	0.112	0.78
	0.375	0.1	0.1	0.170	0.004	0.09639	0.117	0.69
	0.625	0.325	0.325	1.024	0.066	0.25076	0.790	0.77

Sample No	L (mm)	W (mm)	D (mm)	XSA (mm2)	Xal Vol (mm3)	r (mm)	SSA (mm2)	Ratio
XF15-1	0.25	0.125	0.125	0.156	0.004	0.09772	0.120	0.77
	0.175	0.1	0.1	0.090	0.002	0.07477	0.070	0.78
	0.525	0.2	0.2	0.500	0.021	0.17118	0.368	0.74
	0.35	0.2	0.2	0.360	0.014	0.14954	0.281	0.78
	0.2	0.075	0.075	0.071	0.001	0.06453	0.052	0.73
	0.5	0.2	0.2	0.480	0.020	0.16842	0.356	0.74
	0.675	0.375	0.375	1.294	0.095	0.28303	1.006	0.78
	0.375	0.15	0.15	0.270	0.008	0.12631	0.200	0.74
	0.15	0.075	0.075	0.056	0.001	0.05863	0.043	0.77
	0.7	0.2	0.2	0.640	0.028	0.18841	0.446	0.70
	0.75	0.25	0.25	0.875	0.047	0.22371	0.629	0.72
	0.3	0.125	0.125	0.181	0.005	0.10384	0.135	0.75
	0.4	0.15	0.15	0.285	0.009	0.12906	0.209	0.73
	0.475	0.125	0.125	0.269	0.007	0.12103	0.184	0.68
	0.25	0.125	0.125	0.156	0.004	0.09772	0.120	0.77
	0.125	0.075	0.075	0.049	0.001	0.05517	0.038	0.78
	0.3	0.175	0.175	0.271	0.009	0.12995	0.212	0.78
	0.525	0.2	0.2	0.500	0.021	0.17118	0.368	0.74
	0.275	0.125	0.125	0.169	0.004	0.10087	0.128	0.76
	0.275	0.125	0.125	0.169	0.004	0.10087	0.128	0.76
	0.3	0.125	0.125	0.181	0.005	0.10384	0.135	0.75
	0.75	0.325	0.325	1.186	0.079	0.26647	0.892	0.75
	0.5	0.1	0.1	0.220	0.005	0.10610	0.141	0.64
	0.45	0.25	0.25	0.575	0.028	0.18869	0.447	0.78
	0.45	0.15	0.15	0.315	0.010	0.13423	0.226	0.72
	0.175	0.1	0.1	0.090	0.002	0.07477	0.070	0.78
	0.225	0.075	0.075	0.079	0.001	0.06711	0.057	0.72
	0.375	0.075	0.075	0.124	0.002	0.07957	0.080	0.64
	0.625	0.25	0.25	0.750	0.039	0.21052	0.557	0.74
	0.175	0.05	0.05	0.040	0.000	0.04710	0.028	0.70
	0.5	0.2	0.2	0.480	0.020	0.16842	0.356	0.74
	0.375	0.2	0.2	0.380	0.015	0.15302	0.294	0.77
	0.325	0.175	0.175	0.289	0.010	0.13346	0.224	0.77
	0.75	0.175	0.175	0.586	0.023	0.17637	0.391	0.67
	0.2	0.075	0.075	0.071	0.001	0.06453	0.052	0.73
	0.225	0.1	0.1	0.110	0.002	0.08130	0.083	0.75
	0.375	0.1	0.1	0.170	0.004	0.09639	0.117	0.69
	0.3	0.125	0.125	0.181	0.005	0.10384	0.135	0.75
	0.35	0.1	0.1	0.160	0.004	0.09420	0.111	0.70
	0.375	0.25	0.25	0.500	0.023	0.17756	0.396	0.79
	0.375	0.125	0.125	0.219	0.006	0.11186	0.157	0.72
	0.5	0.25	0.25	0.625	0.031	0.19543	0.480	0.77
	0.25	0.15	0.15	0.195	0.006	0.11034	0.153	0.78
	0.225	0.1	0.1	0.110	0.002	0.08130	0.083	0.75
	0.5	0.2	0.2	0.480	0.020	0.16842	0.356	0.74
	0.4	0.15	0.15	0.285	0.009	0.12906	0.209	0.73
	0.225	0.1	0.1	0.110	0.002	0.08130	0.083	0.75
	0.25	0.15	0.15	0.195	0.006	0.11034	0.153	0.78
	0.375	0.125	0.125	0.219	0.006	0.11186	0.157	0.72
	0.625	0.3	0.3	0.930	0.056	0.23773	0.710	0.76

Sample No	L (mm)	W (mm)	D (mm)	XSA (mm2)	Xal Vol (mm3)	r (mm)	SSA (mm2)	Ratio
G1	0.375	0.15	0.15	0.270	0.008	0.12631	0.200	0.74
	0.3	0.2	0.2	0.320	0.012	0.14205	0.253	0.79
	0.375	0.2	0.2	0.380	0.015	0.15302	0.294	0.77
	0.325	0.1	0.1	0.150	0.003	0.09190	0.106	0.71
	0.3	0.1	0.1	0.140	0.003	0.08949	0.101	0.72
	0.375	0.15	0.15	0.270	0.008	0.12631	0.200	0.74
	0.625	0.175	0.175	0.499	0.019	0.16597	0.346	0.69
	0.2	0.125	0.125	0.131	0.003	0.09071	0.103	0.79
	0.45	0.2	0.2	0.440	0.018	0.16261	0.332	0.75
	0.45	0.15	0.15	0.315	0.010	0.13423	0.226	0.72
	0.375	0.15	0.15	0.270	0.008	0.12631	0.200	0.74
	0.3	0.15	0.15	0.225	0.007	0.11726	0.173	0.77
	0.425	0.1	0.1	0.190	0.004	0.10050	0.127	0.67
	0.15	0.075	0.075	0.056	0.001	0.05863	0.043	0.77
	0.25	0.075	0.075	0.086	0.001	0.06951	0.061	0.70
	0.25	0.125	0.125	0.156	0.004	0.09772	0.120	0.77
	0.125	0.075	0.075	0.049	0.001	0.05517	0.038	0.78
	0.25	0.1	0.1	0.120	0.003	0.08421	0.089	0.74
	0.325	0.1	0.1	0.150	0.003	0.09190	0.106	0.71
	0.5	0.2	0.2	0.480	0.020	0.16842	0.356	0.74
	0.8	0.3	0.3	1.140	0.072	0.25812	0.837	0.73
	0.225	0.125	0.125	0.144	0.004	0.09434	0.112	0.78
	0.275	0.1	0.1	0.130	0.003	0.08693	0.095	0.73
	0.225	0.125	0.125	0.144	0.004	0.09434	0.112	0.78
	0.4	0.1	0.1	0.180	0.004	0.09849	0.122	0.68
	0.275	0.1	0.1	0.130	0.003	0.08693	0.095	0.73
	0.325	0.15	0.15	0.240	0.007	0.12043	0.182	0.76
	0.525	0.175	0.175	0.429	0.016	0.15660	0.308	0.72
	0.15	0.1	0.1	0.080	0.002	0.07102	0.063	0.79
	0.175	0.05	0.05	0.040	0.000	0.04710	0.028	0.70
	0.325	0.175	0.175	0.289	0.010	0.13346	0.224	0.77
	0.225	0.125	0.125	0.144	0.004	0.09434	0.112	0.78
	0.4	0.175	0.175	0.341	0.012	0.14303	0.257	0.75
	0.325	0.15	0.15	0.240	0.007	0.12043	0.182	0.76
	0.3	0.1	0.1	0.140	0.003	0.08949	0.101	0.72
	0.3	0.125	0.125	0.181	0.005	0.10384	0.135	0.75
	0.45	0.175	0.175	0.376	0.014	0.14876	0.278	0.74
	0.525	0.15	0.15	0.360	0.012	0.14131	0.251	0.70
	0.775	0.3	0.3	1.110	0.070	0.25540	0.819	0.74
	0.55	0.125	0.125	0.306	0.009	0.12709	0.203	0.66
	0.4	0.125	0.125	0.231	0.006	0.11429	0.164	0.71
	0.575	0.15	0.15	0.390	0.013	0.14566	0.266	0.68
	0.225	0.05	0.05	0.050	0.001	0.05122	0.033	0.66
	0.325	0.175	0.175	0.289	0.010	0.13346	0.224	0.77
	0.275	0.075	0.075	0.094	0.002	0.07176	0.065	0.69
	0.4	0.15	0.15	0.285	0.009	0.12906	0.209	0.73
	0.55	0.15	0.15	0.375	0.012	0.14351	0.259	0.69
	0.15	0.1	0.1	0.080	0.002	0.07102	0.063	0.79
	0.5	0.225	0.225	0.551	0.025	0.18218	0.417	0.76
	0.425	0.15	0.15	0.300	0.010	0.13169	0.218	0.73

D.1.1 FIELD LOCATION MAP: 4TH JUNE (A) and 30TH JUNE (B) LAVAS

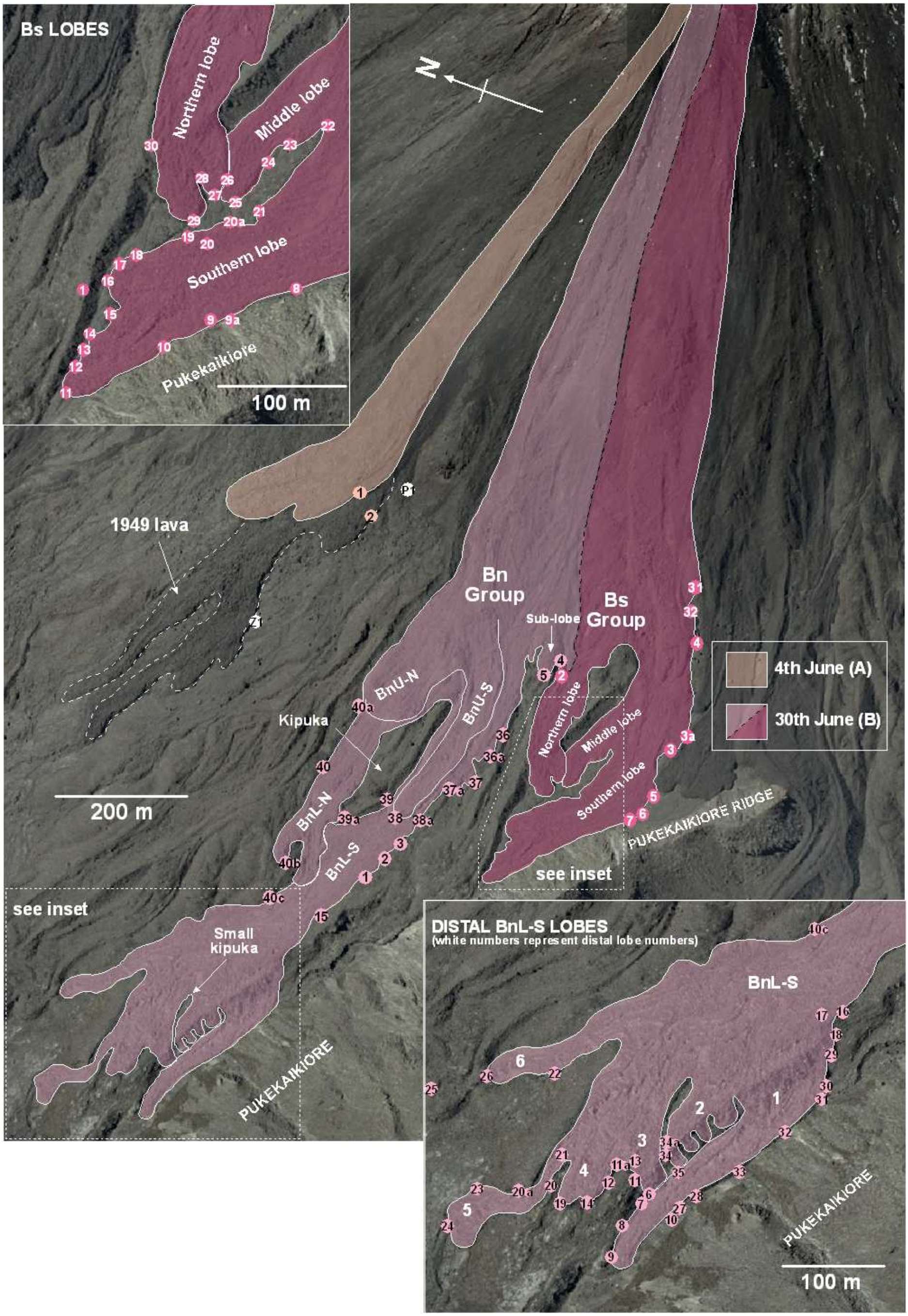

D.1.2 FIELD LOCATION MAP: 14TH JULY (Dc), 29TH JULY (E), 18TH AUGUST (F) and 16TH SEPTEMBER (G) LAVAS